

Universidad Autónoma de Madrid
Programa de Biociencias Moleculares

**Adhesion G protein-coupled
receptor Gpr126 signaling is
essential for placental development**



Rebeca Torregrosa Carrión
Madrid, 2020

Universidad Autónoma de Madrid

Facultad de Medicina

Departamento de Bioquímica

Tesis doctoral

**Adhesion G protein-coupled receptor Gpr126
signaling is essential for placental development**

Rebeca Torregrosa Carrión

Graduada en Biología

Director: José Luis de la Pompa Mínguez

Tutor: Juan José Arredondo Lamas

Centro Nacional de Investigaciones Cardiovasculares (CNIC)



This work was performed in Dr. José Luis de la Pompa laboratory at the Centro Nacional de Investigaciones Cardiovasculares Carlos III (CNIC) in Madrid. This study was funded by grants SAF2016-78370-R, CB16/11/00399, RD16/0011/0021 from the Spanish Ministry of Science, Innovation and Universities (MICIU) to José Luis de la Pompa.

Rebeca Torregrosa Carrión held a PhD fellowship from "la Caixa" Foundation from November 2015 to October 2019 (Reference LCF/BQ/ES15/10360023). The long-term predoctoral stay in the laboratory of Prof. Didier Stainier, in the Department of Developmental Genetics at the Max Plank Institute for Heart and Lung Research (MPI-HLR) (Bad Nauheim, Germany), was funded by an EMBO short-term fellowship (5th April 2018 – 5th July 2018, "Ayudas para Estancias Breves en España y en el Extranjero para Personal Docente e Investigador en Formación de la UAM" (15th August – 15th November), and a Boehringer Ingelheim Fonds Travel Grant (20th May 2019 – 31st July 2019).

A mis abuelos y Alberto

” “The important thing is not to stop questioning.
Curiosity has its own reason for existing”

- **Albert Einstein**

ACKNOWLEDGEMENTS

Este trabajo realmente tiene una larga lista de nombres y apellidos. Gracias a todos los que, de una manera u otra, me habéis ayudado a colocar pieza por pieza hasta llegar a configurar el puzzle final que representa esta tesis.

En primer lugar, quiero agradecer a mi director, **José Luis de la Pompa**, su confianza al abrirme las puertas de su laboratorio y su guía durante estos años de doctorado. Gracias por inculcarme el rigor científico, dar espacio a mis ideas y enseñarme la importancia de perseverar en mi trabajo.

To Prof. **Didier Stainier**, for allowing me to develop part of this thesis work in his laboratory, at the Max Planck Institute for Heart and Lung Research in Bad Nauheim (Germany). I am especially thankful for his interest in this project, valuable suggestions and productive discussion. I have greatly benefitted from his extensive expertise in zebrafish development and his wonderful lab environment.

Gracias también a mi tutor **Juan José Arredondo**, por su rapidez de gestión en momentos de caos con el papeleo de la Universidad, sus comentarios tranquilizadores, y su seguimiento durante todo el periodo predoctoral.

Thank you to all the Dissertation committee members: **Carmelo Bernabeu**, **Catalina Ribas**, **Robert G. Kelly**, **Bill Chaudhry**, **Silvia Martín**, **Joan Isern** and **José María Pérez Pomares**, for dedicating your precious time for the evaluation of this thesis.

A todo el personal de administración, almacén, limpieza, animalario, cultivos, esterilización, seguridad, mantenimiento y recepción, gracias por conseguir que el día a día en el CNIC sea tan fácil. Muchas gracias **Cristina Giménez**, por implicarte tanto con todos los predocs y conseguir modificar las cláusulas de la beca de estancias EMBO para adecuarla a mi situación. A **Almudena**, por la organización de los viajes de congresos. Por supuesto, gracias al personal de la cafetería, que tanto se echa de menos en estos momentos. Gracias **Ángel**, por tu sentido del humor y no fallar nunca con el café. También al servicio de **Informática**, especialmente a **Juan Carlos** y **Alicia**, por llevaros con mi ordenador mucho mejor que yo y resolver nuestros conflictos en un santiamén, y a **Eduardo Maroto**, por rescatar mis correos, mis datos de temporal una y otra vez y asegurarse de que Photoshop no me dejara tirada.

Un enorme gracias a las manos y mentes expertas de las unidades del CNIC por su ayuda e implicación con el proyecto: **Bioinformática**, **Genómica**, **Histopatología**, **Microscopía**, **Proteómica**, **Tecnología de células pluripotentes** y **Transgénesis**. Hacéis una labor impecable y gran parte del trabajo de esta tesis es vuestro. A **Fátima** y **Manuel**, por ayudarme con los datos de RNAseq. A **Vero**, por enseñarme los trucos de los microscopios del CNIC y hacerme ganar calidad de vida con tus fantásticas macros. Al equipo de **Giovanna Giovinzio** y **Luis Miguel**

Criado, por ser los padres de todos los modelos de ratón que se han generado en esta tesis. Gracias **Eduardo Díaz** por cuidar tan bien de los peces y ahorrarnos tantísimo trabajo.

Y qué decir de la segunda familia que he tenido estos cinco años. Aunque la composición ha ido variando con el tiempo, la esencia ha sido la misma: el compañerismo y el gran ambiente de trabajo que define al grupo DLP. Ha sido un placer contar con **Gaetano D'Amato** como supervisor durante mis primeros pasos en el CNIC. Y una experiencia inolvidable, sin duda. Gracias por enseñarme a “funcionar” en el laboratorio y por tu sentido nulo de la vergüenza, me he divertido mucho trabajando contigo. He hecho lo que he podido con el legado que me has dejado, espero haber sido toda una *soddisfazione*!!

Gracias **Belén** por dar siempre con el quid de la cuestión en cuanto a clonajes se refiere y por compartir todos tus trucos “moleculares”. Gracias **Luis** por tu seriedad y sobriedad en el laboratorio y fuera de él, por los ratos de cháchara entre pipeteo y pipeteo, y por tu enorme ayuda para sacar el secretoma adelante. Gracias **Quim**, por tu incansable espíritu de lucha y querer hacer del laboratorio un lugar mejor. **Dimitrios**, thanks for being such a good example of great devotion to science and rigorous work, and for being willing to help me at anytime. Obrigado **Vítor** por tu compañerismo, fomentar el trabajo en equipo y aplicar tus conocimientos de fisiología cardíaca a este proyecto, aunque eso te supusiese echar horas extra. Gracias **Donal**, por estar siempre atento en los lab meeting e interrogar a Gpr126 hasta hacerlo hablar. **Abel** y **Luci**, no sé qué habría hecho sin vosotros. Mil gracias por el trabajo tan impecable que hacéis con los ratones y resolver tan rápido cualquier petición a destiempo. Gracias también **Luci** por los ratos en los que subes a revolucionar el patio con tu desparpajo y por tu predisposición a adelantarme trabajo. Gracias **Vanessa García**, por tu esfuerzo y estar siempre dispuesta a echar una mano. **Marcos**, gracias por enseñarme el fascinante mundo del CRISPR-Cas9 y estar tan actualizado con las noticias del trasvase Tajo-Segura. Gracias **Vera**, mi compañera de “promoción”, por tu entrañable espontaneidad y simpatía, por conseguir que contar BrdU sea tan fácil como hacer un click y compartir conmigo este último “trago” de tesis. **Tamara**, eres la caña. Gracias por contagiarme de la pasión que transmites por la ciencia, amenizar las largas jornadas en el laboratorio hablando de cualquier tema y estar siempre dispuesta a hacer un favor. Es un lujo trabajar contigo. **Ale** (ahora **cachas**), el compi Cicerone que comenzó conmigo esta andadura. Hemos compartido prácticamente todos estos años y has sido un gran apoyo tanto dentro como fuera del laboratorio. Gracias por tu confianza, tu sentido del humor (con karma incluido) y conseguir que sonría al echar la vista atrás. No te olvides de tus inicios cuando te conviertas en una estrella del rock! Y con especial cariño a **Rebequiña**, gracias por absolutamente todo. Ha sido una experiencia muy gratificante guiarte durante tu primer año en el laboratorio, aprender contigo y ser partícipe de tu evolución. Muchas gracias por tu enorme dedicación y compromiso con el proyecto e incluso

llegar a asumirlo durante mi estancia. Y gracias también por todo el tiempo que he disfrutado contigo en el laboratorio, por tu apoyo y tu energía positiva. Gracias por formar un pack conmigo desde el primer día.

También quiero agradecer todo lo que he aprendido de los antiguos miembros del laboratorio, con los que también he compartido muchas horas: **Beatriz Martínez**, mi primera supervisora en el laboratorio; **Mauro**, mi maestro de qPCRs; **Sara**, la maga de las PCRs; **Juli**, la investigadora más aplicada que he conocido; **Beatriz Ríos**, un ejemplo de meticulosidad y perfección en el trabajo; **Patri**, mi codo con codo y y fiel enemiga de la entropía; **Lao** y sus locuras; **Tania**, gran promotora del team building y **Vanessa Bou**, la narradora de anécdotas más divertida.

Muchas gracias también a la 3N al completo, el ala más concurrida de todo el CNIC. Gracias por buena compañía todos estos años y compartir protocolos y reactivos salvaexperimentos. A los **Beneditos**, por las discusiones científicas de los Notch Meeting, y a los **Torres**, por las conversaciones y la música en común. **Wen**, thank you for being such an amazing lab mate, for your kindness and be willing to help everybody at anytime. Thank you very much also for the gifts and sweets you always bring from China! Gracias **Macarena** por poder compartir contigo las preocupaciones que arrastra la tesis, tu ayuda con todos los papeleos y ser una compi tan maja y salá. **Javi**, gracias por tus bromas y buen rollo. Gracias **Susana**, por tu cariño y compañía en la zona de los geles, donde probablemente hemos pasado más tiempo hablando que pipeteando. **Héctor**, gracias por demostrarme que sí se puede compaginar una tesis con doscientas tareas más, e invertir tu tiempo en leerte esta tesis y valorarla.

A big thank you to **Didier's lab team**. It is scary to start alone in a new laboratory in a foreign country, and you made it the easiest thing in the world. Thanks for making me feel very welcomed since the very first moment I stepped into the lab, and for all your support and help during my back and forth stay. I learned a lot about zebrafish husbandry, single-cell microinjections, and live imaging in the zebrafish heart. Also, thank you **Albert**, **Alessandra**, **Anaïs**, **Claudia**, **Gabriel**, **Giulia**, **Hadil**, **Jane**, **João**, **Laurie**, **Leonie**, **Mohamed**, **Sarah**, **Srinath**, **Srinivas**, **Teja**, **Vahan**, **Violette**... for the nice plans and activities out of the lab, that I very much enjoyed. I will always take it as a wonderful and unforgettable experience. Thank you, **Sharon**, for organizing every stay and for your generous help with the applications for the traveling fellowships. Arigatô **Nana** for your kindness and your excellent guidance during the generation of the zebrafish lines. Danke **Hans Martin** for teaching me how to work with zebrafish, and **Vanesa** for showing me the best way to do imaging on a zebrafish heart. Thank you, **Rubén**, for the great scientific discussion. And especially, a huge thanks to **Jane**, **Sarah** and **Srinath**, for the great times we spent together and for being my german family.

Trabajar en el CNIC me ha brindado la posibilidad de conocer a gente fantástica, algunos de los cuales se han acabado convirtiendo en grandes amigos. Gracias **Alba, Austin, Carlos, Juanlu, Junior, Marta, Mer, Raquel, Víctor Fanjul y Víctor Manzanilla**, por todo lo que hemos compartido estos años y ser la mejor parte de esta etapa. Que lo que una la tesis no lo separe nadie.

Muchas gracias a **Elena y Gema**, por haber disfrutado y sufrido conmigo esta tesis y ser las mejores compañeras de aventuras (y tontunas). Y viva el método Pomodoro, que me nos ha permitido a escribir la tesis en buena compañía a pesar del confinamiento. **Mao**, gracias por ayudarme a desconectar siempre que lo he necesitado. Gracias **Patri**, por ser tan buena amiga, escucharme y entenderme. Y recuerda: cultivar células madre es como cuidar un tamagochi. **Carol**, gracias por hacer de hermana mayor y revisar esta tesis de manera tan altruista. Muchas gracias, **David**, por aportar el toque artístico y dar forma a mis etéreas ideas.

Mil gracias a mis **abuelos**, por su cariño y amor incondicional. Gracias por ser mi refugio y tener siempre unas palabras de aliento con las que ayudarme a recuperar la confianza en mí misma. Gracias por alegraros por mis logros más que yo. Gracias por darme tanto. A mis **padres**, muchas gracias por todo el esfuerzo que habéis hecho para que haya podido llegar hasta aquí, y estar presentes siempre que he necesitado ayuda o una vía de escape. Gracias por todo el apoyo que me habéis dado y soportar pacientemente mi monotema estos últimos meses. Gracias **David**, por tu peculiar forma de darme ánimos encontrando siempre el vídeo perfecto con el que soltar una carcajada. Siempre hay un yan para un yin. Y a mis queridos primos, **Raquelilla y Alberto**, por vuestro cariño, apoyo e interés durante esta etapa y todas las anteriores. Esta tesis va especialmente dedicada a ti, **Alberto**. No me cabe la menor duda de que te habrías convertido en un excelente investigador, tu curiosidad e ingenio siempre han ido por delante y en este campo se habrían convertido en tus mejores aliados. La pasión y energía que le ponías a todo ha sido y será siempre una enorme fuente de inspiración.

Y, sobre todo, gracias a ti **Luis**. Has sido el techo sobre mi cabeza, el suelo bajo mis pies y la mano en la que apoyarme. Gracias por haberme acompañado con tanto cariño y paciencia en esta etapa y vivirla conmigo como un equipo. Contigo he aprendido a relativizar los problemas y a mirar con otra perspectiva. Como diría tu escritor favorito, gracias por ser mi puerto seguro en un mar infinito y tempestuoso.

SUMMARY

Gpr126 is an adhesion G protein-coupled receptor (GPCR) that is required for peripheral nervous system (PNS) development in mice and zebrafish. In the heart, *Gpr126* is expressed in the endocardium and its inactivation in mice leads to embryonic lethality and defective ventricular trabeculation, defects that are also recapitulated in zebrafish larvae using morpholinos, but the mechanistic bases of this phenotype are unknown. Here, we have generated an allelic series of standard, conditional loss- and gain-of-function alleles in mice and zebrafish, to decipher the role of *Gpr126* in development. We found that *Gpr126* standard knockout mice lacking exons 3 and 4 (*Gpr126^{Δ3,4}*) develop to term and show abnormal joint stiffness in the forelimbs and hindlimbs and impaired mobility, indicating that the deleted CUB and PTX adhesive domains are essential for PNS development. Deletion of exon 7 disrupts GPR126 protein translation, and *Gpr126^{Δ7}* mice show a thinner ventricular wall and trabeculae and die at embryonic day 13.5 (E13.5) with no signs of ventricular patterning, metabolic or proliferation defects. In contrast, endocardial-specific deletion of exon 7 in *Gpr126^{fllox}* mice does not cause lethality, and mutant mice are normal and reach adulthood. In addition, *gpr126* nonsense and promoter-less zebrafish mutants show normal trabeculation. Interestingly, the embryonic lethality of *Gpr126^{Δ7}* mice is not rescued by transgenic expression of *Gpr126* in the endocardium, suggesting that the cause of death is likely due to defective development of another tissue. *Gpr126* is also expressed in the trophoblast giant cells that invade and remodel the maternal spiral arteries of the placenta. *Gpr126^{Δ7}* mutant placentas show downregulation of two placenta-specific cathepsins, *Cts7* and *Cts8*, the last one involved in the maternal uterine vasculature remodeling from high-resistant to low-resistant vessels, by mediating the loss of smooth muscle α -actin. These changes in vessel architecture allow a crucial increase in the blood flow supply to the fetus at much-reduced pressure, and failure of this process can lead to pregnancy pathologies such as early pregnancy loss, intrauterine growth restriction and preeclampsia. We have used the *Sox2-Cre* driver line, active in the maternal germline or the zygote depending on its female or male origin, to establish the requirement of *Gpr126* for placentation and embryonic development. We found that *Gpr126^{Δ7}* homozygous mutants associated with a heterozygous placenta survive to term but show typical *Gpr126*-defective PNS phenotypes. In contrast, homozygous mutants associated with a mutant placenta die at the same stages that *Gpr126^{Δ7}* mutants. In summary, we demonstrated that *Gpr126* is essential for placental development to promote spiral artery remodeling in the trophoblast-derived cell lineage, and sustain normal developmental progression, and propose the placenta-heart axis as an explanation for heart abnormalities concurrent with placental defects in *Gpr126* mouse mutants.

RESUMEN

Gpr126 es un receptor de adhesión acoplado a proteína G (GPCR) implicado en el desarrollo del sistema nervioso periférico (PNS) tanto en ratón como en pez cebra. En el corazón se expresa en el endocardio de las cámaras, y su inactivación ocasiona letalidad embrionaria y defectos en el proceso de trabeculación en ratón, un fenotipo recapitulable en el pez cebra mediante el uso de morfolidos. Sin embargo, poco se conoce acerca de su mecanismo de señalización en el corazón. En este trabajo hemos generado dos modelos constitutivos de pérdida de función (*knock-out*) en ratón y en pez cebra, además de dos alelos condicionales de pérdida (*Gpr126^{lox}*) y ganancia de función (*R26-GPR126^{GOF}*) en ratón, para esclarecer el papel de Gpr126 durante el desarrollo embrionario. Los ratones *knock-out* con una delección en los exones 3 y 4 (*Gpr126^{Δ3,4}*) presentan rigidez en las articulaciones y una limitación del movimiento desde que nacen, lo cual apunta a que los dominios de adhesión CUB y PTX son esenciales para el desarrollo del PNS. Por otro lado, los ratones *knock-out* con una delección del exón 7 (*Gpr126^{Δ7}*), una mutación sin sentido que genera un codón STOP prematuro, mueren durante el desarrollo embrionario (E13.5) y presentan defectos cardíacos, aunque el patrón de expresión génico, el metabolismo y la tasa de proliferación de los ventrículos son normales. La delección condicional del mismo exón en el endocardio no provoca letalidad embrionaria, y los ratones mutantes alcanzan la edad adulta. En el pez cebra, la falta del promotor de *gpr126* tampoco compromete el proceso de trabeculación ni la viabilidad embrionaria. Además, la sobreexpresión de *GPR126* en el endocardio no rescata la letalidad embrionaria de los ratones *Gpr126^{Δ7/Δ7}*, lo cual indica que la muerte temprana podría estar ocasionada por defectos en el desarrollo de otro(s) órgano(s). *Gpr126* también se expresa en las células gigantes del trofoblasto que invaden las arterias espirales maternas de la placenta. Las placentas de embriones *Gpr126^{Δ7/Δ7}* tienen disminuida la expresión de dos catepsinas placentarias, *Cts7* y *Cts8*, esta última implicada en el remodelado de las arterias uterinas mediante la degradación de la capa de músculo liso. Esta modificación permite una dilatación de los vasos fundamental para incrementar el flujo sanguíneo en el útero sin que exista riesgo de hipertensión. Fallos en este proceso están asociados a patologías del embarazo como la preeclampsia, la restricción del crecimiento intrauterino e incluso abortos. Con la línea *Sox2-Cre*, activa en el linaje germinal o en el epiblasto dependiendo del origen materno o paterno de la Cre recombinasa, hemos comprobado que los embriones mutantes asociados a placentas heterocigotas llegan a nacer, pero muestran un fenotipo característico asociado a defectos en el desarrollo del PNS. Por el contrario, los mutantes asociados a placentas homocigotas mueren en los mismos estadios embrionarios que los embriones *Gpr126^{Δ7/Δ7}*. Este trabajo demuestra que Gpr126 juega un papel fundamental en el desarrollo de la placenta para garantizar la viabilidad embrionaria, al promover el remodelado de las arterias espirales uterinas desde el linaje trofoblástico, y resalta la importancia del eje placenta-corazón.

CONTENTS

INTRODUCTION	35
1. Cardiac development in mice and zebrafish	37
2. Development of the mouse placenta	40
2.1 From the blastocyst (E3.5) to the mature placenta (E12.5)	42
2.2 Labyrinth formation and function	43
2.3 Junctional zone formation and function	45
2.4 Role of TGCs in establishing the maternal vasculature of the placenta	45
2.5 TGC-mediated spiral artery remodeling and vasculogenic mimicry	46
2.6 Impaired vascular remodeling in preeclampsia	47
3. Structural basis and signaling mechanism of Gpr126	48
3.1 Gpr126 is essential for PNS, inner ear and heart development in zebrafish and mice	51
4. Notch activity is required for ventricular trabeculation in mice	53
OBJECTIVES	55
MATERIALS AND METHODS	59
1. Mouse lines	61
1.1 Ethics statement	61
1.2 Generation of <i>Gpr126</i> ^{Δ3,4} , <i>Gpr126</i> ^{Δ7} and <i>Gpr126</i> ^{fllox} mouse lines	61
1.3 Generation of <i>R26-GPR126</i> ^{GOF} mouse line	66
1.4 Mouse strains	67
2. Zebrafish lines	67
2.1 Ethics statement	67
2.2 Generation of <i>gpr126</i> ^{bns341} and <i>gpr126</i> ^{bns342} zebrafish lines	67
2.3 Transgenic zebrafish lines	70
3. Genomic DNA extraction, genotyping, and sequencing	72
4. Histological procedures	74
4.1 Tissue collection and processing	74
4.2 Histological staining	75
4.3 Detection of hypoxic cells	75
4.4 DIG-labeled RNA probe synthesis	77
4.5 <i>In situ</i> hybridization (ISH) on sections	78
4.6 Whole-mount <i>in situ</i> hybridization (WISH)	79
5. Gene expression analysis	80
5.1 RNA extraction and cDNA preparation	80
5.2 Quantitative real-time PCR (qRT-PCR)	80
5.3 RNA extraction and RNA sequencing (RNA-seq) analysis	84
6. Bioinformatics and statistics	84
6.1 Bioinformatic analysis of RNAseq data	84
6.2 Sequence similarity analysis of mouse and zebrafish <i>gpr126</i> gene	85
6.3 Statistical analysis	85

7. Imaging.....	86
7.1 Zebrafish embryo preparation for live imaging	86
7.2 Microscopy and confocal imaging	86
7.3 Quantification of cellular proliferation.....	86
7.4 Quantification of hypoxia.....	87
7.5 Quantification of the zebrafish ear area.....	87
7.6 Quantification of PAS-positive areas	87
7.7 Quantification of maternal and fetal blood spaces in the placenta.....	87
7.8 Quantification of Rhodamine 123 fluorescence intensity	88
8. Interventions.....	88
8.1 BrdU injection	88
8.2 Rhodamine 123	88
8.3 Electrocardiographic (ECG) recordings	89
8.4 Measurement of tibial length	89
RESULTS	91
<i>Gpr126</i> expression is restricted to the endocardium during heart development.....	93
Generation of <i>Gpr126</i> ^{Δ3,4} knockout mouse model using CRISPR/Cas9 technology	94
CUB and PTX domains are essential for peripheral nervous system development, but dispensable for heart development.....	96
One-step generation of constitutive and conditional <i>Gpr126</i> knockout mouse models using CRISPR/Cas9 technology	98
Homozygosity of the <i>Gpr126</i> ^{Δ7} knockout allele causes embryonic lethality	102
<i>Gpr126</i> ^{Δ7/Δ7} embryos show cardiac defects.....	103
Chamber patterning, cellular proliferation and metabolism are not affected in <i>Gpr126</i> ^{Δ7/Δ7} mutant hearts.....	105
Disruption of <i>Gpr126</i> signaling in the heart affects vasculature development-related processes	110
Conditional <i>Gpr126</i> deletion in either the endocardium or the heart does not cause embryonic lethality.....	112
<i>Gpr126</i> ^{fl/fl} ; <i>Tie2-Cre</i> adult mice have normal cardiac morphology and electrical activity....	115
Generation of conditional <i>R26-GPR126</i> ^{GOF} transgenic mouse line by homologous recombination in mESC	117
Conditional <i>GPR126</i> overexpression in the <i>Tie2-Cre</i> lineage allows normal heart development and does not rescue <i>Gpr126</i> ^{Δ7} embryonic lethality	119
<i>GPR126</i> overexpression fails to rescue impaired EMT and hypotrabeulation in <i>Dll4</i> ^{fllox} ; <i>Tie2-Cre</i> mutants	121
Generation of zebrafish <i>gpr126</i> mutants using CRISPR-Cas9 technology	123
Sequence similarity analysis of zebrafish <i>gpr126</i> reveals <i>gpr112</i> as a potential adapting gene	126
The <i>gpr126</i> ^{bns341} and <i>gpr126</i> ^{bns342} mutations disrupt inner ear development in zebrafish	126
The <i>gpr126</i> ^{bns341} and <i>gpr126</i> ^{bns342} mutations do not impair heart development	128

<i>Gpr126</i> is expressed in the spongiotrophoblast layer and the four TGC subtypes of the mouse placenta	130
<i>Gpr126</i> expression in the placenta is crucial for embryonic survival	133
<i>Gpr126</i> is required for glycogen accumulation in the placenta	136
<i>Gpr126</i> ^{Δ7/Δ7} mutant placentas show maternal vascular abnormalities in the labyrinth.....	138
Placental transport is unaffected in <i>Gpr126</i> ^{Δ7/Δ7} placentas	140
<i>Gpr126</i> ^{Δ7/Δ7} mutants show downregulation of placental cathepsins	143
<i>Gpr126</i> ^{Δ7/Δ7} placentas show downregulation of the preeclampsia marker <i>Mmp9</i>	147
DISCUSSION	151
The CUB and PTX domains of <i>Gpr126</i> are essential for PNS development in mice	154
<i>Gpr126</i> is dispensable for heart trabeculation in zebrafish	156
The placenta-heart axis underlies cardiac defects in <i>Gpr126</i> mutant mice	157
Regulation of maternal spiral artery remodeling by <i>Gpr126</i> and its potential implication in preeclampsia	162
Altered uteroplacental hemodynamics as a potential explanation for cardiac defects in <i>Gpr126</i> mutants	167
CONCLUSIONS	169
CONCLUSIONES	173
REFERENCES	177
ANNEXES	197
Scripts.....	199
Supplementary Figures.....	203
Supplementary tables	207

INDEX OF FIGURES

Figure 1. Heart development in mice and zebrafish.....	39
Figure 2. Placental development in mice.....	42
Figure 3. Summary of the trophoblast cell lineage and origins of different TGC subtypes.	44
Figure 4. Gpr126 gene, protein, and signaling mechanism.	50
Figure 5. The Notch signaling pathway.	54
Figure 6. Spatio-temporal expression of Gpr126 throughout heart development.	94
Figure 7. Experimental strategy to generate <i>Gpr126</i> ^{Δ3,4} mice using the CRISPR/Cas9 system. 96	
Figure 8. Characterization of <i>Gpr126</i> ^{Δ3,4} mouse line.	98
Figure 9. Experimental strategy to generate conditional and standard <i>Gpr126</i> knockout mouse lines using the CRISPR/Cas9 system.....	101
Figure 10. Detection of <i>Gpr126</i> ^{fllox} and <i>Gpr126</i> ^{Δ7} founders by sequencing.	101
Figure 11. <i>Gpr126</i> ^{Δ7} knockout allele triggers <i>Gpr126</i> downregulation.....	103
Figure 12. Histological analysis of cardiac defects in <i>Gpr126</i> ^{Δ7/Δ7} mutant embryos.	104
Figure 13. Cardiac differentiation and patterning in <i>Gpr126</i> ^{Δ7/Δ7} mutant embryos.....	106
Figure 14. Glycolytic and lipid metabolism in <i>Gpr126</i> ^{Δ7/Δ7} mutant embryonic hearts.....	107
Figure 15. Hypoxyprobe analysis of <i>Gpr126</i> ^{Δ7/Δ7} mutant hearts.....	108
Figure 16. BrdU proliferation analysis of <i>Gpr126</i> ^{Δ7/Δ7} mutant hearts.	109
Figure 17. Gene profiling of E12.5 <i>Gpr126</i> ^{Δ7/Δ7} ventricles.....	111
Figure 18. Histological analysis of embryonic hearts lacking <i>Gpr126</i> in the <i>Nfatc1</i> , <i>Tie2</i> and <i>Mesp1</i> lineages.	114
Figure 19. Analysis of cardiac morphology and function in <i>Gpr126</i> ^{fl/fl} ; <i>Tie2</i> ^{Cre/+} adult mice. .	117
Figure 20. Gene targeting of the <i>Rosa26</i> locus to generate conditional <i>R26-GPR126</i> ^{GOF} -GFP transgenic line.....	118
Figure 21. Analysis of endothelial-specific <i>GPR126</i> overexpression in WT and <i>Gpr126</i> ^{Δ7/Δ7} background.	121
Figure 22. Analysis of <i>GPR126</i> overexpression in a <i>Dll4</i> ^{fl/fl} ; <i>Tie2</i> -Cre background.	122
Figure 23. Generation of zebrafish <i>gpr126</i> ^{bns341} and <i>gpr126</i> ^{bns342} mutant alleles using CRISPR-Cas9.	125
Figure 24. Inner ear development is disrupted in <i>gpr126</i> ^{bns341} and <i>gpr126</i> ^{bns342} zebrafish mutants.....	127
Figure 25. Trabeculation is unaffected in <i>gpr126</i> ^{bns341} and <i>gpr126</i> ^{bns342} zebrafish mutants.	130
Figure 26. Analysis of <i>Gpr126</i> expression pattern in the mouse embryo.	131
Figure 27. Analysis of <i>Gpr126</i> expression pattern in the mouse placenta.	132
Figure 28. Dissection of embryonic and trophoblast-induced effects of <i>Gpr126</i> mutation.	135
Figure 29. Analysis of <i>Gpr126</i> ^{Δ7/Δ7} placentas by H&E and PAS staining.....	137

Figure 30. Analysis of placental labyrinth architecture in <i>Gpr126</i> ^{Δ7/Δ7} mutants.	139
Figure 31. Analysis of placental hypoxia in <i>Gpr126</i> ^{Δ7/Δ7} mutants.	141
Figure 32. Analysis of placental nutrient transport in <i>Gpr126</i> ^{Δ7/Δ7} mutants.	143
Figure 33. Gene expression analysis by qRT-PCR of trophoblast-subtype associated markers in <i>Gpr126</i> ^{Δ7/Δ7} placentas.	144
Figure 34. Gene expression analysis by ISH of trophoblast-subtype associated markers in <i>Gpr126</i> ^{Δ7/Δ7} placentas.	146
Figure 35. Gene expression analysis of preeclampsia markers in <i>Gpr126</i> ^{Δ7/Δ7} placentas.....	149
Figure 36. Summary of the outcomes of embryonic viability when conditionally deleting/overexpressing <i>Gpr126</i> using cardiac-specific Cre drivers.	159
Figure 37. Summary of the outcomes of embryonic viability when conditionally deleting/overexpressing <i>Gpr126</i> using the Sox2-Cre driver.	161
Figure 38. Model of Gpr126 function in the remodeling of the maternal vasculature of the mouse placenta.	166
Supplementary Figure 1. Identification of <i>gpr126</i> active promoters by ChIP-seq data set analysis.....	205

INDEX OF TABLES

Table 1. CRISPR-Cas9 elements used for the generation of mouse lines.	63
Table 2. Summary of the targeting efficiency for the generation of <i>Gpr126</i> ^{A3,4} mouse line using CRISPR/Cas9 technology.	64
Table 3. Summary of the targeting efficiency for the generation of <i>Gpr126</i> ^{lox} and <i>Gpr126</i> ^{A7} mouse lines using CRISPR/Cas9 technology.	65
Table 4. CRISPR-Cas9 elements used for the generation of zebrafish lines.	71
Table 5. List of primers used for genotyping the mouse (top) and zebrafish (bottom) lines.	73
Table 6. List of antibodies used in this study.	76
Table 8. List of primers used for mRNA probes generation in this study.	77
Table 7. List of qRT-PCR primers used in this study.	83
Supplementary Table 1. Genotype analysis of embryos derived from heterozygous <i>Gpr126</i> ^{A3,4/+} intercrosses.	209
Supplementary Table 2. Genotype analysis of embryos derived from heterozygous <i>Gpr126</i> ^{A7/+} intercrosses.	210
Supplementary Table 3 (CD-ROM). RNA-seq analysis of <i>Gpr126</i> ^{A7/A7} versus <i>Gpr126</i> ^{+/+} ventricles at E12.5.	210
Supplementary Table 4 (CD-ROM). GO enrichment analysis of DEG genes.	210
Supplementary Table 5. Genotype analysis of embryos derived from crosses of <i>Gpr126</i> ^{fl/+} ; <i>Nfatc1</i> ^{Cre/+} (male) and <i>Gpr126</i> ^{fl/fl} (female) mice.	211
Supplementary Table 6. Genotype analysis of embryos derived from crosses of <i>Gpr126</i> ^{fl/+} ; <i>Tie2</i> ^{Cre/+} (male) and <i>Gpr126</i> ^{fl/fl} (female) mice.	211
Supplementary Table 7. Genotype analysis of embryos derived from crosses of <i>Gpr126</i> ^{fl/+} ; <i>Mesp1</i> ^{Cre/+} (male) and <i>Gpr126</i> ^{fl/fl} (female) mice.	211
Supplementary Table 8. Genotype analysis of embryos derived from crosses of <i>Gpr126</i> ^{A7/+} ; <i>Tie2</i> ^{Cre/+} (male) and <i>Gpr126</i> ^{fl/fl} (female) mice.	212
Supplementary Table 9. Genotype analysis of embryos derived from crosses of <i>Gpr126</i> ^{A7/+} ; <i>Mesp1</i> ^{Cre/+} (male) and <i>Gpr126</i> ^{fl/fl} (female) mice.	213
Supplementary Table 10. Genotype analysis of embryos derived from crosses of <i>Nkx2.5</i> ^{Cre/Cre} (male) and <i>GPR126</i> ^{GOF/+} (female) mice.	214
Supplementary Table 11. Genotype analysis of embryos derived from crosses of <i>Tie2</i> ^{Cre/Cre} (male) and <i>GPR126</i> ^{GOF/+} (female) mice.	214
Supplementary Table 12. Genotype analysis of embryos derived from crosses of <i>Gpr126</i> ^{A7/+} ; <i>Tie2</i> ^{Cre/+} (male) and <i>GPR126</i> ^{GOF/+} ; <i>Gpr126</i> ^{A7/+} (female) mice.	215
Supplementary Table 13. Genotype analysis of embryos derived from crosses of <i>Dll4</i> ^{fl/+} ; <i>Tie2</i> ^{Cre/+} (male) and <i>Dll4</i> ^{fl/+} ; <i>GPR126</i> ^{GOF/+} (female) mice.	216
Supplementary Table 14 (CD-ROM). Sequence similarity analysis of zebrafish <i>gpr126</i>	217
Supplementary Table 15 (CD-ROM). Sequence similarity analysis of mouse <i>Gpr126</i>	217

Supplementary Table 16. Genotype analysis of embryos derived from crosses of *Gpr126^{fl/+}*; *Sox2^{Cre/+}* (male) and *Gpr126^{fl/fl}* (female) mice.217

Supplementary Table 17. Genotype analysis of embryos derived from crosses of *Gpr126^{fl/fl}* (male) and *Gpr126^{fl/+}*; *Sox2^{Cre/+}* (female) mice.217

Supplementary Table 18. Genotype analysis of embryos derived from crosses of *Gpr126^{Δ7/+}*; *Sox2^{Cre/+}* (male) and *GPR126^{GOF/GOF}*; *Gpr126^{Δ7/+}* (female) mice.....218

LIST OF ABBREVIATIONS

ADAM	A disintegrin and metalloprotease-containing
ATP	Adenosine triphosphate
ADGRG6	Adhesion G protein-coupled receptor 6
AIS	Adolescent idiopathic scoliosis
AMC	Arthrogryposis multiplex congenita
AVC	Atrioventricular canal
BP	Base pair
BRE	B recognition element
BrdU	Bromodeoxyuridine / 5-bromo-2'-deoxyuridin
C-TGC(s)	Canal-associated trophoblast giant cell(s)
CTS	Cathepsin
CSL	CBF1/Su(H)/Lag-1
CRISPR	Clustered regularly interspaced short palindromic repeats
CUB	Complement C1r/C1s, Uegf, Bmp1
crRNA	Crispr RNA
CTF	C-terminal fragment
cAMP	Cyclic adenosine monophosphate
Dpf	Days post-fertilization
Dll1-4	Delta-like 1-4
DREG	Developmentally regulated G protein-coupled receptor
DEG	Differentially expressed gene(s)
DPE	Downstream promoter element
DTA	Diphtheria toxin
EPC	Ectoplacental cone
ECG	Electrocardiogram
E	Embryonic day
ES	Embryonic stem
EMT	Epithelial-to-mesenchymal transition
EGF	Epidermal growth factor
ERG	ETS-related gene
ECD	Extracellular domain
ExE	Extraembryonic ectoderm
FHF	First heart field
GO	Gene ontology

GAPDH	Glyceraldehyde-3-phosphate dehydrogenase
GlyT	Glycogen trophoblast
GAIN	GPCR autoproteolysis-inducing
GPS	GPCR proteolytic site
GPR126	G protein-coupled receptor 126
GPCR	G protein coupled receptor
GFP	Green fluorescent protein
GDP	Guanosine diphosphate
GTP	Guanosine triphosphate
H&E	Hematoxylin and eosin
HDR	Homology-driven repair
HPf	Hours post-fertilization
HRP	Horseradish peroxidase
HUVEC	Human umbilical vein endothelial cell
IHC	Immunohistochemistry
ISH	In situ hybridization
ICM	Inner cell mass
IRES	Internal ribosome entry site
IVS	Interventricular septum
ICD	Intracellular domain
Jag1, 2	Jagged1, 2
LA	Left atria
LV	Left ventricle
MAML	Mastermind-like
MIB1	Mind bomb-1
MV	Mitral valve
NEB	New England Biolabs
neoR	Neomycin resistance gene
NHEJ	Non-homologous end-joining
NMD	Nonsense-mediated mRNA decay
NECD	Notch extracellular domain
NICD	Notch intracellular domain
NTF	N-terminal fragment
NLS	Nuclear localization signal
OFT	Outflow tract
ORF	Open reading frame

P-TGC(s)	Parietal trophoblast giant cell(s)
PAM	Protospacer adjacent motif
PFA	Paraformaldehyde
PIMO	Pimonidazole
PTX	Pentraxin
PAS	Periodic acid–Schiff
PNS	Peripheral nervous system
PTC	Premature termination codon
PAM	Protospacer adjacent motif
qRT-PCR	Real-time quantitative reverse transcription PCR
RBPJK	Recombination signal-binding protein 1 for J-Kappa sequence
RT-PCR	Reverse transcription PCR
RA	Right atria
RV	Right ventricle
SHF	Second heart field
7TM	Seven-transmembrane
ssODN	Single-stranded oligodeoxynucleotides
S-TGC(s)	Sinusoidal-associated trophoblast giant cell(s)
α -SMA	Smooth muscle α -actin
SEA	Sperm protein, enterokinase and agrin
Spa-TGC(s)	Spiral artery-associated trophoblast giant cell(s)
SpT	Spongiotrophoblast
SynT	Syncytiotrophoblast
tracrRNA	Trans-activating crisper RNA
TSS	Transcription starting site
TV	Tricuspid valve
TE	Trophectoderm
TGC(s)	Trophoblast giant cell(s)
WISH	Whole-mount in situ hybridization
WT	Wild-type

1

INTRODUCTION

1. Cardiac development in mice and zebrafish

The heart is the first organ to form and function during vertebrate embryonic development, and key steps of cardiovascular development are conserved among species. It begins beating and pumping blood at E8.5 in mice, and at 22 hours post-fertilization (hpf) in zebrafish, highlighting its early critical function (Andrés-Delgado and Mercader, 2016).

Cardiac progenitor cells derive from the mesoderm, which emerges from the primitive streak during gastrulation, at E7.0 in mice (Fig. 1A) and 5 hpf in zebrafish (Fig. 1G). Then, they move anterior-laterally to form a crescent in the cephalo-medial region at E7.5 in mice (Buckingham et al., 2005; Liu and Stainier, 2012; Moorman and Christoffels, 2003) (Fig. 1B). In zebrafish, progenitor cells migrate towards the embryonic midline to end up at the anterior lateral plate mesoderm at 16 hpf (Fig. 1H), and they converge at the midline at about 22 hpf to form the cardiac disk (Brown et al., 2016; Liu and Stainier, 2012) (Fig. 1I). At this time, the cardiac mesoderm contains two populations of progenitors: the first heart field (FHF) and the second heart field (SHF) (Fig. 1B, H). At E8.0 and 28 hpf, the FHF migrates to the midline of the embryo and builds the primitive heart tube (Fig. 1C, J), which consists of an inner layer of a specialized endothelium called endocardium, a middle layer of extracellular matrix called cardiac jelly, and an outer layer of myocardial cells. This linear heart tube will form the left ventricle and part of both atria of the four-chambered heart of mammals (Buckingham et al., 2005) (Fig. 1C), and the atria and part of the ventricle in the two-chambered heart of zebrafish (Perl and Waxman, 2019) (Fig. 1J). Subsequently, the primitive heart tube grows by the addition of cells from the SHF, which migrate anteriorly (arterial pole) and posteriorly (venous pole) and contribute to the future outflow tract (OFT), the right ventricle, and portions of both atria in mammals (Buckingham et al., 2005; Kelly et al., 2001) (Fig. 1D). In zebrafish, the SHF gives rise to the distal half of the ventricle, the bulbous arteriosus in the outflow tract (Grant et al., 2017), and a small portion of the atrium (Perl and Waxman, 2019) (Fig. 1K). Simultaneously, the heart tube undergoes a characteristic rightward looping (R-loop), by which the initial anteroposterior axis of the primitive heart leads switches into a left-right orientation (Moorman and Christoffels, 2003) (Fig. 1D, K).

In mice, the still immature E9.5 heart consists of four anatomically and molecularly distinct regions: the atrium, the ventricle, the atrioventricular canal (AVC) at the border of both chambers, and the OFT (Fig. 1E). In zebrafish, by 48 hpf, the heart consists of a sinus venosus (the inflow tract), one atrium, the AVC, one ventricle and the OFT. Later in development, this outflow tract will further develop into the bulbous arteriosus, a pseudo-chamber that serves as a resistor to regulate flow through the aorta (Fig. 1L). Besides, the epicardium develops from an extra-cardiac population of cells called the pro-epicardium, which spread over the myocardial surface. Once the epicardial cells have covered the ventricle, endocardial cells from the AVC and the OFT

1. INTRODUCTION

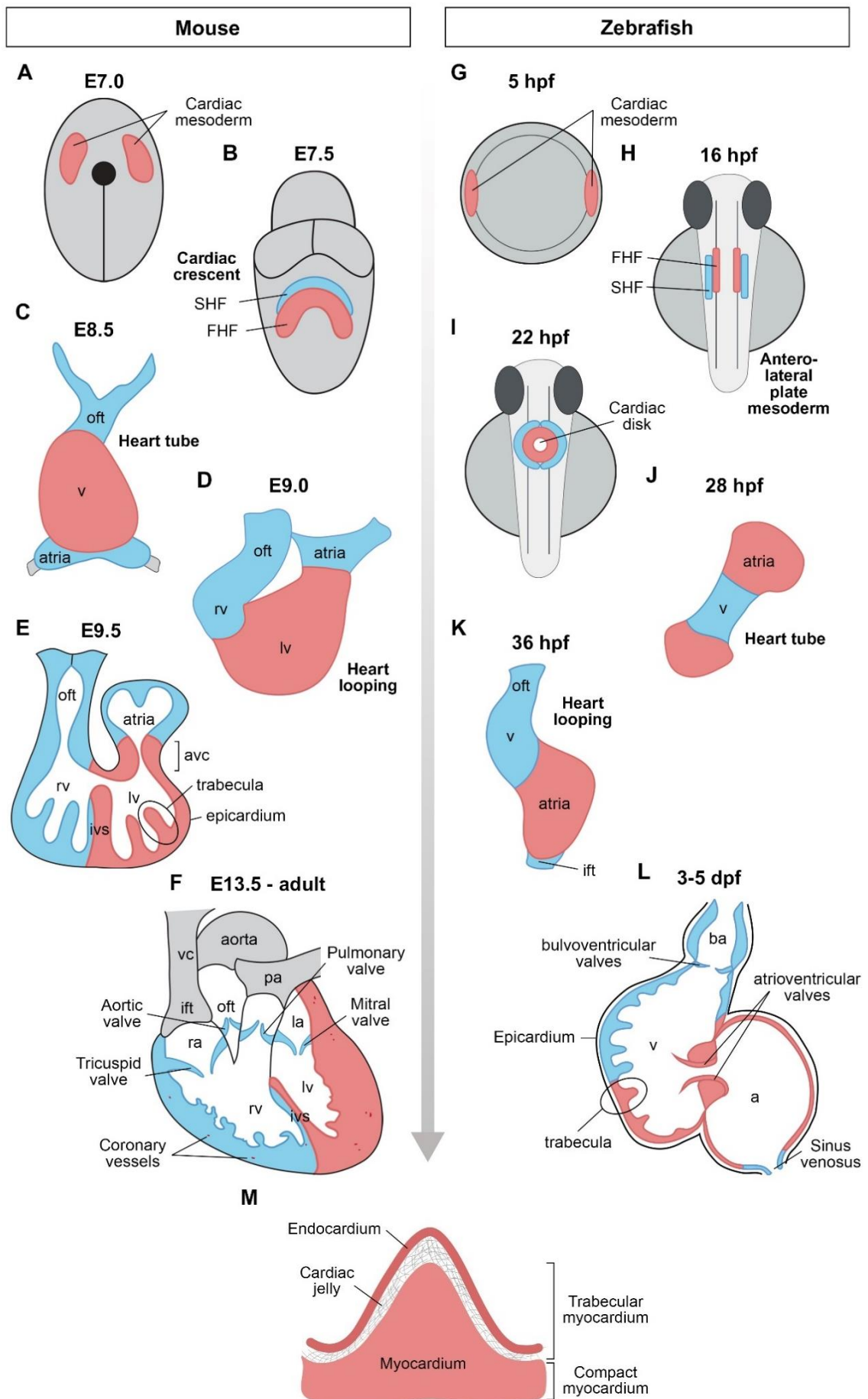


Figure 1. Heart development in mice and zebrafish. (A-E) Stages of heart development in mouse embryos in a ventral view. (A) At E7.0, cardiac progenitors (pink) migrate to the center of the embryo to form the cardiac crescent (B). (B) At E7.5, two cardiac fields can be distinguished: the first heart field (FHF; pink) and the second heart field (SHF; blue). (C) At E8.0, the cardiac tube is formed, which undergoes an R-loop to form a looped heart (D). (E) Transversal section depicting an E9.5 heart, with four anatomically distinct regions: atria, atrioventricular canal (avc), ventricles (rv, right ventricle; lv, left ventricle) and outflow tract (oft). Trabecular ridges emerge in the ventricular chambers. (F) Longitudinal section of an E13.5 heart, in which valve primordia are remodeled and trabeculae undergo compaction to form a thick ventricular wall. Coronary vessels (red circles) irrigate the maturing ventricular wall. Adapted from (D'Amato et al., 2016a). (G-L) Stages of heart development in zebrafish embryos in a dorsal (G-I) and ventral (J-L) view. (G) At 5 hpf, cardiac progenitors are located at the lateral margin of the egg. (H) At 16 hpf, the FHF closer to the embryonic midline, and SHF in the margins, migrate bilaterally to the anterior lateral plate mesoderm. (I) By 22 hpf, cardiac progenitors fuse to form the cardiac disk. (J) From 24 to 28 hpf, the disk elongates into the linear heart tube, which begins a leftward looping. (K) Concurrently, from 28 to 36 hpf, SHF cells are added to the arterial and venous poles. (L) Longitudinal section of the heart at 3 to 5 days post-fertilization (dpf), featuring trabeculae in the outer ventricle wall, cardiac valves, and covering of the heart by the epicardium. Adapted from (Brown et al., 2016). (M) Trabecular ridge, formed by trabecular cardiomyocytes covered by endocardium, and separated by the cardiac jelly. The outer layer of cardiomyocytes forming the cardiac wall is the compact myocardium.

undergo an epithelial-to-mesenchymal transition (EMT) to form the endocardial cushions, which are primordia of the future cardiac valve leaflets (Brown et al., 2016; D'Amato et al., 2016a) (Fig. 1F, L).

The first sign of chamber development is the formation of trabeculae. Starting at E8.5 in mice (Grego-Bessa et al., 2007; Sedmera et al., 2000), and 72 hpf in zebrafish (Liu et al., 2010), trabeculation is the process by which protrusions of ventricular cardiomyocytes grow towards the ventricular lumen, forming a complex sponge-like meshwork (Ben-Shachar et al., 1985) (Fig. 1E, L, M). In mice, it is speculated that occurs via polarized cell division (Passer et al., 2016), whereas in zebrafish embryos, trabeculae emerge through delamination (Liu et al., 2010). This process leads to two distinct myocardial layers in the ventricle: an outer compact zone and an inner trabecular zone (Sedmera et al., 2000) (Fig. 1M). Trabeculae increase the myocardial mass and facilitate oxygen and nutrient exchange in the heart muscle before coronary vascularization. At later stages of mouse chamber development, trabeculae become compressed within the ventricular wall resulting in the formation of a thicker, compact ventricular wall (Fig. 1F). This process is termed compaction, occurs at E13.5, and requires enhanced oxygen delivery, triggering an influx of endothelial cells that undergo vasculogenesis to form a capillary plexus (D'Amato et al., 2016a) (Fig. 1F). In contrast, trabecular projections in zebrafish do not undergo compaction and the

compact layer remains as one cell thick, while the complexity of trabeculae organization increases (Liu et al., 2010) (Fig. 1L).

Trabeculation plays a key role in cardiac ontogeny. Failure of trabeculae formation frequently causes embryonic lethality in mice, while excessive trabeculation causes cardiomyopathy and heart failure in humans. A finely tuned communication between the endocardium and the myocardium is a prerequisite for ventricular chamber development, as several signaling molecules released from both layers have been implicated in this process (Liao et al., 1997; Luxán et al., 2016; Stainier et al., 1995).

2. Development of the mouse placenta

The placenta is the transient support organ that connects the embryo to the mother during gestation (Hemberger et al., 2020). It forms the interface between the maternal and fetal circulation, facilitating metabolic and gas exchange, as well as fetal waste disposal. Besides, the placenta produces hormones that alter maternal physiology during pregnancy and forms a barrier that protects the fetus against the maternal immune system (Watson and Cross, 2005). Thus, the survival and growth of the fetus are critically dependent on a functional placenta. Primate and rodent placentas are hemochorial, meaning that the maternal vasculature of the placenta is lined by fetal-derived trophoblasts, and not by endothelial cells like fetal blood vessels (Wooding and Flint, 1994).

The mature placenta in rodents is composed of three broad zones including the maternal decidua on the outside, the junctional zone, and the innermost labyrinth, these last of fetal origin (Fig. 2F). The decidua is devoid of trophoblast cells until mid-gestation, when fetal trophoblast cells invade into the decidua and reach spiral arteries, replacing the endothelium and thereby promoting the transition from endothelial cell-lined to trophoblast cell-lined maternal blood spaces of the hemochorial placenta (Hu and Cross, 2010) (Fig. 2F). Next is the junctional zone, consisting of spongiotrophoblast cells and a layer of TGCs that line the implantation site (Fig. 2F). The inner compartment is the labyrinth, named for the tortuous network of maternal and fetal blood spaces, and is the region of nutrient, gas and waste exchange between the fetal and maternal circulations (Simmons et al., 2008a) (Fig. 2F). The mouse placenta is defined mature when the fetal-maternal interface is established and evidenced by the presence of maternal blood in the placental labyrinth, which takes place at embryonic day 12.5 (E12.5).

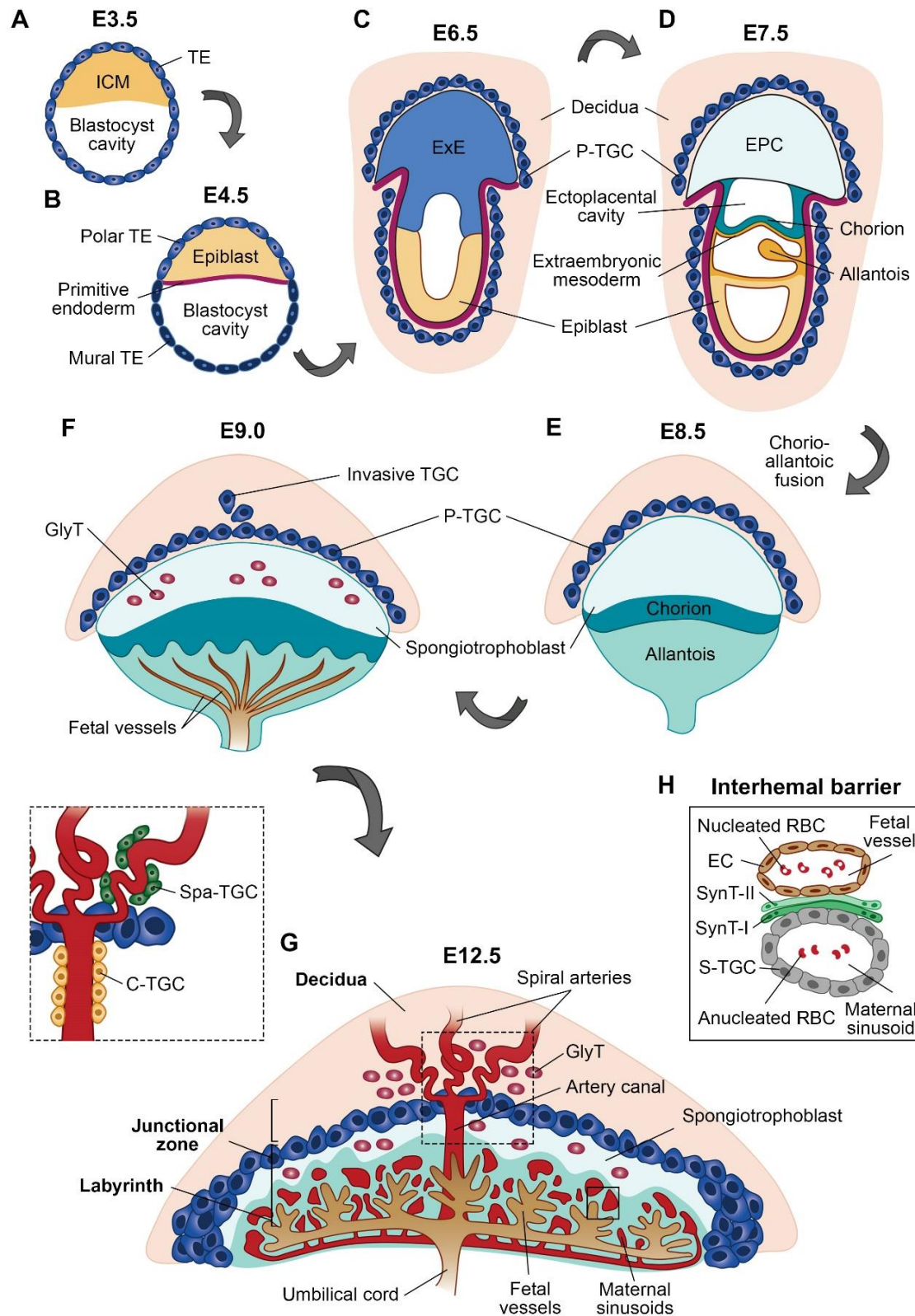


Figure 2. Placental development in mice. (A) The blastocyst forms by E3.5 and consists of the outer trophoblast (TE) and inner cell mass (ICM) cells. (B) Between E3.5 and E4.5, the inner cell mass further differentiates into epiblast and primitive endoderm lineages, and the TE divides into polar TE and mural TE. (C) The continued proliferation of the polar TE gives rise to the extraembryonic ectoderm (ExE) by E6.5. (D) With gastrulation, ExE cells that are located farther away from the embryo form the ectoplacental cone (EPC), whereas ExE cells close to the embryo form the chorion. The allantois emerges from the epiblast-derived extraembryonic mesoderm at E7.5. (E) At E8.5, the ectoplacental cavity collapses, and the chorioallantoic fusion takes place. (F) Shortly after, mesoderm-derived blood vessels invaginate into the chorionic trophoblast layer to form the placental labyrinth. (G) The placenta develops further and grows in size, giving rise to the mature placenta at E12.5, which consists of three main layers: the decidua; the junctional zone consisting of a layer of parietal trophoblast giant cells (P-TGCs), spongiotrophoblast and glycogen cells; and the labyrinth. Three new subtypes of TGC originate and associate with the maternal vasculature, (from the maternal to the fetal side): spiral artery-associated TGC (Spa-TGC), canal associated TGC (C-TGC) and sinusoidal TGC (S-TGC). (H) The interhemal barrier in the labyrinth is made up of three trophoblast cell types (from the maternal to the fetal side), which are sinusoidal trophoblast giant cells (S-TGC), syncytiotrophoblast I (SynT-I), syncytiotrophoblast II (SynT-II), and an endothelial cell (EC) layer of the fetal vasculature. RBC, red blood cells.

2.1 From the blastocyst (E3.5) to the mature placenta (E12.5)

In mice, placental development begins in the blastocyst at E3.5, with the formation of two cell lineages: the trophoblast, which will give rise to a variety of differentiated trophoblast cell types, and the inner cell mass (ICM), which will give rise to the allantois (a component of the umbilical cord), and the fetal vasculature of the placenta (Dunwoodie, 2009). At this stage, the trophoblast forms an outer shell of cells surrounding the inner cell mass (Fig. 2A). Following implantation (E4.5), the ICM differentiates into the epiblast, which will generate the embryo proper, and the primitive endoderm. Besides, the trophoblast is subdivided into polar trophoblast, which covers the epiblast, and mural trophoblast, which overlays the blastocyst cavity (Fig. 2B).

Mural trophoblast cells stop dividing and undergo endoreduplication, consisting of repeated rounds of DNA replication in the absence of intervening mitosis to become polyploid, thus giving rise to primary trophoblast giant cells (TGCs). They are termed parietal TGC (P-TGC) due to their location lining the implantation site (Fig. 2C, 3). Their main function is helping the embryo to penetrate the uterine epithelium and implanting into the endometrium (Woods et al., 2018), hence forming an anastomosing network of blood sinuses for the early diffusion of oxygen, nutrients and endocrine signals from the maternal circulation into the embryo (Bevilacqua and Abrahamsohn, 1988). In contrast, the polar trophoblast continues to proliferate. Initially, an arising column of trophoblast cells forms the extraembryonic ectoderm, comprising a population

of trophoblast stem cells responsible for the proliferative potential of this region (Fig. 2C, 3). With gastrulation starting at E6.5, the extraembryonic ectoderm expands to form the ectoplacental cone, farthest away from the epiblast, and the chorionic ectoderm, at the base, both separated by the ectoplacental cavity (Woods et al., 2018) (Fig. 2C, 2D, 3). The ectoplacental cone comprise progenitor cells that will ultimately form the junctional zone and remodel the maternal vasculature, whereas the chorion will lead to the formation of the labyrinth, in proximal contact to the embryo.

Historically, it has been thought that at E7.5, *Tpbpa* (*Trophoblast specific protein alpha*)⁺ (initially called *4311*) trophoblast stem cells residing in the ectoplacental cone proliferate and differentiate into all specialized trophoblast subtypes that will populate the different layers of the placenta: diploid spongiotrophoblasts (SpT) and glycogen trophoblasts (GlyT), diploid and multinucleated syncytiotrophoblasts I and II (SynT-I and -II), and four different subtypes of polyploid TGCs (Simmons and Cross, 2005). This later wave of TGCs is called ‘secondary’ to distinguish them from the initial ‘primary’ group (Simmons et al., 2007), and are named according to their spatial location in the placenta (from the decidua to the labyrinth): spiral artery-associated TGC (Spa-TGC), parietal-associated TGC (P-TGC), canal-associated TGC (C-TGC) and sinusoidal-associated TGC (S-TGC) (Dunwoodie, 2009). Of particular interest is the SpT, which in turn acts as a precursor of Spa-TGCs, P-TGCs, C-TGCs and GlyT. However, lineage-tracing studies have shown that only Spa-TGCs and GlyT cells arise from *Tpbpa*⁺ precursor cells, whereas S-TGCs emerge from *Tpbpa*⁻ precursors and both P-TGCs and C-TGCs have mixed developmental origins (Fig. 3). Based on these results, a new hypothesis is proposed, in which the outer ectoplacental cone and later in undifferentiated and differentiated SpT cells form a previously uncharacterized *Tpbpa*⁺ precursor population, whereas the base of the ectoplacental cone nearest to the chorion contain *Tpbpa*⁻ precursor cells (Simmons et al., 2007).

2.2 Labyrinth formation and function

Late in gastrulation (E7.5), the extraembryonic mesoderm lineage is generated from the epiblast, forming the allantois, which is a projection at the posterior end of the embryo, as well as the chorionic epithelium, a thin layer that lines beneath the chorion, also derived from the extraembryonic mesoderm (Rossant and Cross, 2001) (Fig. 2D). The occlusion of the ectoplacental cavity takes place at ~E8.0, bringing cells from the bottom of the ectoplacental cone in contact with the distal side of the chorion, which results in the loss of trophoblast stem cell potential of the chorionic ectoderm. Shortly after ectoplacental cavity occlusion, the allantois grows and attaches to the basal side of the chorion at ~E8.5 (Simmons et al., 2008a) (Fig. 2E).

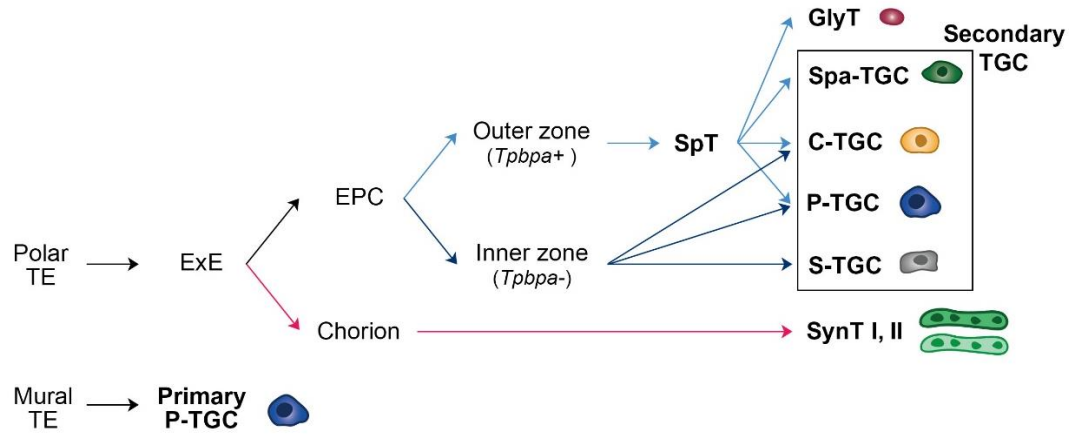


Figure 3. Summary of the trophoblast cell lineage and origins of different TGC subtypes.

(A) C-TGC, canal-associated trophoblast giant cells; EPC, ectoplacental cone; ExE, extraembryonic ectoderm; GlyT, glycogen trophoblast; P-TGC, parietal trophoblast giant cells; S-TGC, sinusoidal trophoblast giant cells; Spa-TGC, spiral artery-associated trophoblast giant cells; SpT, spongiotrophoblast; SynT-I, syncytiotrophoblast I; SynT-II, syncytiotrophoblast II; TE, trophoblast; Tpbpa, trophoblast specific protein alpha.

This event is termed chorioallantoic fusion, although no actual cell fusion takes place, and is critical for further developmental progression (Watson and Cross, 2005). At E9.0, immediately after allantoic attachment occurs, the extraembryonic mesodermal cells that are in direct contact with the chorionic ectoderm start to invaginate in finger-like projections that will generate the vascular network of the placental labyrinth (Woods et al., 2018) (Fig. 2F). Trophoblast cells at the tips of these primary branches elongate, differentiate and fuse to form the innermost layer of syncytia, the syncytiotrophoblast layer-II (SynT-II). As branching continues, SynT-II cells get in contact with cells on the distal side of the chorion, which express the fusogenic gene *Syncytin-A* (*Syna*), and induce their lateral fusion giving rise to the outermost layer of syncytia, the syncytiotrophoblast layer-I (SynT-I). Both SynT-I and SynT-II cells become intimately juxtaposed and function together as the transporting epithelium of the definitive placenta (Woods et al., 2018) (Fig. 2H, 3). Continued elongation of the primary branches extends them into the developing maternal sinuses at the base of the ectoplacental cone, through which maternal blood (brought in by the spiral arteries and canals) percolates into the labyrinth. These maternal blood spaces are lined by a TGC subtype called S-TGC, which is likely of chorionic trophoblast origin (Fig. 2H, 3). Together, a trilaminar layer of trophoblast-derived cells are in direct contact with maternal blood, leading to the so-called hemotrichorial placenta. Indeed, the definitive interhaemal barrier consist (from maternal to fetal side) of a discontinuous layer of S-TGCs, two layers of syncytiotrophoblasts (SynT-I and -II), and the extraembryonic mesoderm-derived fetal endothelial cells (Fig. 2H). Together, these layers provide a selectively permeable barrier between

the two circulations. Between E10.5 and E14.5, continued branching morphogenesis ultimately produces a complex intricate structure, in which maternal and fetal blood circulations come into close contact but never mix (Fig. 2G). This architecture achieves a large surface area required for nutrient and gas exchange to support fetal growth past E10.5, at which time the switch from yolk sac nutrition to placental nutrient supply takes place (Simmons et al., 2008a).

2.3 Junctional zone formation and function

The junctional zone is positioned between the labyrinth and the maternal decidua and is composed of three main cell types: SpT, GlyT and a layer of P-TGCs that directly border the decidua (Fig. 2G). The SpT forms the bulk of the junctional zone, just beneath P-TGCs, and provides structural support to the expanding labyrinth. As suggested by the names, this region exhibits a spongy appearance and discernible glycogen stores accumulated in GlyT cells. Although GlyT cells differentiate from spongiotrophoblast, from ~E12.5 onwards they start invading into the decidua and become associated with maternal blood spaces (Woods et al., 2018) (Fig. 2G). The placenta achieves its maximum weight by E16.5, but whereas the labyrinth keeps on expanding after that stage, the junctional zone reduces in volume, which may reflect that the release of glycogen storage provides a substantial energy source for the final phase of fetal growth (Coan et al., 2006). Besides, the junctional zone constitutes the main endocrine compartment of the placenta, by producing hormones, growth factors and cytokines that are important for the normal progression of pregnancy (Woods et al., 2018).

2.4 Role of TGCs in establishing the maternal vasculature of the placenta

After implantation, the pregnant uterus undergoes a radical transformation in structure. Uterine stromal cells proliferate and differentiate, a process called decidualization, resulting in a wall that is about fivefold thicker than in the nonpregnant state. The maternal arterial supply to the placenta originates from radial arteries that enter the uterus through the myometrium, which branch into several spiral-shaped arteries in the decidua (Fig. 2G). They converge to form a few straight and centrally located arterial canals that carry the oxygenated blood to the base of the labyrinth before leading into the small tortuous sinusoid spaces (Fig. 2G). After the exchange of gases and nutrients between the maternal and fetal circulation, deoxygenated blood then moves out through venous channels that cross the SpT and P-TGCs into peripherally located venous sinuses in the decidua, which are lined by endothelial cells. The venous sinuses drained into wide radial veins that exit the myometrium (Adamson et al., 2002).

In mice, TGCs are instrumental in promoting blood flow towards the mouse embryo by invading the uterine endometrium and remodeling the maternal vasculature (Screen et al., 2008). The development of TGCs requires the transition from the mitotic to the endoreduplication cell cycle, thus leading to large cytoplasmic size, polyploid nuclei, and extensive rough endoplasmic reticulum (Bevilacqua and Abrahamsohn, 1988). Although the importance of endoreduplication and polyploidy for TGC function is a matter of speculation, it has been suggested that it may increase their capacity for protein synthesis, which is consistent with their ability to secrete a wide array of hormones and paracrine factors that regulate maternal adaptations to pregnancy and the fetal-maternal interface (Hu and Cross, 2010).

The defining feature of the hemochorial placenta is that trophoblast cells and not endothelial cells line the maternal vasculature within the placenta. In mice, the four different TGC subtypes can be distinguished by distinct cell lineage origins, differential gene expression of members belonging to the prolactin family, and their location with respect to the maternal circulation (Simmons et al., 2007; Simmons et al., 2008b). Proceeding from upstream to downstream within the maternal blood space, there are SpA-TGCs that invade into the spiral arteries in the decidua displacing the maternal endothelial cell, C-TGC that line the maternal blood canals as they pass through the junctional zone to the bottom of the labyrinth, S-TGC that sit within the tortuous maternal blood spaces of the labyrinth, and P-TGC that surround lacunae of blood leading into the uterine veins and line the implantation site (Rai and Cross, 2014) (Fig. 2G, H).

2.5 TGC-mediated spiral artery remodeling and vasculogenic mimicry

Fetal trophoblast cells assume the location and function of endothelial cells within the maternal vascular spaces in the placenta through two different processes: vasculogenic mimicry, describing the ability of trophoblast cells to create vascular tubes *de novo* (P-TGC, C-TGC and S-TGC), and vascular invasion and endothelial mimicry, referring to trophoblast cells that invade the decidua and displace the endothelial cells from preexisting arteries (Spa-TGC) (Hemberger et al., 2003; Rai and Cross, 2014). Maternal canals, sinusoids, and lacunar spaces in the placenta are created *de novo* by C-TGC, S-TGC, and P-TGC, respectively, without the participation of endothelial cells. Instead, these TGCs mimic the expression of some endothelial genes and secrete growth factors and cytokines necessary for vessel generation (Rai and Cross, 2014).

Trophoblast invasion begins at E7.5 in mice, when secondary Spa-TGCs acquire invasive characteristics, penetrate deeply into the decidua and make contact with maternal arteries (Woods et al., 2018). In resistance vessels such as the spiral arteries, vascular smooth muscle cells are coiled around a layer of extracellular matrix and central lumen lined by a single layer of endothelial cells. Upon invasion, Spa-TGCs degrade the perivascular smooth muscle layer and

the elastic lamina from the vessel wall and secrete fibrinoid material, likely retaining vessel integrity. Besides, they temporally replace the maternal vascular endothelium, leading to trophoblast-lined arteries embedded in fibrinoid deposits that behave like a pseudo-endothelium. As a result of this vascular remodeling process, spiral arteries are transformed from high-resistance, small-diameter vessels into large, dilated vessels that allow an increased blood flow at reduced pressure. This step is critical to establish the definitive uteroplacental circulation by increasing the blood supply to the fetus (Whitley and Cartwright, 2010). Maternal immune cells, such as natural killer cells and macrophages, have been also implicated in this remodeling process, likely cooperating with fetal SpA-TGCs (Chakraborty et al., 2011; Croy et al., 2000). Several mechanisms have been associated with these physiological changes, like extracellular matrix restructuring, vascular cell de-differentiation, migration, changes in cellular adhesion, and sensitivity to apoptosis-inducing signals triggered by Spa-TGCs and maternal immune cells (Whitley and Cartwright, 2010).

2.6 Impaired vascular remodeling in preeclampsia

Preeclampsia is a multisystem disorder of pregnancy characterized by the new onset of hypertension and proteinuria after 20 weeks of gestation in a previously normotensive woman. It also associates with endothelial dysfunction in both the maternal and fetoplacental circulation, and with long-term adverse outcomes for the mother and the offspring (Bokslag et al., 2016). This syndrome has a worldwide prevalence of 2–10% and is a major contributor to maternal morbidity, fetal growth restriction (FGR), premature delivery and pregnancy loss. Even though the exact pathophysiology of preeclampsia is not completely understood, the impaired vascular remodeling of the uterine spiral arteries by the trophoblasts in the first trimester is considered a hallmark of this syndrome (Gutiérrez et al., 2020). In humans, the perfusion with maternal blood is enabled by the remodeling of the uterine spiral arteries through the highly invasive action of extravillous trophoblast cells, a cell type analogous in function to invasive Spa-TGCs in the mouse (Hemberger et al., 2020). Failure of vessel remodeling alters the uteroplacental hemodynamics, resulting in a poorly perfused fetoplacental unit.

A two-stage disease model has been proposed to describe the pathogenesis of preeclampsia (Cheng and Wang, 2009). The first stage involves abnormal placentation characterized by poor trophoblast invasion, incomplete vascular remodeling of spiral arteries, and placental hypoxia. The second stage is manifested as the maternal syndrome of hypertension and proteinuria with systemic endothelial dysfunction. The link bridging the two stages is thought to be the release of factors from the abnormally developed placenta into the maternal circulation triggered by a

dysfunctional uteroplacental circulation, and the subsequent activation of the immune/inflammatory response (Sones and Davisson, 2016).

3. Structural basis and signaling mechanism of Gpr126

G protein-coupled receptors (GPCRs) are a large family of integral membrane proteins that communicate through heterotrimeric G proteins and other signaling pathways to transduce endogenous signals (Moriguchi et al., 2004). Based on the phylogenetic comparison of their highly conserved seven-transmembrane-spanning (7TM) domain, GPCRs are classified into five families: Glutamate, Rhodopsin, Frizzled/Taste, Secretin and Adhesion, to which Gpr126 belongs (Monk et al., 2015). In fact, the official name for Gpr126 is adhesion G protein-coupled receptor G6 (Adgrg6), although it was originally known as a developmentally regulated G protein-coupled receptor (DREG) (Moriguchi et al., 2004). *Gpr126* is encoded by 25 coding exons in mice and zebrafish (Fig. 4A) and has several alternatively spliced forms, which differ in the presence of exon 6 and exon 25, the last changing the usage of termination codons (Patra et al., 2014).

Structurally, adhesion GPCRs (aGPCRs) are defined by a large extracellular domain (ECD) containing various adhesion domains capable of mediating cell-cell and cell-matrix interactions, a 7TM domain and a short intracellular domain (ICD) (Liebscher et al., 2014; Monk et al., 2015) (Fig. 4B). The hallmark of this family is the presence of a conserved GPCR proteolytic site (GPS) within the juxtamembrane GPCR autoproteolysis-inducing (GAIN) domain (Fig. 4B). During receptor processing, autoproteolysis in the GAIN domain cleaves aGPCRs into N- and C-terminal fragments (NTF and CTF, respectively) that remain noncovalently associated at the cell surface (Paavola et al., 2014) (Fig. 4C, D). While the NTF comprises most of the ECD, the CTF is characteristically composed of a residual ECD, the 7TM domain, and the intracellular domain (ICD) (Monk et al., 2015) (Fig. 4B). Importantly, key amino acids in the CTF portion of the GAIN domain, termed the *Stachel* sequence (German word for stinger), can function as a tethered agonist for CTF activation (Liebscher et al., 2014). The *Stachel* sequence is physically embedded within the N-terminal portion of the GAIN domain (Fig. 4E). However, upon ligand interaction or mechanical removal of the NTF, it is exposed and able to bind the 7TM, thus activating the G protein-signaling cascade (*cis* signaling) (Fig. 4E). The *Stachel* sequence is predicted to interact with extracellular loops and upper helix bundles of the 7TM, which requires low affinity, thus suggesting a fast on-off ligand-receptor interaction (Liebscher et al., 2014). Another non-mutually exclusive model for Gpr126 activation is that the NTF can function independently of the CTF (*trans* activation) (Fig. 4E) (Patra et al., 2013; Petersen et al., 2015). The 7TM is classically defined by its ability to bind heterotrimeric G-proteins. G-proteins are a complex of three proteins (α , β , γ) that utilize guanosine triphosphate (GTP) as part of the signaling pathway. When GTP

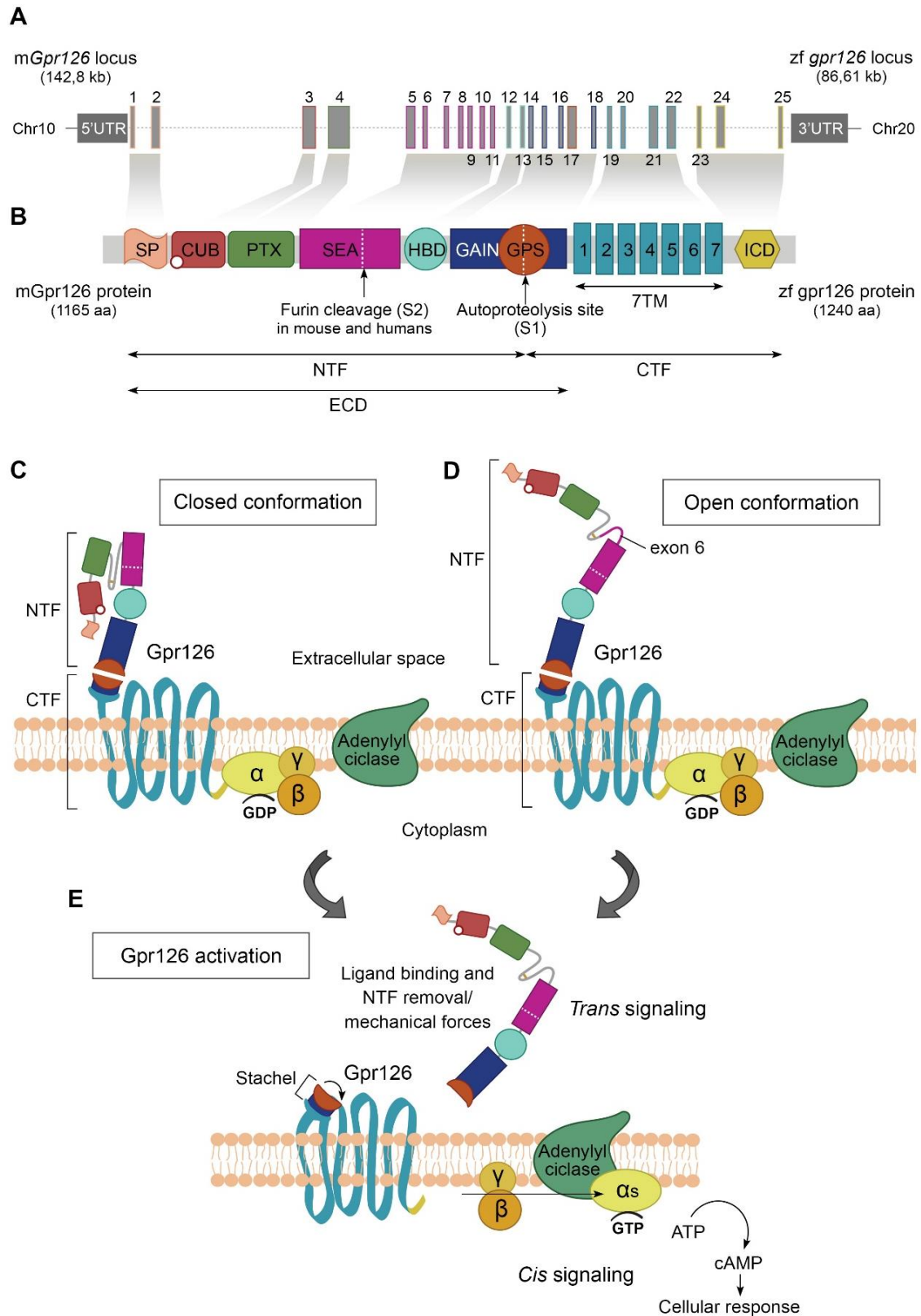


Figure 4. Gpr126 gene, protein, and signaling mechanism. (A-B) Diagrams of *Gpr126* gene (A) and Gpr126 protein (B) in mice and zebrafish. Grey shadows indicate the encoded functional domains in Gpr126. (B) In the Gpr126 protein, cleavage sites (furin cleavage and autoproteolysis) are indicated by white dashed lines. The white circle in the CUB domain depicts a calcium-binding site. Chr, chromosome. SP, signal peptide; CUB, Complement, Uegf, Bmp1; PTX, pentraxin domain; SEA, Sperm protein, Enterokinase and Agrin; HBD, hormone-binding domain; GAIN, G protein-coupled receptor autoproteolysis-inducing domain; GPS, G protein-coupled receptor proteolytic site; 7TM, type II seven-transmembrane domain; ECD, extracellular domain; ICD, intracellular domain; NTF, N-terminal fragment; CTF, C-terminal fragment. (C-E) Gpr126 protein conformation in the plasma membrane before (C-D) and after (E) receptor activation. Alternative splicing of exon 6 triggers different NTF conformations, such that its absence generates a closed conformation (C), whereas its presence allows a more dynamic and open-like conformation (D). (E) Proposed activation mechanism of Gpr126, based on the tethered agonist region, the *Stachel* sequence. Binding of extracellular ligand, possibly combined with mechanical force, removes the NTF, thereby exposing the *Stachel* structure, which interacts with extracellular loops of the 7TM domain and initiates conformational changes leading to G protein activation. This in turn activates adenylyl cyclase to convert ATP to cAMP, which acts as a second messenger by activating other proteins in a cascade that yield a response. Adapted based on (Liebscher et al., 2014) and (Leon et al., 2020).

binds to the α subunit, it becomes active and dissociates from the β/γ subunit (Fig. 4E). $G_{\alpha s}$ (stimulatory) subunits activate the enzyme adenylyl cyclase, which increases the production of cyclic adenosine monophosphate (cAMP) from adenosine triphosphate (ATP). cAMP itself is a second messenger molecule activating cAMP-dependent protein kinases, thus initiating a signaling cascade (Fig. 4E). G_i (inhibitory) proteins work opposite of G_s proteins, and Gpr126 couples to both $G_{\alpha s}$ and $G_{\alpha i}$ subunits (Mogha et al., 2013). Some of the Gpr126 functions rely upon an elevation of intracellular cAMP levels are peripheral nervous system (PNS) development in mouse (Mogha et al., 2013) and zebrafish (Monk et al., 2009), and inner ear development in zebrafish (Geng et al., 2013).

The Gpr126 locus is highly conserved in vertebrates, and the synteny of the genomic region surrounding these genes is conserved in fish, birds, reptiles, and mammals, indicating that the predicted genes are true orthologues (Waller-Evans et al., 2010). Four domains have been identified in the ECD of Gpr126 through sequence-based bioinformatics: Complement C1r/C1s, Uegf, Bmp1 (CUB), Pentraxin (PTX), Hormone binding domain (HBD), and GAIN domain (Moriguchi et al., 2004) (Fig. 4B). The CUB domain contains a conserved calcium-binding site necessary to adopt a close ECD conformation (Fig. 4B, C), and is critical for zebrafish gpr126 function *in vivo*. Recently, a fifth domain has been described within the full-length ECD of zebrafish gpr126, between PTX and HBD, which is the Sperm protein, Enterokinase and Agrin (SEA) domain (Leon et al., 2020) (Fig. 4B). Furin, a Golgi-localized protease, is reported to cleave human and mouse GPR126 in this region (S2 cleavage) (Moriguchi et al., 2004), but this

cleavage site is not conserved in zebrafish (Patra et al., 2013) (Fig. 4B). Also, alternative splicing of exon 6 in Gpr126, which occurs in humans, mice and zebrafish, produces two different isoforms regarding the SEA domain, that are distinct in terms of ECD conformation dynamics and G protein signaling activity (Leon et al., 2020). The extracellular domain is in a closed conformation in the absence of the alternatively spliced exon 6, while its insertion gives rise to a dynamic open-like extracellular conformation that increases downstream basal signaling (Leon et al., 2020) (Fig. 4C, D).

3.1 Gpr126 is essential for PNS, inner ear and heart development in zebrafish and mice

Gpr126 functions in diverse essential processes, including the myelination of peripheral nerves (Mogha et al., 2013; Monk et al., 2009), osteoblast differentiation and bone formation (Sun et al., 2020), development of the semicircular canals of the inner ear (Geng et al., 2013), and prior to this study, trabeculation of the developing heart (Patra et al., 2013). Furthermore, variations and mutations at the GPR126 locus have been associated with an increasing number of developmental defects in humans, like adolescent idiopathic scoliosis (AIS) (Kou et al., 2013), arthrogryposis multiplex congenita (Ravenscroft et al., 2015) and periodontitis (Kitagaki et al., 2016).

A zebrafish screen for disruptions in myelin formation discovered mutations in *gpr126* (Monk et al., 2009; Pogoda et al., 2006). In the peripheral nervous system, Schwann cells wrap axons to form myelin, which allows the rapid propagation of action potentials and proper nervous system function. Gpr126 acts as a receptor in Schwann cells to initiate myelin formation, and this function is conserved in mammals (Monk et al., 2009). In the basal lamina, type IV collagen binds the CUB/PTX-containing region of zebrafish *gpr126 in vitro*, and is thought to be a putative ligand necessary for this function (Monk et al., 2011; Paavola et al., 2014). On the other hand, laminin-211 physically interacts with the zebrafish *gpr126*-NTF to drive Schwann cell differentiation and myelination (Petersen et al., 2015). In this case, laminin-211 can either suppress or promote *Stachel*-mediated activation of Gpr126-CTF depending on its concentration and subsequent polymerization, thus suggesting a mechanical force to remove Gpr126-NTF and activate signaling and cAMP accumulation.

Zebrafish *gpr126* mutants also have defects in the morphogenesis of the semicircular canals in the inner ear (Diamantopoulou et al., 2019; Geng et al., 2013; Leon et al., 2020; Paavola et al., 2014). Semicircular canals are three interconnected tubes that provide sensory input for experiences of rotary movements. In zebrafish, they develop from an ovoid epithelial vesicle, the otic vesicle, in which finger-like projections grow towards the center, where they fuse to form the

three semicircular ducts of the vestibular system (Geng et al., 2013). Extracellular matrix gene expression is high during projection outgrowth and then rapidly downregulated after fusion, and *Gpr126* controls this switch. Thus, sustained expression of extracellular matrix components causes an abnormal projection outgrowth and failure to form the semicircular canals, resulting in ear swelling. In fact, *gpr126* zebrafish mutants were initially called *lauscher* mutants (german word for eavesdropper) due to their swollen ear phenotype, before identifying mutations in the *gpr126* locus (Geng et al., 2013; Whitfield et al., 1996).

In addition, *Gpr126* has been shown to play a role in heart development in mice (Patra et al., 2013; Waller-Evans et al., 2010), supported by additional studies in zebrafish using morpholinos (Patra et al., 2013). Studies on two different *Gpr126* knockout mice have shown that *Gpr126* disruption leads to fully penetrant embryonic lethality between E11.5 and E12.5 due to cardiovascular failure (Patra et al., 2013; Waller-Evans et al., 2010). Waller-Evans generated a presumable *Gpr126* null allele in which part of the 7TM domain was replaced by a *LacZ* reporter gene cassette (*GPR126^{LacZ}*), and homozygous mutants displayed thinner myocardial walls, but no defects in trabeculation at E11.5 (Waller-Evans et al., 2010). Patra et al. used R-*Gpr126* knockout mice from RIKEN (The Institute of Physical and Chemical Research), in which the exon 2 has been replaced by a *LacZ* reporter cassette. The authors reported that homozygous mutants were characterized not only by a thinner ventricular wall, but also by fewer trabeculae, bradycardia, cardiac arrhythmia, and mitochondrial dysfunction at E11.5 (Patra et al., 2013). They confirmed the same results in a third T- *Gpr126* knockout mouse line from Taconic/Lexicon, in which exons 3 and 4 (termed 2 and 3 in the original paper) were replaced by a selection cassette in the mutant allele, with the only exception that some homozygous embryos survive until birth (Monk et al., 2009; Patra et al., 2013). Besides, heart trabeculation was also disrupted in *gpr126* zebrafish morphants using translation-inhibitory and splicing-inhibitory morpholinos targeting the *gpr126*-NTF, but not in morphants in which the NTF remained intact (Patra et al., 2013). This heart phenotype was rescued by coinjection of the morpholino with the *gpr126*-NTF mRNA. Thus, Patra and co-workers support that *Gpr126*-NTF is necessary and sufficient for cardiac trabeculation in mice and zebrafish, whereas the CTF is dispensable for this function (Patra et al., 2013). However, and despite the large number of *gpr126* mutant lines that have been analyzed (*gpr126^{st49}*, *gpr126^{st63}*, *gpr126^{st86}*, *gpr126^{stl47}*, *gpr126^{stl215}*, *gpr126^{stl464}*, *gpr126^{tb233c}*, *gpr126^{fr24}*, *gpr126^{tk256a}*, *gpr126^{vu39}* ...), no heart phenotype has been mentioned or reported apart from the morpholino experiments (Diamantopoulou et al., 2019; Leon et al., 2020; Liebscher et al., 2014; Monk et al., 2009; Paavola et al., 2014; Petersen et al., 2015).

4. Notch activity is required for ventricular trabeculation in mice

The Notch pathway is a key player in the endocardial-myocardial communication during cardiac development (de la Pompa and Epstein, 2012; High and Epstein, 2008).

Notch is an evolutionary conserved cell-to-cell signaling pathway (Artavanis-Tsakonas et al., 1999). Notch proteins are single-pass transmembrane receptors with a large extracellular domain (NECD), followed by a shorter membrane-spanning portion and an intracellular domain (NICD), which contains a transcriptional activation domain (Fig. 5A). Most surface Notch proteins are cleaved by furin-like convertases during the secretory pathway at site 1 (S1), which converts the Notch polypeptide into a NECD/NICD heterodimer held together by noncovalent interactions (Kopan and Ilagan, 2009). In the cell surface, NECD can interact with membrane-bound ligands of the Delta (Dll1-4 in mammals) or Jagged (Jag1 and Jag2) families expressed by neighboring cells (Fig. 5A). Productive ligand-receptor interaction depends on the activity in the signaling cell of E3 ubiquitin ligases such as mind bomb-1 (MIB1), which ubiquitylates the ligand in its cytoplasmic C-terminal tail (Itoh et al., 2003) (Fig. 5B). Subsequent ligand endocytosis generates mechanical force to pull on Notch, which in turn induces conformational changes leading to exposure of the S2 site of the receptor, recognized by ADAM (A Disintegrin And Metalloprotease) proteins (Meloty-Kapella et al., 2012; Parks et al., 2000) (Fig. 5C). The remaining Notch fragment becomes susceptible to cleavage by γ -secretase (at the S3 site), resulting in the release of NICD, which translocates to the nucleus of the signal-receiving cell and functions as a transcription factor (Fig. 5D-F). In the nucleus, NICD binds directly to the DNA-binding protein RBPJ, otherwise known as CSL (CBF1, Suppressor of Hairless, Lag-1), thus displacing corepressors and allowing the recruitment of the transcriptional coactivator mastermind-like (MAML) (Jarriault et al., 1995) (Fig. 5F). Formation of the RBPJ-NICD-MAML ternary complex allows the recruitment of additional coactivators to activate transcription of target genes (Jarriault et al., 1995; Luxán et al., 2016) (Fig. 5F).

In the developing E9.5 ventricle, Notch1 is active in ventricular endocardial cells at the base of the forming trabeculae (Grego-Bessa et al., 2007), where its ligand *Dll4* is also expressed (D'Amato et al., 2016b). *Dll4*-Notch1 interaction is crucial for early ventricular chamber development, and targeted inactivation of *Notch1* or *Dll4* in the embryonic endocardium severely disrupts trabeculation, resulting in embryonic lethality at mid-gestation (E10.5) (D'Amato et al., 2016b; Grego-Bessa et al., 2007). Gene expression profiling of wild-type (WT) and mutant E9.5 ventricles by RNA-seq analysis revealed that transcription of *Gpr126* was strongly downregulated in endothelial/endocardial *Dll4* and *Notch1* mutants. In zebrafish larvae, *Gpr126* cardiac expression is also abrogated when Notch activity is genetically or chemically impaired. Furthermore, *Gpr126* contains two-conserved putative RBPJ binding sites in intron four that

1. INTRODUCTION

respond to Notch stimulation in luciferase assays, and human umbilical vein endothelial cells (HUVEC) respond to Dll4 stimulation by increasing *Gpr126* expression (D'Amato et al., 2016b). Altogether, *in vivo*, *in vitro*, and *in silico* studies point to *Gpr126* as a potential Notch effector in chamber endocardium during trabeculation.

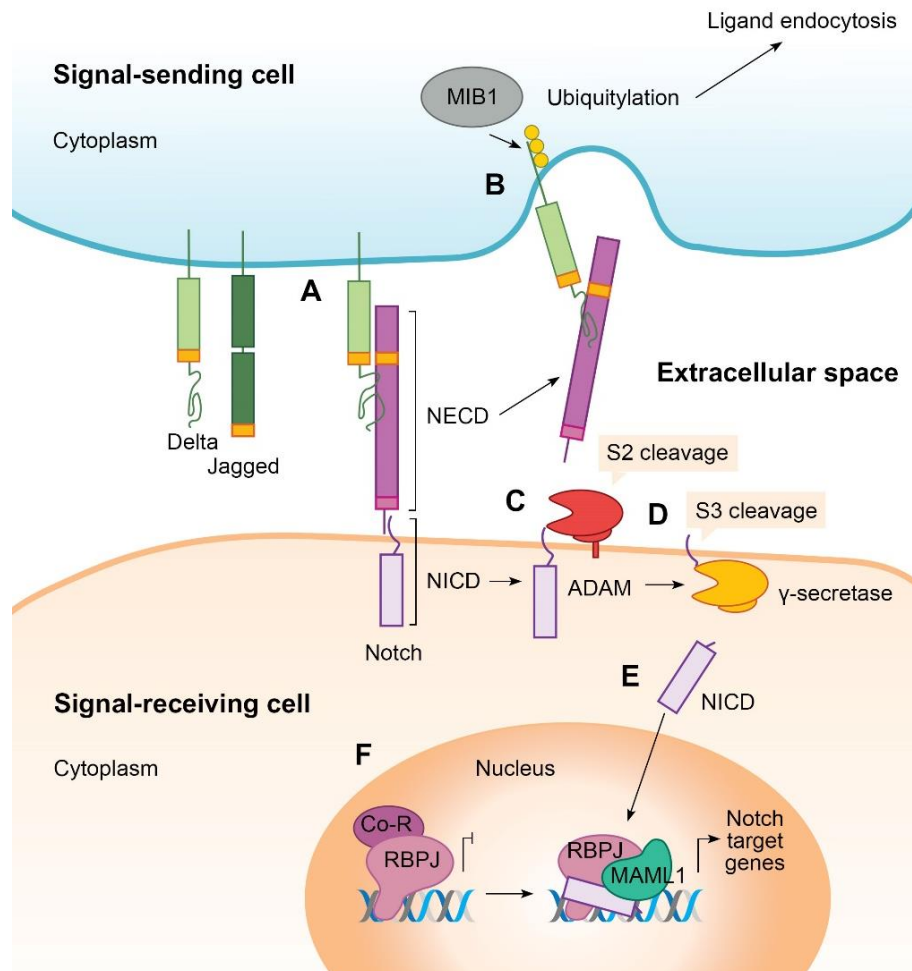


Figure 5. The Notch signaling pathway. (A) In the signaling cell, membrane-bound Notch ligands (Delta and Jagged) bind to Notch receptors in the neighboring cell through interaction with the Notch extracellular domain (NECD). (B) Upon ligand interaction, the ubiquitin ligase Mind bomb-1 (MIB1) ubiquitinylates the ligand intracellular domain (yellow circles) and induces ligand endocytosis. This process exerts a force on the Notch receptor in the receiving cell that exposes a site for cleavage (S2) by ADAM (A Disintegrin And Metalloprotease) proteases (C). This cleavage renders the residual transmembrane Notch fragment as a substrate for proteolysis (S3) by the γ -secretase protease (D), which releases the Notch intracellular domain (NICD) (E). (F) NICD then travels to the nucleus and forms a transcriptional activation complex after binding to RBPJ and the coactivator Mastermind-like (MAML) to promote gene transcription. In the absence of NICD, RBPJ associates with corepressor proteins (Co-R) to repress transcription.

2

OBJECTIVES

This doctoral thesis aims to understand the role of Gpr126 in mouse and zebrafish development, paying particular attention to the heart. Previous work has demonstrated that *Gpr126* deletion in mice causes fully penetrant embryonic lethality due to cardiac defects, and knockdown in zebrafish impairs trabeculation. However, the molecular mechanism behind Gpr126 cardiac function remained elusive.

The four main objectives of this thesis were:

- To determine the expression pattern of *Gpr126* in mouse embryonic development.
- To characterize the role of Gpr126 in mouse and zebrafish heart development by generating constitutive loss-of-function alleles.
- To establish the primary cause of embryonic lethality of constitutive *Gpr126* loss-of-function mutants.
- To characterize the tissue-specific functions of mouse Gpr126 by generating conditional loss- and gain-of-function alleles.
- To dissect the roles of Gpr126-NTF adhesive domains in mouse embryonic development.

3

**MATERIALS AND
METHODS**

1. Mouse lines

1.1 Ethics statement

Animal studies were approved by the CNIC Animal Experimentation Ethics Committee and by the Community of Madrid (Ref. PROEX 118/15). All animal procedures conformed to EU Directive 2010/63EU and Recommendation 2007/526/EC regarding the protection of animals used for experimental and other scientific purposes, enforced in Spanish law under Real Decreto 1201/2005.

1.2 Generation of *Gpr126*^{Δ3,4}, *Gpr126*^{Δ7} and *Gpr126*^{lox} mouse lines

Conditional knock-in *Gpr126*^{lox} and standard knock-out *Gpr126*^{Δ3,4} and *Gpr126*^{Δ7} mouse lines were generated using CRISPR/Cas9 technology. The mouse *Gpr126/Adgrg6* gene (ENSMUST00000041168) located in chromosome 10, contains 25 coding exons that produce 5 different transcripts (annotated as *Adgrg6-201* to *Adgrg6-205* in Ensemble). *Adgrg6-201*, with a length of 6507 bp, is the largest transcript containing an open reading frame (ORF). *In silico* analysis showed that the deletion of exons 3 and 4, encoding for the CUB and PTX domains, respectively, does not alter the ORF. In contrast, exon 7 is the first exon whose deletion triggers a translational frameshift and a premature termination codon (PTC) in exon 8. Exon 7 is termed as Exon 6 in the *Adgrg6-201* transcript from Ensemble (<https://www.ensembl.org/>) because the exon 6 is alternatively spliced in this isoform. CRISPR RNA (crRNA) sequences targeting introns 2 and 4 (to generate the *Gpr126*^{Δ3,4} mouse line) and introns 6 and 7 (to generate the *Gpr126*^{Δ7} and the *Gpr126*^{lox} mouse lines) were designed using the Spanish National Biotechnology Centre (CNB)-CSIC web tool Breaking-Cas (<http://bioinfogp.cnb.csic.es/tools/breakingcas/>) and CRISPOR-TEFOR online tool (<http://crispor.tefor.net/crispor.py>). Those sequences with higher specificity and efficiency scores were selected (Table 1). For the generation of the knock-in *Gpr126*^{lox} line, two complementary and asymmetric single-stranded oligodeoxynucleotides (ssODNs) were designed to insert two loxP sites on either side of exon 7, according to published guidelines (Richardson et al., 2016). Each ssODN bears a loxP sequence with a 67-bp 5' homology arm, a 36-bp 3' homology arm, a single base substitution at the protospacer adjacent motif (PAM) sequence, and an *EcoRI* recognition site (Table 1).

crRNA sequences were used as annealed two-part synthetic crRNA (Alt-R^R CRISPR-Cas9 crRNA, 2 nmol, Integrated DNA Technologies, IDT) and tracrRNA (Alt-R^R CRISPR-Cas9 tracrRNA, 5 nmol, IDT, 1072532) molecules, known as the Alt-R CRISPR-Cas9 System. The Cas9 protein was the Alt-R^R *Streptococcus pyogenes* Cas9 Nuclease (IDT, 1081058). ssDNA templates were custom synthetic genes (MegamerTM single-stranded Gene Fragments, IDT).

3. MATERIALS AND METHODS

The complete guide RNA complex (annealed crRNA and tracrRNA) was diluted in microinjection buffer (1mM Tris HCl, pH 7.5; 0.1mM EDTA) and incubated with Cas9 protein to obtain active ribonucleoprotein (RNP) complexes. The final concentration of components in RNP preparations was 0.61 pmol/μl of crRNA and tracrRNA, 30 ng/μl of Cas9 protein and 10 ng/μl of ssODN (Table 2, 3). The final injection mixes were passed through Millipore Centrifugal Filter units (UFC30VV25, EMD Millipore) and spun at 21,000 g for 5 min at room temperature.

Microinjections were performed by the Transgenesis Unit at CNIC. Mouse zygotes were obtained by mating C57BL/6 stud males with superovulated C57BL/6 females (Charles River Laboratories). One-cell stage fertilized mouse embryos were injected into the male pronuclei and the cytoplasm with the corresponding preparations (Table 2, 3). Microinjected zygotes were cultured overnight at 37°C in Potassium supplemented simplex optimized medium (KSOM), RS-1 medium, or KSOM plus RS-1 before embryo transfer into the oviduct of a synchronized recipient doe. RS-1 is a homology driven repair (HDR) enhancer that increases knock-in efficiency (Song et al., 2016). Two-cell stage embryos (E2C) were transferred to one CD-1 recipient doe (~25 embryos per female). Microinjections were performed as described previously (Harms et al., 2014).

Weaned pups were screened for the targeted knock-out or knock-in mutation by PCR analysis and sequencing, and the selected founders were bred to C57BL/6 mice to pass the mutation through the germline.

Mouse line	Type	Position	Sequence (5' - 3')	Length (bp)
All	tracrRNA	-	AGCAUAGCAAGUUAAAUAAGGCUAGUCCGUUAUCAACUUGAAAAAGUGG CACCGAGUCGGUGCUUU	67
<i>Gpr126</i> ^{Δ3,4}	crRNA	Intron 2	UGCAGGGCUUGACACCCAUUCGUUUUAGAGCUAUGCU	36
	crRNA	Intron 4	CAUGCUACUUAGUGAAAGTGUUUUAGAGCUAUGCU	36
<i>Gpr126</i> ^{lox} & <i>Gpr126</i> ^{Δ7}	crRNA	Intron 6	AUUAAAGGACACACAGGCGCGUUUAGAGCUAUGCU	36
	crRNA	Intron 7	GGCGGAAGAUCGACAGGUGCGUUUAGAGCUAUGCU	36
	ssODN	Intron 6 - LoxP	CTAATCAGGAGCTACTTCTAAGCGGTGCAACAGTAATTTTAAACATCAAAATT GGCCCCAAACTTCATGCGATAACTTCGTATAATGTATGCTATACGAAGTTA	147
			TGAATTCCCTGTGTGTCCTTTAATATATGCAATGACGTGACG	
	ssODN	Intron 7 - LoxP	TTTCAGATCTTCTAGTTTCAGTTCCTCCAGCGCCCACTTTTGGAGGCTCACACAC ACGCTGCCACTCGAGCAATAACTTCGTATAATGTATGCTATACGAAGTTA TGAATTCCCTGTGTCGATCTTCGCCCTCTCTCTGTTGCTGTGGG	147

Legend

crRNA (target sequence)

tracrRNA/ sequence complementary to tracrRNA

EcoRI site

PAM site modified

LoxP site

Table 1. CRISPR-Cas9 elements used for the generation of mouse lines.

Sequences of Alt-R tracrRNA, crRNAs and ssODNs used to generate *Gpr126*^{Δ3,4}, *Gpr126*^{Δ7} and *Gpr126*^{lox} mouse lines by CRISPR/Cas9 technology. crRNA, crispr RNA; tracrRNA, trans-activating crispr RNA; ssODN, single-stranded oligodeoxynucleotide.

MI	MIX-1		MIX-2			Weaned pups				GMO (%)	Comments					
	Prot Cas9 (ng/uL)	crRNA 5' Intron2 (μM)	tracrRNA (μM)	Prot Cas9 (ng/uL)	crRNA 3' Intron 4 (μM)	tracrRNA (μM)	E2C	TFs	Born pups			Male	Female	+/+	+/-	-/-
1	30	0.610	0.610	30	0.610	0.610	107	4	15	7	4	14	1	0	6.7	RS-1 (7.5-uM) O/N
							18	1	2	0	2	2	0	0	-	
							10	1	0			0	0	0	-	
2	30	0.610	0.610	30	0.610	0.610	16	1								KSOM + RS-1 (7.5-uM) O/N KSOM + RS-1 (7.5-uM) O/N KSOM O/N
							13	1	4	1	2	3	1	0	25	
							23	1								
							187	9	21	8	8	19	2	0	9.5	

Table 2. Summary of the targeting efficiency for the generation of *Gpr126*^{Δ3,4} mouse line using CRISPR/Cas9 technology.

crRNA, crispr RNA; tracrRNA, trans-activating crispr RNA; E2C, two-cell stage; TFs, transferences; GMO, genetically modified organisms.

MI	MIX-1				MIX-2	Weaned pups				Alleles				HDR (%)	NHEJ (%)	GMO (%)	Comments
	Prot Cas9 (ng/uL)	crRNA 5' Intron 6 (uM)	Alt-R CRISPR tracrRNA (uM)	ssODN 5' Intron 6 - LoxP (ng/uL)	Same with crRNA 3' Intron 7 and ssODN 3' Intron 7 - LoxP	E2C	TFs	Born pups	Male	Female	5' loxP in	3' loxP in	2 loxP in (in cis)	Del			
1	30	0.610	0.610	10		101	5	8	3	2	-	-	-	2	0	40	
2	30	0.610	0.610	10		30	4	4	1	1	1	-	-	0	50	50	E2C incubated in RS-1 (7.5-uM) O/N
						49	1	0	-	-	-	-	-	-	-	-	E4C incubated in RS-1 (7.5-uM) O/N
3	30	0.610	0.610	10		104	5	9	5	4	7	7	2	2	63.6	86	E2C incubated in KSOM + RS-1 (7.5-uM) O/N
Total						284	15	21	9	7	8	7	2	4			

Table 3. Summary of the targeting efficiency for the generation of *Gpr126^{lox}* and *Gpr126⁴⁷* mouse lines using CRISPR/Cas9 technology.

crRNA, crispr RNA; tracrRNA, trans-activating crispr RNA; ssODN, single-strand oligodeoxynucleotide; E2C, two-cell stage; TFs, transferences; in, insertions; del, deletions; HDR, homology-driven repair; NHEJ, non-homologous end joining; GMO, genetically modified organisms.

1.3 Generation of *R26-GPR126^{GOF}* mouse line

Human GPR126 cDNA N-terminally tagged with a hemagglutinin (HA) epitope and C-terminally tagged with a FLAG epitope was gently provided by Torsten Schöneberg's laboratory (Mogha et al., 2013). The sequence was digested with *SpeI* and cloned into the *SpeI* and *XbaI* sites of the intermediary vector *pBigT-IRES-GFP*, which contains a selectable marker cassette (PGK-NeoR) flanked by loxP sites, followed by an internal ribosome entry site (IRES) and the enhanced green fluorescent protein (eGFP) (Fig. 20A). A polyadenylation sequence (pA) is located to the 3' end of the neo expression cassette to prevent transcriptional read-through (Soriano, 1999). *GPR126* cloning was targeted between pA and IRES sequences (Fig. 20A). The resulting plasmid was digested with *PacI* and *AscI* to release the *loxP-PGK-NeoR-STOP-loxP-GPR126-IRES-eGFP* construct and get it inserted into the *PacI-AscI* linearized modified version of the *pROSA26-1* plasmid (Soriano, 1999) (Fig. 20A). This vector harbors 5.4 kb Rosa26 homology regions (extending 1.1 kb 5' and 4.3 kb from the *PacI-AcsI* sites), along with a diphtheria toxin expression cassette (PGK-DTA) for negative selection (Fig. 20A). The final *ROSA26-GPR126^{GOF}-GFP* construct was linearized with *PvuI* and electroporated into G4 mouse embryonic stem (mES) cells derived from a mixed 129X1/Bl6 genetic background. After G418 (200 µg/ml) selection for 7 days, 100 clones were picked. Neomycin-resistant ES clones were expanded and screened by Southern blot analysis using external 5'- and 3'-hybridization probes to detect homologous recombination events (Fig. 20A). Upon *EcoRV* digestion, the 5' probe detects an 11.5 kb WT band and a 4 kb targeted band, due to the presence of an extra *EcoRV* site in the transgene (Fig. 20A). Upon *EcoRI* digestion, the 3' probe detects a 15.5 kb WT band and a 13.2 kb targeted band (Fig. 20A). In total, 7 out of 86 ES neo-resistant clones integrated the entire construct, as determined by the presence of the aforementioned bands (data not shown). Three clones were selected to confirm the karyotype. Electroporation, mES cell expansion, screening by Southern Blot and karyotyping was performed by the Pluripotent Cell Technology Unit at CNIC. One positive clone was microinjected into C57BL/6 blastocysts, which were subsequently transferred into pseudopregnant females to generate chimeric offspring. Microinjections were performed by the Transgenesis Unit at CNIC. The resulting chimeric mice were genotyped by PCR of tail genomic DNA samples using primers in the *R26* locus before and after the cloning site and in the polyA signal of the transgene. A male founder was selected and bred to C57BL/6 females to pass the mutation through the germline.

1.4 Mouse strains

Mouse strains used in this study are as follows: *Tie2-Cre* (Kisanuki et al., 2001), *Nfatc1pan-Cre* (Wu et al., 2012), *Nkx2.5-Cre* (Stanley et al., 2002), *Mesp1-Cre* (Saga et al., 1999), *Sox2-Cre* (Hayashi et al., 2002) and *Dll4^{fllox}* (Koch et al., 2008).

2. Zebrafish lines

2.1 Ethics statement

All experiments using zebrafish (*Danio rerio*, strain AB) were done according to German Animal Protection Laws approved by the local governmental animal protection committee. Embryonic and adult zebrafish were raised and maintained under standard conditions (Westerfield, 2000). All experiments were performed on zebrafish embryos or larvae between 48 hpf and 5 dpf.

2.2 Generation of *gpr126^{bns341}* and *gpr126^{bns342}* zebrafish lines

Mutant zebrafish lines were generated in Prof. Stainier's laboratory at the Max Planck Institute for Heart and Lung Research (MPI-HLR) in Bad Nauheim, Germany, during a 7 months-long stay.

Target site selection. The zebrafish *gpr126/adgrg6* locus (ENSDARG00000054137), located in chromosome 20, contains 25 coding exons that produce 4 different transcripts (annotated as *adgrg6-201* to *adgrg6-204* in Ensemble). *Adgrg6-204*, with a length of 4246 bp, is the largest transcript containing an open reading frame (ORF). *In silico* analysis showed that the deletion of exons 7-9, encoding for part of the SEA domain, triggers a translational frameshift and a PTC in exon 10. crRNA sequences targeting introns 6 and 9 (generating the *gpr126^{Δ7,8}* zebrafish line, officially called *gpr126^{bns341}*) were designed using the CRISPOR-TEFOR online tool. Those sequences with higher specificity and efficiency scores were selected.

To identify the promoter region of *gpr126*, we used Ensemble to allocate different promoter sequences: **TATA boxes** (consensus sequence of TATAA) 700 bp to 1 kb away from the transcriptional start site (TSS), **CAAT boxes** (GGCCAATCT or CAAT), B recognition elements (**BRE**) (G/C-G/C-G/A-CGCC), initiator elements (YYANWYY), and downstream promoter elements (**DPE**) (RGWYV):

5' TATTTGTTAATAAGAATTCTTAAAAAAGAGACCATTTCATGAATAAATCTATTATTTTT
TATTATCTATTATTATTATTTTAACTTAA**TATAAAA**TATTAAGTAAAAATTTTTTAAAAAGTTA
CGTTTTTTTTTCATTAAATATTAGTGTTAAATAACATCTATGTTTTAGAACAGTCAGTTTCATT

3. MATERIALS AND METHODS

GGCAATACAAATATGTAAACAATGAAACACATTGATTAATTAGGATTAAGTAATGTTGAATC
TTTATTTAAAAATAGTTTTGTAACTAATACCGCATATTGACATTTTAAGCTAATAAAATGTGA
AAATAAAATAAAAAAAGTAATCTGCAAATCCCTGTTGTTTTCTTCTCAAATCTCTGATTCCTA
CATTGAATTAGCAGTGCCAGTTTTCTTTTACCACAGTATTGCCTGAAGTGTAATAGAAAAG
GCTTTTGATTTATCTGGAAGCAGACTGAGCTTTATCACTGCATGCATTTGCCTGAATCCTTTC
CTGCATCATTGTGGATGCAAATGATGAACATCACCAGTGATTATTTCCGTTTCGCTCCCTTA
TACTCTGCTTAATTGGCTCAAGTGAATTTACAAAGCAGTTTAGTGCTTCAGATGCAATCCAT
CTTGCATATGCATTTACACCACAACAGGAATAAACCACAATGACCATAACATTTTGTCAATTT
AACTTTTAAAAATTAACCTGGGGGATTTTGTGACTTGTAATCCCTCTTTAGTGTTAACGTGT
GTTTAAGGTATTGACTTAGACGCTCAAAGAGATAACGTTTATTACTTGATCGCTATCTGTTCT
GTGGGAATCGAGAAAGCTCACCTTTTTTCTCTATTTCTTTTTCTTTATTTTATTTTTCTCCAT
TGCAAATGCAGGATTATCATTAAACATTTATATTGGCTATCGAGCAGAATAATTGAGTAATTT
GTGAAGAGCTAAGCATCTGGAAGGATCGTCCAAATTGTAATTTCTGGCACTTAAGTTGTTTT
ACATTCAAAATCTTCATCCAAGTTCCCTGTGTTCTGGTGATAAAACGTCACCGTGGCTGTAAAT
CTCAACGCTAAACAAAACACATAAATGAAGCTAGCCTGTAATAAATGTCCATGTTATTGTGC
ATGGCTTCTCACACCCAATAGATCAAAACCAAAACCAATCCTCAACAGGGACGAAAAACA
AAAAGGCAGATTTTTCATCTGAATAAATGTGTGCTATTATCATTATCTACCAGCTCACAGGCT
TGTAACAGCTACATAACCTGAGATTTCTGTGCGAGCATGCTATTTGACCTGAATGTTGTAAT
GTAAATATCAGAGGTACATGCAAATTCAGCTATCCGACTTAGGAGCTATCTAACTGGAAGAT
CTTCTCTGACGTTGAAAACAAAGCAGCTAGCATGGCTTAATGAGGACAAAACAGTGCATAC
AAGTCTTTGACTAGTTTGTTCATGGAATTATAGCAAATGTTTACAGTATGTTGTTTTTATT
TTCTTTATATAATCTAACAGAAAACTAATTACAAAAGGTACTTTCATCATATTAATTATATT
TTGCATATTGGTTAGTTGGTGGAATTGTGTCATTTAAATTTAAGCACAAGCTACACTATCGGT
CAAACCTTTTAGGGTTTTATTTTTTTCATTTATTTTATTTATTTATTTTGTCTTTTATTACTATTA
CCATGAATAATATTGATAATAATAATATTAATTATTATTAGAGTGATTCTGAAGGATCATGT
GACTGAAGACTGGAGTAATGAAGCTAAAATTTAATCTTTAAAATCACTGGAATAAATGATTA
AATTAAATATATACTACTTTTGAACAGTTATTTTATAGTGTAATAACATTTCAATATTTA
ATAAAAGAAATGCAGCTTTGGTGAGCAGGATAGGCTGTTTTAAATTAGACTCAAACATCTT
ACTGATCCTAAACTCTCTATATAAGCAAAAAAGCTAATGTTTTATTAATAGCCTATCTGTTCTC
TGTTTCTCTCTACACTTGCAGACATGCATATTTAAATGTAAGTATATAAATATTTGATT
TTGCATAAGCACTATTTAGAAATGTAGTTATTTTATTTTTAAGCATGAACAAAAATAAATAG
CACACAATAGAAAAAAGTATTTTAATACACGATTATGATATAATTTTGTGTGTGTTGTGT
ACACCCCCCTCCCCCACATCTCATTTAACTAATGTTTTCTAAAGGATGCATTAATCAAT
ATTCTATTTTTGCAAATTCATTAGTTTATTCAGTACTGAAGCCAGATCTAAGGCTAATCTAAC
AAAACAACCTTAATGGTTCAAAAATGAGTAGCCCAAATTTATATGTTAGGGGAAAAT
ATTAAATACATTTTTCAAAAATAGCAAAAATCAAGAGAAGCAAAAATATATACAGTTTTGTT
AAAATGTTGTAGTTTGTAATATTTATTATTATTTTTTGATCTTTCCATTTCTAAAG
ATGTTTTGTGACAAAATATTATTTTTAATAAATATATCTCTTTAATAAATCTGTTTTGTTCAAA
TGCACATGTGAAGAGTTCAGATGCAAAAACCTCTAAATCCCGTCTGAAATTTTCTCT
AACTGAGCATTTTTATCAGGCTCCTGTGGGTATGTTTCAGTAATATTACTTTTATGGGAAAGA
ATAAGTTATCTTCTGGTCTTTAAAGTAAATATCTCAACATAAACAAAGGAGGCTGATAAA
ATTTCTAATGATTTTTGATAGAAATTTACACGGCACTTAGAGTTTTTGTATCTAACTTTTT
ATATATTCCCATATTCAGTAAACTGGATACAACCTGTTTCATGTTGTTTCGTTTCATATTGTCA
CTGTTCAAACCTGTTTCGATGTTTTGTTTCATATCAAAAATAGGGTGTACTCATTATGCTGTA
TAAATCCTATTATTATATATATATATATATATATATATATATATATATATATATATATATAT
ATATATATATATACATTTTATATATATATATATATATATATATATATATATATATATATAT
ATATATATATATACATTTTATATATATATATATATATATATATATATATATATATATATAT
ACATTATATATATATATGCCTATTGTTTACACATACATTGTTTATTTTTTGTAAAACATGT
AAATTACATGTGTAGGTCTGTTTGTAATAAACATAAATTATACATAATCACATGTTACTTTTA
ACTGGCTACATTTCTATCCGCCGTTTGGACAAAGACTTTTGTATCTCATTTACTGCT
AGGAAATGCTTAAGAAATGTTTCATAGATGTAAATATGACAAACTATTGTGAAGAATTGGT
GTTTAACTGTTTAACTACTTGTCTCTTTTTGGGGGTCTCCTCGGGATTTCTCTGCTGAAGGG
TGGGGCTCCAGTCAGAACTGCCTCCAGCGGTTGGACAAGCGCAGTATTGTCTAGTAACTCT
TGTTAACGCTTAACCCAGCATCTGTCTGCCTGGAGCGCAATCTGTCAAAAAACCGAC
ATTTAATTGATTTTCAGAATATCTGCGATGATGATAAAGAAGATGATGGTGTGTTTTAGCTGA
GCTGTGGAGAGGCTCGTGTAATTGACGGTGAAGTGACTGACTGACGCTCAAACCTCTCTCA
AGTTGTTCAAACAGAAGAGATATCATGCTTCAAGCAGAGCTTCAATGAAACAAT 3'

3505 bp until *gpr126* 5'UTR

Because *gpr126* has a big intron 1 (9848 bp), which likely contains regulatory regions, it was targeted for deletion to prevent transcriptional activation. The H3K4me3 histone marks along the *gpr126* locus were evaluated using ChIP-seq data from the UCSC genome browser (<https://genome-euro.ucsc.edu/cgi-bin/hgGateway?redirect=manual&source=genome.ucsc.edu>). The Zv9 was selected as the reference genome assembly and the tab called UMass ChIP-seq was activated. crRNA sequences targeting 5' of the first TATA sequence and the end of intron 1 (generating the *gpr126*^{promoterless} zebrafish line, officially called *gpr126*^{bns342}) were designed using the CRISPOR-TEFOR online tool. Those crRNA sequences with higher specificity and efficiency scores were selected.

sgRNA template generation and transcription. To generate the *gpr126*^{bns341} zebrafish line, one sense and one antisense oligonucleotide were designed based on the target sequence. To create 5' overhangs for directional cloning, TAGG and AAAC nucleotides were added to the 5' end of the sense and antisense oligonucleotide, respectively (Table 4). 5 µl of each oligonucleotide (1mM) were annealed in a final volume of 10 µl by heating the mixture at 95°C for 5 minutes and then cooling it down overnight at room temperature in a T4 ligase buffer (10x) (Promega, M1801). Annealed oligonucleotides were subsequently cloned into a *BsmBI* (New England Biolabs, R0739)-digested pT7-gRNA vector (Addgene, plasmid 46759) using the T4 ligase (Promega, M1801) in a final volume of 10 µl for 2 hours at room temperature. The resulting plasmid was transformed into DH5α competent *E. coli* cells using Promega's heat shock protocol. Two colonies were transferred to a 10 ml sterile culture tubes containing 3 ml of Luria-Bertani (LB) medium supplemented with ampicillin (1:1000) (Fisher Scientific, 10419313) and grew overnight at 37°C with shaking (~250 rpm). Plasmid DNA was isolated using the QIAprep Spin Miniprep Kit (QIAGEN, 27104) and confirmed by sequencing via the Eurofins LightRun Sequencing Service. The plasmids were linearized by digestion with *BamHI*-HF (NEB, R3136S) and purified using a Gel DNA Recovery kit (Zymo Research, D4001). The linearized DNA template was transcribed by the T7 polymerase using a MEGAshortscript T7 Transcription Kit (Life Technologies) following the manufacturer's instructions for 5 hours at 37°C. The gRNAs were treated with 1 µl DNase for 15 minutes at 37°C, purified using an RNA Clean and Concentrator kit (Zymo Research, R1013), quantified using a Nanodrop spectrophotometer, and examined by gel electrophoresis. Then, they were stored at -80°C.

To generate the *gpr126*^{bns342} zebrafish line, the templates for gRNA transcription were generated as described in (Gagnon et al., 2014). Zebrafish *gpr126*-specific oligonucleotides contained the T7 (5'-TAATACGACTCACTATA-3') promoter sequence, the 20-base target site without the PAM, and a complementary region (Table 4). The gene-specific oligo (10 µM) was annealed to a constant oligonucleotide encoding the reverse-complement of the tracrRNA tail (10 µM) in a final volume of 10 µl at 95°C for 5 minutes, followed by slow cooling at room

temperature and 20 minutes at 4°C. The ssDNA overhangs were filled in with T4 DNA polymerase (NEB, M0203), BSA (NEB), and dNTPs (10 µM) (Promega, U1511) in a final volume of 10 µl for 20 minutes at 12°C. The resulting sgRNA template was purified using a QIAquick nucleotide removal kit (QIAGEN, 28304) and stored at -20°C. 1 µl of template DNA was transcribed in a 5 µl transcription reaction using MEGAscript™ T7 Kit (Invitrogen, AMB13345) according to the manufacturer's instructions for 5 hours at 37°C. The gRNAs were treated with 1 µl DNase for 15 minutes at 37°C, purified using an RNA Clean and Concentrator kit (Zymo Research, R1013), and quantified using a Nanodrop spectrophotometer. Then, they were stored at -80°C.

Cas9 mRNA generation. pT3TS-nCas9n plasmid for *in vitro* synthesis of nls-Cas9-nls mRNA was purchased from Addgene (Addgene, plasmid 46757). *Xba*I linearized pT3TS-nCas9n was purified with the Zymoclean Gel DNA Recovery kit (Zymo Research) and used as a template for *in vitro* transcription of capped, polyadenylated mRNA with the mMESSAGE mMACHINE™ T3 kit (Invitrogen, AM1348) according to the manufacturer's instructions for 3 hours at 37°C. Cas9 mRNA was treated with 1 µl DNase for 15 minutes at 37°C, purified using an RNA Clean and Concentrator kit (Zymo Research, R1013), and quantified using a Nanodrop spectrophotometer. Then, it was stored at -80°C.

Zebrafish embryo microinjection. The microinjection mix for the generation of mutant lines contained 75 ng/µl of each gRNA (2 for the *gpr126^{bns341}* line, and 4 for the *gpr126^{bns342}* line), 200 ng/µl Cas9 mRNA, and phenol red in a final volume of 10 µl. Zebrafish Tübingen/AB zygotes were collected and microinjected into the yolk at the one-cell stage using the Narishige IM 300 microinjector. The injected embryos were genotyped at 24 hpf to examine the presence of deletions in the targeted regions and genomic DNA was extracted from 10 pools of 5 embryos each. If the deletion was detected, the embryos were grown to adults for founder analysis.

2.3 Transgenic zebrafish lines

Transgenic lines used in this study are *Tg(kdrl:Hsa.HRAS-mCherry)* (Chi et al., 2008) and *Tg(myf17:EGFP-Hsa.HRAS)* (D'Amico et al., 2007), kindly provided by Prof. Stainier's laboratory (Max Planck Institute for Heart and Lung Research, Bad Nauheim, Germany).

Genetic line	Type	Name	Sequence (5' - 3')	Length (bp)
<i>gpr126^{bns341}</i> (47,8)	Oligo	crRNA 5' T7 sense (I6)	TAGGGGAGTCTCCTAAGAAAAGCCT	24
	Oligo	crRNA 5' T7 antisense (I6)	AAACAGGCTTTCTTAGGAGACTCC	24
	Oligo	crRNA 3' T7 sense (I8)	TAGGAGATATTCCATTAGGCTAAT	24
	Oligo	crRNA 3' T7 antisense (I8)	AAACATTAGCCTAATGGAATATCT	24
<i>gpr126^{bns342}</i> (promoter-less)	Oligo	Constant oligo	AAAAAGCACCGACTCGGTGCCACTTTTTCAAGTTGATAACGGACTAGCCTTATTTTAA CTTGCTATTTCTAGCTCTAAAC	80
	Oligo	crRNA prless 5'1 (T7)	TAAATACGACTCACTATAAGTCTGTTCTCTGTAAGAGTGCGAGTTTTTAGAGCTAGAAAATA GCAAG	62
	Oligo	crRNA prless 5'2 (T7)	TAAATACGACTCACTATAAGGCTCTTACAGGAACGACCACA GTTTTAGAGCTAGAAAATA GCAAG	62
	Oligo	crRNA prless 3'1 (T7)	TAAATACGACTCACTATAAGGCGGACGATGAGGTTTACAAA GTTTTAGAGCTAGAAAATA GCAAG	62
	Oligo	crRNA prless 3'2 (T7)	TAAATACGACTCACTATAAGGATTGTATGGAGCATTGCCCC GTTTTAGAGCTAGAAAATA GCAAG	61
	Oligo	crRNA prless 3'2 (T7)	TAAATACGACTCACTATAAGGATTGTATGGAGCATTGCCCC GTTTTAGAGCTAGAAAATA GCAAG	61

Table 4. CRISPR-Cas9 elements used for the generation of zebrafish lines.

Sequences of constant and crRNA oligos used to generate *gpr126^{bns341}* and *gpr126^{bns342}* zebrafish lines by CRISPR/Cas9 technology. crRNA, crispr RNA; tracrRNA, trans-activating crispr RNA.

Legend

Target sequence

Sequence complementary to constant oligo

T7 promoter

3. Genomic DNA extraction, genotyping, and sequencing

Mouse genomic DNA was extracted from biopsies of the tail tip of weaned or adult mice by incubating the samples with 300 μ L of 50mM NaOH at 95°C for 10 minutes, and equilibrating with 50 μ L of 1M Tris-HCl pH8. For embryonic and fetal samples, DNA was extracted from the yolk sac or a piece of the tail tip by digesting the tissue with 5 μ L Proteinase K (Roche, 03115801001) in 100 μ L of lysis buffer [50mM KCl, 10mM Tris-HCl pH8.3, 2mM MgCl₂, 0.45% Igepal-CA630 (Sigma-Aldrich, I3021), 0.45% Tween-20 (Sigma-Aldrich, P9416), 0.01% gelatin (Sigma-Aldrich, G2500)] for 2 hours at 55°C. To screen for adult carriers and genotyping adult zebrafish, genomic DNA was extracted from clipped fins by incubating the samples with 100 μ L of 50mM NaOH at 95°C for 20 minutes, and then equilibrating with 25 μ L of 1M Tris-HCl pH8. To genotype zebrafish embryos, DNA was extracted by digestion of the whole embryo with 5 μ L Proteinase K in 100 μ L of elution buffer (EB) of the QIAprep Miniprep Kit (QIAGEN, 27104) for 2 hours at 55°C. The primer sequences used for genotyping all mouse and zebrafish lines are listed in Table 5. For mouse samples, PCR reactions were performed using 500 nM of each primer, 1 μ L of extracted DNA, and DreamTaq Green PCR Master Mix (2X) (Thermo Scientific, K1081) or AccuStart™ II PCR Supermix (2x) (Quanta Biosciences, 95137) in a total reaction volume of 20 μ L. For zebrafish samples, PCR reactions were performed using 500 nM of each primer, 1 μ L of extracted DNA, and PrimeSTAR® Max DNA Polymerase (2x) (Takara, R045A) in a total reaction volume of 10 μ L. The amplicons were separated on a 1–3% agarose gel. The size of amplicons was estimated using the 1Kb Plus DNA ladder (Invitrogen, 10787018). For sequencing, the gel-purified amplicons were subjected to TA cloning in the pGEM-T Easy vector (Promega, A137A). Sequencing was performed by Sanger-style BigDye terminator chemistry on an ABI730xl sequencer at CNIO's DNA Sequencing Service (mouse-derived sequences), or by Eurofins LightRun Sequencing Service (zebrafish-derived sequences).

Genetic line	Primer sequence (5' - 3')	Ann. T ^a	WT amplicon (bp)	Mut/ tg amplicon (bp)
<i>Gpr126</i> ^{Δ3,4}	F: TTTGTAAACATTGAGCTCTCCCT R: TCATTAGGGTAACACGGAGA R: TATGTATGAAAAGATGGCCTGGT	60°C	495	288
<i>Gpr126</i> ^{Δ7}	F: CAACAGTAATTTTAACATCA R: GCATTATTTGTTGGTTTCATTCA	52°C	824	357
<i>Gpr126</i> ^{lox}	F: CAACAGTAATTTTAACATCA R: GCATTATTTGTTGGTTTCATTCA	52°C	824	904
	F: CAACAGTAATTTTAACATCA R: GCATTATTTGTTGGTTTCATTCA	50.4°C	322	362 (5'LoxP)
	F: TGAAACCAACAAATAATGCTT R: AAAAATAAGTAAAAAGAACAC	51°C	521	561 (3'LoxP)
<i>R26-GPR126</i> ^{GOF}	F: AAAGTCGCTCTGAGTTGTTAT R: GGAGCGGGAGAAATGGATATG F: TGCCCGACAACCACTACCTGA	60.5°C	585	853
<i>Dll4</i> ^{lox}	F: GTGCTGGGACTGTAGCCACT R: TGTTAGGGATGTCGCTCTCC	60°C	408	455
<i>Nfatc1-Cre</i>	F: GAAGCAACTCATCGATTGATTTACG R: AACCCCTGGACGCCTGGGACAC	58°C		1000
<i>Tie2-Cre</i>	F: GGGAAGTCGCAAAGTTGTGAGTT R: CTAGAGCCTGTTTTGCACGTTT	58°C		500
<i>Nkx2.5-Cre</i>	F: GATGACTCTGGTCAGAGATACCTG R: GCGCACTCACTTTAATGGGAAGAG	60°C		583
<i>Mespl/ Sox2-Cre</i>	F: TGACGGTGGGAGAATGTTAAT R: GCCGTAAATCAATCGATGAGT	58°C		286
<i>gpr126</i> ^{bs341}	F: CGAGAGAATCCTTGTGTGGA R: TTGATGGTCCATTTGCTGAA	55°C	1171	387
<i>gpr126</i> ^{bs342}	F: GGCTTTCAGGCATTTTCTTC R: TCACACACACAGGAGCACAA R: CAATGCACACAATAAAGGAACTCC	55°C	906	322
<i>Tg(kdrl:Hsa.HRAS-mCherry)</i>	F: CCCGCCGACATCCCCGACT R: ACTTGTACAGCTCGTCCATGCC	62°C		469
<i>Tg(myf7:EGFP-Hsa.HRAS)</i>	F: ATGGTGAGCAAGGGCGAGGA R: TTAATTGTACAGCTCGTCCA	62°C		720

Table 5. List of primers used for genotyping the mouse (top) and zebrafish (bottom) lines.

Ann, annealing; T^a, temperature; F, forward; R, reverse; mut, mutated; tg, transgene.

4. Histological procedures

4.1 Tissue collection and processing

Pregnant females at different gestational stages were euthanized according to laboratory animal welfare guidelines by cervical dislocation. The uterus was dissected and transferred to phosphate-buffered saline (PBS). For examination of the embryonic hearts, whole embryos (E9.5-E10.5) or thoracic cavities (E11.5-E18.5) were isolated in ice-cold PBS and fixed in 4% (vol/vol) paraformaldehyde (PFA) (Electron Microscopy Sciences, 50980487) in PBS overnight at 4°C with gentle shaking. The same procedure was applied to the dissected placentas. For examination of neonatal mouse hearts, pups were euthanized by decapitation, and hearts were dissected, washed in PBS, and fixed overnight in 4% PFA at 4°C with gentle shaking. For examination of adult hearts, mice were euthanized by cervical dislocation and, after resection of the descending aorta, the heart was perfused through the right ventricle with 1 mL of PBS and 1 mL of 4% PFA. The heart was dissected, weighed, and incubated for 48 hours in 4% PFA at room temperature with gentle shaking. After fixation, the samples were washed in PBS.

Paraffin-embedding of embryos, hearts and placentas was performed by immersion in a series of ethanol solutions of increasing concentrations (30%, 50%, 70%, 90%, 2x 100%). Incubation times were longer for large samples. Following the dehydration, the tissue is cleared with xylene washes and embedded in melted paraffin. The samples were properly oriented in a plastic mold and left on a cooled plate until solid. Paraffin-embedded embryos/organs were cut into 7 µm sections using a semi-automated rotary microtome (Leica Biosystems).

E9.5 embryos used for whole-mount *in situ* hybridization were washed in PBS-T (PBS containing 0.1% Tween-20) and dehydrated by washing in a methanol series of increasing concentrations (25%, 50%, 75%, 90%, 2x 100%, 15 minutes each). Embryos were stored at -80°C until proceeding with the protocol. Immunofluorescence (IF)

7-µm paraffin sections were washed twice for 5 minutes with xylene and rehydrated by a series of ethanol solutions of decreasing concentrations (2x 100%, 90%, 70%, 50%, 30%, 3 minutes each), followed by Milli-Q (MQ) water washes. For antigen retrieval, the sections were boiled for 15 minutes in 10mM citrate buffer (Sigma-Aldrich, 25114) pH 6, and endogenous peroxidases were quenched with 1% hydrogen peroxide solution (Sigma-Aldrich, H1009) in methanol for 40 minutes. The tissues were permeabilized with 0.3% Triton-X100 (Bio-Rad, 1610407) in PBS, and washed with PBS-T before incubation with the blocking solution [3% bovine serum albumin (BSA) (Sigma-Aldrich, A9418), 5% goat serum (Vector laboratories, S-1000), 20mM MgCl₂, and 0.3% Tween-20] for 1 hour at room temperature. The primary antibodies (Table 6) were diluted in blocking solution and the sections were incubated at 4°C

overnight. The following day, sections were washed with PBS, followed by incubation with fluorescent-dye-conjugated secondary antibodies (Table 6) in 5% BSA/ PBS for 1 hour at room temperature. For signal amplification, a secondary biotin-conjugated antibody was used, followed by the formation of avidin-biotinylated-Horseradish peroxidase (HRP) complexes using the VECTASTAIN[®] Elite ABC kit (Vector Laboratories, PK-6100). Signal detection was performed using the Tyramide Signal Amplification (TSA) Plus Fluorescein (PerkinElmer, NEL741B001KT) for 3.5 minutes at room temperature according to the manufacturer instructions. Sections were washed in PBS before incubation with DAPI (Sigma-Aldrich, D9542) for 10 minutes at room temperature. Alexa Fluor-647-conjugated Isolectin GS-IB4 from *Griffonia simplicifolia* (ThermoFisher, I32450) and Rhodamine-conjugated wheat germ agglutinin (WGA) (Vector laboratories, RL-1022) were incubated in PBS (1:200) for 2 hours at room temperature prior to DAPI counterstaining. The slides were mounted with Fluoromount (Southern Biotech, 0100-01).

4.2 Histological staining

Hematoxylin and eosin (H&E), Masson's trichrome, and periodic acid–Schiff (PAS) stainings were performed according to standard protocols by the Histopathology Unit at CNIC.

4.3 Detection of hypoxic cells

The Hypoxyprobe[™]-1 Plus Kit (Chemicon, HP2-100) was used according to the manufacturer's instructions. The hypoxia-marker pimonidazole hydrochloride (PIMO) was injected intraperitoneally (60 mg/kg of body weight) into pregnant mice 30 minutes before euthanasia. Embryonic thoracic cavities and placentas were isolated in sterile PBS, fixed with 4% PFA at 4°C overnight, processed for paraffin embedding, and sectioned at 7 µm. The slides were incubated with FITC-conjugated α -PIMO primary antibody (included in the kit), a secondary rabbit α -FITC-HRP-conjugated antibody (Dako, P5100), and TSA-Fluorescein for signal detection, following the same protocol detailed in the *Immunofluorescence (IF)* subsection.

Type	Name	Dilution	Amplification	Host	Type	Company	Catalog
Primary	α -BrdU (B44)	1/100	TSA	Mouse	Monoclonal	BD Biosciences	347580
	α -SMA-Cy3	1/200	-	Mouse	Monoclonal	Sigma-Aldrich	C6198
	α -ERG	1/100	-	Rabbit	Monoclonal	Abcam	EPR3863
	α -Endomucin (V.5C7)	1/100	-	Rat	Monoclonal	Santa Cruz Biotechnology	sc-53941
	α -GLUT-1	1/100	-	Rabbit	Polyclonal	MERCK Millipore	07-1401
	α -CD31/Pecam	1/100	-	Rat	Monoclonal	Santa Cruz Biotechnology	sc-18916
	α -pimonidazole (FITC-MAb1)	1/100	TSA	Mouse	Monoclonal	Chemicon	HP2-100
Secondary	Biotinylated α -mouse IgG (H+L)	1/100		Goat	Polyclonal	Vector laboratories	BA-9200
	α -Rat IgG (H+L), Alexa Fluor 647	1/200		Goat	Polyclonal	Invitrogen	A21247
	α -Rabbit IgG (H+L), Alexa Fluor 647	1/200		Goat	Polyclonal	Invitrogen	A21245
	α -Rabbit IgG (H+L), Alexa Fluor 488	1/200		Goat	Polyclonal	Invitrogen	A11034
	α -Rat IgG (H+L), Alexa Fluor 488	1/200		Goat	Polyclonal	Invitrogen	A11006
	α -FITC/HRP	1/200		Rabbit	Polyclonal	Dako	P5100

Table 6. List of antibodies used in this study.

4.4 DIG-labeled RNA probe synthesis

Antisense RNA probes were designed to be exon spanning or complementary to the 5' or 3'UTR sequences. Targeted regions were amplified by PCR using as template ~100 ng cDNA from embryos, hearts, or placentas, and DreamTaq Green PCR Master Mix (2X), compatible with TA cloning. The primer sequences used for probe generation are listed in [Table 8](#).

Gene	Primer sequence (5' - 3')		Probe length (bp)
<i>Bmp10</i>	Constructed by Hanying Chen		888
<i>Cx40</i>	Provided by Rober Kelly's laboratory		
<i>Ednrb</i>	For	TCTTCATGGGCAATAATCGTC	435
	Rev	CGGCTTTATTACAAGTGCAT	
<i>Eng</i>			938
<i>GPR126</i>	For	TGGCAAAATGACTTCTGGAATA	631
	Rev	GTCCCCAGTAGGTTACCAATG	
<i>Gpr126 (3'UTR)</i>	GenePaint, template T36447		705
<i>Gpr126 (Ex3-4)</i>	For	TCCTGTCCAATCCTTCCGGTA	660
	Rev	GGAGCCCCAAGAATTATTCCAC	
<i>Hey2</i>	Constructed by Hiroki Kokubo		
<i>Irx5</i>	Constructed by Antje Bosse		740
<i>Ldha</i>	For	CTGCAGTTGGCAGTGTGTCT	543
	Rev	GGAAGGAGGTTCAACAAGCAG	
<i>Mash2</i>	Constructed by Sara Austin		301
<i>Nfatc1</i>			1029
<i>N-myc</i>	Provided by Cecilia B. Moens laboratory		215
<i>Pcdh12</i>	For	ACAGTTTCCCAAAGACGAGCA	764
	Rev	GACCGTTGTTTCCTGAGTCCA	
<i>Pdk1</i>	For	GCCAGCTACTCCACGTTCTT	575
	Rev	CTGGGTTTGGTTACGGATTG	
<i>Prl2c2</i>	For	AACATTATTCTAACGTGTCTGG	441
	Rev	TGTAACACTTCAGGACGTTG	
<i>Tpbpa</i>	For	CAACATAGAAATGAGTGCC	638
	Rev	ACACAGTTAATTATGCCTT	

Table 8. List of primers used for mRNA probes generation in this study.

The PCR product was ligated to the pGEM-T easy vector using the pGEMTM-T easy vector system (Promega, A1360) and the resulting plasmid was transformed into DH5 α competent *E. coli* cells using Promega's heat shock protocol. White colonies were selected for colony PCR screening using a vector-specific primer and an insert-specific primer to check the insert orientation. Positive colonies were transferred to 10 ml sterile culture tubes containing 3 ml of Luria-Bertani (LB) medium supplemented with ampicillin (1:1000) (Fisher Scientific, 10419313), and grew overnight at 37°C with shaking (~250 rpm). Plasmid DNA was isolated using the QIAprep Spin Miniprep Kit (QIAGEN, 27104) and sequenced by the Eurofins LightRun Sequencing Service. The plasmids were linearized by digestion with an appropriate restriction endonuclease cutting downstream of the insert sequence and purified using a Gel DNA Recovery kit (Zymo Research, D4001). The linearized cDNA template was transcribed by the T7 or Sp6 polymerase using the DIG RNA labeling mix (Roche, 11277073910) for 2 hours at 37°C. The RNA probes were purified using the Illustra AutoSeq G-50 Kit (Cytiva, 27534001) and stored at -80°C.

4.5 *In situ* hybridization (ISH) on sections

7- μ m paraffin sections were washed twice for 5 minutes with xylene and rehydrated by a series of ethanol solutions of decreasing concentrations (2x 100%, 90%, 70%, 50%, 30%, 10 minutes each), followed by PBS washes and postfixation with 4% PFA for 20 minutes at room temperature. The tissue was digested with 10 μ g/ml proteinase K for 15 minutes at 37°C and postfixed with 4% PFA for 5 minutes. The slides were treated with 0.07N hydrochloric acid (HCl) (Sigma-Aldrich, 320331) for 15 minutes, and 0.25% acetic anhydride (Sigma-Aldrich, 242845) in 0.1M triethanolamine solution (Sigma-Aldrich, 90279) pH 8 for 10 minutes. For prehybridization, the slides were incubated with hybridization buffer [50% formamide (Sigma-Aldrich, F903), 20X saline-sodium citrate (SSC) buffer (Sigma-Aldrich, S0902), 0.1% Tween-20, 50 μ g/ml heparin (Sigma-Aldrich, H4784), 5 mg/ml yeast tRNA (Roche, 10109525001)] for 5 hours at 65°C, before adding the RNA probe to the hybridization buffer for overnight incubation. The following day, sections were washed twice with post-hybridization buffer-I [50% formamide, 0.2X SSC pH 5.5, 1% sodium dodecyl sulfate (SDS) (Bio-Rad, 1610418)] and -II (50% formamide, 5X SSC pH 5.5, 5% SDS) for 30 minutes at 65°C each, and then in maleic acid buffer containing Tween-20 (MABT) for 15 minutes at room temperature. Next, the sections were incubated with a blocking solution [2% heat-inactivated fetal bovine serum (FBS), 1% blocking reagent (Roche, 11096176001) in MABT] for 2 hours at room temperature. The slides were incubated with the anti-digoxigenin antibody coupled to alkaline phosphatase (AP) (Roche, 11093274910) (1:2000) in blocking solution at 4°C overnight. The following day, the sections were washed for 3 hours in MABT, and then in AP buffer [0.1M NaCl, 0.05M MgCl₂, 0.1M Tris-

HCl pH 9.5, 10% Tween-20, 2mM tetramisole hydrochloride (Sigma-Aldrich, T1512)], twice for 10 minutes each. BM-purple (Roche, 11442074001) was added for the development of the signal. The reaction was stopped by PBS washes, and the sections were postfixed in 4% PFA for 15 minutes at room temperature, followed by dehydration through a series of ethanol solutions of increasing concentrations. After xylene washes, the slides were mounted with Entellan (Sigma-Aldrich, 107960) and dried at room temperature.

4.6 Whole-mount *in situ* hybridization (WISH)

E9.5 embryos stored in 100% methanol at -80°C were rehydrated by a series of methanol solutions of decreasing concentrations (75%, 50%, 25%, 10 minutes each), followed by PBS-T washes. The embryos were digested with proteinase K (20µg/ml) for 5 minutes at room temperature and the reaction was stopped by washing with 2 mg/ml glycine in PBS (Sigma-Aldrich, 50046). Postfixation was performed by incubation with 4% PFA and 0.2% glutaraldehyde (Fisher Bioreagents, 10418543) in PBS for 20 minutes at room temperature. The embryos were incubated with the hybridization solution (50% formamide, 5X SSC pH 4.5, 1% SDS, 50 µg/ml yeast tRNA, 50 µg/ml heparin) for 3-5 hours at 70°C. Then, the RNA probe was added to the embryos for overnight incubation. The following day, the embryos were washed with post-hybridization buffer-I (50% formamide, 5X SSC pH 4.5, 1% SDS) twice for 30 minutes each at 70°C, post-hybridization buffer-II (0.5M NaCl, 10mM Tris-HCl pH 7.5, 0.1% Tween-20) three times for 5 minutes each at room temperature, and post-hybridization buffer-III (50% formamide, 2X SSC pH 4.5) for 5 minutes at room temperature and then twice for 30 minutes at 65°C. Then, the embryos were washed with tris-buffered saline containing 0.1% Tween-20 (TBS-T) at room temperature, incubated with blocking solution (10% heat-inactivated FBS in TBS-T) for 90 minutes, and anti-digoxigenin antibody coupled to alkaline phosphatase (AP) (1:2000) in 1% heat-inactivated FBS/TBS-T overnight at 4°C. The next day, the embryos were washed in TBS-T containing 2mM tetramisole hydrochloride, initially 3 times for 5 minutes each at room temperature, 8 times for 30 minutes each, and finally overnight at 4°C. The following day, the embryos were washed with NTMT buffer (0.1M NaCl, 0.1M Tris-HCl pH 9.5, 50mM MgCl₂, 0.1% Tween-20) containing 2mM tetramisole hydrochloride 3 times for 10 minutes each. 4-Nitro blue tetrazolium chloride (NBT) solution (0.45 µl/ml) (Roche, 11383213001) and 4-toluidine salt (BCIP) (0.45 µl/ml) (Roche, 11383221001) were added into the NTMT buffer containing 2mM tetramisole hydrochloride for the development of the signal. The reaction was stopped by PBS-T washes, and the embryos were postfixed in 4% PFA overnight at 4°C. To intensify the color, the embryos were dehydrated by a series of methanol solutions of increasing concentrations (25%, 50%, 75%, 100%) for 10 minutes each, followed by rehydration through the inverse methanol

series to PBS-T. For imaging, the embryos were floating in PBS-T. For paraffin-embedding and sectioning, see *Tissue collection and processing for histological procedures* subsection.

5. Gene expression analysis

5.1 RNA extraction and cDNA preparation

Mouse embryos, embryonic hearts and placentas were dissected in ice-cold PBS and stored at -80°C. Pools of 3-5 embryonic hearts (E9.5, E10.5) or individual embryos and placentas (E11.5, E12.5) were homogenized in TRI Reagent™ Solution (Invitrogen, AM9738) using steel beads for 5 minutes at 50 Hz in the TissueLyser LT Adapter (QIAGEN, 85600). For RNA extraction, the direct-zol RNA MiniPrep kit (Zymo Research, R2051) was used according to the manufacturer's instructions. Complementary DNA (cDNA) was obtained from 1 µg of total RNA using the High Capacity cDNA Reverse Transcription Kit with random hexamers (Applied Biosystems, 4368814) according to the manufacturer's instructions.

DNA and RNA were extracted from single zebrafish embryos or larvae by phenol-chloroform extraction. The samples were homogenized in TRI Reagent™ Solution using the NextAdvance Bullet Blender® Homogenizer (Scientific instrument services, SIS). 200 µl of chloroform was added per mL of TRI Reagent, and phase separation was obtained by vortexing and centrifugation. The top aqueous phase (containing RNA) was isolated and stored at -80°C for RNA isolation procedure. The bottom organic phase (containing DNA) was subjected to ethanol purification to precipitate the DNA. Purified DNA was dissolved in MQ water and genotyping was performed by PCR as described in the *Genomic DNA extraction, genotyping, and sequencing* subsection. RNA from WT, heterozygous and homozygous *gpr126^{bns341}* and *gpr126^{bns342}* zebrafish (derived from at least 3 different crosses) was pooled (3 embryos per pool) for RNA precipitation. 500 µl of 100% isopropanol (Sigma-Aldrich, I9516) was added per mL of TRI Reagent, and samples were incubated for 10 minutes at room temperature, followed by centrifugation. The RNA pellet was washed with 1 ml of 75% ethanol per ml of TRI Reagent and centrifuged for 5 minutes at 4°C. The RNA pellet was dried for 10 minutes at room temperature and resuspended with Biopak RNase-free water. cDNA was obtained from 600 ng of total RNA using the Maxima First Strand cDNA synthesis kit (Thermo Scientific, K1641) according to the manufacturer's instructions.

5.2 Quantitative real-time PCR (qRT-PCR)

Two to five biological replicas (pools of mouse embryos or hearts) and three technical replicas per sample were done for mouse gene expression analysis. One to three biological

replicas (pools of zebrafish embryos) and three technical replicas per sample were done for zebrafish gene expression analysis. The primer sequences used for qRT-PCR are listed in [Table 7](#). PCR reactions were performed using 200nM of each primer, 2 μ L of cDNA template previously diluted 1:10, and Power SYBR Green PCR Mastermix (2X) (Applied Biosystems, 4367659) in a total reaction volume of 10 μ L. For mouse samples, qPCR was carried out using an ABI PRISM 7900HT FAST Real-Time PCR System (Applied Biosystems) at CNIC, programmed with an initial denaturation step at 95°C for 10 minutes, followed by 40 cycles of denaturation at 95°C for 15 seconds, and a combined annealing and extension step at 60°C for 1 minute. Upon completion of the amplification steps, a final melting-curve analysis was done (95°C - 60°C - 95°C, for 15 seconds each). For zebrafish samples, qPCR was carried out using a CFX Connect Real-Time System (Biorad) in the MPI-HLR (Bad Nauheim, Germany).

Relative expression levels were calculated based on comparative Ct values after normalizing with the geometric mean of internal control genes, being *Gapdh* or β -*actin* for mouse samples, and *ribosomal protein L13a* (*rpl13a*) for zebrafish samples. The analysis was performed using the $2^{-\Delta\Delta C_T}$ method described in (Livak and Schmittgen, 2001). A two-tailed unpaired Student's t-test was used for statistical analysis using the GraphPad Prism version 8 software and differences were considered statistically significant at $P < 0.05$. Data are presented as mean \pm standard deviation (SD).

3. MATERIALS AND METHODS

Organism	Gene	Primer sequence (5' - 3')
Mouse	<i>Adam17</i>	For AGCTTATTACAACCCAACTG Rev CAGCTTCCTTTGTGAGAATAG
	<i>Apobec2</i>	For ACATCCTGAAGTAGGCAACAG Rev CCAAGTAGAATCAGGAAGCCAG
	<i>Cst3</i>	For CCGAACTACATGTACCAAGTCC Rev GCACGCTGTAGATCTGGAAG
	<i>Cts7</i>	For CTATGTGACTCCAGTGCGAAG Rev GGGATCAGTTTGCCAGTTTTC
	<i>Cts8</i>	For GAATGGCAGGAGTGGAAGAG Rev TTATGCTGTTTGACCAGTTTCATG
	<i>Ctsq</i>	For CAGTAGTGGTCATCCCAGAAAG Rev CTGGGATCAAATGCTGAAACAC
	<i>Cxcr4</i>	For AGGTAGCAGTGAAACCTC Rev ATACTCACACTGATCGGTTC
	<i>Cxcr7</i>	For AAAACATTTGAGTTTCAGGGG Rev TACAGCAAGTTTCACTCAAC
	<i>Dlx5</i>	For AGCCCCTACCACCAGTAC Rev TTTACCATTACCATCCTCACC
	<i>Eng</i>	For GTTCCTGGTCCTCGTTTCG Rev TTGGCTGTCCTTGGAAGATG
	<i>eNOS</i>	For GGTCTGTCATGGATGAGT Rev CACAGAAGTGGGGGTATGCT
	<i>Gapdh</i>	For AACTTTGGCATTGTGGAAGG Rev ACACATTGGGGGTAGGAACA
	<i>Gata3</i>	For CTTATCAAGCCCAAGCGAAG Rev GTCCCCATTAGCGTTCCTC
	<i>Gpr126 (Ex24-3'UTR)</i>	For ATCATCAAGAAGAGCTCCGAT Rev TGGGCATTACAGTAACCCTT
	<i>Gpr126 (Ex4-Ex7)</i>	For TGAGCTGTGGTTCCTACCTG Rev GATATTCGATACATTATTCGCTCT
	<i>Gpr126 (Ex9-10)</i>	For GGATGAAAGTCAAGAGAGAC Rev GACGTTATTGGTAGCATTGTAG
	<i>Il1a</i>	For CTGCAGTCCATAACCCATGA Rev GAGCGCTCACGAACAGTTG
	<i>Mash2</i>	For GGATCTGCACTCGAGGATTTT Rev GACCCCGTACCAGTCAAG
	<i>Mest</i>	For GAGTGATCGCCCTTGATTCT Rev AGAAGGGACTCTACGATGCT
	<i>Mmp9</i>	For ACGACATAGACGGCATCCA Rev GCTGTGGTTCAGTTGTGGTG
	<i>Pcdh12</i>	For GAGCCTGTTGGACCCTAATAC Rev ATGACAATCTCGCCATCCAG

Continue on next page

Mouse	<i>Pgf</i>	For	TCAGGATGTGCTCTGTGAATG
		Rev	TCCTCTTCCTCTTCCCCTTG
	<i>Prl2c2/Plf</i>	For	CTTTGATTCAACCATGCTCCTG
		Rev	ACGACCATTCCCTCATTGCAC
	<i>Prl3b1/Pl2</i>	For	GCAGGGATACACATAAAGTTGAC
		Rev	AGGGACCTTCTAAGAGACAGAG
	<i>Prl3d1/Pl1</i>	For	CACTTCCCCTGTGTCATACTG
		Rev	ATTGATCATTGCTTTCAGAAGGTC
	<i>Prl7b1/Prlpn</i>	For	CTGGATCGCATCATGAAGATTG
		Rev	TCATTGGCTGACTGTAAGGATG
	<i>Prl8a2/Dtprp</i>	For	CTGCTCAGATCCCCTTGTG
		Rev	GCTGAGAATGGGTTGTGGTA
	<i>Serpine1</i>	For	GAAGACCCCTTTCTTAGAGGC
		Rev	ATAACATCTCCAGTTTCGTCCC
	<i>Syna</i>	For	TCACCACCTCAACTGTGTATTT
Zebrafish		Rev	CTGATGATGGAGGTGGCTATT
	<i>Synb</i>	For	AAGGGAGGGAAGGAGAGAAA
		Rev	CTGGTAACATCTCCAGCATGAA
	<i>Tgfbβ1</i>	For	TGGAGCAACATGTGGAAGTC
		Rev	CAGCAGCCGGTTACCAAG
	<i>Tgfbβ2</i>	For	GAGATTTGCAGGTATTGATGG
		Rev	CAACAACATTAGCAGGAGATG
	<i>Timp1</i>	For	CATCCTCTTGTTGCTATCAC
		Rev	CATGAATTTAGCCCTTATGACC
	<i>Tpbpa</i>	For	CCAAATCAGCCACAGTAACATG
		Rev	TCAGGCAGTTCATATGTTGGG
	<i>Vegfa</i>	For	TAGAGTACATCTTCAAGCCG
		Rev	TCTTTCTTTGGTCTGCATTC
	β -actin	For	CTAAGGCCAACCGTGAAAG
		Rev	ACCAGAGGCATACAGGGACA
	<i>rpl13a</i>	For	GCCGCCCTGTTTCAAG
		Rev	CTCGACCATCAAGCACCAG
	<i>gpr126 (5'UTR)</i>	For	CGCAGGTTTCATCTGTCAAAA
		Rev	TTTACACGAGCCTCTCCACA
	<i>gpr126 (Ex7-10)</i>	For	CGGCGATAATATCTCAATGG
		Rev	TGTCGTGTGGTTGTGATCCT
	<i>gpr126 (3'UTR)</i>	For	GAAGGCCGGGATGGATATTA
		Rev	GCTTGCCCTCTCTATGCATTT
	<i>gpr112a</i>	For	TTCTTTACCTGTTTTTGCGTTG
		Rev	CCCCCATAGTGATTCTGCAT

Table 7. List of qRT-PCR primers used in this study.

5.3 RNA extraction and RNA sequencing (RNA-seq) analysis

E12.5 ventricles were collected from embryonic hearts after removing atria and the valve region in sterile ice-cold PBS, and then stored at -80°C. Upon genotyping, 4 pools of *Gpr126*^{+/+} and *Gpr126*^{Δ7/Δ7} embryonic ventricles (4 ventricles per pool) were homogenized in TRI Reagent™ Solution (Invitrogen, AM9738) using steel beads in the TissueLyser LT Adapter for 5 minutes at 50 Hz. For RNA extraction, the PicoPure™ RNA Isolation kit (Applied Biosystems, KIT0204) was used according to the manufacturer's instructions. RNA was quantified and its purity checked with a NanoDrop ND-1000 spectrophotometer (Thermo Scientific). RNA integrity was verified with an Agilent 2100 Bioanalyzer instrument (Agilent Technologies). Index-tagged cDNA libraries were constructed from 500 ng of total RNA using the TruSeq RNA Sample Preparation v2 Kit (Illumina). Libraries were quantified by Quant-iT™ dsDNA HS assay in a Q-bit fluorometer (Life Technologies). The average library size and size distribution were determined by DNA 1000 assay in an Agilent 2100 Bioanalyzer. Libraries were normalized to 10nM using 10mM Tris-HCl pH 8.5 containing 0.1% Tween-20, and then applied to an Illumina flow cell for cluster generation (NEBNext Ultra RNA Library Prep Kit) and sequencing by synthesis. Single reads of length 75 bp were generated with the HiSeq 2500 system (Illumina) on the Genome Analyzer IIx platform, following the standard RNA sequencing protocol. Reads were further processed using the CASAVA package (Illumina) to split reads according to adapter indexes and produce fast q files. New generation sequencing (NGS) experiments were performed in the Genomics Unit at CNIC.

6. Bioinformatics and statistics

6.1 Bioinformatic analysis of RNAseq data

The quality of sequencing reads was assessed by pre-processing through a pipeline that used FastQC (Andrews S). Sequencing reads were trimmed using Cutadapt v1.6 (Martin, 2011) to eliminate Illumina adaptor remains and reads shorter than 30 bp were discarded. The resulting reads were mapped against the mouse transcriptome (GRCm38 assembly, Ensembl release 70) and quantified using RSEM (RNA-Seq by Expectation Maximization) v1.2.3 (Li and Dewey, 2011). Raw expression counts were processed with an analysis pipeline that used the Bioconductor package EdgeR (Robinson et al., 2010) for normalization (using the TMM method) and differential expression testing. One sample was classified as an outlier given multidimensional scaling plots produced as part of the pipeline output and was discarded. Only genes expressed at a minimal level of 1 count per million in at least 2 samples were considered for differential expression analysis. Changes in gene expression were considered significant if

associated with a Benjamini-Hochberg adjusted P -value < 0.05 (Suppl. Table 3). NGS data analysis was performed in the Bioinformatics Unit at CNIC.

For the set of differentially expressed genes (DEGs), Gene Ontology (GO) and Kyoto encyclopedia of genes and genomes (KEGG) Pathway enrichment analyses were performed in GO-Elite (www.genmapp.org/go_elite/; 1.2.5, EnsMart77Plus database version) (Zambon et al., 2012) with a permuted P -value cutoff < 0.05 (Suppl. Table 4). Bar charts representing the z-score values of the terms belonging to the “biological processes” category were generated with GraphPad Prism version 8 software.

6.2 Sequence similarity analysis of mouse and zebrafish *gpr126* gene

Sequence similarity analysis was performed by the Bioinformatics and Deep Sequencing Platform in the MPI-HLR (Bad Nauheim, Germany), as described in (El-Brolosy et al., 2019). To identify similarity to zebrafish *gpr126* (ENSDARG00000054137) (Suppl. Table 14) and mouse *Gpr126* (ENSMUSG00000039116) (Suppl. Table 15) genes, the longest respective transcripts were selected (ENSDART00000145927 in zebrafish and ENSMUST00000041168.5 in mouse), and compared to the whole genome using BLASTn (Altschul et al., 1990). Genes were defined to be similar to the query gene when a partial match was identified inside the target gene body or the promoter region (2 kb upstream of the TSS). Several alignment parameters were surveyed to identify the optimal degree of similarity: alignment length, bit score (combination of alignment quality and length), and E value (probability that the match resulted by chance, when considering the whole target database). The thresholds were established as follows: from 21 onwards for the alignment length, from 40 to 100 for the bit score, and from 5×10^{-15} to 5.5 for the E value. These thresholds translate into local nucleotide sequence alignments that range from 21 to 273 nucleotides in length, and 71.06 to 100% identity (Suppl. Tables 14, 15).

6.3 Statistical analysis

Sample sizes, statistical tests and P -values are specified in the corresponding figure legends and corresponding subsections of *Materials and methods*. Statistical analysis and graphical representation were performed using the GraphPad Prism version 8 software and all values are presented as mean \pm SD.

7. Imaging

7.1 Zebrafish embryo preparation for live imaging

Embryos were treated from 28 hpf onwards with phenylthiourea (PTU; Sigma-Aldrich, P7629) to avoid pigmentation, and dechorionated just before live imaging using pronase (Sigma-Aldrich, P6911) (30 mg/ml).

7.2 Microscopy and confocal imaging

Whole-mount images were acquired using a Leica MZFL III binocular scope coupled to an Olympus DP 71 CCD camera and Olympus cellSense software. Brightfield imaging was performed using an Olympus BX51 Microscope and Olympus cellSense software. Confocal images were acquired using a Nikon A1R confocal microscope.

For *in vivo* confocal imaging, zebrafish embryos and larvae were mounted and anesthetized in 1% low-melting agarose (Sigma-Aldrich, A9414) containing 0.2% (w/v) tricaine on glass-bottom dishes. Before the gel solidified, the samples were manually oriented towards the microscope lens to enhance optical access to the heart. Z-plane images were taken using a spinning disc confocal microscope (Zeiss, CSU-X1 Yokogawa) and a 40X [1.1 numerical aperture (NA)] water-immersion objective. The optical section thickness was 1 μ m. Three non-consecutive single-plane images per larvae were taken using a Zeiss LSM780 confocal microscope and a 40X [1.1 numerical aperture (NA)] water-immersion objective. Confocal data were processed using the ZEN 2012 software (black edition) and image analysis was performed using the ImageJ software.

7.3 Quantification of cellular proliferation

BrdU positive cells were detected by immunofluorescence following the protocol described in (Del Monte et al., 2007). Total cells and BrdU-positive cells were counted in the compact myocardium, trabecular myocardium (counterstained with α -smooth muscle actin, α -SMA), and endocardium (counterstained with ETS-related gene, ERG) in 6 non-consecutive sections (3 from the right ventricle and 3 from the left ventricle) from 5 embryos of each genotype using the ImageJ software. Statistical analyses were performed using unpaired two-tailed Student's t-test, and differences were considered statistically significant at $P < 0.05$. Data are presented as mean \pm SD.

7.4 Quantification of hypoxia

PIMO's positive areas were quantified using the ImageJ software and a Macro designed by the Microscopy Unit at CNIC ([Annexes, Script 1](#)). Images were binarized by splitting color channels and PIMO's mean intensity was calculated. PIMO's positive areas (green) were selected using the intensity threshold "Otsu dark" (578, 4095), the total placental area was manually selected using DAPI staining, and the ratio between them was calculated. 2 non-consecutive sections were measured per placenta. Statistical analyses were performed using unpaired two-tailed Student's *t*-test, and differences were considered statistically significant at $P < 0.05$. Data are presented as mean \pm SD.

7.5 Quantification of the zebrafish ear area

5 dpf zebrafish larvae were mounted in 1% low-melting agarose and manually oriented in a dorsal position. Whole-mount images were acquired using a Leica MZFL III binocular scope coupled to an Olympus DP 71 CCD camera and Olympus cellSense software. Ear cross-sectional area was calculated from the perimeter drawn using the ImageJ software. Statistical analyses were performed using unpaired two-tailed Student's *t*-test in GraphPad Prism version 8 software, and differences were considered statistically significant at $P < 0.05$. Data are presented as mean \pm SD.

7.6 Quantification of PAS-positive areas

PAS-stained sections acquired with an Olympus BX51 Microscope and a 4X objective were converted to 8-bit grayscale using the ImageJ software. The contrast was enhanced (1% saturated pixels) and the Gaussian Blur filter was applied (Sigma 2). The outer placental zone was manually selected, thresholded ("Otsu dark" 0, 220) and the total area was measured. The PAS-positive area was digitally identified by selecting the threshold "Otsu dark" (0, 188) and the corresponding area was measured. The percentage of glycogen trophoblasts (PAS-positive) in the outer zone was obtained by calculating the ratio of the PAS-positive area/ outer zone area. 2 non-consecutive sections were measured per placenta. Statistical analyses were performed using unpaired two-tailed Student's *t*-test in GraphPad Prism version 8 software, and differences were considered statistically significant at $P < 0.05$. Data are presented as mean \pm SD.

7.7 Quantification of maternal and fetal blood spaces in the placenta

Images were binarized by splitting color channels using the ImageJ software. The Endomucin-containing channel (for quantification of the fetal vessel area) or the WGA-containing channel (for quantification of the maternal sinusoid area) were selected. The contrast

was enhanced (14% saturated pixels for Endomucin; 100% for WGA) and the Gaussian Blur filter was applied (Sigma 1.5 for Endomucin; 2 for WGA). The placental labyrinth was manually selected, thresholded (“RenyiEntropy” 524, end) and the total area was measured. The Endomucin-positive area was digitally identified by selecting the threshold “RenyiEntropy” (0, 14000) and the corresponding area was measured. The largest black spaces in the labyrinth (corresponding to maternal sinusoids) were digitally identified by selecting the threshold “Otsu” (0, 12000) and the corresponding area was measured. The percentage of fetal vessels (Endomucin-positive) in the labyrinth was obtained by calculating the ratio of the Endomucin-positive area/ labyrinth area. The percentage of maternal sinusoids (dark lacunae) in the labyrinth was obtained by calculating the ratio of the lacunae area/ labyrinth area. 2 non-consecutive sections were measured per placenta. Statistical analyses were performed using unpaired two-tailed Student’s *t*-test in GraphPad Prism version 8 software, and differences were considered statistically significant at $P < 0.05$. Data are presented as mean \pm SD.

7.8 Quantification of Rhodamine 123 fluorescence intensity

Rhodamine 123 fluorescence intensity was quantified using the ImageJ software. Images were converted to 8-bit grayscale, the sample was manually delineated and the mean intensity was calculated. Statistical analyses were performed using unpaired two-tailed Student’s *t*-test in GraphPad Prism version 8 software, and differences were considered statistically significant at $P < 0.05$. Data are presented as mean \pm SD.

8. Interventions

8.1 BrdU injection

Cell proliferation in E12.5 *Gpr126*^{+/+} and *Gpr126* ^{$\Delta 7/\Delta 7$} hearts was evaluated by 5-bromo-2'-deoxyuridine (BrdU) incorporation. Pregnant females were intraperitoneally injected with 300 μ l BrdU (BD Pharmingen, 550891) at 10 mg/ml, 2 hours before euthanasia. The embryos were isolated in sterile PBS, and thoracic cavities were fixed with 4% PFA at 4°C overnight, processed for paraffin embedding and sectioned at 7 μ m.

8.2 Rhodamine 123

Rhodamine 123 (Sigma-Aldrich, R8004) was injected subcutaneously (1 μ g/g of body weight) into pregnant mice 20 minutes before euthanasia. Embryos and placentas were dissected in cold PBS and imaged directly on a Leica MZFL III fluorescent scope linked to an Olympus DP 71 CCD camera and Olympus cellSense software.

8.3 Electrocardiographic (ECG) recordings

ECGs were recorded on anesthetized mice as previously described (Rivera-Torres et al., 2016). Briefly, mice were placed in a supine position on a temperature-controlled surface and were anesthetized with 1.5-2% isoflurane. Four-needle electrodes were subcutaneously inserted in the limbs. ECG recordings were acquired using MP36R Biopac Systems and analyzed offline using the LabChart7 software (AD Instruments, Australia). A high-pass filter setting of 0.5 Hz was applied to remove the baseline wander using a bidirectional filtering strategy. The PR interval was measured taking the beginning of the positive deflection of the P wave to the peak of the R wave; QRS interval was measured from the starting of the Q wave to the point where the S wave crosses the isoelectric line, and the QTc interval was measured from the point where Q wave starts to the point where the T wave reaches the 90% of the decline, considering the correction for RR intervals according to Bazett's formula for murine ECG (Mitchell et al., 1998). All these intervals were calculated from the average of ~ 450 ECG measurements. Short-term QT variability markers such as QT variance (QTvar), the standard deviation of the QT intervals (SDqt), short-term variability of the QT intervals (STVqt); QT variance normalized for mean QT interval (QTVN), QT variability index (QTVI_{HR}), and root mean square of the successive QT interval differences (RMSSDqt) were calculated considering the formulas:

<p>QTvar</p> $\frac{1}{n-1} \sum_{i=1}^n (QT_i - QT_m)^2$	<p>SDqt</p> $\sqrt{QT_{var}}$	<p>STVqt</p> $\sum_{i=1}^n \frac{ QT_{i+1} - QT_i }{n\sqrt{2}}$
<p>QTVN</p> $\frac{QT_{var}}{QT_m^2}$	<p>QTVI_{HR}</p> $\log_{10} \left[\frac{(QT_{var} / QT_m^2)}{(HR_{var}) HR_m^2} \right]$	<p>RMSSDqt</p> $\sqrt{\frac{1}{n-1} \sum_{i=1}^{n-1} (QT_{i+1} - QT_i)^2}$

The results are presented as the mean \pm SD of 31-36 weeks old *Gpr126^{fl/fl}*; *Tie2^{+/+}* (4 males and 3 females) and *Gpr126^{fl/fl}*; *Tie2^{Cre/+}* (5 males and 9 females) mice. Statistical significance was determined by unpaired Student's t-test subjected to Welch's correction. To take into account repeated sample assessments, data were analyzed with multilevel mixed-effects models. The differences were considered statistically significant at $P < 0.05$.

8.4 Measurement of tibial length

The tibia was dislocated, and muscle tissue was removed after one hour in distilled water at 95°C.

4

RESULTS

***Gpr126* expression is restricted to the endocardium during heart development**

We first examined the spatiotemporal expression of *Gpr126* in the mouse embryonic heart. Whole-mount *in situ* hybridization (WISH) at E9.5 showed prominent expression in the heart and the somites (Fig. 6A, A'). Transversal sections revealed that cardiac *Gpr126* mRNA is confined to the endocardium of the chambers, either in the atria or in the ventricles (Fig. 6B, B'). This expression pattern is maintained at later stages (E11.5, E13.5 and E15.5) (Fig. 6C-E'). Additionally, we defined its expression profile using quantitative real-time PCR (qPCR) in hearts at the same developmental time-points. *Gpr126* shows significant enrichment at E11.5, coinciding with the most active proliferation of the ventricular wall (Savolainen et al., 2009) (Fig. 6F). These results indicate that *Gpr126* is specifically expressed in the embryonic endocardium and may be functionally relevant at mid-gestation.

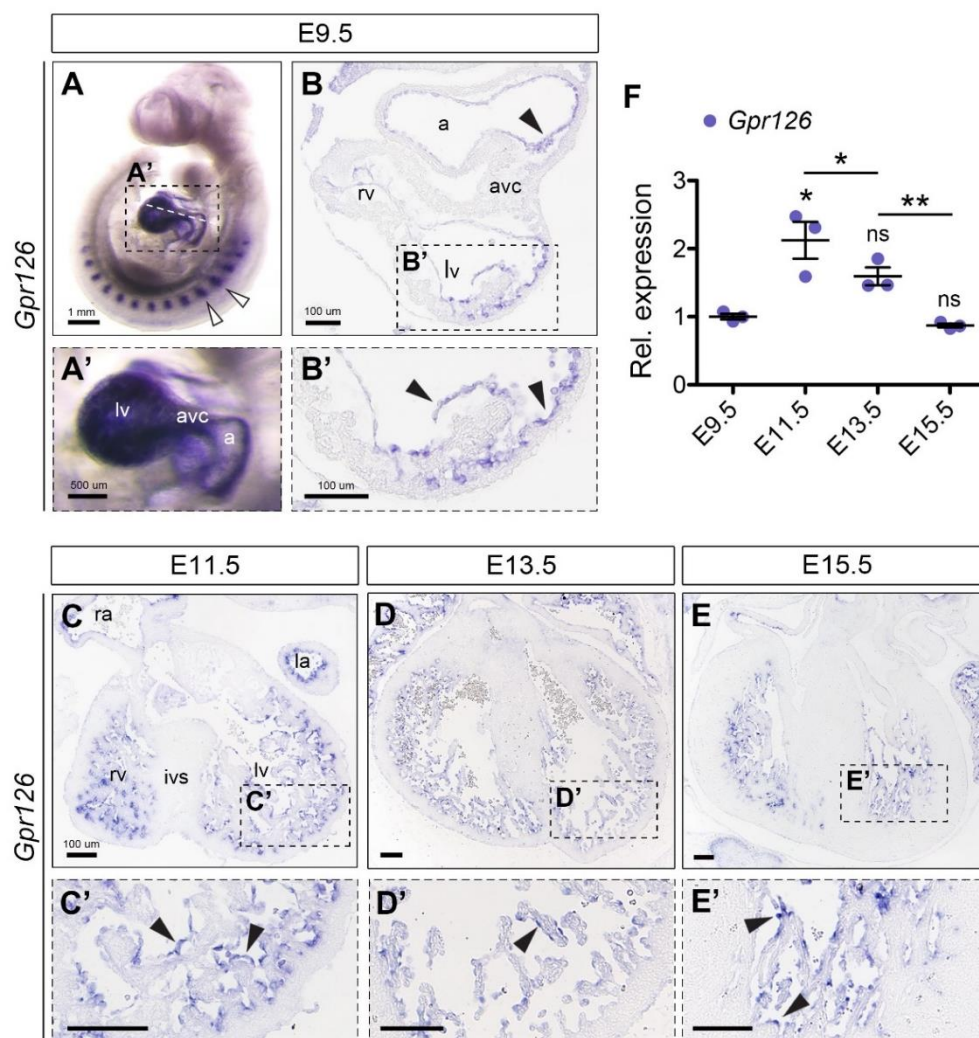


Figure 6. Spatio-temporal expression of *Gpr126* throughout heart development. (A, A') WISH showing *Gpr126* expression in the somites (white arrowheads in A) and the heart (close-up in A') of an E9.5 WT embryo. (B-E') ISH of *Gpr126* in transversal heart sections of E9.5, E11.5, E13.5 and E15.5 WT embryos, indicating expression confined to the endocardial layer (black arrowheads). a, atrium; avc, atrioventricular canal; ivs, interventricular septum; la, left atrium; lv, left ventricle; ra, right atrium; rv, right ventricle. Scale bars, 1 mm, 500 μ m, and 100 μ m as indicated. (F) qRT-PCR showing relative *Gpr126* gene expression (to *Gapdh* as housekeeping gene) of E9.5 to E15.5 WT hearts. Data are means \pm SD (n= 3 pools of 3 WT hearts per pool for each stage analyzed). Relative values are normalized to E9.5 as the reference group. Statistical significance was determined by unpaired Student's t-test (ns, not significant; * $P < 0.05$; ** $P < 0.01$).

Generation of *Gpr126* ^{Δ 3,4} knockout mouse model using CRISPR/Cas9 technology

It has been proposed that the N-terminal fragment of *Gpr126*, in contrast to the C-terminal fragment, is required for heart development in mouse and zebrafish (Patra et al., 2013). We focused on the CUB and PTX domains for two reasons. First, analysis of zebrafish *gpr126*^{st86} mutants, carrying a premature stop codon 3' to the PTX domain, shows a phenotype consisting of myelination and ear defects. However, the heart is unaffected, suggesting that if the N-terminal region is important for heart development, it is mediated by the region containing the CUB and PTX domains (Paavola et al., 2014). Second, the exons encoding these domains (exons 3 and 4) have been replaced by a selection cassette in the *Gpr126* knockout mice from Taconic/Lexicon Pharmaceuticals, in which heart abnormalities have been described (Patra et al., 2013). In addition, a recent publication identified a calcium-binding site in the CUB domain that is essential for the conformation of the receptor and indeed, for the *in vivo* functions of *gpr126* in zebrafish (ear and PNS defects) (Leon et al., 2020).

Using CRISPR/Cas9-mediated genome editing technology, we generated a new *Gpr126* knockout mouse model with an in-frame deletion of exons 3 and 4 (*Gpr126* ^{Δ 3,4}) (Fig. 7A). Two crRNA targeting sequences in intron 2 and intron 4 of the *Gpr126* gene (located in chromosome 10 in mice) were designed to delete exons 3 and 4 (Fig. 7A); (Table 1). Thus, WT zygotes derived from C57BL/6JCrI mice were co-injected with both gRNAs (crRNA + tracrRNA) and the Cas9 protein, and then implanted into pseudopregnant female mice. We recovered 21 born pups (F0) and screened them for the intended mutation (Table 2). PCR analysis using external primers to the two cutting sites revealed a PCR product of roughly 288 bp in two different pups (numbers 4 and 20 in Fig. 7C), which is the DNA length expected upon non-homologous end joining (NHEJ)-mediated DNA repair (Fig. 7B). Sequencing analysis confirmed the Δ 3,4 mutation and the newly formed junction between intron 2 to intron 4 (Fig. 7D). This mutation does not disrupt the reading frame, but rather is predicted to encode a shortened protein lacking the adhesive domains CUB and PTX in the NTF (Fig. 7E). Since founder mice from a CRISPR-Cas9 experiment often are

mosaic, both F0 mice (males) were initially bred with WT female mice of the same strain, and we confirmed that the mutant allele was effectively transmitted to the F1 generation (data not shown) (Qin et al., 2016).

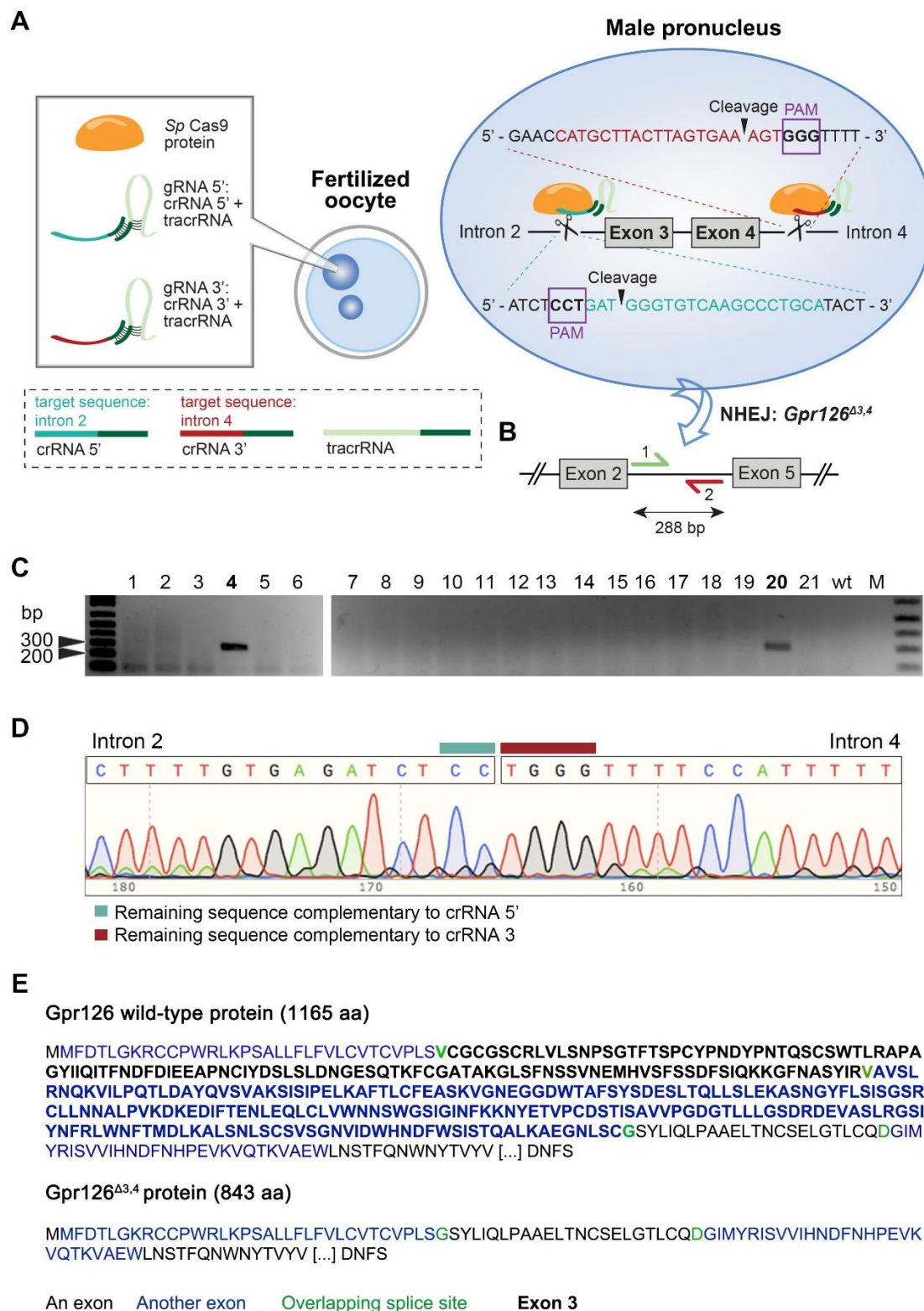


Figure 7. Experimental strategy to generate *Gpr126*^{Δ3,4} mice using the CRISPR/Cas9 system. (A) Left panel. Schematic diagram of pronuclear and cytoplasmatic microinjection of Cas9 protein and chemically synthesized gRNAs (crRNA and tracrRNA) into fertilized oocytes. Right panel. Cartoon illustrating the event of Cas9-induced cleavage prior to NHEJ-mediated DNA repair. crRNA, crispr RNA; gRNA, guide RNA; NHEJ, non-homologous end joining; PAM, protospacer adjacent motif; *Sp*, *Streptococcus pyogenes*; tracrRNA, trans-activating crRNA. (B) Schematic representation of PCR strategy to assess the deletion of exons 3 and 4 by NHEJ (the expected band is 288 bp long). Bp, base pair. (C) PCR screening of F0 newborns. M, mix. Bp, base pair. (D) Sequencing data of targeted regions confirming deletion of exons 3 and 4 in pups 4 and 20 from (C). (E) WT *Gpr126* and *Gpr126*^{Δ3,4} protein sequences.

CUB and PTX domains are essential for peripheral nervous system development, but dispensable for heart development

Gpr126^{Δ3,4/+} heterozygous matings yielded homozygous offspring in the expected Mendelian inheritance ratio during embryonic development and were born (Suppl. Table 1), indicating that the loss of CUB and PTX domains is dispensable for embryonic progression.

To determine whether heart development was impaired in *Gpr126*^{Δ3,4} homozygous mutants, we examined the morphology of mutant embryonic hearts from E12.5 to postnatal day 2 (P2). By histological analysis, no obvious phenotypic differences were detected, in contrast with other *Gpr126*^{-/-} mutants carrying null alleles (Patra et al., 2013; Waller-Evans et al., 2010) (Fig. 8A-F'). Nevertheless, as soon as birth, forelimbs and hindlimbs of the mutant pups were severely affected and could be easily identified. Mutants were slightly smaller than their WT and heterozygous siblings and displayed joint contractures that impeded body balance and normal locomotion (Fig. 8G). The affected joints were permanently fixed in a bent (flexed) or straightened (extended) position that restricted their movement. Mutant neonates were euthanized at P2, the latest, to avoid suffering, so the stage at which death occurs could not be determined. Interestingly, this limb phenotype has been previously described in (Monk et al., 2011), in which authors show that *Gpr126* is essential for Schwann cell myelination in mammals and zebrafish, but also recapitulates a human disorder called arthrogryposis multiplex congenita (AMC), due to the functional conservation of *Gpr126* signaling in humans (Ravenscroft et al., 2015).

By qPCR using primers downstream of exons 3 and 4, we detected normal *Gpr126* mRNA levels in heterozygous and homozygous mutant embryos (Fig. 8H). Also, we found an alternative splicing event of exon 25 by RT-PCR using primers that span from exon 24 to exon 26 (containing the 3'UTR region) (Fig. 8I). This spliced isoform has been already described in mice and changes the usage of termination codons (including: isoforms 1 and 5; excluding: isoform 3) (Patra et al., 2014). Thus, we demonstrated that the lack of the CUB and PTX domains within the NTF of

Gpr126 compromises myelination of the peripheral nerves but does not affect heart development in mice.

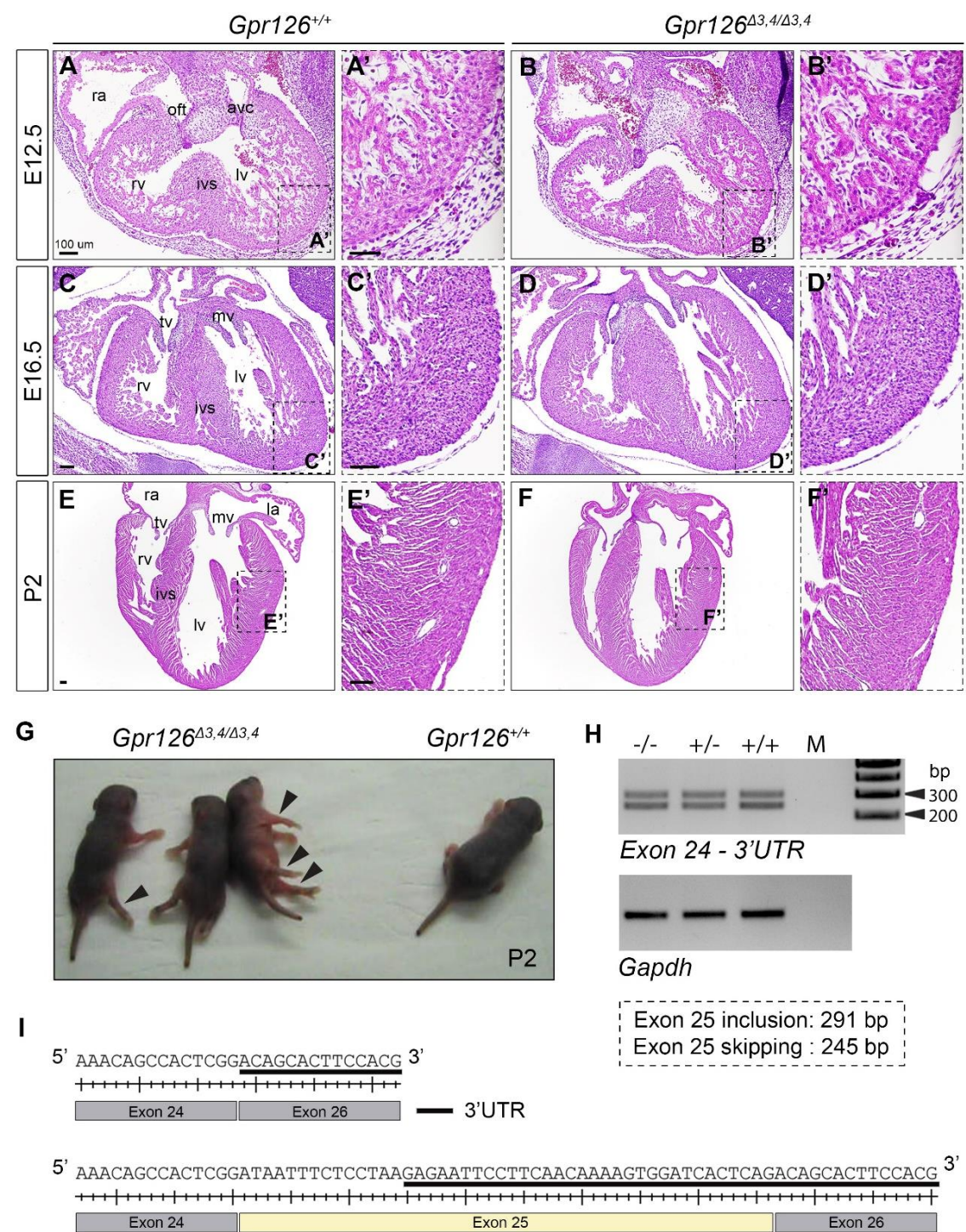


Figure 8. Characterization of *Gpr126*^{Δ3,4} mouse line. (A-F') H&E staining of WT (A, C, E) and *Gpr126*^{Δ3,4/Δ3,4} (B, D, F) heart sections at different developmental stages (E12.5, E16.5, and P2). Higher magnification views of the left ventricle are shown in ('). avc, atrioventricular canal; ivs, interventricular septum; lv, left ventricle; of, outflow tract; ra, right atrium; rv, right ventricle. Scale bar, 100 μm. (G) WT and *Gpr126*^{Δ3,4/Δ3,4} littermates at P2. Arrowheads point joint contractures and rigid limbs in the mutants. (H) RT-PCR of *Gpr126* in *Gpr126*^{+/+}, *Gpr126*^{Δ3,4/+} and *Gpr126*^{Δ3,4/Δ3,4} embryos at E9.5. Primers span from exon 24 to the 3'UTR region. The two RT-PCR products represent two *Gpr126* transcript isoforms based on the inclusion/exclusion of exon 25 as an alternative spliced exon. Relative expression was normalized to *Gapdh* as a housekeeping gene (I) Sequencing analysis of the two transcript variants.

One-step generation of constitutive and conditional *Gpr126* knockout mouse models using CRISPR/Cas9 technology

Previous studies on mice homozygous for null *Gpr126* alleles showed that disruption of the gene leads to fully penetrant lethality in a narrow time window of E11.5 – E12.5, and associated cardiac defects appeared as the most likely cause of embryonic death (Patra et al., 2013; Waller-Evans et al., 2010). These results suggested that endocardial *Gpr126* signaling was required for heart development, but further work was needed to support this role and gain more detail on the underlying mechanism.

Thus, we aimed to generate a new conditional null *Gpr126* allele, that would allow tissue specificity of *Gpr126* abrogation during development. The targeting strategy relied on shifting the ORF at the beginning of the *Gpr126* locus, truncating the coding sequence (CDS), and leading the corresponding transcript for degradation by nonsense-mediated mRNA decay (NMD). Based on computational analysis, we predicted that the deletion of exon 7 yields a translational frameshift and the presence of a PTC in exon 8 (Fig. 9A). From the 5'UTR, this is the first exon that does not contain a unit number of codons, so that the Cre-mediated recombination event will produce a frameshift and a null allele. Besides, exon 7 is contained in every splice variant, ensuring that translation will be prevented in all *Gpr126* isoforms.

We employed the CRISPR/Cas9-mediated HDR using two sgRNAs and two short ssODNs to introduce two loxP sites on either side of exon 7 (Fig. 9A). Importantly, this approach facilitates the simultaneous production of knockout animals, when DNA double-strand breaks (DBSs) are resolved by NHEJ rather than HDR. According to the guidelines published in (Lanza et al., 2018), the Cas9 cleavage site should be more than 100 bp apart from the exon to be floxed to minimize effects on splicing. Hence, we designed two crRNA targeting sequences within intron 6 (being the Cas9 cleavage site 103 bp 5' to exon 7) and intron 7 (being the Cas9 cleavage site 279 bp 3' to exon 7) (Table 1). Regarding the ssODNs, Richardson et al. reported that ssODNs

complementary to the non-target strand and with asymmetric homology arms around the DSB optimize the annealing to the DNA strand first released after Cas9 cleavage and increases the frequency of HDR events *in vitro* and *in vivo* (Richardson et al., 2016). Accordingly, we used an asymmetrical design with 67 bp PAM-proximal and 36 bp PAM-distal homology arms, that were complementary to the non-target strand. To prevent further cutting by Cas9 after efficient HDR-mediated DNA repair, ssODN donors included a single base substitution at the PAM site and harbored the loxP sequence upon the Cas9 cut site. We also incorporated a restriction enzyme recognition sequence (*EcoRI*) besides the loxP sequence for future analysis (Table 1).

Subsequent PCR amplification of loci flanking the crRNA sequences was designed to allow identification of either HDR-mediated insertion of each loxP site or NHEJ-mediated deletion of exon 7. Fig. 9B shows how the combination of four different primers can be used to detect successful incorporation of the 5' loxP sequence (primers 1 and 2), the 3' loxP sequence (primers 3 and 4), or deletion of exon 7 (primers 1 and 4).

C57BL/6JCrI fertilized oocytes were microinjected with two sgRNAs (crRNA + tracrRNA), two ssODNs, and Cas9 protein into both cytoplasm and male pronucleus. In this experiment, 2-cell or 4-cell microinjected embryos were cultured overnight with or without the chemical compound RS-1, an HDR enhancer that increases CRISPR/Cas9-mediated knock-in efficiency (Song et al., 2016) (Table 3). Overall, microinjections and transfers into foster mothers resulted in 21 born pups, out of which 16 reached weaning (hereafter referred to as F0). Those were genotyped by PCR analysis:

- Using primers 1 and 2 for the 5' region, we found 7 pups (bold numbers in Fig. 9C) potentially carrying the 5' loxP sequence, according to the PCR product length (~362 bp). 3 F0 harbored homozygous floxed alleles (number 6, 8, 9) and heterozygous floxed alleles (11, 13, 15). F0 number 10 showed multiple bands, which appeared to be mosaicism.
- Using primers 3 and 4 for the 3' region, we found 7 pups (bold numbers in Fig. 9D) potentially carrying the 3' loxP sequence, according to the PCR product length (~561 bp). 3 F0 harbored homozygous floxed alleles (number 8, 9, 16) and heterozygous floxed alleles (10, 13, 15).
- Using primers 1 and 4 flanking the whole targeted region (5' and 3' of exon 7), we detected 6 putative carriers of the floxed allele in *cis* configuration, including 2 homozygotes (number 8 and 9 showing a unique PCR product of ~904 bp in Fig. 9E) and 4 heterozygotes (10, 11, 13, 15), as well as 2 potential F0 mice heterozygous for a null allele (number 3 and 4 showing a PCR product of ~357 bp in Fig. 9E).

In total for the 16 F0 animals from microinjections using ssODNs with asymmetrical homology arms, 66.7% had both 5' and 3' loxP sites integrated in *cis* and 18% harbored a null

4. RESULTS

allele (Table 3). Of note, we only obtained knock-in alleles in mice belonging to the RS-1 treatment group, highlighting its beneficial effect on the overall knock-in efficiency by HDR.

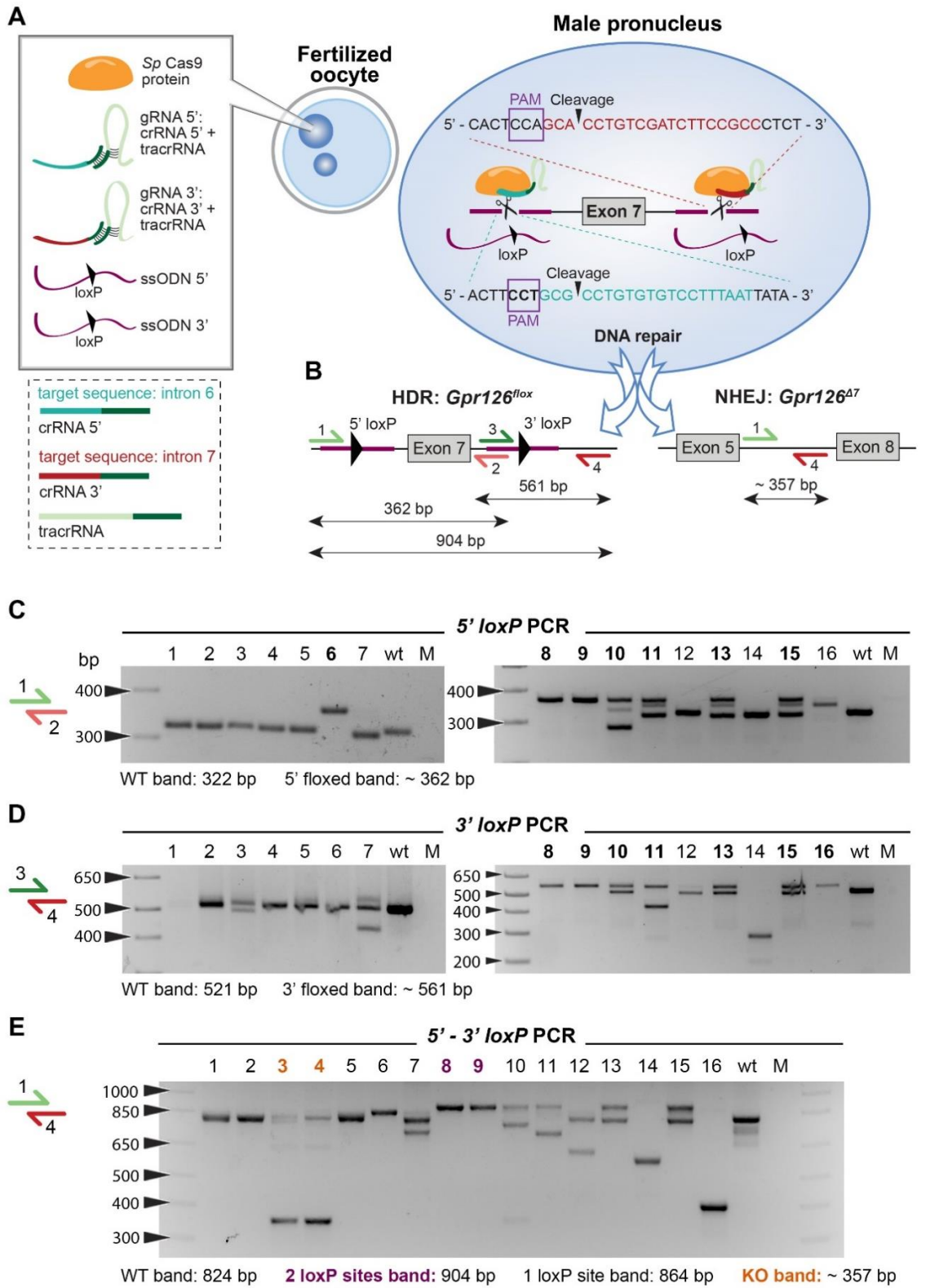


Figure 9. Experimental strategy to generate conditional and standard *Gpr126* knockout mouse lines using the CRISPR/Cas9 system. (A) Schematic diagram of pronuclear and cytoplasmic microinjection of Cas9 protein, chemically synthesized gRNAs (crRNA and tracrRNA), and ssODNs into fertilized oocytes. The event of Cas9-induced cleavage is shown prior to the targeted insertion of two loxP sites flanking exon 7. crRNA, crispr RNA; gRNA, guide RNA; PAM, protospacer adjacent motif; Sp, *Streptococcus pyogenes*; tracrRNA, trans-activating crRNA. (B) Schematic representation of PCR strategy to assess either the integration of loxP sequences upon HDR-mediated DNA repair, or deletion of exon 7 by NHEJ. Forward primers are depicted in green (1 and 3); reverse primers are depicted in red (2 and 4). Bidirectional arrows indicate the expected length of the PCR products. HDR, homology-driven repair; NHEJ, non-homologous end joining. (C) PCR analysis of F0 mice to detect the insertion of the 5'loxP site, using primers 1 and 2. Bp, base pair; M, mix. (D) PCR analysis of F0 mice to detect the insertion of the 3'loxP site, using primers 3 and 4. Bp, base pair; M, mix. (E) PCR analysis of F0 mice to detect either the incorporation of both loxP sites or the deletion of the targeted exon, using primers 1 and 4. Bp, base pair; M, mix.

Next, Sanger sequencing confirmed the deletion of exon 7 in F0 number 3 (Fig. 10A), and the correct insertion of 5' and 3' loxP sites in F0 number 8 (Fig. 10B, C). Both F0 male chimeras were bred with WT females of the same strand and transmitted the genetic modification through the germline to generate the F1 generation (data not shown).

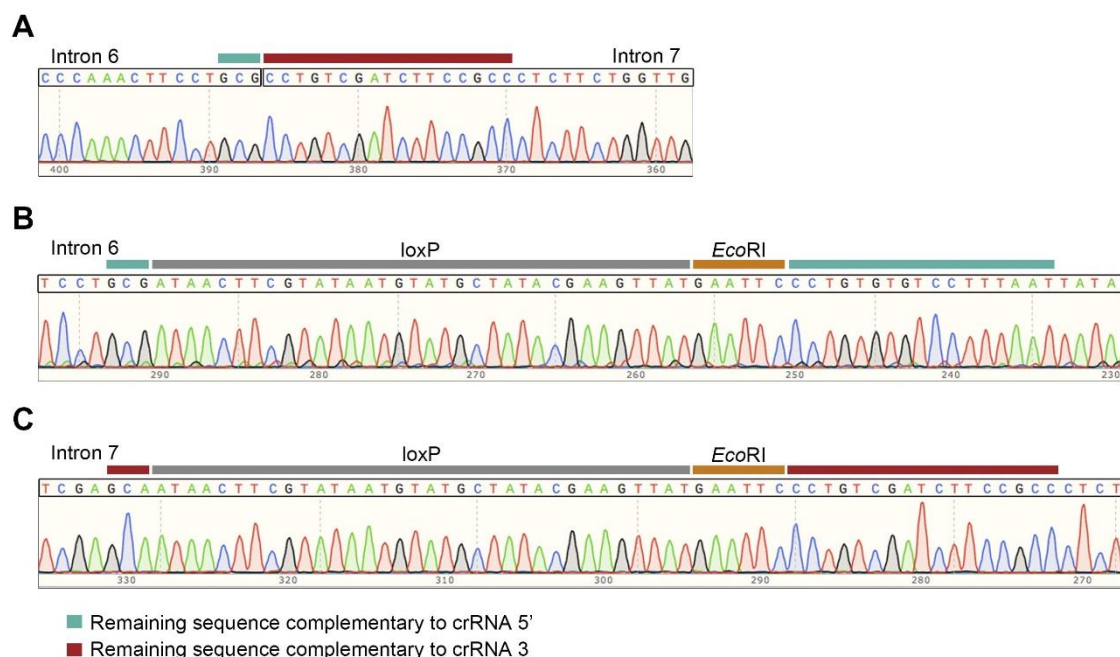


Figure 10. Detection of *Gpr126*^{lox} and *Gpr126*^{Δ7} founders by sequencing. (A) Sanger sequencing of PCR band (~357 bp) corresponding to F0 number 3 in (Fig. 9E), verifying deletion of exon 7. (B) Sanger sequencing of PCR band (~362 bp) corresponding to F0 number 8 in (Fig. 9C), confirmed loxP site integration 5' of the targeted region. (C) Sanger sequencing of PCR band (~561 bp) corresponding to F0 number 8 in (Fig. 9D), confirming loxP site integration 3' of the targeted region.

Thus, we generated two different mouse lines in the same microinjection experiment using the CRISPR/Cas9 technology, a *Gpr126* conditional knockout allele (hereafter referred to as *Gpr126^{lox}* allele), and a *Gpr126* null allele (hereafter referred as *Gpr126^{Δ7}* allele).

Homozygosity of the *Gpr126^{Δ7}* knockout allele causes embryonic lethality

To determine whether the *Gpr126^{Δ7}* allele is transcribed, we performed qPCR using primers spanning exons 9 and 10. In homozygous *Gpr126^{Δ7/Δ7}* mutants, *Gpr126* mRNA levels were substantially lower than in *Gpr126^{+/+}* littermates (Fig. 11A). As expected, primers targeting exon 7 failed to detect *Gpr126* expression (Fig. 11A). In addition, *in situ* hybridization (ISH) corroborated the marked attenuation of endocardial *Gpr126* expression in homozygous mutant hearts (Fig. 11B-C'). These results suggest that frameshift $\Delta 7$ mutation is a null allele and does not lead to the production of a truncated protein, but instead the nascent mRNA is targeted for rapid degradation by the NMD pathway. Unfortunately, due to the current lack of reliable commercial Gpr126 antibodies, we could not experimentally confirm the absence of a shorter Gpr126 truncated protein.

Next, we carried out intercrosses of heterozygous *Gpr126^{Δ7/+}* animals, that were viable and fertile, and no homozygous mutant offspring was observed at birth, indicating that mutant embryos were dying during gestation. Timed matings were performed to determine at what stages the embryonic lethality took place. We found heterozygous and homozygous mutants in the expected Mendelian ratios at E9.5. However, we observed that nearly 18% of homozygous mutant mice were dead in utero between E10.5 and E12.5 (18.2% at E10.5; 18.2% at E11.5 and 17.9% at E12.5), as judged by the absence of a heartbeat, internal hemorrhage or by tissue necrosis (Fig. 11D); (Suppl. Table 2). Beyond this stage, the proportion of dead embryos increase up to 75% at E13.5, and beyond E15.5 no viable embryos were recovered, indicating that *Gpr126* disruption leads to fully penetrant embryonic lethality in a broad time-window, from E10.5 to E13.5 (Fig. 11D); (Suppl. Table 2).

These data are consistent with previous reports claiming that Gpr126 is essential for embryonic progression (Patra et al., 2013; Waller-Evans et al., 2010), and constitute additional evidence to consider the targeted allele as a null mutation.

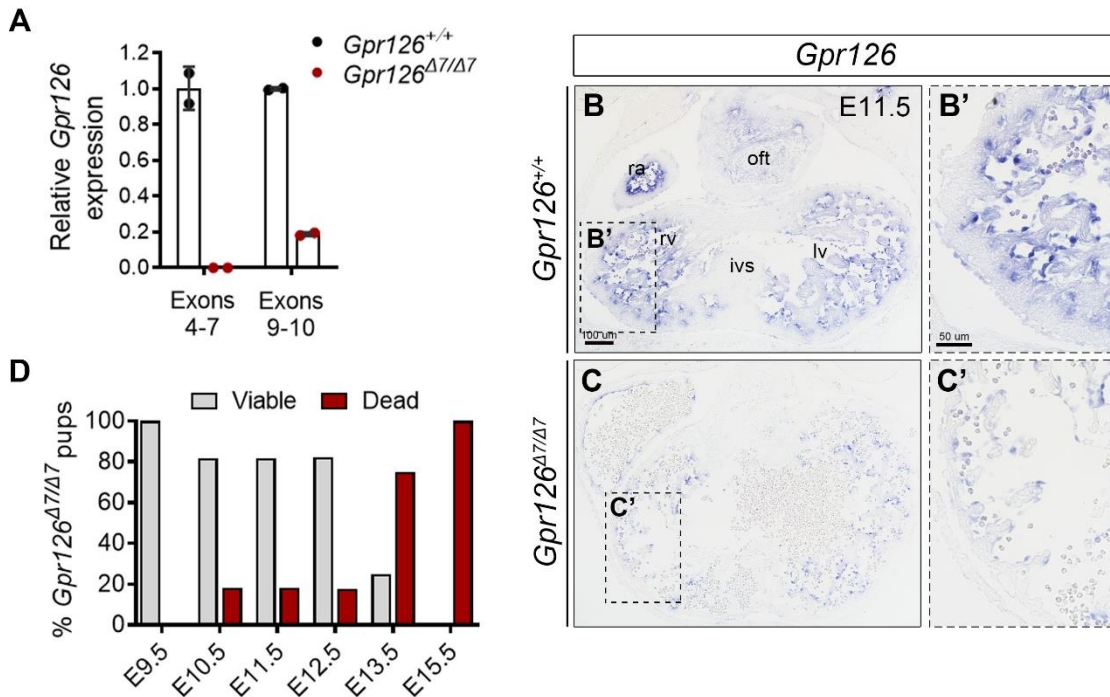


Figure 11. *Gpr126*^{Δ7} knockout allele triggers *Gpr126* downregulation. (A) qRT-PCR analysis showing relative *Gpr126* gene expression (to *Gapdh* as housekeeping gene) of E12.5 *Gpr126*^{+/+} and *Gpr126*^{Δ7/Δ7} embryonic hearts. Bars in the left indicate *Gpr126* transcript levels using primers encompassing exons 4-7; bars on the right illustrate transcript levels using primers spanning exons 9-10. Data are means ± SD (n= 2 embryonic hearts). (B-C') *Gpr126* ISH in E11.5 WT (B, B') and *Gpr126*^{Δ7/Δ7} heart sections, where gene expression is dramatically reduced (C, C'). a, atrium; avc, atrioventricular canal; ivs, interventricular septum; lv, left ventricle; oft, outflow tract; ra, right atrium; rv, right ventricle. Scale bars, 100 μm in (B, C); 50 μm in (B', C'). (D) Graph showing the percentage (%) of viable and dead *Gpr126*^{Δ7/Δ7} mutant embryos at different developmental stages.

Gpr126^{Δ7/Δ7} embryos show cardiac defects

Defective chamber myocardium development has been suggested as the most likely cause of death of *Gpr126*^{-/-} mutants (Patra et al., 2013; Waller-Evans et al., 2010). Thus, we began examining the cardiac phenotype associated with the removal of exon 7 of *Gpr126*. At E9.5, before embryonic lethality occurs, *Gpr126*^{Δ7/Δ7} mutant embryos were grossly indistinguishable from their WT littermates (data not shown). Cardiac defects were not observed, as the AVC and ventricular myocardium appeared to be normal in histological sections stained with H&E (data not shown). At E11.5, however, we detected certain variability in the phenotype of *Gpr126*^{Δ7/Δ7} mutant embryos: some were viable and showed normal morphology (data not shown); some others were viable but exhibited blood accumulation in the chambers (Fig. 12A, B), and the rest were already dead, with large regions of internal hemorrhage. Histological analysis revealed that

4. RESULTS

6 out of 10 mutant hearts displayed severe cardiac defects, with dilated ventricles (Fig. 12C, D), thinner compact myocardium and trabeculae (Fig. 12C', D') and underdeveloped interventricular septa (Fig. 12C'', D''). In contrast, the AVC and OFT cushions appeared normal, suggesting that EMT is unaffected in the mutants (Fig. 12A, B). The incomplete penetrance of the cardiac phenotype is also recapitulated at E12.5 (6 out of 20 mutant hearts), and might be a result or consequence of the wide range of embryonic lethality (from E10.5 to E13.5) (Suppl. Table 2). These abnormalities were identical to those described for the three different *Gpr126* knockout mouse alleles that have been previously generated (from RIKEN, Taconic, and Andreas Russ's laboratory), indicating that *Gpr126*^{Δ7/Δ7} mutants faithfully reflect the effects caused by *Gpr126* loss-of-function.

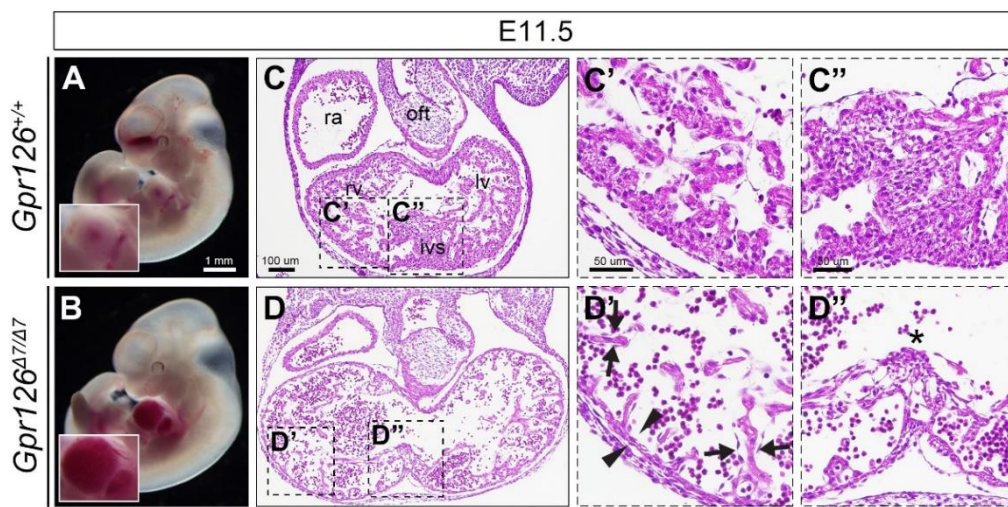


Figure 12. Histological analysis of cardiac defects in *Gpr126*^{Δ7/Δ7} mutant embryos. (A, B) Whole-mount views of E11.5 *Gpr126*^{+/+} (A) and *Gpr126*^{Δ7/Δ7} embryos (B). Mutant embryos show blood accumulation in the heart (see zoomed-in boxed areas). (C-D'') H&E stained heart sections of *Gpr126*^{+/+} (C) and *Gpr126*^{Δ7/Δ7} embryos (D). ('', '') are higher magnification views of boxed areas in (C) and (D). Note the thinning of the compact myocardium (indicated with arrowheads) and trabeculae (indicated with arrows) in mutant hearts (C', D') and the poorly structured ventricular septum (indicated with an asterisk) (C'', D''). a, atrium; avc, atrioventricular canal; ivs, interventricular septum; lv, left ventricle; oft, outflow tract; ra, right atrium; rv, right ventricle. Scale bars, 1 mm in (A, B); 100 μm in (C, D); 50 μm in (C', C'', D', D'').

Chamber patterning, cellular proliferation and metabolism are not affected in *Gpr126*^{A7/Δ7} mutant hearts

To determine the molecular mechanisms underlying heart abnormalities, we first evaluated whether *Gpr126* loss-of-function has an impact on genes known to be relevant for chamber morphogenesis. Compact and trabecular cardiomyocytes display different gene expression profiles that are associated with different features, being the compact myocardium more proliferative and less mature than the trabecular myocardium (Sedmera et al., 2003). Thus, we conducted ISH to examine the expression pattern of *Hey2* (*Hairy/E(spl)-related with YRPW motif 2*) (Koibuchi and Chin, 2007; Sakata et al., 2002; Sakata et al., 2006) (Fig. 13A, B) and *N-myc* (Moens et al., 1993) (Fig. 13C, D), that are markers for the compact zone, as well as *Bmp10* (*Bone morphogenetic protein 10*) (Chen et al., 2004) (Fig. 13E, F) and *Cx40* (*Connexin 40*) (Van Kempen et al., 1996) (Fig. 13G, H), that are highly expressed in the trabecular zone. Despite myocardial defects, all these markers show normal spatial expression in *Gpr126*^{A7/Δ7} mutant hearts (Fig. 13A-D), indicating that myocardial patterning is not affected. Endocardial-specific detection of *Gpr126* transcripts prompted us to explore the expression of chamber endocardium markers, such as *Irx5* (*Iroquois homeobox 5*) (Christoffels et al., 2000) (Fig. 13I, J). However, no changes were detected compared to WT hearts, suggesting that chamber endocardial identity is also conserved in *Gpr126*^{A7/Δ7} mutants. In summary, we can conclude from these data that myocardial and endocardial ventricular chamber identities are unaffected in *Gpr126*^{A7/Δ7} mutants.

The connection between bioenergetics and ventricular myocardium differentiation was another feature worth analyzing. It has been reported that myocardial metabolism in the embryonic heart is compartmentalized at midgestation, with an enhanced glycolytic program in the compact myocardium and an oxidative metabolism in trabeculae (Menendez-Montes et al., 2016). Alteration of this metabolic signature impairs cardiac maturation and gives rise to cardiac defects that resemble the phenotype of *Gpr126*^{A7/Δ7} embryos, such as the reduced thickness of the ventricular wall or chamber dilation (Menendez-Montes et al., 2016). To test whether impaired cardiac metabolism was associated with *Gpr126*^{A7/Δ7} heart abnormalities, we carried out ISH of glycolytic genes lactate dehydrogenase a (*Ldha*) (Fig. 14A-B') and pyruvate dehydrogenase kinase I (*Pdk1*) (Fig. 14C-D'). Both transcripts were similarly enriched in the compact myocardium and interventricular septum at E12.5 in WT and *Gpr126*^{A7/Δ7} mutant hearts (Fig. 14A-D'), except for a higher trabecular expansion of *Ldha* in the right ventricle of the mutants (Fig. 14B'). The most abundant glucose transporter in the heart, GLUT1, paralleled the same expression pattern and was abundant in the compact zone and septum, and scarce in the trabeculae of either WT or mutant hearts (Fig. 14E-F').

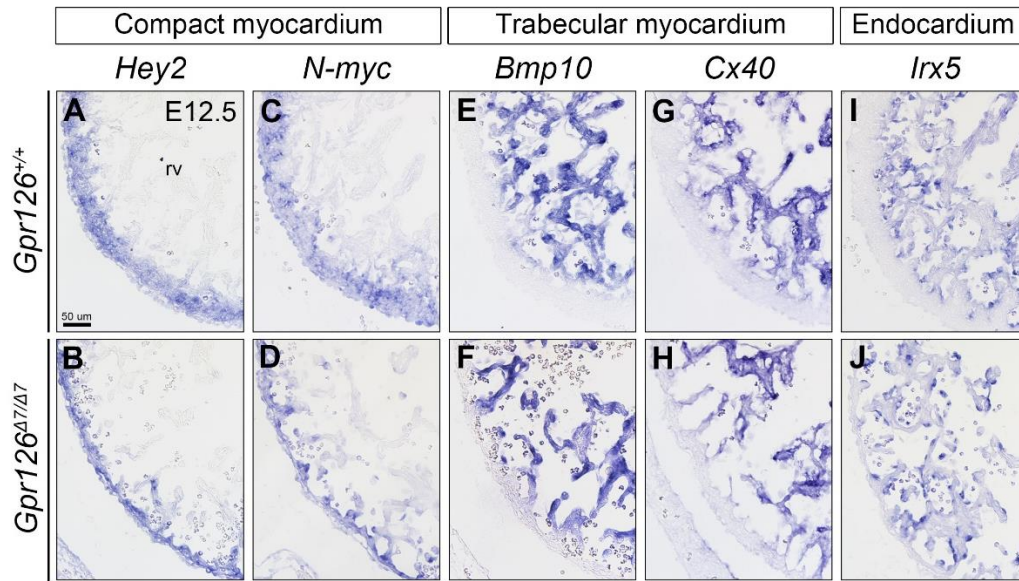


Figure 13. Cardiac differentiation and patterning in *Gpr126* ^{$\Delta 7/\Delta 7$} mutant embryos. ISH analysis of compact myocardial markers *Hey2* (**A**, **B**) and *N-myc* (**C**, **D**); trabecular myocardial markers *Bmp10* (**E**, **F**) and *Cx40* (**G**, **H**); and the endocardial marker *Irx5* (**I**, **J**) in *Gpr126*^{+/+} and *Gpr126* ^{$\Delta 7/\Delta 7$} heart sections at E12.5. Panels show the right ventricle. rv, right ventricle. Scale bar, 50 μ m.

As hypoxia is pivotal to drive the glycolytic program in the developing heart (Menendez-Montes et al., 2016), we speculated that mutant myocardium was not ischemic. To further confirm this hypothesis, we employed the Hypoxyprobe™ system, which facilitates the detection of hypoxic cells using pimonidazole hydrochloride. Pimonidazole is reductively activated under hypoxic conditions, forming stable adducts with proteins bearing thiol groups that can be visualized by a specific antibody. Thus, increased dye-binding reflects decreased tissue pO₂. Hypoxyprobe immunoreactivity was restricted to the cushion-associated myocardium of the outflow tract, and a lesser extent in the interventricular septum at E12.5, in agreement with previous publications (Dunwoodie, 2009; Ream et al., 2008), and was not enhanced in *Gpr126* ^{$\Delta 7/\Delta 7$} hearts compared with littermate controls (Fig. 15A-B''). Taken together, these results suggest that the alteration of cardiac energy metabolism or increased hypoxia are not the primary causes of the heart abnormalities found in *Gpr126* ^{$\Delta 7/\Delta 7$} mutant hearts.

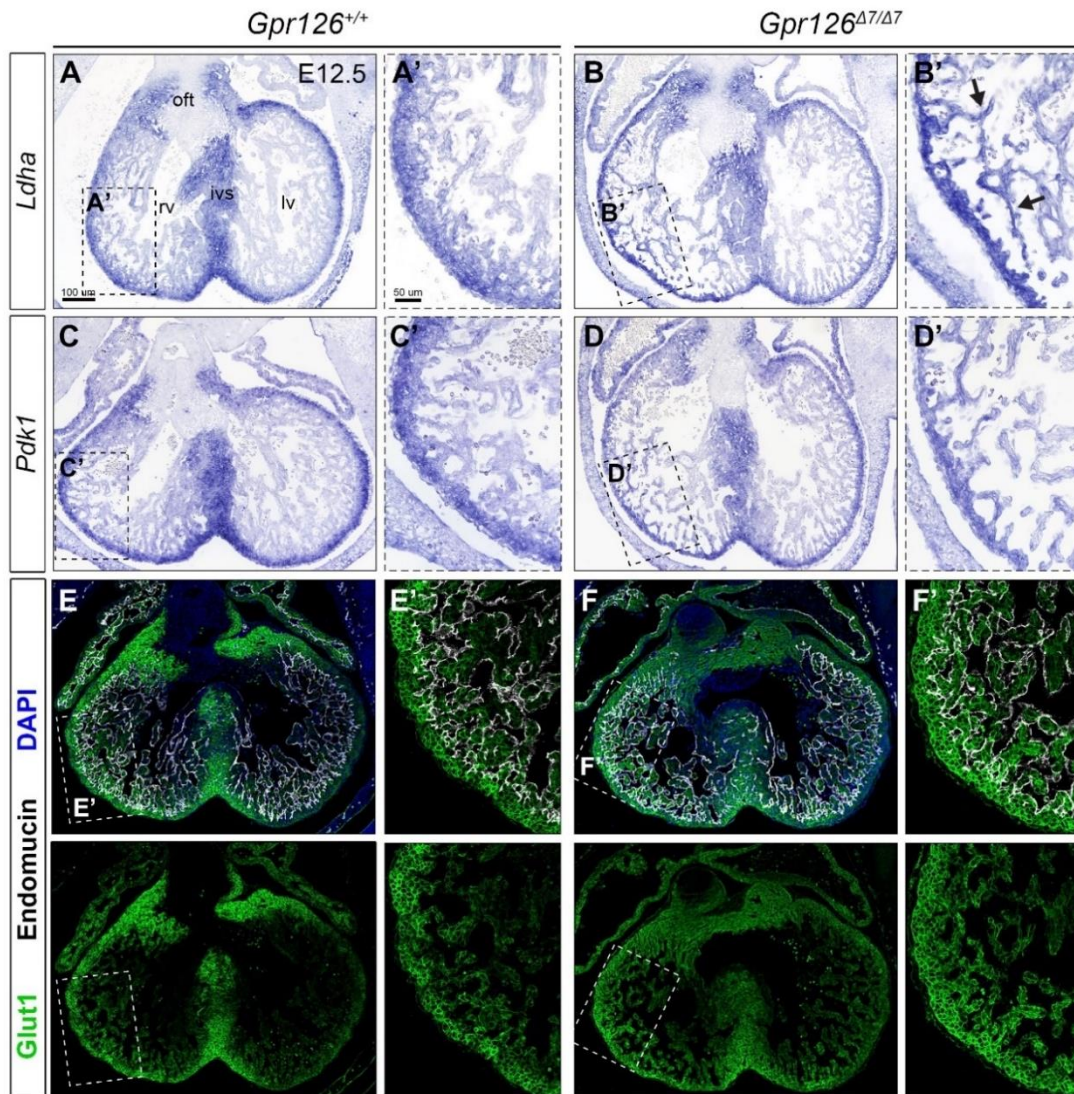


Figure 14. Glycolytic and lipid metabolism in *Gpr126*^{Δ7/Δ7} mutant embryonic hearts. ISH analysis of glycolytic enzymes *Ldha* (A-B') and *Pdk1* (C-D') in *Gpr126*^{+/+} and *Gpr126*^{Δ7/Δ7} heart sections at E12.5. Arrows denote the trabecular expansion of *Ldha* in the right ventricle of mutants (arrowheads in B'). (E-F') Immunofluorescence staining of E12.5 *Gpr126*^{+/+} and *Gpr126*^{Δ7/Δ7} heart sections for GLUT1 (green), endomucin to demarcate the endocardium (white) and DAPI for nuclear counterstain (blue). (') are higher magnification views of boxed areas. ivs, interventricular septum; lv, left ventricle; oft, outflow tract; rv, right ventricle. Scale bars, 100 μm (low magnification); 50 μm (insets).

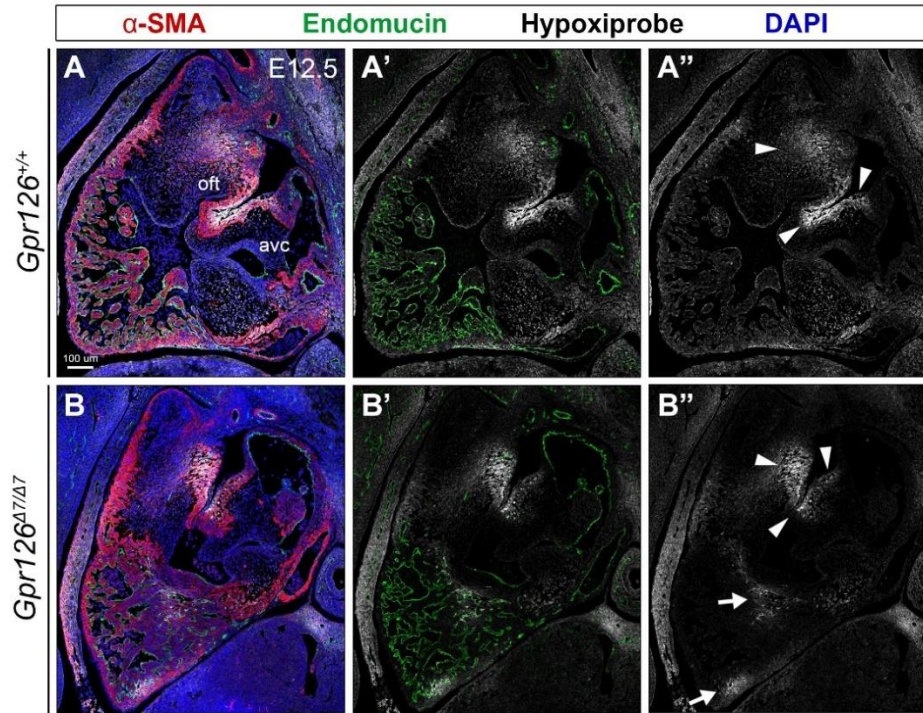


Figure 15. Hypoxyprobe analysis of *Gpr126*^{Δ7/Δ7} mutant hearts. Hypoxyprobe labeling of E12.5 *Gpr126*^{+/+} and *Gpr126*^{Δ7/Δ7} sagittal heart sections. (A-B''). Sections were stained for Hypoxyprobe (white, revealing hypoxic regions), alpha-smooth muscle actin to counterstain the myocardium (α -SMA) (red), endomucin to demarcate the endocardium (green) and DAPI (blue). ('', '') are higher magnification views of boxed areas. Arrowheads highlight the hypoxyprobe signal of the myocardium in the outflow tract. Arrows point the hypoxyprobe signal in the interventricular septum. avc, atrioventricular canal; oft, outflow tract. Scale bar, 100 μ m.

Next, we asked whether a defect in proliferation was responsible for the myocardial thinning observed in *Gpr126*^{Δ7/Δ7} mutant hearts. Bromodeoxyuridine (BrdU) is an analog of the nucleoside thymidine that incorporates into the newly synthesized DNA of replicating cells during the S phase of the cell cycle. Thus, cell proliferation was measured by BrdU incorporation in *Gpr126*^{+/+} and *Gpr126*^{Δ7/Δ7} hearts at E12.5 (Fig. 16A-B''), when heart defects start to become apparent. For quantification, compact myocardium, trabecular myocardium, and endocardium were analyzed separately to allow visualization of cell-type-specific behaviors. We observed a high proliferation rate in cardiomyocytes within the compact myocardium, less pronounced within the trabecular zone, and still less within the endocardial layer, as expected (Fig. 16C, D) (Sedmera et al., 2003). Strikingly, proliferation was normal in all compartments either at E11.5 or E12.5 (Fig. 16C, D), indicating that the reduction of the wall thickness is not a result of altered myocardial growth.

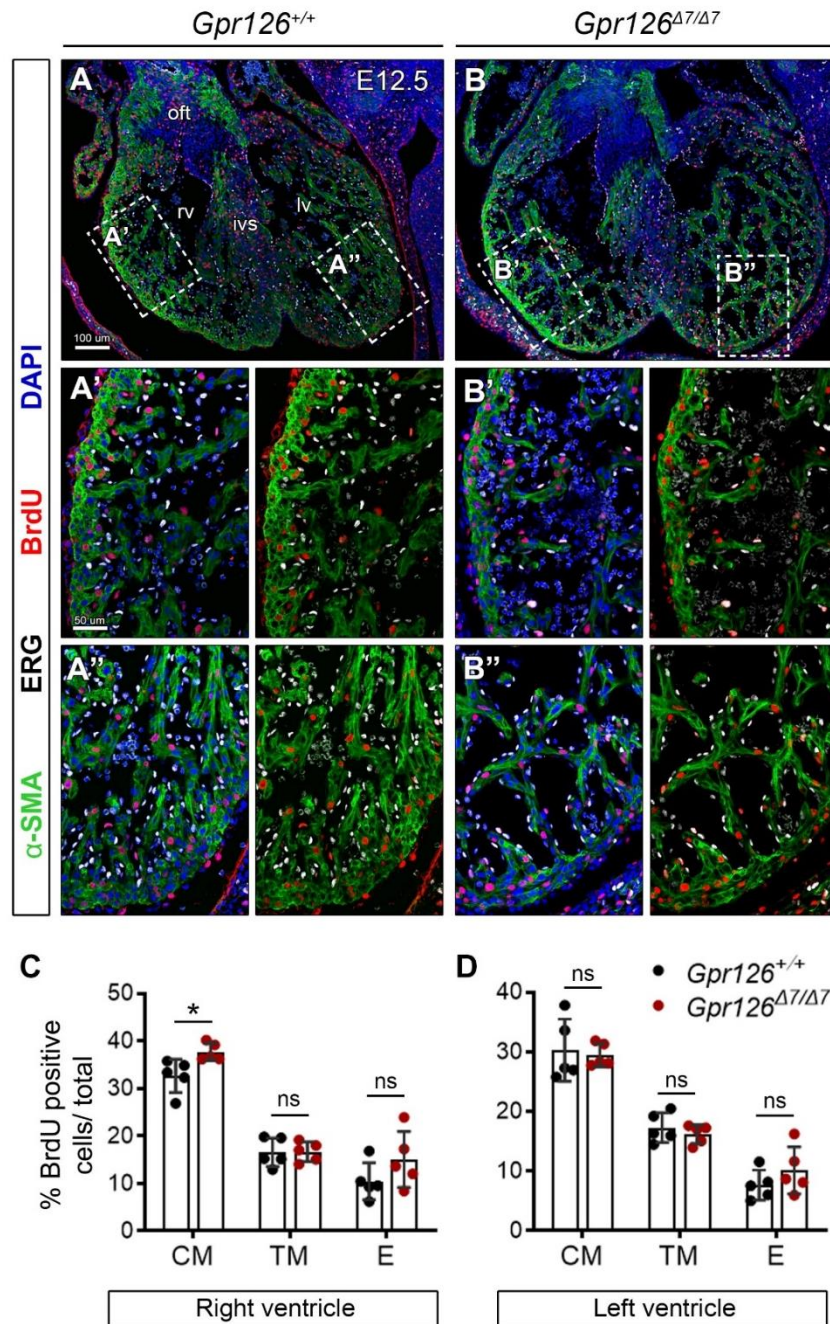


Figure 16. BrdU proliferation analysis of *Gpr126*^{Δ7/Δ7} mutant hearts. (A-B'') BrdU immunostaining of E12.5 *Gpr126*^{+/+} and *Gpr126*^{Δ7/Δ7} transversal heart sections. BrdU-positive (proliferating) cells are shown in red. The myocardium is counterstained with α-SMA (green), the endocardium with (ERG) (white), and nuclei with DAPI (blue). ('', ''') are higher magnification views of boxed areas. ivs, interventricular septum; lv, left ventricle; oft, outflow tract; rv, right ventricle. Scale bars, 100 μm (low magnification); 50 μm (insets). (C, D) Quantification of BrdU-positive nuclei as a percentage of total nuclei in compact myocardium (CM), trabecular myocardium (TM), and endocardium (E) of E12.5 *Gpr126*^{+/+} and *Gpr126*^{Δ7/Δ7} mouse hearts. Data are represented as mean ± SD. Statistical significance was determined by unpaired Student's *t*-test (ns, not significant).

Disruption of Gpr126 signaling in the heart affects vasculature development-related processes

To identify the molecular targets downstream of Gpr126 signaling in the heart, we performed comparative transcriptome profiling using RNA sequencing (RNA-seq) analysis in *Gpr126*^{+/+} and *Gpr126*^{Δ7/Δ7} mutant ventricles at E12.5. We only extracted RNA from the ventricular chambers (excluding the atria, AVC canal and OFT), to ensure gaining insight into the molecular changes resulting from *Gpr126* abrogation in the endocardial cells lining the trabeculae (Fig. 17A). RNA-seq analysis identified 156 DEGs, 77 of which were upregulated and 79 downregulated (adj. *P*-value < 0.05) (Fig. 17B); (Suppl. Table 3). Gene ontology (GO) analysis revealed the overrepresentation of “vasculature development”, “cell migration” and “angiogenesis” terms for the downregulated genes (Fig. 17C, upper panel); (Suppl. Table 3), whereas for the upregulated genes the most enriched functions were “cellular response to amino acid”, “skeletal system development”, “cell adhesion” and “negative regulation of cell signaling”, among others (Fig. 17C, bottom panel); (Suppl. Table 3). Interestingly, a large subset of genes associated with endothelial-related functions are known to be expressed in the embryonic endocardium (*Tmem100*, *Ednrb*, *Stab1*, *Eng*, *Kdr*, *Plxd1*, *Adamts1*, *Tie1*) (Conway and Molkentin, 2008; Gitler et al., 2004; Hua et al., 2014; Kaipainen et al., 1993; Li et al., 1999; Puri et al., 1995; Somekawa et al., 2012; Thai and Iruela-Arispe, 2002) (Fig. 17D); (Suppl. Table 3), since it is a regionally specialized endothelium and both cell types share structural and functional genes (Harris and Black, 2010). Since ventricular endocardium also contributes to the primary coronary plexus at E11.5 (MacGrogan et al., 2018), these results might point at *Gpr126* as a regulator of endocardial homeostasis and/ or coronary vessel development. Moreover, we detected the upregulation of two regulators of G-protein signaling (*Rgs*), *Rgs2*, and *Rgs16* (Fig. 17D); (Suppl. Table 3), which have been reported to be highly expressed in the heart (Perschbacher et al., 2018). *Rgs* proteins stimulate the GTPase activity of Gα subunits, leading to their deactivation and termination of GPCR downstream signals. Specifically, *Rgs2* acts as a negative modulator of vasoconstriction in the peripheral vasculature (Heximer et al., 2003), while *Rgs16* is a negative modulator of platelet function and thrombosis in mice (Hernandez et al., 2019). Thus, our data suggest a possible participation of these *Rgs* family members in the modulation of Gpr126-mediated signaling, but further validation would be needed.

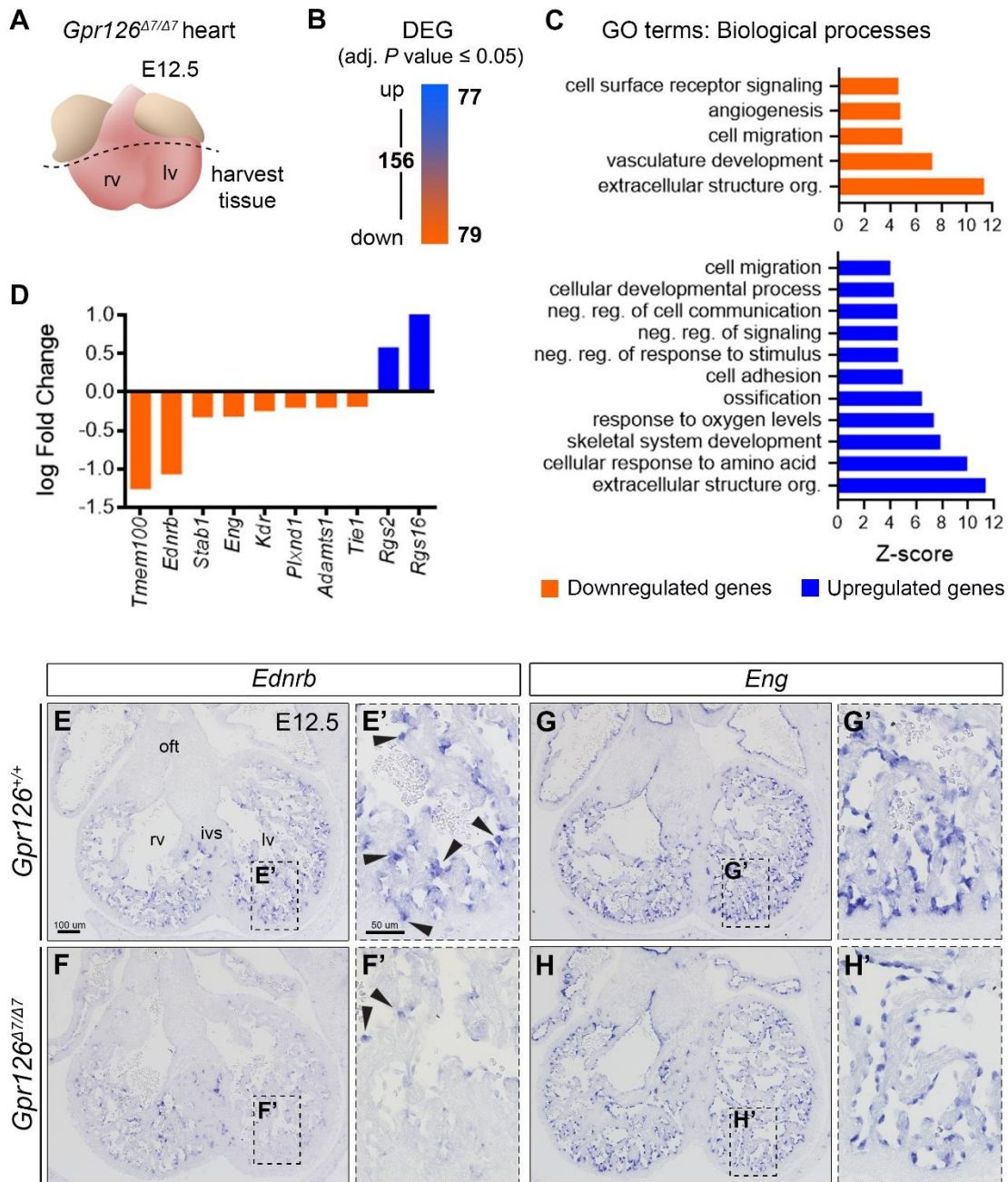


Figure 17. Gene profiling of E12.5 *Gpr126*^{Δ7/Δ7} ventricles. (A) Cartoon illustrating the dissection of E12.5 heart ventricles (dotted line). (B) Chart showing the total number of differentially expressed genes (DEGs) detected by RNA-seq analysis in *Gpr126*^{Δ7/Δ7} ventricles (*P* < 0.05). The blue section indicates upregulated genes; orange depicts downregulated genes. (C) Up. GO enrichment analysis of downregulated genes (orange color). Bottom. GO enrichment analysis of upregulated genes (blue color). (D) Graph of the log-fold change (logFC) showing the downregulation of endothelial/ endocardial genes (orange color) and the upregulation of regulators of G-protein signaling genes (*Rgs*). (E-H'). ISH analysis of *EdnrB* (E-F') and *Eng* (G-H') in E12.5 *Gpr126*^{+/+} and *Gpr126*^{Δ7/Δ7} hearts. Endocardial expression is slightly reduced in mutant hearts. Boxed areas are magnified in ('). ivs, interventricular septum; lv, left ventricle; oft, outflow tract; rv, right ventricle. Scale bars, 100 μm (low magnification); 50 μm (insets).

Endothelin receptor type B (EdnrB) is a G protein-coupled receptor that increases the release of relaxing factors in endothelial cells (Mazzuca and Khalil, 2012) and whose expression is restricted to chamber endocardium in the embryonic heart (Fig. 17E, E'). Endoglin (Eng) is a transmembrane receptor that induces EMT from the AVC endocardium, and myocardial trabeculation from the chamber endocardium of the mouse embryonic heart (Arthur et al., 2000) (Fig. 17G, G'). ISH analysis confirmed that *EdnrB* and *Eng* expression was attenuated in *Gpr126^{Δ7/Δ7}* mutants (Fig. 17E-H'), and the magnitude of downregulation coincides with the expression levels measured by RNA-seq analysis (Fig. 17D). In summary, our results suggest that global *Gpr126* deletion impacts endocardial/ endothelial gene expression in the embryonic heart.

Conditional *Gpr126* deletion in either the endocardium or the heart does not cause embryonic lethality

To investigate the implication of endocardial *Gpr126* signaling in embryonic and cardiac chamber development, we used our conditional *Gpr126^{lox}* line, in which the Cre-mediated excision of exon 7 results in the same loss of coding sequence of standard *Gpr126^{Δ7}* knockout mice. We initially crossed the conditional *Gpr126^{lox}* line with the endocardial-specific driver line *Nfatc1pan-Cre*, in which the Cre recombinase is active throughout the endocardium starting at E8.5 (Wu et al., 2012). Surprisingly, *Gpr126^{lox/lox}; Nfatc1-Cre* mutant embryos were viable throughout embryonic development (Suppl. Table 5) and showed grossly normal morphology (data not shown). Close examination of mutant hearts revealed no abnormalities, and compact and trabecular myocardium exhibited normal architecture and thickness (Fig. 18A-B''). To confirm that *Gpr126* deletion in endocardial cells is compatible with embryo survival and heart development, we crossed mice bearing the conditional *Gpr126^{lox}* allele with the pan-endothelial driver line *Tie2-Cre* (Kisanuki et al., 2001), which drives the recombination in the common progenitor of endothelial and hematopoietic stem cells at E7.5 (Braren et al., 2006). Because *Gpr126* is only expressed in the specialized endothelial cells forming the endocardium, we did not expect to detect secondary effects due to the lack of *Gpr126* in the vasculature, whilst we would achieve *Gpr126* deletion in the early endocardium. Nevertheless, *Gpr126^{lox/lox}; Tie2-Cre* mutant embryos were also viable (Suppl. Table 6), exhibited normal cardiac morphology (Fig. 18C-C''), and reached adulthood. These data indicated that embryonic lethality caused by *Gpr126* deficiency does not depend on its function in endothelial/ endocardial cells.

Finally, to exclude the possibility that *Gpr126* is playing an earlier function involving cardiac mesoderm progenitors, we used the *Mespl-Cre* line, which promotes recombination in the nascent mesoderm at the onset of gastrulation (E6.5), that will give rise to all cardiac cell

lineages (Saga et al., 1999). *Gpr126^{fl/fl}*; *Mesp1-Cre* mutants were viable (Suppl. Table 7) and did not show any obvious heart phenotype either (Fig. 18D-D’’).

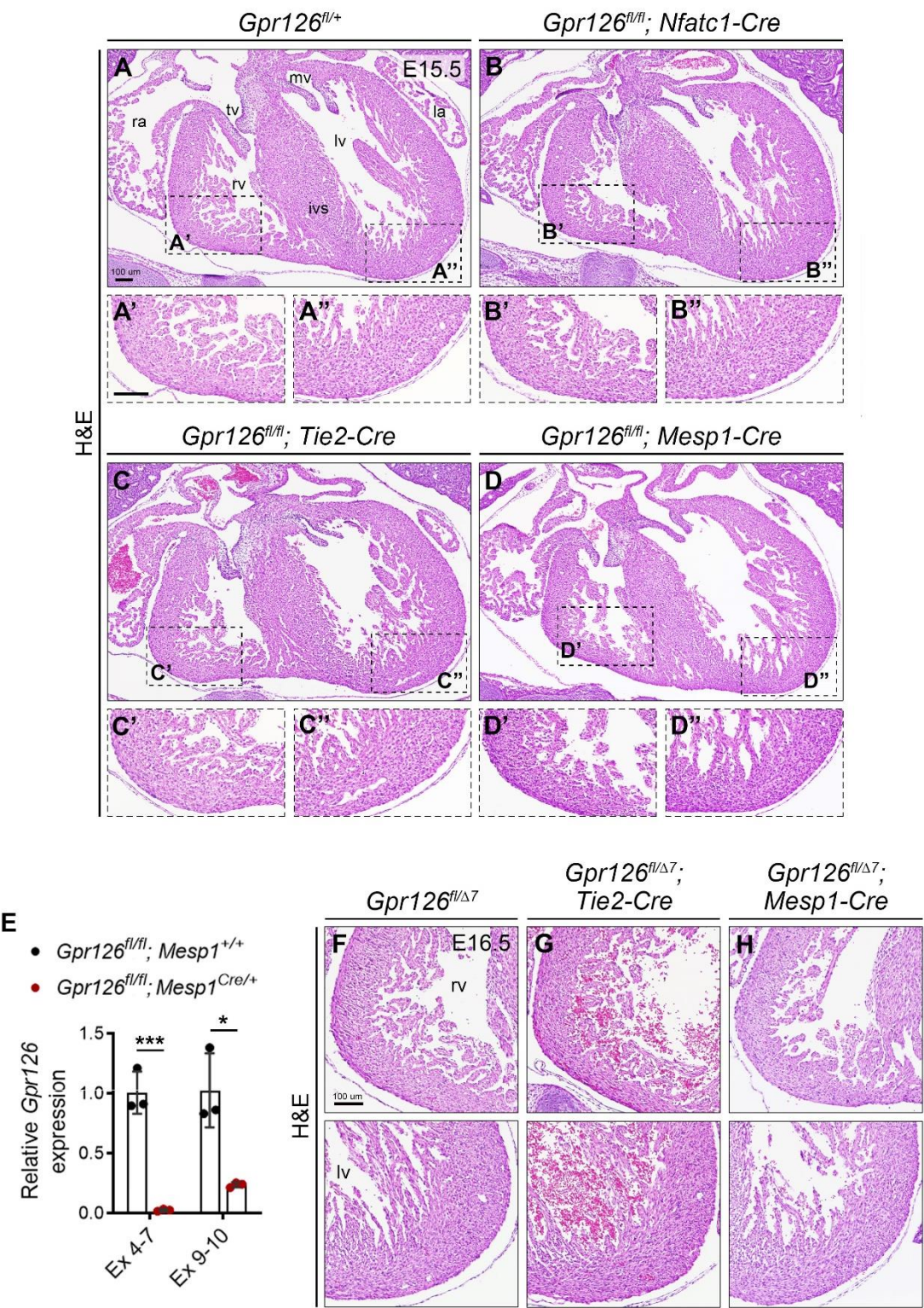


Figure 18. Histological analysis of embryonic hearts lacking *Gpr126* in the *Nfatc1*, *Tie2* and *Mesp1* lineages. (A-D'') H&E staining of transversal heart sections from WT (A-A''), *Gpr126^{fl/fl}; Nfatc1^{Cre/+}* (B-B''), *Gpr126^{fl/fl}; Tie2^{Cre/+}* (C-C'') and *Gpr126^{fl/fl}; Mesp1^{Cre/+}* (D-D'') mutants at E15.5. Magnified views of the right ventricle are shown in (*), and of the left ventricle in (**). ivs, interventricular septum; lv, left ventricle; mv, mitral valve; rv, right ventricle; tv, tricuspid valve. Scale bars, 100 μ m. (E) qRT-PCR analysis showing relative *Gpr126* gene expression (to *Gapdh* as housekeeping gene) *Gpr126^{fl/fl}; Mesp1^{+/+}* and *Gpr126^{fl/fl}; Mesp1^{Cre/+}* embryonic hearts at E12.5. Bars in the left indicate *Gpr126* transcript levels using primers encompassing exons 4-7; bars on the right illustrate transcript levels using primers spanning exons 9-10. Data are means \pm SD (n= 3 embryonic hearts); t-test, * P < 0.05, *** P < 0.001. (F-H) H&E staining of transversal heart sections from WT (F), *Gpr126^{fl/ Δ 7}; Tie2^{Cre/+}* (G) and *Gpr126^{fl/ Δ 7}; Mesp1^{Cre/+}* mutants at E16.5. Panels in the left show the left ventricle; panels on the right show the right ventricle. lv, left ventricle; rv, right ventricle. Scale bar, 100 μ m.

As none of these mutants recapitulated the phenotype observed with the global *Gpr126^{Δ7}* deletion, we next assessed the fidelity of Cre recombinase activity to ensure that low recombination efficiency was not associated with the lack of phenotype in our conditional *Gpr126^{lox}* mutants. Owing to the unavailability of commercial antibodies to examine *Gpr126* protein loss, we conducted qRT-PCR analysis to assess the reduction of *Gpr126* mRNA levels upon Cre-mediated activity. Thus, we crossed *Gpr126^{fl/fl}* mice with the *Mesp1-Cre* driver line and used embryonic hearts as a cDNA template. The rationale is that this organ should behave like *Gpr126^{Δ7}* because of conditional gene inactivation in heart progenitor cells. Similar to constitutive *Gpr126^{Δ7/Δ7}* mutants, *Gpr126* transcript levels were undetectable in E12.5 *Gpr126^{fl/fl}; Mesp1^{Cre/+}* hearts when using primers specific for the deleted exon 7 (Fig. 18E). Also, gene expression was strongly reduced using primers targeting 3' of the floxed region (exons 9 and 10), compared to WT littermates (Fig. 18E), indicative of efficient Cre-mediated activity.

Finally, we attempted to combine *Gpr126* conditional (*Gpr126^{lox}*) and constitutive (*Gpr126^{Δ7}*) alleles *in trans*, to generate the most extreme loss-of-function situation and confirm that the discrepancies between phenotypes cannot be attributed to differential *Gpr126* mRNA dosage. To test this, we crossed homozygous *Gpr126^{fl/fl}* mice with both double heterozygotes *Gpr126^{Δ7/+}; Tie2^{Cre/+}* and *Gpr126^{Δ7/+}; Mesp1^{Cre/+}*, to obtain triple heterozygotes *Gpr126^{fl/ Δ 7}; Tie2^{Cre/+}* and *Gpr126^{fl/ Δ 7}; Mesp1^{Cre/+}* offspring, respectively. However, no evidence of embryonic lethality (Suppl. Tables 8, 9) nor cardiac defects (Fig. 18F-H) was observed in any of these mutants.

Taken together, these data lend support to the idea that *Gpr126* is dispensable for cardiac development, so the lethality associated to *Gpr126^{Δ7}* knockouts is likely due to the requirement of *Gpr126* in non-cardiac tissues.

***Gpr126^{fl/fl}*; *Tie2-Cre* adult mice have normal cardiac morphology and electrical activity**

In the heart, cAMP levels are tightly controlled to modulate a variety of cellular functions, including heart rate and contractility, and its biological effects are mainly associated with the activity of protein kinase A (PKA) (Cazorla et al., 2009). Since cAMP/PKA elements have been reported as downstream mediators of *Gpr126* signaling (Glenn and Talbot, 2013; Mogha et al., 2013), we asked whether *Gpr126* embryonic expression was required for adult cardiac electrical activity or homeostasis, despite it is not expressed in the heart at postnatal stages (data not shown). To address this question, we used the conditional *Gpr126^{fl/fl}*; *Tie2^{Cre/+}* mutant mice, which were viable, reached adulthood at the expected Mendelian frequency and did not display any phenotypic abnormality. Electrocardiograms (ECGs) obtained from 31-36 weeks-old male and female *Gpr126^{fl/fl}*; *Tie2^{Cre/+}* mice revealed normal values for all measured ECG parameters (heart rate, PR-, QRS-, corrected QT- and RR intervals, as well as P- and R- wave amplitudes), compared to control mice of each gender (Fig. 19A).

Moreover, *Gpr126^{fl/fl}*; *Tie2^{Cre/+}* mice showed no difference in cardiac size, as determined by normalizing heart weight to tibia length (Fig. 19B), cardiac morphology nor collagen deposition, as assessed by Masson's trichrome staining of histological sections (Fig. 19C-D''). Collectively, these data demonstrated that endothelial *Gpr126* function is dispensable for adult heart homeostasis.

4. RESULTS

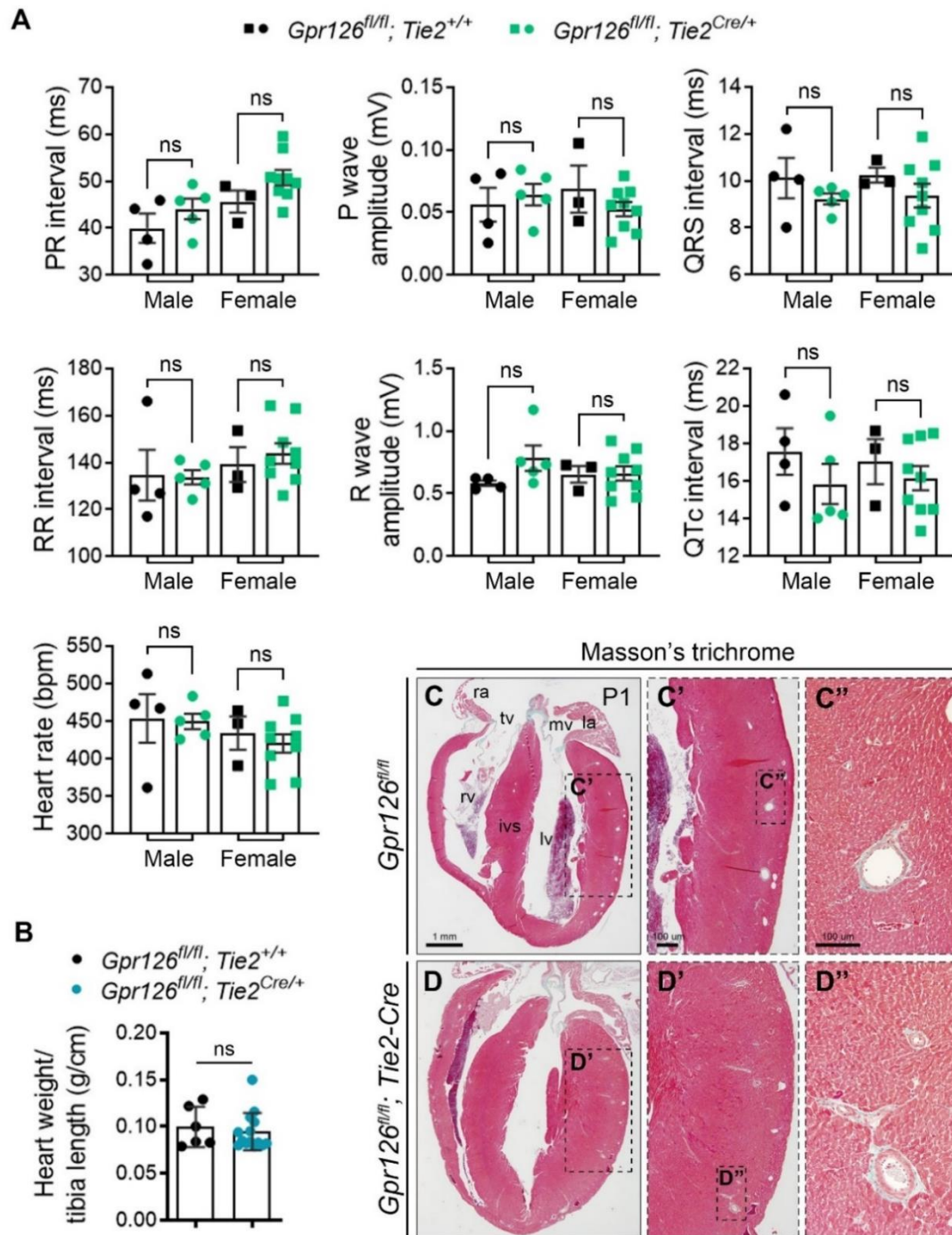


Figure 19. Analysis of cardiac morphology and function in *Gpr126^{fl/fl}*; *Tie2^{Cre/+}* adult mice. (A) ECG analysis of male and female *Gpr126^{fl/fl}*; *Tie2^{+/+}* (control) and *Gpr126^{fl/fl}*; *Tie2^{Cre/+}* adult mice at 31-36 weeks old. The graphs show PR interval, P wave amplitude, QRS interval, RR interval, R wave amplitude, corrected QT interval (cQT) and heart rate, considering males (squares) and females (circles) separately. Data are presented as mean \pm SD (n= 4 control and 5 mutant males; 5 control and 9 mutant females). Statistical significance was determined by unpaired Student's *t*-test subjected to Welch's correction (ns, not significant). (B) Chart depicting heart weight (mg) to tibia length (cm) ratios of *Gpr126^{fl/fl}*; *Tie2^{+/+}* (control) and *Gpr126^{fl/fl}*; *Tie2^{Cre/+}* adult mice at 46-55 weeks old, distinguishing between males (squares) and females (circles). Data are means \pm SD (n= 4 control and 5 mutant males; 5 control and 9 mutant females). Statistical significance was determined by unpaired Student's *t*-test (ns, not significant). (C-D'') Masson's trichrome staining of transversal heart sections from WT (C-C'') and *Gpr126^{fl/fl}*; *Tie2^{Cre/+}* mutants (D-D'') at 46 weeks old. Boxed regions in (C, D) are magnified in ('); boxed regions in (C', D') are magnified in (''). ivs, interventricular septum; la, left atrium; lv, left ventricle; mv, mitral valve; ra, right atrium; rv, right ventricle; tv, tricuspid valve. Scale bars, 1 mm (low magnification); 100 μ m (insets).

Generation of conditional *R26-GPR126^{GOF}* transgenic mouse line by homologous recombination in mESC

Embryonic lethality and cardiac defects observed in *Gpr126^{A7/A7}* null embryos appeared to be independent of *Gpr126* expression in the chamber endocardium. To reinforce the idea that cardiac *Gpr126* signaling is dispensable to sustain embryonic progression, we combined conditional loss-and gain-of-function studies. To this purpose, we generated a transgenic line conditionally overexpressing human *GPR126* cDNA under the control of the endogenous and ubiquitous *Rosa26* promoter (*R26-GPR126^{GOF}*) (Fig. 20A) (See *Materials and Methods*). Overexpression of human *GPR126* instead of mouse, will enable us to test whether human and mouse genes are functionally equivalent and interchangeable. Both heterozygous and homozygous *R26-GPR126^{GOF}* mice (hereafter referred to as *GPR126^{GOF}*) were subjected to Southern blot analysis to confirm the presence of one or two copies of the transgene, respectively (Fig. 20B). Besides, they were phenotypically normal, viable and fertile.

We evaluated the efficacy of Cre-mediated removal of the NeoR-STOP cassette and subsequent activation of eGFP expression *in vivo* by crossing heterozygous *GPR126^{GOF/+}* mice with the *Nkx2.5-Cre* strain, which drives Cre-mediated recombination in cardiac precursors from E7.5 (Stanley et al., 2002). This recombination is complete in cardiomyocytes and affects a large part of endocardial (Stanley et al., 2002) and epicardial (Zhou et al., 2008) precursors. At 9.5, transgenic *GPR126^{GOF/+}*; *Nkx2.5^{Cre/+}* embryos showed widespread GFP expression in the heart, compared to the background fluorescence of heterozygous control littermates (Fig. 20C, D).

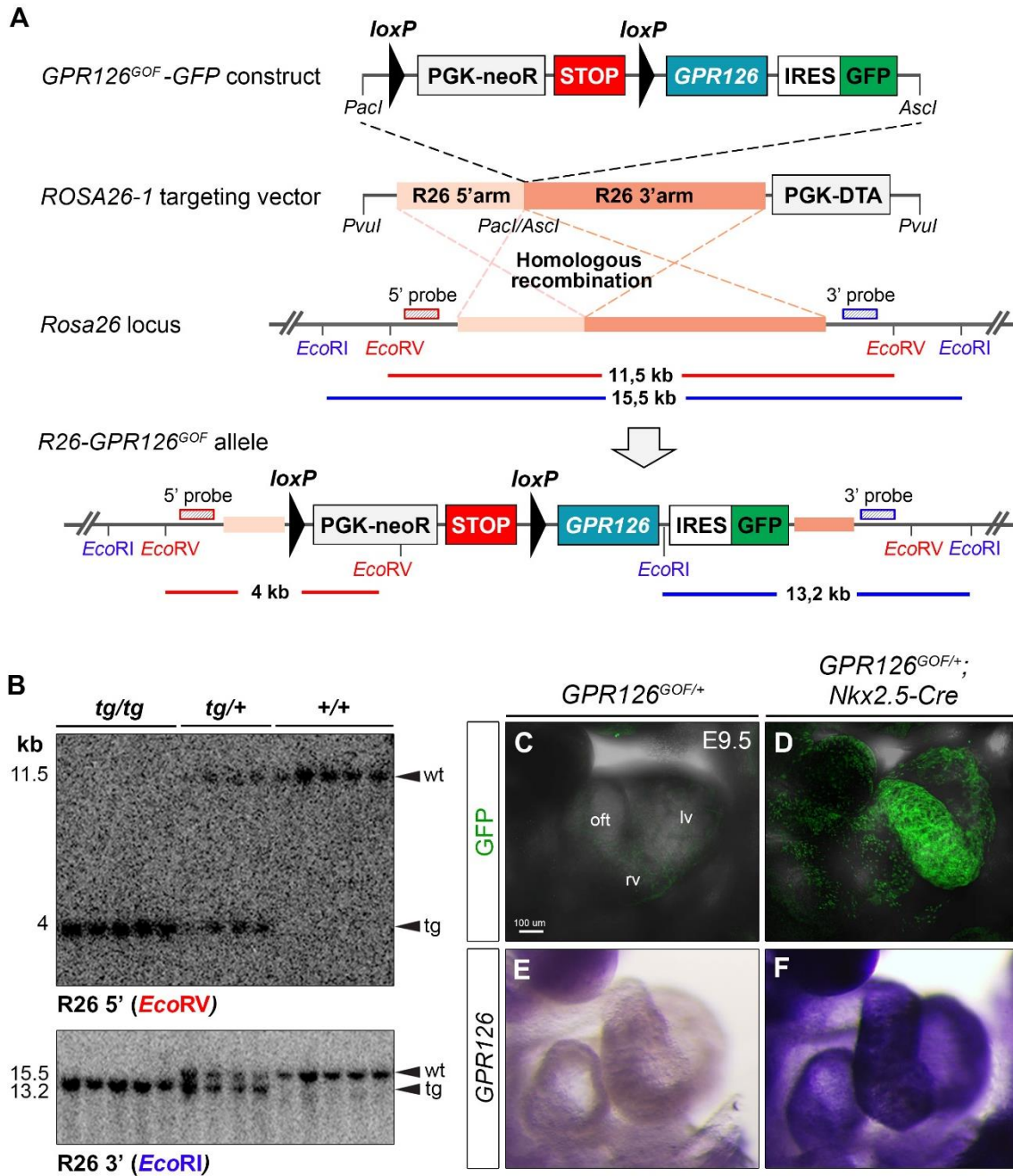


Figure 20. Gene targeting of the *Rosa26* locus to generate conditional *R26-GPR126^{GOF}-GFP* transgenic line. (A) Gene targeting strategy for the generation of conditional *GPR126^{GOF}* transgenic line. Top to bottom: modified *pROSA26-1* plasmid vector harboring the *loxP*-PGK-NeoR-STOP-*loxP*-*GPR126*-IRES-eGFP construct between *Rosa26* 5' and 3' homology arms. Targeted WT *Rosa26* locus showing the location of the 5' and 3' hybridization probes used for Southern analysis, *EcoRV* and *EcoRI* sites. Resulting *R26-GPR126^{GOF}* allele upon homologous recombination in ES cells. PGK, phosphoglycerate kinase; neoR, neomycin resistance gene; IRES, internal ribosome entry site; GFP, green fluorescent protein; DTA, diphtheria toxin. (B) Southern blot analysis of *EcoRV*- (top panel) and *EcoRI*-digested DNA (bottom panel) from homozygous (*tg/tg*), heterozygous (*tg/+*) and WT (*+/+*) *GPR126^{GOF}* offspring. (C, D) Confocal images of eGFP expression in E9.5 *GPR126^{GOF/+}* (C) and *GPR126^{GOF/+}; Nkx2.5^{Cre/+}* (D) hearts. (E, F) WISH showing *GPR126* expression in E9.5 *GPR126^{GOF/+}* (E) and *GPR126^{GOF/+}; Nkx2.5^{Cre/+}* (F) hearts. oft, outflow tract; lv, left ventricle; ra, right atrium. Scale bar, 100 μ m.

Additionally, WISH revealed that *GPR126* mRNA was exclusively expressed in *GPR126^{GOF/+}; Nkx2.5^{Cre/+}* hearts (Fig. 20E, F) (Suppl. Table 10). In summary, we generated a bona fide conditional *GPR126* gain-of-function mouse model that could be used as a genetic tool to investigate *Gpr126* essential developmental role.

Conditional *GPR126* overexpression in the *Tie2-Cre* lineage allows normal heart development and does not rescue *Gpr126^{Δ7}* embryonic lethality

Since the global loss of *Gpr126* results in abnormal thinning of compact myocardium and trabeculae, we next tested whether *GPR126* overexpression affects heart development. Thus, we conditionally overexpressed *GPR126* in the endothelium using the *Tie2-Cre* driver (Fig. 21A) and examined cardiac morphology at different developmental stages. *GPR126* overexpression did not produce overt phenotypical alterations (data not shown) nor embryonic lethality (Suppl. Table 11), and *GPR126^{GOF/+}; Tie2^{Cre/+}* embryos presented normal cardiac morphology by histological examination from E10.5 to E16.5, compared to *GPR126^{GOF/+}; Tie2^{+/+}* littermates (Fig. 21B-E’'). We conclude that endothelial-specific *Gpr126* overexpression is compatible with normal heart development.

Next, we took advantage of the transgenic *GPR126^{GOF/+}* line to discard the possibility that endocardial *Gpr126* function is critical for embryonic and heart development. To this end, we bred *Gpr126^{Δ7/+}; Tie2^{Cre/+}* males with *GPR126^{GOF/+}; Gpr126^{Δ7/+}* females to obtain *GPR126^{GOF/+}; Gpr126^{Δ7/Δ7}; Tie2^{Cre/+}* embryos, in which endogenous *Gpr126* is globally disrupted, and *GPR126* expression is exclusively confined to the *Tie2-Cre* lineage (Fig. 21F). If cardiovascular defects were the primary reason for *Gpr126^{Δ7}* embryonic lethality, we would expect to detect embryonic survival past E13.5. However, *GPR126^{GOF/+}; Gpr126^{Δ7/Δ7}; Tie2^{Cre/+}* embryos died at the same gestational stages than *Gpr126^{Δ7/Δ7}* mutants (Suppl. Table 12), indicating that the cause of death was due to defective development of another organ than the heart.

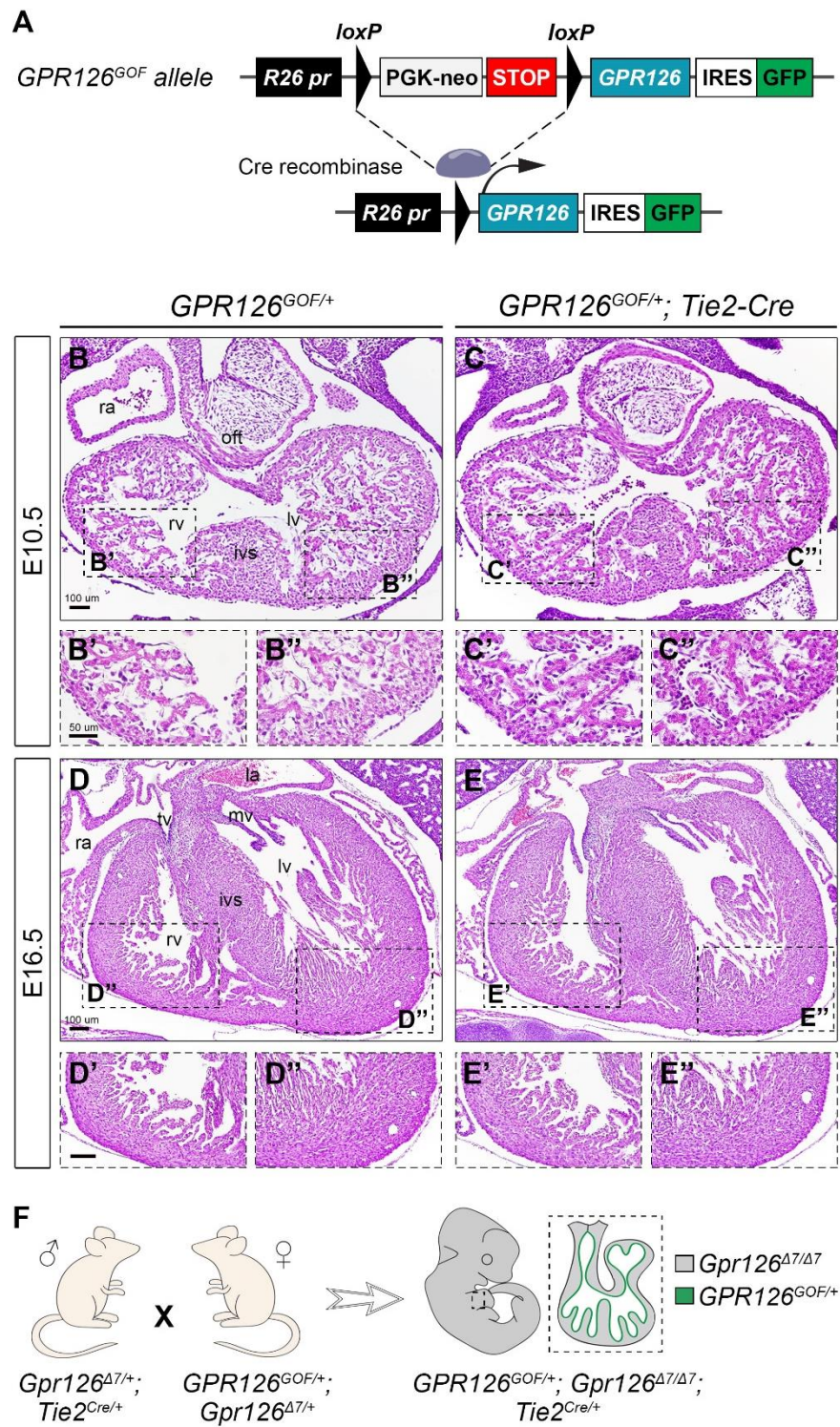


Figure 21. Analysis of endothelial-specific *GPR126* overexpression in WT and *Gpr126*^{Δ7/Δ7} background. (A) Schematic showing the gain-of-function *R26-GPR126*^{GOF} reporter construct. *GPR126* expression is activated upon Cre-mediated excision of the *NeoR-STOP* cassette. (B-E'') H&E staining of transversal heart sections from *GPR126*^{GOF/+} (control) and *GPR126*^{GOF/+}; *Tie2*^{Cre/+} embryos at E10.5 (B-C'') and E16.5 (D-E''). Magnifications of the right ventricle are shown in ('), and the left ventricle in ('). ivs, interventricular septum; la, left atrium; lv, left ventricle; mv, mitral valve; of, outflow tract; ra, right atrium; rv, right ventricle; tv, tricuspid valve. Scale bars, 100 μm (low magnification); 50 μm (insets). (F) Schematic showing the strategy of crossing *Gpr126*^{Δ7/+}; *Tie2*^{Cre/+} males with *GPR126*^{GOF/+}; *Gpr126*^{Δ7/+} females to obtain *GPR126*^{GOF/+}; *Gpr126*^{Δ7/Δ7}; *Tie2*^{Cre/+} embryos.

***GPR126* overexpression fails to rescue impaired EMT and hypotrabeculation in *Dll4*^{fllox}; *Tie2-Cre* mutants**

Previous studies in our lab brought *Gpr126* into focus as a Notch target gene (D'Amato et al., 2016b). These results pointed toward a scenario in which endocardial *Gpr126* acts as a downstream effector of Notch activation to regulate the process of trabeculation. To test whether the sole expression of *GPR126* was able to compensate for the lack of the Notch ligand *Dll4* and the loss of endogenous *Gpr126* expression (D'Amato et al., 2016b), we crossed double heterozygotes mice bearing a conditional *Dll4*^{fllox} allele (Koch et al., 2008) (hereafter referred as *Dll4*^{fl}) and the pan-endothelial driver *Tie2-Cre* with double heterozygotes mice bearing a conditional *Dll4*^{fl} allele and a conditional *GPR126*^{GOF} allele (Fig. 22A). However, transgenic expression of *GPR126* in the endothelium/ endocardium was not sufficient to prevent the phenotype of *Dll4*^{fl/fl}; *Tie2*^{Cre/+} mutants, nor to rescue their early embryonic lethality (Suppl. Table 13). At E9.5, mutant embryos were smaller than WT littermates and showed pericardial distension (Fig. 22B, C), regardless of the expression of the *GPR126* transgene (Fig. 22D). Consistent with previous observations (D'Amato et al., 2016b), H&E staining of *Dll4*^{fl/fl}; *Tie2*^{Cre/+} mutant hearts revealed defective EMT in the AVC region, evidenced by the absence of mesenchymal cells invading the cushions (Fig. 22E-F'), and poorly formed trabeculae in the ventricles (Fig. 22E'', F''). This cardiac phenotype was persistent in *Dll4*^{fl/fl}; *GPR126*^{GOF/+}; *Tie2*^{Cre/+} littermates (Fig. 22G-G').

We conclude that *GPR126* overexpression cannot rescue nor ameliorate the cardiac defects caused by *Dll4*-Notch inactivation.

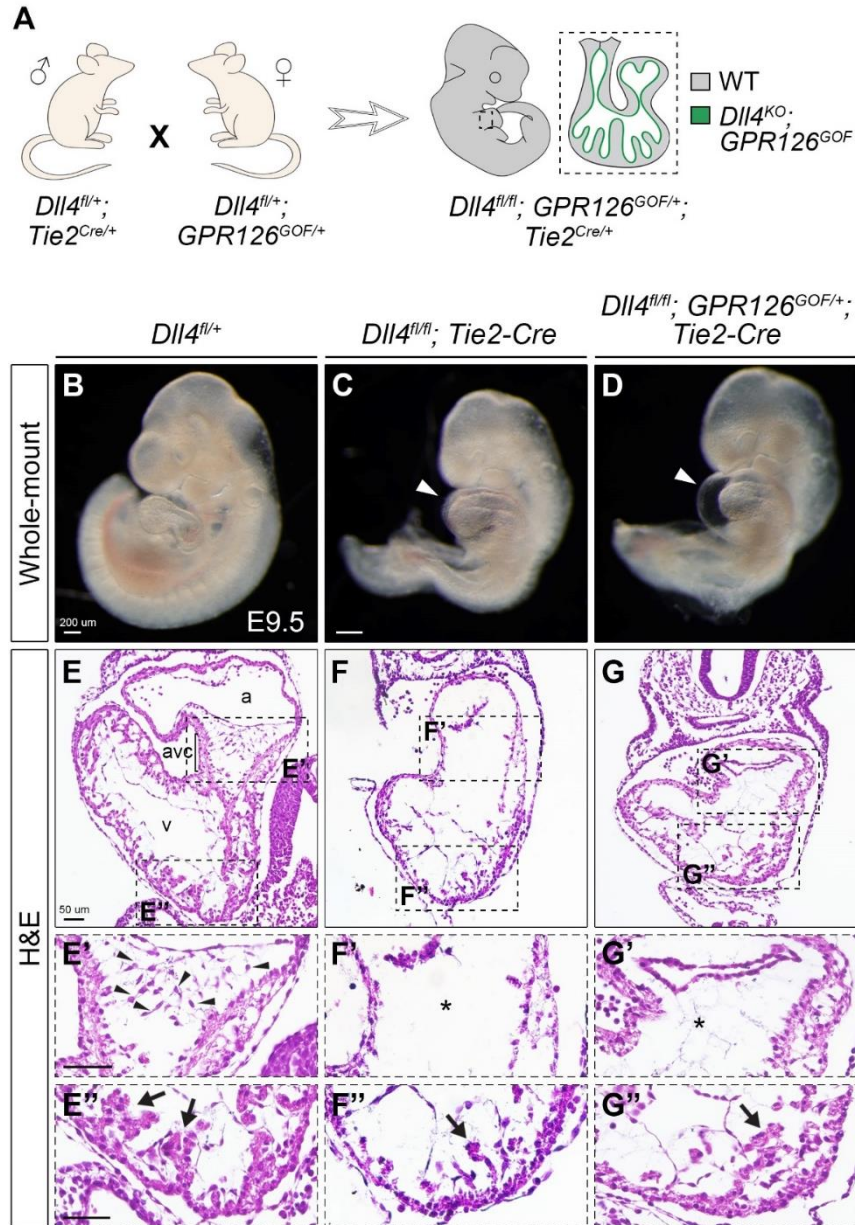


Figure 22. Analysis of *GPR126* overexpression in a *Dll4*^{fl/fl}; *Tie2-Cre* background. (A) Schematic showing the strategy of crossing *Dll4*^{fl/+}; *Tie2*^{Cre/+} males with *Dll4*^{fl/+}; *GPR126*^{GOF/+} females to obtain *Dll4*^{fl/fl}; *GPR126*^{GOF/+}; *Tie2*^{Cre/+} embryos. (B-D) Whole-mount views of E9.5 *Dll4*^{fl/+}; *GPR126*^{+/+}; *Tie2*^{+/+} (control) (B), *Dll4*^{fl/fl}; *GPR126*^{+/+}; *Tie2*^{Cre/+} (C) and *Dll4*^{fl/fl}; *GPR126*^{GOF/+}; *Tie2*^{Cre/+} embryos (D). Note the pericardial edema (indicated with white arrowheads) in (C, D). Scale bars, 200 μ m. (E-G'') H&E staining of transversal heart sections from E9.5 *Dll4*^{fl/+}; *GPR126*^{+/+}; *Tie2*^{+/+} (control) (E), *Dll4*^{fl/fl}; *GPR126*^{+/+}; *Tie2*^{Cre/+} (F) and *Dll4*^{fl/fl}; *GPR126*^{GOF/+}; *Tie2*^{Cre/+} (G) embryos. Boxed areas of the right ventricle are magnified in ('), and boxed areas of the left ventricle are shown in (''). Black arrowheads point to mesenchymal cells invading the cushion in (E'), whilst their absence is depicted with an asterisk in (F', G'). Arrows point to developing trabeculae in (E'', F'', G''). a, atrium; avc, atrioventricular canal; v, ventricle. Scale bars, 50 μ m.

Generation of zebrafish *gpr126* mutants using CRISPR-Cas9 technology

Our results obtained in mice raised the intriguing idea that defective cardiac development and death observed in full *Gpr126* mutants is secondary to the loss of Gpr126 in another organ. In addition to mice, the zebrafish model has been widely used for understanding the multiple roles of *gpr126*, including heart development. To date, only one report described a morpholino-based model in which the NTF of *gpr126* acts as a paracrine signal that is required for trabeculation (Patra et al., 2013). Notably, despite the large number of zebrafish *gpr126* mutant lines that have been analyzed (*gpr126^{st49}*, *gpr126^{st63}*, *gpr126^{st86}*, *gpr126^{stl47}*, *gpr126^{stl215}*, *gpr126^{stl464}*, *gpr126^{tb233c}*, *gpr126^{fr24}*, *gpr126^{tk256a}*, *gpr126^{vu39}* ...), no heart phenotype has been described (Diamantopoulou et al., 2019; Leon et al., 2020; Liebscher et al., 2014; Monk et al., 2009; Paavola et al., 2014; Petersen et al., 2015). The phenotypic discrepancies observed between knockdown and knockout experiments, along with the unexpected results obtained in mice, led us to ascertain the *gpr126* function in zebrafish heart development.

To this end, we used CRISPR-Cas9 technology to generate two *gpr126* knockout alleles, *gpr126^{bns341}* and *gpr126^{bns342}* (See *Materials and methods*) (Fig. 23A). The zebrafish *gpr126^{bns341}* allele is a nonsense mutation caused by the deletion of exons 7 and 8, leading to a frameshift and a PTC in exon 10. Interestingly, our strategy was designed to eliminate a 788 bp region harboring exons 7-9, which also generates a PTC in exon 10 (Fig. 23B), but we achieved a 663 bp deletion excluding exon 9 instead (Fig. 23C). Since mouse and zebrafish *Gpr126* are considered true orthologs (Harty et al., 2015; Waller-Evans et al., 2010), the similarity to our *Gpr126^{Δ7}* mouse line will illustrate the parallels of gene function in both animal models. The Δ7,8 mutation truncates the protein between the recently identified linker (encoded by exon 5) and the SEA domain (encoded from exon 7 to 10). Since a previously reported *gpr126^{st86}* mutation harboring a PTC after the PTX domain does not affect the amount of mutant *gpr126* mRNA, we hypothesize that the *gpr126^{bns341}* mutant allele will likely produce a severely truncated protein of 428 aa formed by the SP, CUB, PTX and linker domains of the ECD (Fig. 23D).

In contrast, the zebrafish *gpr126^{bns342}* allele is a promoter-less allele that lacks the promoter region of *gpr126*. A recent work demonstrated the requirement of mutant mRNA decay to promote transcriptional adaptation, a form of genetic compensation that involves the transcriptional upregulation of genes (referred to as “adapting genes”) that can potentially compensate for the loss of gene function. Hence, alleles that fail to transcribe the mutated gene did not display this response and uncovered phenotypes not observed in those harboring nonsense mutations and undergoing mutant mRNA degradation (El-Brolosy et al., 2019). Thus, cardiac phenotypic differences encountered in zebrafish *gpr126* knockouts and morphants could be explained by the process of transcriptional adaptation taking place in mutants, but not in

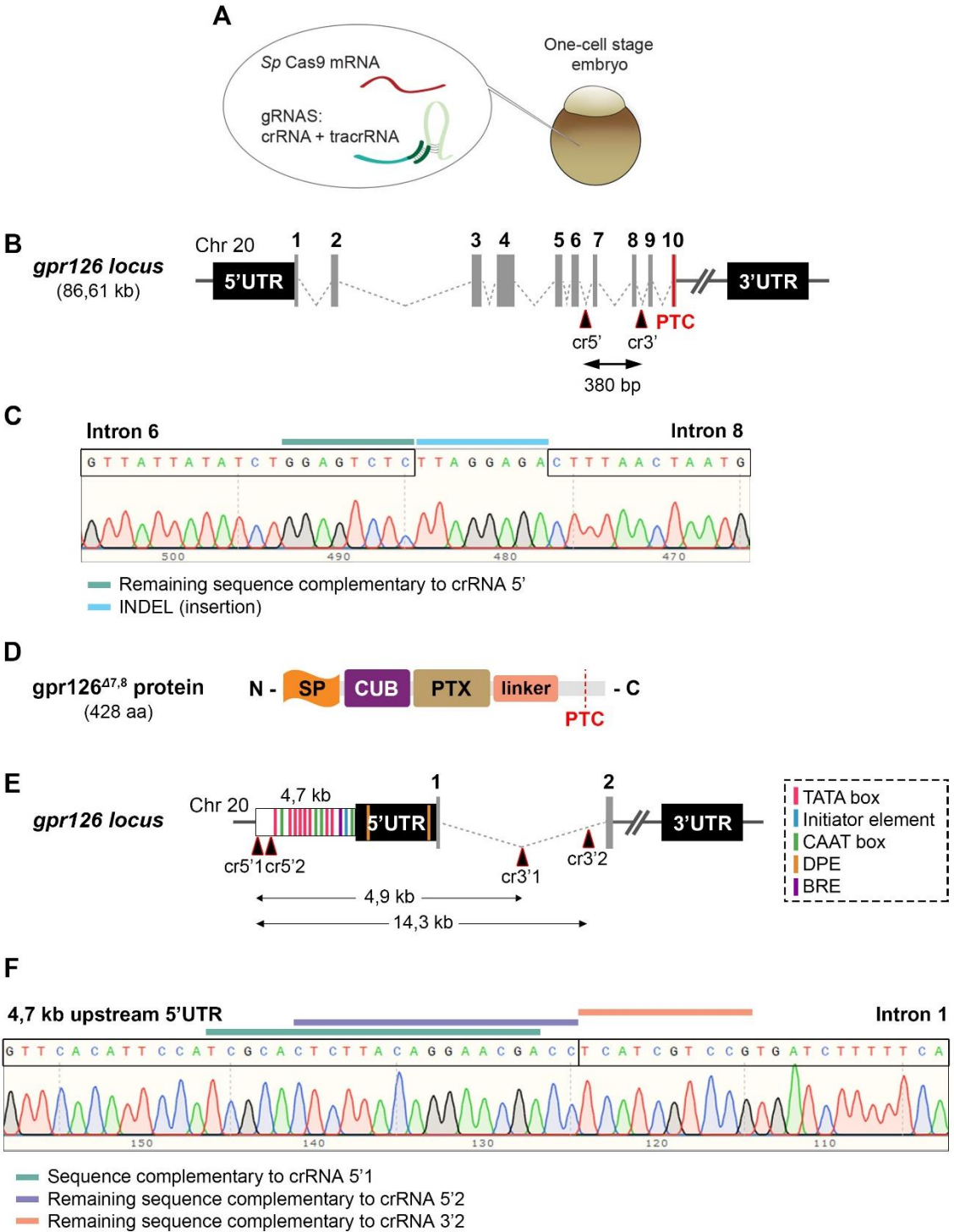


Figure 23. Generation of zebrafish *gpr126^{bns341}* and *gpr126^{bns342}* mutant alleles using CRISPR-Cas9. (A) Schematic showing injection of CRISPR-Cas9 elements into the yolk of the one-cell stage zebrafish embryo. (B) Schematic diagram showing 2 crRNA (5' and 3') target sites in introns 6 and 8 within zebrafish *gpr126* locus (located in chromosome 20) to generate *gpr126^{bns341}* mutant allele. The deletion of exons 7 and 8 will generate a PTC in exon 10 (shown in red). Grey boxes depict exons; dashed grey lines illustrate introns. (C) Chromatogram of sequencing data from F1 heterozygous *gpr126^{bns341/+}* fish showing deletion of exons 7 and 8, plus an 8 bp insertion (indel). (D) Schematic diagram showing the presumable structure of the *gpr126^{Δ7,8}* protein, formed by 428 aa. SP, signal peptide; CUB, complement, Uegf, Bmp1; PTX, pentraxin; PTC, premature termination codon. (E) Schematic diagram showing 4 crRNA (5'1, 5'2, 3'1, 3'2) target sites within zebrafish *gpr126* locus (located in chromosome 20) to generate *gpr126^{bns342}* mutant allele. Grey boxes depict exons; dashed grey lines illustrate introns. DPE, downstream promoter element; BRE, B recognition element. (F) Chromatogram of sequencing data from F1 heterozygous *gpr126^{bns342/+}* fish showing deletion of the targeted promoter region.

morpholino-treated animals. The generation and characterization of the *gpr126 RNA-less* allele will help to test this hypothesis. To identify the promoter region within the *gpr126* locus, we first searched for known core promoter elements upstream the transcription starting site (TSS), like TATA box and CAAT box sequences, B recognition element (BRE), the initiator element and downstream promoter element (DPE) (Fig. 23E). Second, we used available ChIP-seq data sets of zebrafish embryos at 24 hpf and tracked histone modifications that are quintessentially associated with transcriptional activation, like the trimethylation of histone H3 lysine 4 (H3K4me3) (Suppl. Fig. 1A). Two open chromatin regions (displayed as peaks) were found in the zebrafish *gpr126* locus, one around the TSS (~500 bp) (Suppl. Fig. 1A') and the other mapping exon 23 (Suppl. Fig. 1A''). Given the large size of intron 1 (~10 kb) and the likely presence of regulatory elements that can affect gene expression, we targeted altogether a large region of ~14.3 kb covering the aforementioned sequences and part of intron 1 (Fig. 23E). We checked whether this deletion could affect the expression of an additional gene by removal of a certain region, and we only found a small overlap with part of the 3'UTR of the vacuolar protein sorting-associated protein VTA1 homolog (*vta1*) (Suppl. Fig. 1B).

CRISPR-injected zebrafish embryos (F0) were raised to adulthood, outcrossed with the WT AB line, and the F1 progeny was genotyped by conventional PCR. Targeted mutations were confirmed by sequencing (Fig. 23D, F), and outbreeding of heterozygous F1 carriers (*gpr126^{bns341/+}* and *gpr126^{bns342/+}*) was performed two consecutive generations to avoid potential target effects. Incross of heterozygous F2 and F3 fish resulted in WT, heterozygous and homozygous embryos (F3 and F4) that were characterized during development.

Sequence similarity analysis of zebrafish *gpr126* reveals *gpr112* as a potential adapting gene

Given that *gpr126* is not duplicated in the zebrafish genome (Waller-Evans et al., 2010), we next searched for genes with high sequence similarity (see *Materials and methods*). The rationale was that some of them may represent potential compensatory paralogues (hereafter referred to as “adapting genes”) in zebrafish accounting for the lack of heart phenotype in *gpr126* knockouts. We inferred homology when two sequences shared more similarity than would be expected by chance; being the simplest explanation that high similar sequences do not arise independently but from a common ancestor (Pearson, 2013). Thus, we relied on E-values and bit scores to identify genes similar to mouse and zebrafish *Gpr126* (Suppl. Tables 14 and 15). We observed that *adgrg4b* (also known as *gpr112b*), *adgrg4a* (or *gpr112a*), and *adgrg2a* (or *gpr64a*) were the closest homologs to zebrafish *gpr126*, in agreement with previous reports (Suppl. Table 14) (Harty et al., 2015; Waller-Evans et al., 2010). The same homolog genes were found for mouse *Gpr126* (Suppl. Table 15) (*Adgrg4/Gpr112* and *Adgrg2/Gpr64*). Although there is no evidence that these genes are expressed in the zebrafish embryonic heart, they are indeed expressed during development (Harty et al., 2015). Moreover, it has been reported that *Gpr112* shares more homology to *Gpr126* at the protein level in zebrafish than in mammals (Waller-Evans et al., 2010), suggesting that *gpr112* could be an adapting gene candidate compensating for the loss of *gpr126* and preventing abnormal heart trabeculation in zebrafish knockouts.

The *gpr126^{bns341}* and *gpr126^{bns342}* mutations disrupt inner ear development in zebrafish

We next determined whether *gpr126^{bns341}* and *gpr126^{bns342}* mutations affected gene expression by examining *gpr126*, *gpr112a*, and *gpr112b* transcript levels at 3 dpf, when *gpr126* starts to be expressed (Harty et al., 2015). By RT-qPCR, the amount of mRNA was similar in *gpr126^{+/+}*, *gpr126^{bns341/+}* heterozygous and *gpr126^{bns341/+}* homozygous larvae (Fig. 24A), suggesting that the *gpr126^{bns341}* mutant allele truncates the protein between the PTX and the HBD within the NTF, and does not trigger transcriptional adaptation through *gpr112a/b* upregulation. As mutant mRNA degradation is not taking place, the upregulation of the adapting genes is not expected either. In contrast, the *gpr126^{bns342}* allele fails to transcribe the mutated gene, and *gpr112a/gpr112b* levels remain unchanged compared to WT siblings (Fig. 24B). Thus, we confirmed that *gpr126^{bns342}* mutation prevents gene transcription and genomic compensation via transcriptional adaptation.

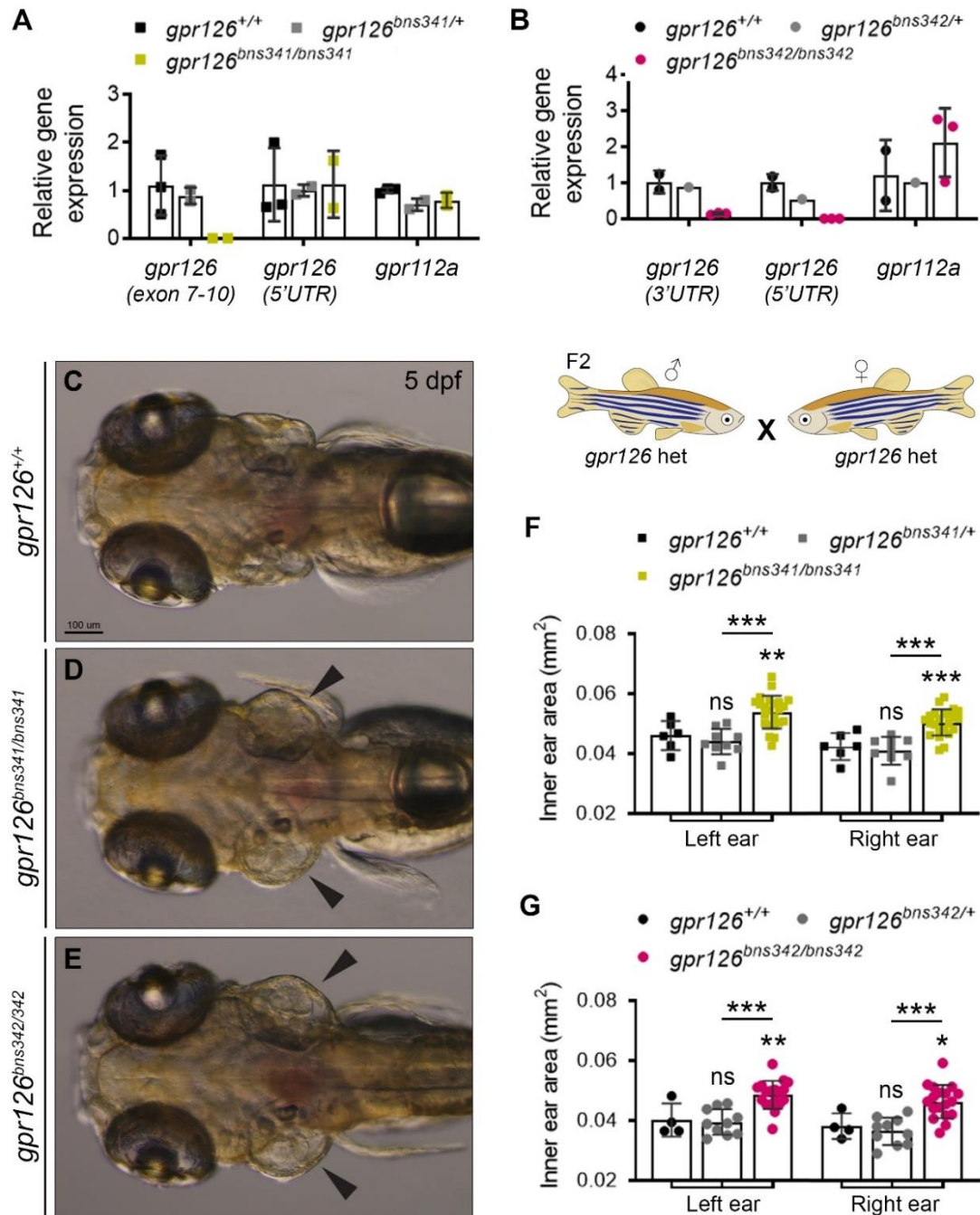


Figure 24. Inner ear development is disrupted in *gpr126*^{bns341} and *gpr126*^{bns342} zebrafish mutants. (A-B) RT-qPCR analysis of relative *gpr126*, *gpr112a* and *gpr112b* mRNA expression levels to *rpl13a* as housekeeping gene) in *gpr126*^{bns341/bns341} (A) and *gpr126*^{bns342/bns342} (B) zebrafish mutants at 3 dpf. (C-E) Dorsal view of WT (C), *gpr126*^{bns341/bns341} (D) and *gpr126*^{bns342/bns342} (E) zebrafish mutants at 5 dpf, showing inner ear morphology. Arrowheads mark swollen ears in the mutants. Scale bar, 100 μ m. (F, G) Quantification of left and right ear area in *gpr126*^{bns341} (F) and *gpr126*^{bns342} (G) heterozygous and homozygous zebrafish mutants, compared to WT siblings. Data are means \pm SD. Statistical significance was determined by unpaired Student's *t*-test (ns, not significant, **P* < 0.05; ***P* < 0.01, ****P* < 0.001).

In zebrafish, *gpr126* has been shown to play an essential role in the regulation of inner ear development by elevating cAMP levels, and mutants can be easily identified by a swollen ear phenotype (Geng et al., 2013; Leon et al., 2020; Paavola et al., 2014). Therefore, we first assessed ear morphology prior to heart analysis to evaluate *gpr126* functional activity. Notably, both *gpr126^{bns341/bns341}* and *gpr126^{bns342/bns342}* homozygous mutants displayed enlarged ears at 5 dpf (Fig. 24C-E), indicative of disrupted gene function.

The *gpr126^{bns341}* and *gpr126^{bns342}* mutations do not impair heart development

Next, we explored the role of *gpr126* in cardiac trabeculation. Previous studies have shown that *gpr126* is expressed in the zebrafish heart 48 hpf, before the onset of trabeculation (D'Amato et al., 2016b; Patra et al., 2013). Like other *gpr126* zebrafish mutants, homozygous *gpr126^{bns341}* and *gpr126^{bns342}* fish reached adulthood and exhibited grossly normal phenotype, indicating that these mutations did not cause lethal heart defects. Using brightfield microscopy, homozygous *gpr126^{bns341}* and *gpr126^{bns342}* larvae were recognized by their swollen ears, but did not show pericardial edema at 100 hpf, when trabeculation is already advanced (Fig. 25A-C).

To examine cardiac trabeculation in more detail, we first introduced *gpr126^{bns342/+}* fish in the *Tg(kdrl:Hsa.HRAS-mCherry); Tg(myl7:EGFP-Hsa.HRAS)* background (Chi et al., 2008; D'Amico et al., 2007), so that endocardial and myocardial membranes are labeled in red and green, respectively. Trabeculae start to form in zebrafish around 60 hpf and become clearly apparent by 72 hpf (Liu et al., 2010). Confocal imaging at 80 hpf revealed no obvious differences between mutants and WT littermates (Fig. 25D-E'). Few delaminated cardiomyocytes forming nascent trabecular ridges were observed in mutant ventricles, indicative of a normal onset of trabeculation (Fig. 25D', E'). Observation at later stages confirmed no trabeculation defects, as trabecular projections were formed throughout the luminal side of the outer curvature of the ventricle at 96 hpf, similarly to WT larvae (Fig. 25F-G'). Based on the absence of a heart phenotype in *gpr126^{bns342/bns342}* mutants, which lack *gpr126* transcriptional activity, one might expect to obtain the same results in *gpr126^{bns341/bns341}* larvae, which presumably encode a shorter truncated *gpr126* protein. To test this possibility, we incrossed the *gpr126^{bns341}* mutation into the *Tg(myl7:EGFP-Hsa.HRAS)* transgenic line. Likewise, confocal microscopy analysis revealed extensive trabeculation by 96 hpf in *gpr126^{bns341/bns341}* mutant hearts, as in WT siblings (Fig. 25H-I').

Taken together, these data indicate that *gpr126* signaling is not required for heart development in zebrafish.

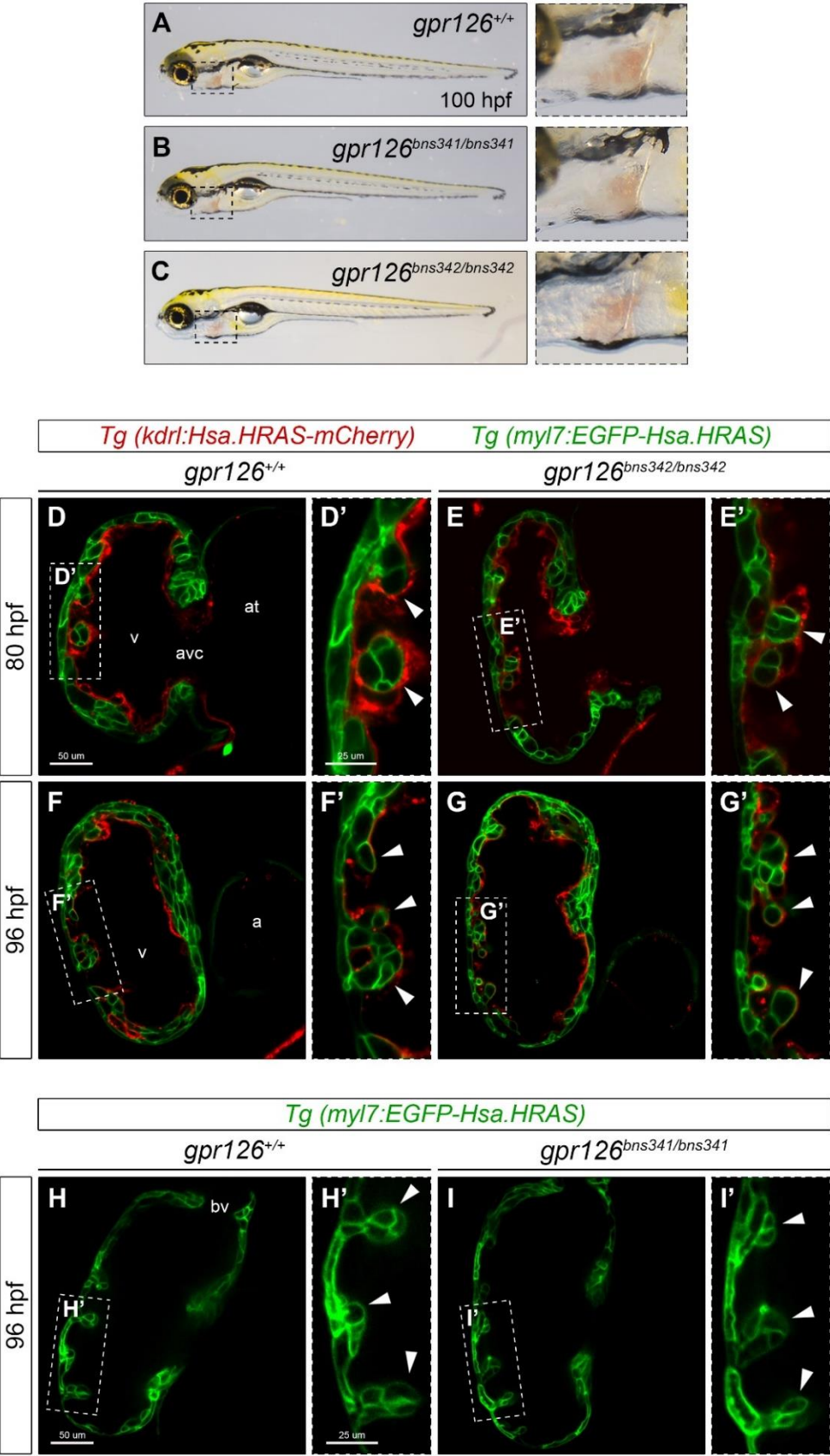


Figure 25. Trabeculation is unaffected in *gpr126*^{bns341} and *gpr126*^{bns342} zebrafish mutants. (A-C) Lateral views (anterior to the left) of 100 hpf *gpr126*^{+/+}, *gpr126*^{bns341/bns341} and *gpr126*^{bns342/bns342} zebrafish larvae derived from heterozygous *gpr126*^{bns341/+} and *gpr126*^{bns342/+} incrosses, respectively. Boxed areas display high power magnification views of the heart. (D-G') Mid-sagittal confocal sections of *gpr126*^{+/+} and *gpr126*^{bns342/bns342} zebrafish hearts at 80 hpf (D-E') and 96 hpf (F-G'). Zebrafish larvae derived from *gpr126*^{bns342/+}; *Tg(kdrl:Hsa.HRAS-mCherry)*; *Tg(my17:EGFP-Hsa.HRAS)* incrosses. Endocardial and myocardial membranes are labeled in red and green, respectively. Higher magnification views of the outer curvature of the ventricular wall are shown on the right (*). Arrowheads indicate emerging trabeculae. at, atrium; avc, atrioventricular canal; v, ventricle. Scale bars, 50 μ m (low magnification); 25 μ m (insets). (H-I') Mid-sagittal confocal sections of *gpr126*^{+/+} and *gpr126*^{bns341/bns341} zebrafish hearts at 96 hpf. Zebrafish larvae derived from *gpr126*^{bns341/+}; *Tg(my17:EGFP-Hsa.HRAS)* incrosses. Myocardial membranes are labeled in green. Higher magnification views of the outer curvature of the ventricular wall are shown on the right (*). Arrowheads indicate emerging trabeculae. bv, bulboventricular valve. Scale bars, 50 μ m (low magnification); 25 μ m (insets).

***Gpr126* is expressed in the spongiotrophoblast layer and the four TGC subtypes of the mouse placenta**

To further investigate how *Gpr126* loss-of-function contributes to developmental demise, we first defined the expression pattern of *Gpr126* in the mouse embryo at E12.5, which could be indicative of a putative role in the corresponding organ(s) (Fig. 26A-b''). The combination of ISH and H&E staining permitted visualization of tissue morphology for precise localization of *Gpr126* transcripts. Thus, *Gpr126* transcripts were specifically found in the chamber endocardium (Fig. 26a, b), in the cartilage primordium of the vertebral body (Fig. 26a', b') and to a lesser extent in the lung epithelium (Fig. 26a'', b''), in agreement with previous publications (Kou et al., 2013; Musa et al., 2019). However, targeted *Gpr126* deletion in cartilaginous tissues using the *Col2-Cre* driver is compatible with embryo survival (Kou et al., 2013), and no lung phenotype has been described in *Gpr126* knockout mutants, suggesting that loss of *Gpr126* in these tissues does not underlie the embryonic lethality of *Gpr126*^{A7/A7} mutants.

It has been previously shown that *Gpr126* is expressed in the trophoblast giant cells (TGC) of the mouse placenta, by examination of β -galactosidase expression in the *GPR126*^{LacZ} knock-in mice (expressing a *LacZ* reporter gene under the control of the GPR126 promoter) (Waller-Evans et al., 2010). For a more detailed analysis, we also examined the spatiotemporal expression pattern of *Gpr126* in the extraembryonic tissues at different developmental stages by ISH analysis. At E9.5, we detected expression in the Spa-TGC lining maternal blood vessels within the decidua (Fig. 28A, a, B, b), in the P-TGC that delineate the implantation site (Fig. 27a', b') and in the S-TGC lining maternal blood sinusoids within the labyrinth layer of the placenta (Fig. 27a'', b''). A similar expression pattern to that at E9.5 was observed at E10.5, but showing higher levels of

transcription and scattered staining in the SpT layer (Fig. 27C-d''). Later in development, at E11.5, *Gpr126* expression was maintained in the same cell types (Fig. 27E, f'), and also found in the C-TGC surrounding maternal canal spaces within the labyrinth at the base of the placenta (Fig. 27e'', f'', white arrowheads) and passing through the JZ (Fig. 27e''', f''', white arrowheads).

Taken together, we found that *Gpr126* is expressed in the SpT layer and the four TGC subtypes of the mouse placenta, pointing out a potential association between placental *Gpr126* function and embryonic development.

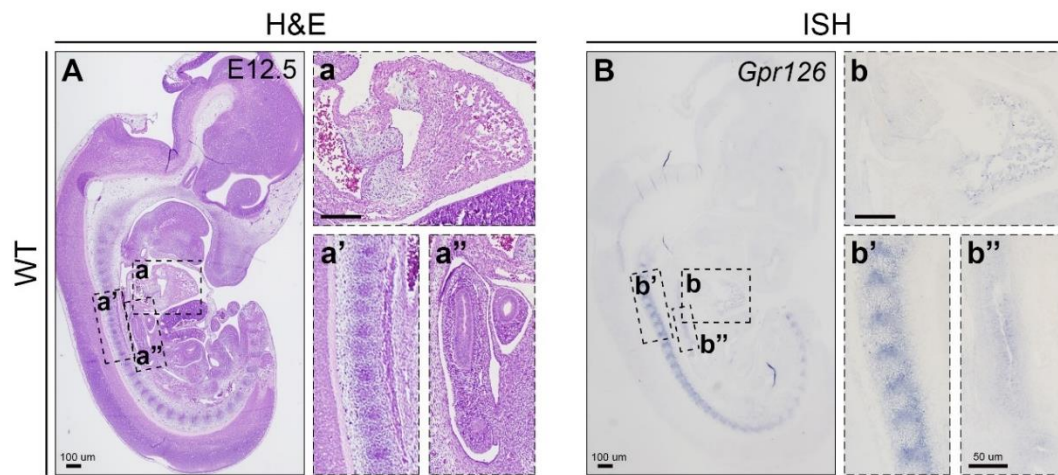


Figure 26. Analysis of *Gpr126* expression pattern in the mouse embryo. (A-a'') H&E-stained sagittal sections of an E12.5 WT embryo. High power magnification views corresponding to the boxed areas are displayed on the right, as insets of the heart (a), vertebral bodies (a') and lungs (a''). (B-b'') ISH of *Gpr126* on sagittal sections of an E12.5 WT embryo. High power magnification views corresponding to boxed areas are displayed on the right, as insets of the heart (b), vertebral bodies (b') and lungs (b''). Scale bars, 100 µm (low magnification and insets excluding b''); 50 µm (b'' inset).

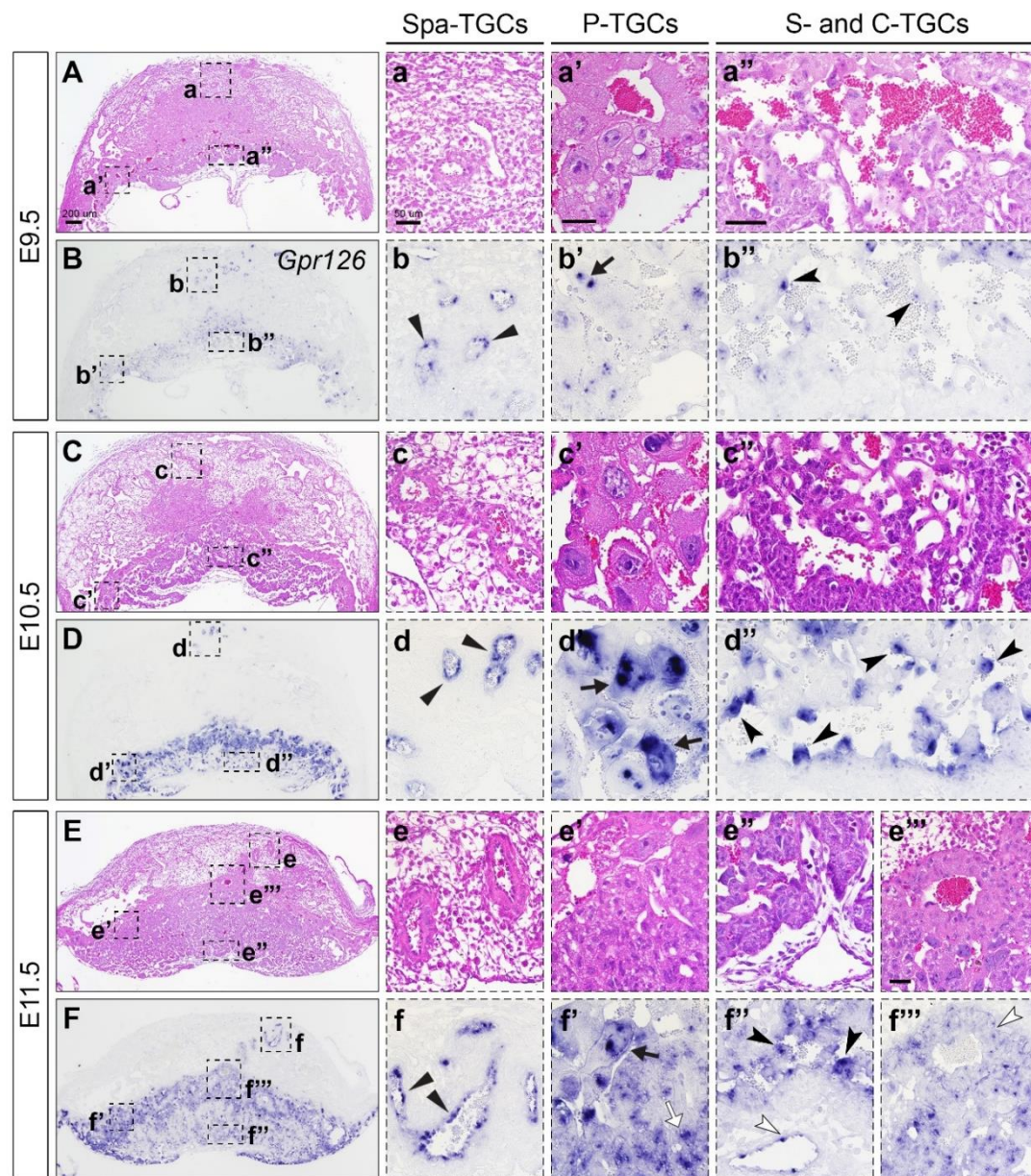


Figure 27. Analysis of *Gpr126* expression pattern in the mouse placenta. (A-f'') H&E staining (A-a'', C-c'', E-e'') and ISH analysis of *Gpr126* (B-b'', D-d'', F-f'') on sagittal sections of E9.5 (A-b''), E10.5 (C-d'') and E11.5 (E-f'') WT placentas. High power magnification views corresponding to boxed areas are displayed on the right, as insets of the Spa-TGCs (a-f, where gene expression is indicated with black arrowheads), P-TGCs (a'-f', where gene expression is indicated with black arrows), S-TGC (a''-f'', where gene expression is pointed with black dog arrowheads) and C-TGCs (e'''-f''', where gene expression is shown white dog arrowheads). Scale bars, 200 μ m (low magnification); 50 μ m (insets).

***Gpr126* expression in the placenta is crucial for embryonic survival**

To determine the contribution of the placenta to the *Gpr126*^{Δ7/Δ7} lethal phenotype and specifically dissect the role of *Gpr126* in the development of the embryo proper, we bred mice bearing the conditional *Gpr126*^{fl^{ox}} allele with the *Sox2-Cre* driver line (Hayashi et al., 2002). The *Sox2-Cre* promoter drives recombination in the epiblast cells that give rise to the entire embryo, as well as in the extraembryonic mesoderm that forms the fetal vasculature in the placental labyrinth, but not in the trophoblast-derived cells of the placenta nor the visceral yolk sac endoderm (Hayashi et al., 2002; Tallquist and Soriano, 2000). Thus, we initially crossed *Gpr126*^{fl/fl} females with *Gpr126*^{fl/+}; *Sox2*^{Cre/+} males to produce an embryonic-specific deletion of *Gpr126*, while leaving heterozygous expression in the extraembryonic trophoblast compartment (Fig. 28A). If placental defects were the cause of *Gpr126*^{Δ7/Δ7} embryonic lethality, we would expect survival of the *Gpr126*^{KO/fl}; *Sox2*^{Cre/+} offspring past E12.5, a stage when the standard knockout is already dead. Indeed, 73% of these mutants were viable beyond E12.5 and 64% survived to birth (Suppl. Table 16). However, mutant pups associated with a heterozygous placenta were distinguishable by their smaller size, stiff joint contractures of the forelimbs and hindlimbs, and the inability to maintain the balance (Fig. 28B), a phenotype that resembled that of *Gpr126*^{Δ3,4/Δ3,4} mutants (Fig. 13G). Histological analysis of mutant embryonic hearts at E16.5 revealed no evidence of morphological defects (Fig. 28C-D''). Examination at postnatal stages (P1) also showed normal heart structure, but the global size appeared to be reduced compared to heterozygous siblings (Fig. 28E-F''), likely because mutant embryos are also substantially smaller. These results demonstrated that embryonic *Gpr126* function is essential for peripheral nervous system development, whilst its extraembryonic function sustains embryonic progression.

To confirm these results, we took advantage of the different Cre recombination activity depending on whether it is transmitted from the female or the male parent. In contrast to the paternal inheritance of the *Sox2-Cre* transgene, the maternal transmission leads to Cre activity in all the progeny, including extraembryonic tissues, since the Cre is active in the female germline and the encoded protein can persist in the early embryo (Hayashi et al., 2003) (Fig. 28G). Accordingly, the reciprocal cross of *Gpr126*^{fl/fl} males with *Gpr126*^{fl/+}; *Sox2*^{Cre/+} females generates null animals lacking *Gpr126* expression in both embryonic and extraembryonic tissues, regardless of the presence of the *Cre* transgene. As a result, the percentage of expected homozygous mutants was increased from 25% to 50%. As predicted, we observed that homozygous offspring for the *Gpr126*^{fl^{ox}} allele (referred to as *Gpr126*^{KO/KO} owing to global recombination), phenocopied standard *Gpr126*^{Δ7/Δ7} mutant embryos and did not survive past E12.5 (Suppl. Table 17). Only 2 out of 10 homozygous embryos lacking the *Cre* transgene were found alive at E15.5, presumably due to variable post-zygotic transmission of the Cre protein between littermates.

4. RESULTS

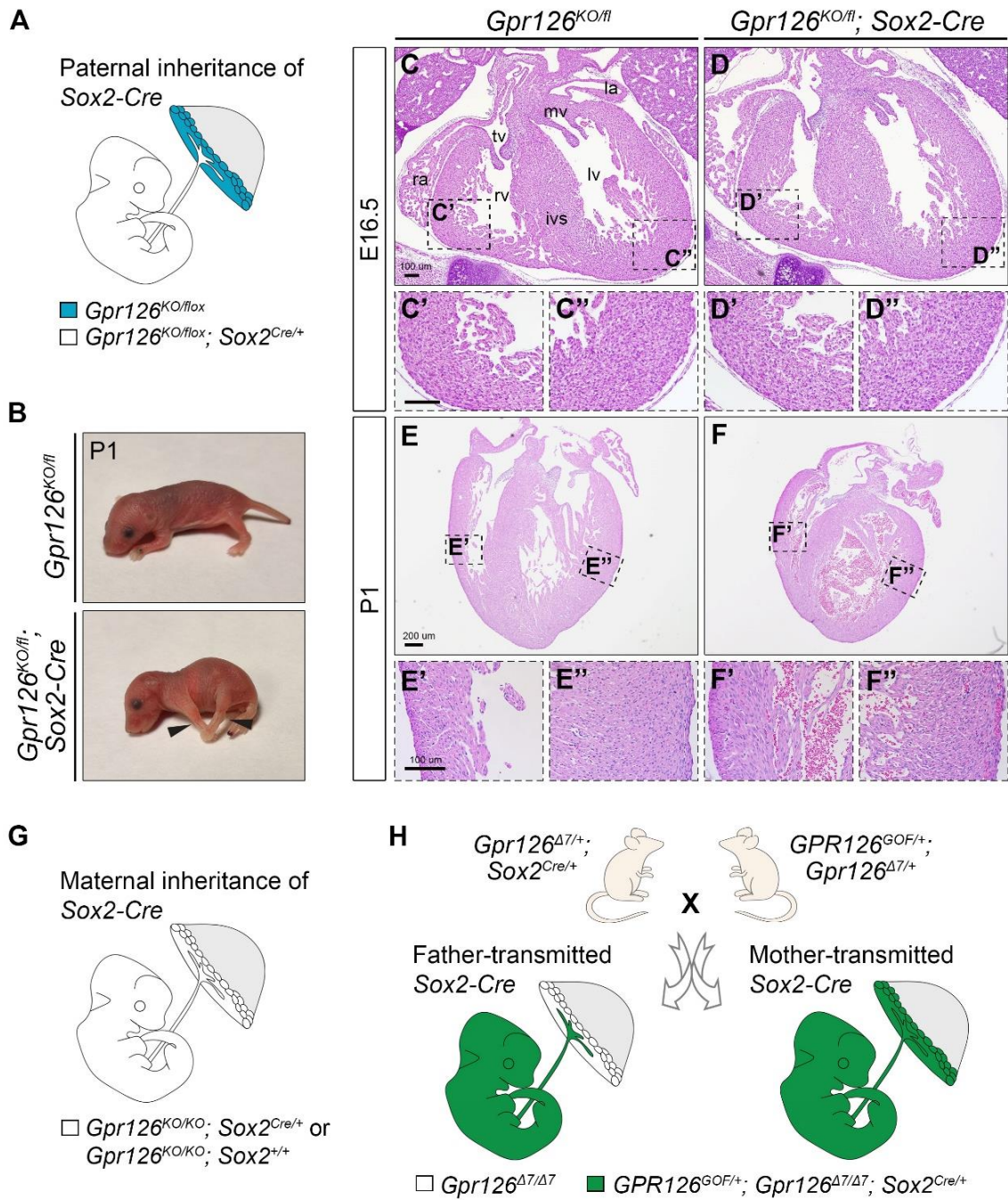


Figure 28. Dissection of embryonic and trophoblast-induced effects of *Gpr126* mutation. (A) Schematic representation of the embryonic and extraembryonic genetic constitution of *Gpr126^{fl/fl}; Sox2-Cre* embryos when the *Sox2-Cre* transgene is inherited paternally. The Cre is active in the epiblast and extraembryonic mesoderm, but not in the trophoblast nor the visceral yolk sac endoderm. (B) Images of *Gpr126^{KO/fl}* and *Gpr126^{KO/fl}; Sox2-Cre* animals at P1. Arrowheads point to joint contractures in the forelimbs and hindlimbs of the mutants. (C-D'') H&E staining of transversal heart sections from *Gpr126^{KO/fl}* (C-C'') and *Gpr126^{KO/fl}; Sox2-Cre* mutant embryos (D-D'') at E16.5. (E-F'') H&E staining of transversal heart sections from *Gpr126^{KO/fl}* (E-E'') and *Gpr126^{KO/fl}; Sox2-Cre* mutant embryos (F-F'') at P1. Boxed areas of the right ventricle are magnified in ('), and boxed areas of the left ventricle are shown in (''). ivs, interventricular septum; la, left atrium; lv, left ventricle; mv, mitral valve; ra, right atrium; rv, right ventricle; tv, tricuspid valve. Scale bars, 100 μ m. (G) Schematic showing the breeding strategy to obtain *GPR126^{GOF/+}; Gpr126 ^{$\Delta 7/\Delta 7$} ; Sox2^{Cre/+}* embryos. The parental origin of the *Cre* transgene will determine whether *GPR126^{GOF}* overexpression takes place only in the epiblast (paternal inheritance) or widespread in embryonic and extraembryonic tissues (maternal inheritance).

To support the notion that *Gpr126* is required in the mouse placenta, we investigated whether transgenic overexpression of *GPR126* in the epiblast-derived cells failed to rescue the lethal defects of *Gpr126 ^{$\Delta 7/\Delta 7$}* mutants. To this end, we bred double heterozygous *R26-GPR126^{GOF/+}; Gpr126 ^{$\Delta 7/+$}* females to double heterozygous *Gpr126 ^{$\Delta 7/+$} ; Sox2^{Cre/+}* males, and contrariwise, to obtain *R26-GPR126^{GOF/+}; Gpr126 ^{$\Delta 7/\Delta 7$} ; Sox2^{Cre/+}* embryos. In the *Gpr126 ^{$\Delta 7/\Delta 7$}* mutant background, offspring inheriting *Sox2-Cre* paternally will overexpress *R26-GPR126^{GOF}* in the embryo, whereas maternal inheritance will allow overexpression also throughout the trophoblast-derived cells of the placenta (Fig. 28H). No viable heterozygous *GPR126^{GOF/+}* embryos associated with a *Gpr126 ^{$\Delta 7/\Delta 7$}* mutant placenta were recovered beyond E12.5 (Suppl. Table 18), indicating that abrogation of *Gpr126* expression in the trophoblast lineage accounts for the lethality of *Gpr126 ^{$\Delta 7/\Delta 7$}* embryos. Although the opposite mating is still ongoing, we speculate that heterozygous *GPR126^{GOF/+}* embryos associated with a heterozygous *GPR126^{GOF/+}* placenta will develop normally and survive to birth, so that that Cre-mediated restoration of *GPR126* levels in the trophoblast lineage would rescue the lethal embryonic condition of the *Gpr126 ^{$\Delta 7/\Delta 7$}* animals, while its expression in the epiblast lineage would prevent myelination defects distinctive of these mutants.

Collectively, these data demonstrate that loss of *Gpr126* expression in trophoblast cells underlies the embryonic lethality and secondary heart defects of *Gpr126 ^{$\Delta 7/\Delta 7$}* null mutants.

***Gpr126* is required for glycogen accumulation in the placenta**

Expression of *Gpr126* in the trophoblast lineage of the placenta and embryonic lethality resulting from loss of *Gpr126* function in this organ demonstrates that *Gpr126*^{Δ7/Δ7} lethality is associated with a defective placenta. To address how *Gpr126* signaling contributes to placental development, we first examined the morphology of *Gpr126*^{Δ7/Δ7} mutant placentas at E11.5, before embryonic death occurs. Histological examination by H&E revealed grossly normal organization of the three main layers of the mature placenta: the outer maternal decidua basalis, that contains spiral arteries providing maternal blood to the placenta, the junctional zone consisting of SpTs, GlyTs and P-TGCs that line the implantation site, and the innermost labyrinth, the main site of nutrient and gas exchange between fetal and maternal blood compartments (Fig. 29A-B).

One of the main functions of the junctional zone is to act as an energy supplier for the embryo, through the accumulation of glycogen deposits in the cytoplasm of GlyT cells. Thus, we next evaluated the energy storage capacity of *Gpr126*^{Δ7/Δ7} mutant placentas using Periodic acid–Schiff (PAS) staining, which allows visualization of glycogen deposits in magenta. At E11.5, PAS-positive areas were abundantly observed throughout the junctional zone and forming wrapping layers around maternal spiral arteries in the decidua (Fig. 29C, D). At higher magnification, we also detected a large number of glycogen granules in the cytoplasm of small round cells in the decidua (Fig. 29C', D'), and clusters of GlyT all along the junctional zone, clearly recognizable by their “foamy” appearance due to the presence of large vacuoles storing glycogen (Fig. 29C'', D''). Since the boundary between the junctional zone and the PAS-negative labyrinth was clearly defined with this staining, we quantified the PAS-positive area in the outer placental zone, which encompass the junctional zone and the maternal decidua, and found it significantly decreased in *Gpr126*^{Δ7/Δ7} mutants (Fig. 29E). These results indicate that placental glycogen storage is impaired in *Gpr126*^{Δ7/Δ7} mutants, likely reflecting that *Gpr126* signaling is essential for normal differentiation and invasion of GlyT cells.

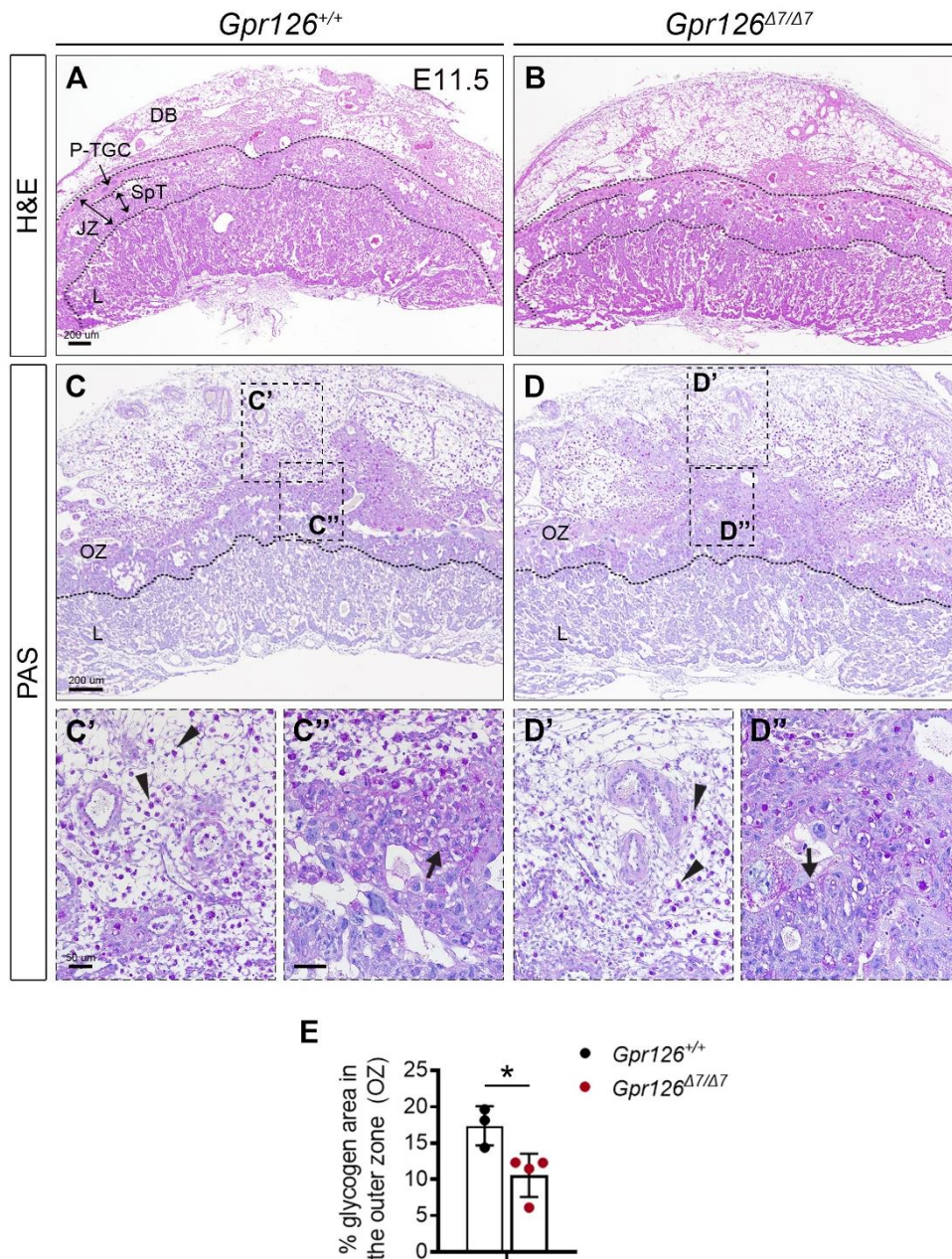
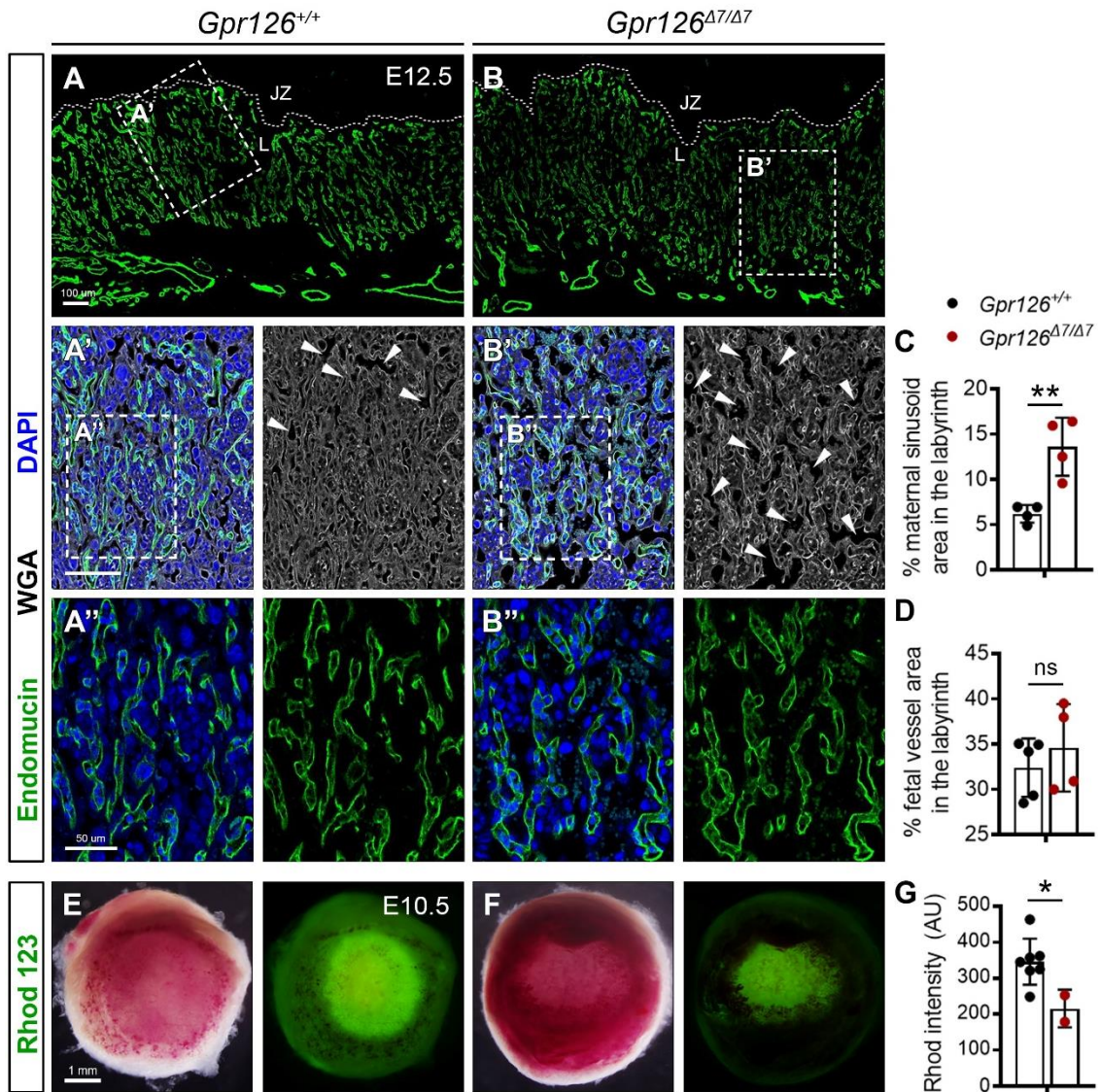


Figure 29. Analysis of *Gpr126*^{Δ7/Δ7} placentas by H&E and PAS staining. (A-D'') H&E staining (A, B) and PAS staining (C-D'') of E11.5 *Gpr126*^{+/+} and *Gpr126*^{Δ7/Δ7} sagittal placental sections. The black dotted lines delineate the different placental layers. (C', D') Insets of the maternal decidua, in which cytoplasmatic glycogen stores are indicated with arrowheads. (C'', D'') Insets of the junctional zone, in which vacuolated glycogen stores are indicated with arrows. Scale bars, 200 μm (low magnification); 50 μm (insets). DB, decidua basalis; JZ, junctional zone; L, labyrinth; OZ, outer zone; P-TGC, parietal trophoblast giant cells; SpT, spongiotrophoblast. (E) Quantification of the PAS-stained glycogen trophoblast area in relation to the total outer zone (OZ) area, which includes the junctional zone and the maternal decidua, in E11.5 *Gpr126*^{+/+} and *Gpr126*^{Δ7/Δ7} placentas. Data are represented as mean ± SD (n= 3 *Gpr126*^{+/+} and 4 *Gpr126*^{Δ7/Δ7} placentas). Statistical significance was determined by unpaired Student's *t*-test (**P* < 0.05).

***Gpr126*^{Δ7/Δ7} mutant placentas show maternal vascular abnormalities in the labyrinth**

The labyrinth zone is the site of nutrient and gas exchange between maternal and fetal circulatory systems and relies on a delicate balance between fetal metabolic demands and the capacity of the placenta to meet that need. Defects in labyrinth formation and disruption of this balance stand out as a leading cause of placental failure and fetal growth restriction and death (Watson and Cross, 2005; Woods et al., 2018). The crucial role of the labyrinth layer for sustaining embryonic development, together with *Gpr126* expression in the S-TGC within this compartment, prompted us to examine the labyrinth organization of *Gpr126*^{Δ7/Δ7} mutant placentas. Immunostaining for endomucin, labeling fetal endothelial cells, revealed an intricate vascular branching at E12.5 similar to WT littermates (Fig. 30A-B''), indicative of normal invasion and branching of the fetal vasculature. However, closer examination showed an aberrant labyrinth architecture in *Gpr126*^{Δ7/Δ7} mutants concerning maternal vascular abnormalities (Fig. 30A', B'). The plasma membrane marker WGA (Wheat germ agglutinin) facilitated visualization of maternal blood sinusoids, which contained small enucleated erythrocytes, and their distinction from fetal blood vessels, which are endomucin-positive and comprise nucleated red blood cells (Fig. 30A'', B''). In contrast to the compact and continuous intermingle of maternal and fetal blood spaces observed in the labyrinth of WT placentas, maternal blood sinusoids were significantly enlarged in the mutants (Fig. 30A', B', C). However, the overall distribution and shape of fetal vessels appeared to be similar in control and mutant placentas (Fig. 30A'', B'', D). The increase in the size of maternal sinusoids may diminish the surface area available for material exchange between maternal and fetal blood niches.

For the overall visualization of blood pools in the placental labyrinth, we injected the fluorescent dye rhodamine 123 into pregnant females and analyzed the fluorescence intensity derived from dye accumulation in WT and mutant placentas at E10.5, prior to embryonic lethality. *Gpr126*^{Δ7/Δ7} placentas displayed an increase of blood accumulation in the labyrinth leading to large opaque areas, whereas control placentas presented disperse blood spots allowing greater fluorescence intensity (Fig. 30E, F, G). Altogether, these data indicate that *Gpr126* plays a role in the organization of the trophoblast-lined maternal sinusoid spaces during placental development.



Placental transport is unaffected in *Gpr126*^{Δ7/Δ7} placentas

To determine whether maternal sinusoids expansion accounted for an inefficient exchange of gases between oxygenated maternal blood and deoxygenated fetal blood, we assessed hypoxia levels in *Gpr126*^{Δ7/Δ7} placentas using the Hypoxyprobe staining. Pimonidazole immunostaining revealed the SpT layer of the junctional zone as the main hypoxic area, although widespread positive staining was also found in the P-TGC layer and the decidua (Fig. 31A-B'), in agreement with previous publications (Dunwoodie, 2009). However, the comparison between WT and *Gpr126*^{Δ7/Δ7} mutant placentas yielded no significant differences in the intensity levels (Fig. 31C) nor the positive area of stain (Fig. 31D), indicating that oxygen delivery to the embryo is not impaired.

Besides oxygen, we also evaluated the maternal-fetal nutrient transport. Glucose is the primary nutrient required for fetal growth, and its uptake from the maternal circulation relies on placental glucose transporters (Winterhager and Gellhaus, 2017). Thus, we analyzed GLUT1 protein expression in mutant placentas, which is the predominant isoform expressed during pregnancy in mice (Das et al., 1998). At E12.5, GLUT1 protein was ubiquitously expressed in the GlyTs invading the decidua, which act as a source of stored energy (Coan et al., 2006), in the SpTs of the junctional zone, and in the two syncytiotrophoblast layers (I and II) of the labyrinth, which mediate trophic exchange between fetal and maternal bloodstreams (Dupressoir et al., 2009) (Fig. 32A-B'). Protein levels appeared to be similar in WT and mutant placentas, suggesting that embryonic lethality is not associated with a reduction in the glucose transport capacity.

Then, we measured transplacental passage efficiency by injecting pregnant females with the fluorescent dye rhodamine 123 and examining embryo fluorescence after two hours. *Gpr126*^{Δ7/Δ7} mutants exhibited similar levels of dye accumulation than WT siblings at E11.5, reinforcing the idea that the labyrinth defects observed in *Gpr126*^{Δ7/Δ7} mutants do not alter the transfer capacity of the placenta (Fig. 32C, D, E). To further corroborate this, we analyzed the expression levels of key markers expressed in the interhaemal membrane, the specialized interface that mediates selective and bidirectional exchange between the fetal and maternal circulations. From the maternal to the fetal side, it consists of a layer of S-TGCs lining maternal sinusoids (*cathepsin Q*, *Ctsq*-positive), two layers of syncytiotrophoblast, being SynT-I (*syncytin a*, *Syna*-positive) and SynT-II (*syncytin b*, *Synb*-positive), and an endothelial cell layer of the fetal blood vessels (*mesoderm specific transcript*, *Mest*-positive) (Woods et al., 2018) (Fig. 32F). Indeed, qRT-PCR analysis revealed no differences in gene expression for all these markers between WT and *Gpr126*^{Δ7/Δ7} placentas (Fig. 32G), likely reflecting an adequate placental transport.

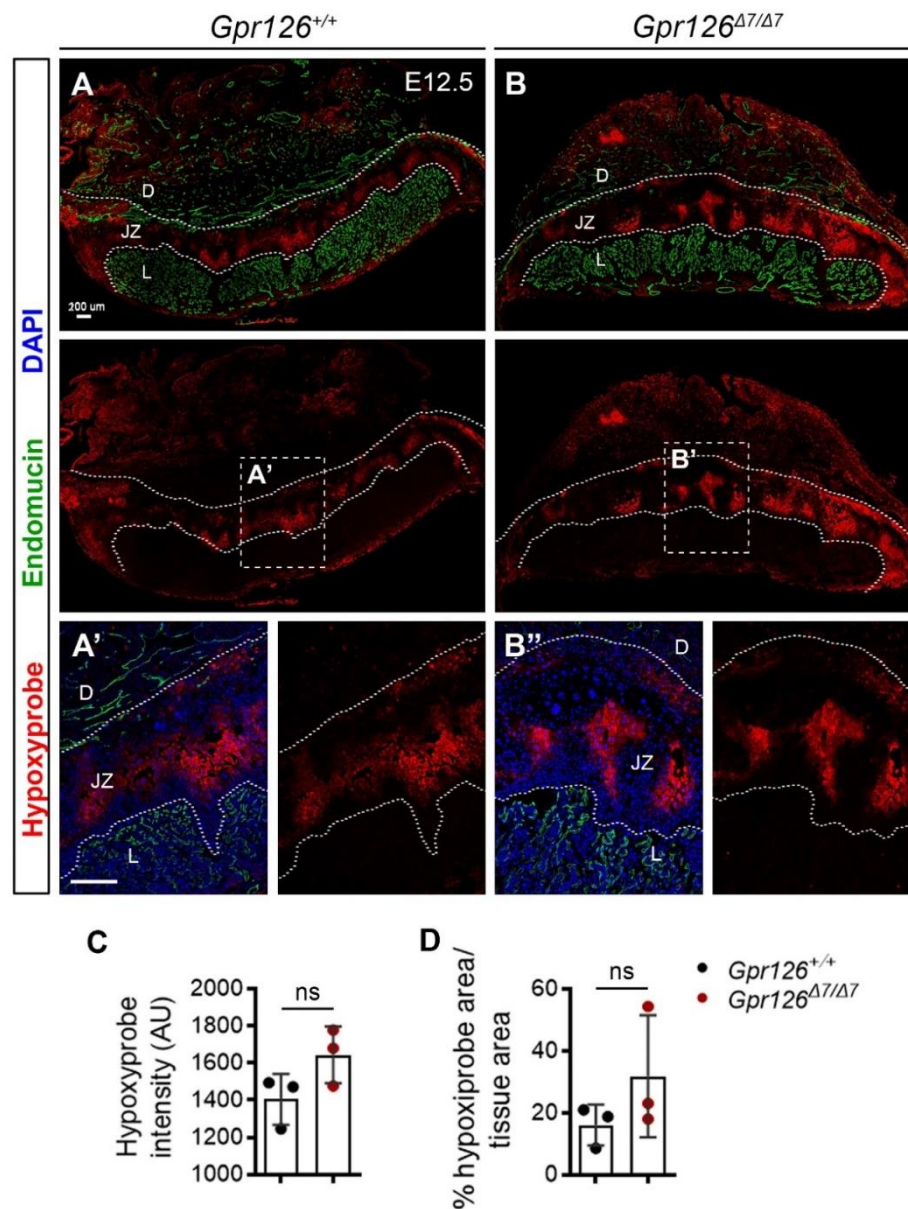


Figure 31. Analysis of placental hypoxia in *Gpr126*^{Δ7/Δ7} mutants. (A-B') Hypoxyprobe labeling (red) of E12.5 *Gpr126*^{+/+} (A, A') and *Gpr126*^{Δ7/Δ7} (B, B') sagittal placental sections. Sections were counterstained with endomucin (green) and DAPI (blue). Higher magnification views of boxed areas are shown on the right (*). The white dotted lines in (A, B) delineate the decidua (D), junctional zone (JZ) and labyrinth (L) layers. Scale bars, 200 μm. (C, D) Quantification of Hypoxyprobe mean thresholded intensity levels (AU) (C) and of the area occupied by the Hypoxyprobe positive staining as a proportion of the total placental area (ratio) (D) in E12.5 *Gpr126*^{+/+} and *Gpr126*^{Δ7/Δ7} placentas. Data are represented as mean ± SD (n= 3 *Gpr126*^{+/+} and 3 *Gpr126*^{Δ7/Δ7} placentas). Statistical significance was determined by unpaired Student's t-test (ns, not significant).

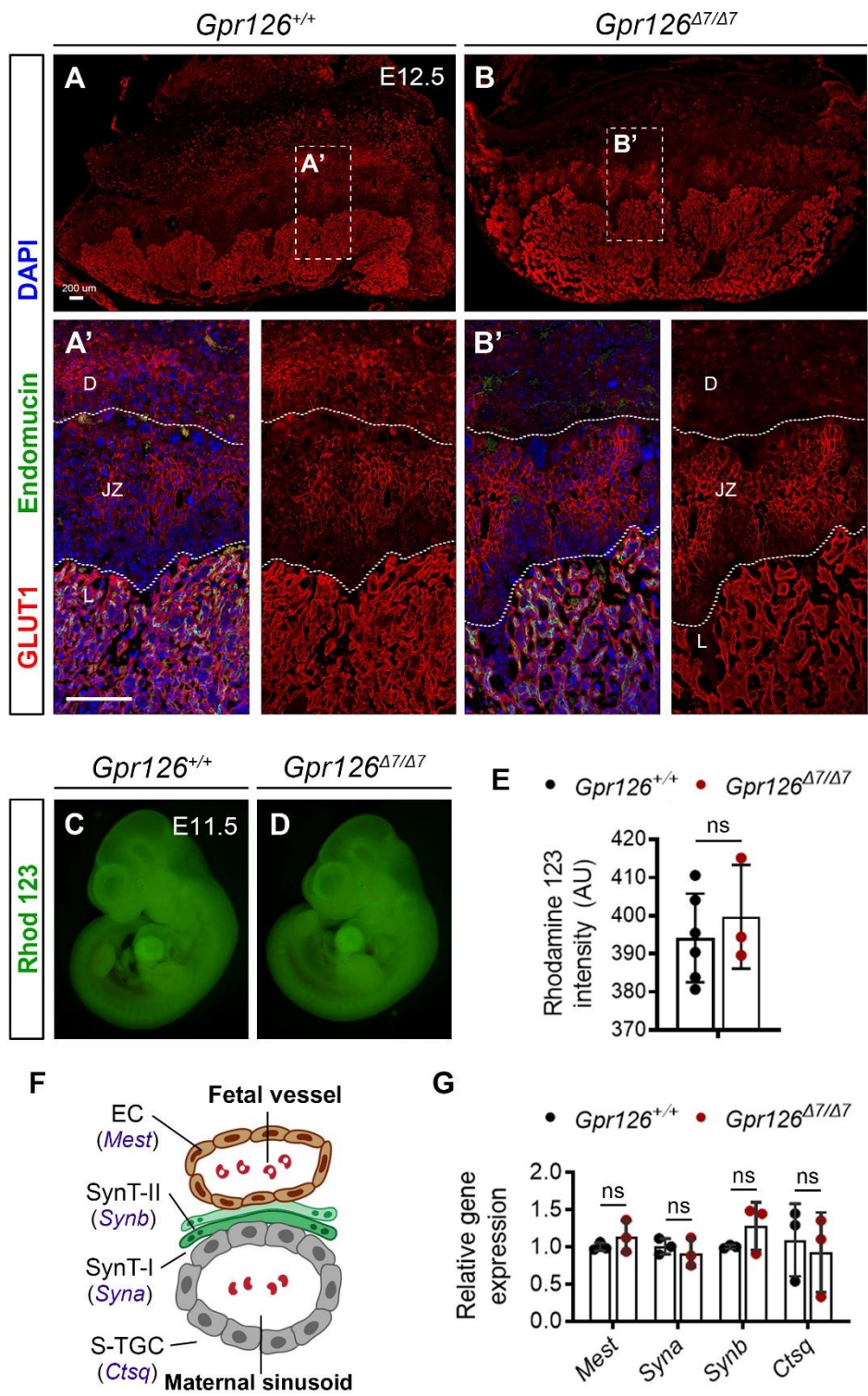


Figure 32. Analysis of placental nutrient transport in *Gpr126*^{Δ7/Δ7} mutants. (A-B') IHC for the glucose transporter GLUT1 (red) and the endothelial marker endomucin (green) of E12.5 *Gpr126*^{+/+} (A, A') and *Gpr126*^{Δ7/Δ7} (B, B') sagittal placental sections. DAPI was used for counterstaining (blue). Higher magnification views of boxed areas are shown beneath in ('). The white dotted lines in (A, B) delineate the decidua (D), junctional zone (JZ) and labyrinth (L) layers. Scale bars, 200 μm. (C, D) Whole-mount images of the transplacental passage of rhodamine 123 in E11.5 *Gpr126*^{+/+} (C) and *Gpr126*^{Δ7/Δ7} (D) embryos. (E) Quantification of rhodamine 123 fluorescence intensity (AU) in E11.5 *Gpr126*^{+/+} and *Gpr126*^{Δ7/Δ7} embryos. Data are represented as mean ± SD (n= 6 *Gpr126*^{+/+} and 3 *Gpr126*^{Δ7/Δ7} embryos). Statistical significance was determined by unpaired Student's *t*-test (ns, not significant). (F) Cartoon illustrating the interhemal barrier separating fetal blood vessels (containing nucleated red blood cells) and maternal sinusoids (filled with anucleated red blood cells). EC, endothelial cells; SynT-II, syncytiotrophoblast II; SynT-I, syncytiotrophoblast I; S-TGC, sinusoidal trophoblast giant cells. (G) qRT-PCR showing relative gene expression of the fetal endothelial marker *Mest*, the syncytiotrophoblast markers *Syna* and *Synb*, and the S-TGC marker *Ctsq* shown in (F) from E11.5 *Gpr126*^{+/+} and *Gpr126*^{Δ7/Δ7} placentas. *B-actin* was used as a housekeeping gene. Data are means ± SD (n= 3 WT and 3 mutant placentas). Statistical significance was determined by unpaired Student's *t*-test (ns, not significant).

***Gpr126*^{Δ7/Δ7} mutants show downregulation of placental cathepsins**

Because *Gpr126* is expressed in the four TGC subtypes and the SpT, we next asked whether *Gpr126* signaling was instrumental for the development and/or differentiation of these placental cell populations, each having specialized functions during pregnancy. By E12.5, these trophoblast cells can be readily distinguished by their spatial localization and gene expression profiles (Simmons et al., 2007) (Fig. 33A). Thus, to study the effect of *Gpr126* mutation on the differentiation of the trophoblast lineage, we conducted a comprehensive gene expression analysis of known cell-type-specific markers in *Gpr126*^{Δ7/Δ7} placentas.

First, we confirmed by qRT-PCR the downregulation of *Gpr126* transcripts in *Gpr126*^{Δ7/Δ7} mutant placentas (Fig. 33B). Next, we examined the expression levels of several hormones and cytokines that are produced by TGCs for the maintenance of the fetal-maternal interface and regulation of maternal adaptations to pregnancy. Some members belong to the prolactin (also known as placental lactogen or prolactin-like protein gene family (PRL/PL/PLP) (Wiemers et al., 2003), like *Prl8a2* (also termed *decidual trophoblast prolactin-related protein*, *Dtprp*), which is located in the uterine decidua; *Prl2c2* (also termed *proliferin*, *Plf*), which is expressed by Spa-TGCs and C-TGCs; *Prl3b1* (also termed *placental lactogen 2*, *Pl2*), which is expressed by P-, C- and S-TGCs; *Prl3d1* (also termed *placental lactogen 1*, *Pl1*), which is confined in the P-TGCs; and *Prl7b1* (also termed *prolactin-like protein N*, *PlpN*), which is expressed by invasive GlyT and Spa-TGCs (Croy et al., 2014; Simmons et al., 2007; Simmons et al., 2008b). Of them, only *Prl7b1* was downregulated in *Gpr126*^{Δ7/Δ7} placentas (Fig. 33B). Since *Prl7b1* is uniquely

4. RESULTS

expressed by invasive trophoblast cells involved in maternal spiral artery remodeling (Simmons et al., 2008b) and placental-associated adaptations to physiological stressors (Bu et al., 2016), these results suggest a defect in maternal vascular remodeling and sensing pregnancy quality.

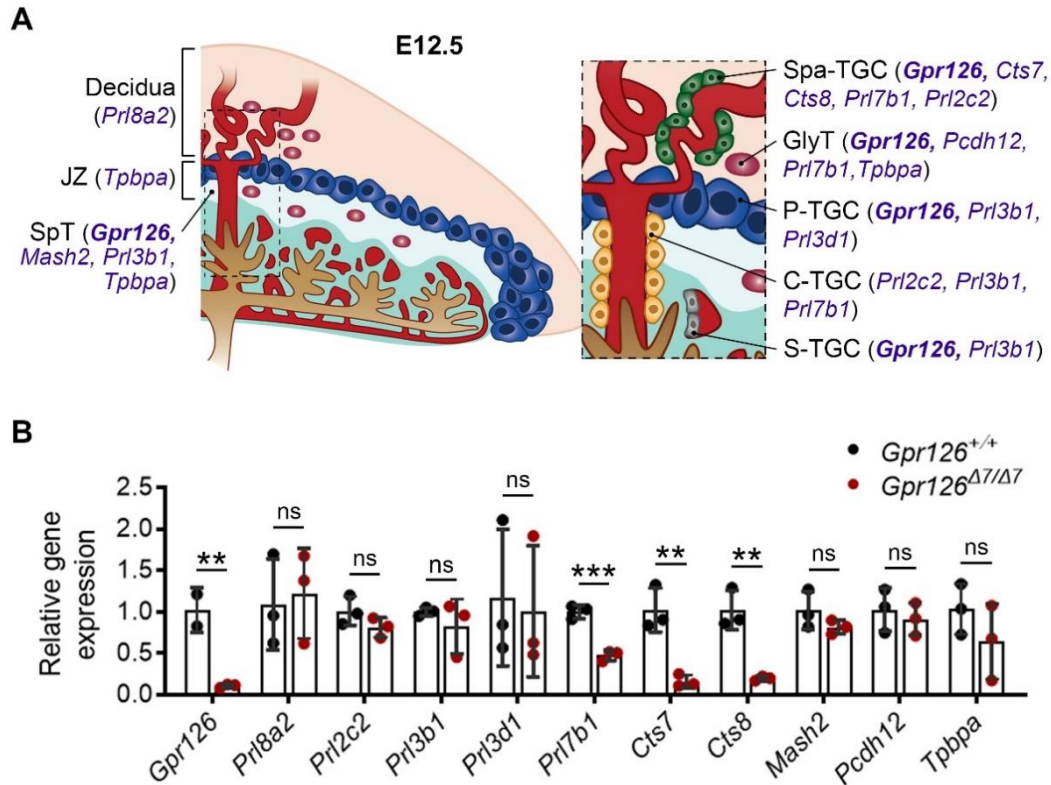


Figure 33. Gene expression analysis by qRT-PCR of trophoblast-subtype associated markers in *Gpr126*^{Δ7/Δ7} placentas. (A) Cartoon illustrating the main structures and cell types of a WT E12.5 mouse placenta and the key marker genes that are expressed in each cell type. Note that family members of the trophoblast giant cell-expressed “prolactin/ placental lactogen/ prolactin-like protein” genes are also known as follows: *Pr13d1*=*Pl1*, *Pr13b1*=*Pl2*, *Pr12c2*=*Plf*, *Pr18a2*=*Dtprp*, *Pr17b1*=*PlpN*. Spa-TGC, spiral artery-associated trophoblast giant cell; GlyT, glycogen trophoblast cell; P-TGC, parietal trophoblast giant cell; C-TGC, canal trophoblast giant cells; S-TGC, sinusoidal trophoblast giant cells. (B) qRT-PCR showing relative gene expression of key markers shown in (A) from E11.5 *Gpr126*^{+/+} and *Gpr126*^{Δ7/Δ7} placentas. *B-actin* was used as a housekeeping gene. Data are means ± SD (n= 3 WT and 3 mutant placentas). Statistical significance was determined by unpaired Student's *t*-test (ns, not significant; ***P* < 0.01; ****P* < 0.001).

We also examined placental-specific cathepsins, which are a family of cysteine proteases that are mainly involved in extracellular matrix remodeling and invasion (Rawn and Cross, 2008). Strikingly, *Cts7* and *Cts8*, which are expressed in giant cells that are in direct contact with maternal arteries (Spa-TGCs), show a dramatic decrease of mRNA levels in *Gpr126*^{Δ7/Δ7} placentas compared to WT littermates (Fig. 33B). Since the junctional zone underpins the major origin of

progenitors for invasive trophoblasts, we evaluated expression levels of the SpT marker *Mash2* (also known as *Ascl2*), the GlyT marker *Pcdh12*, and the whole junctional zone marker *Tpbpa*. However, no significant changes were observed in the mutant placentas (Fig. 33B).

Then, to discard the possibility that *Gpr126* deletion affected the spatial localization of trophoblast subtype markers rather than the expression levels, we examined *Prl2c2*, *Mash2*, *Pcdh12* and *Tpbpa* transcripts by ISH analysis on placental sections from E11.5 WT and *Gpr126^{Δ7/Δ7}* mutants. Staining of invading SpA-TGCs by *Prl2c2* revealed thinner spiral arteries in the decidua close to the junctional zone in *Gpr126^{Δ7/Δ7}* placentas, while expression in the C-TGCs appeared to be similar WT littermates (Fig. 34A-B'). The junctional zone, distinguished by expression of *Tpbpa* (Fig. 34C-D'), and specifically the SpT, detected by *Mash2* (Fig. 34E-F'), showed normal patterning in WT and mutant placentas. At E11.5, *Mash2* expression was also detected in the labyrinth trophoblasts (Fig. 34E-F'). Interestingly, we detected that the distinctive wrapping of WT *Pcdh12*-positive GlyT cells around maternal blood spaces was reduced in *Gpr126^{Δ7/Δ7}* placentas (Fig. 34G-H'). Hence, mutant GlyT showed a patchy-like distribution, in contrast to the highly organized layered pattern of WT GlyT. This observation was especially noticeable in the decidua, around maternal spiral arteries (Fig. 34G', H'). As expected, *Gpr126* expression was markedly reduced in *Gpr126^{Δ7/Δ7}* mutant placentas (Fig. 34I-J').

Altogether, our marker gene expression analyses indicate that Spa-TGCs are the only trophoblast subtype exhibiting aberrant gene expression in *Gpr126^{Δ7/Δ7}* placentas. In particular, the dysregulation of placental cathepsins *Cts7* and *Cts8*, which are critical for the remodeling of maternal spiral arteries during pregnancy, suggest a potential requirement of *Gpr126* in controlling this process.

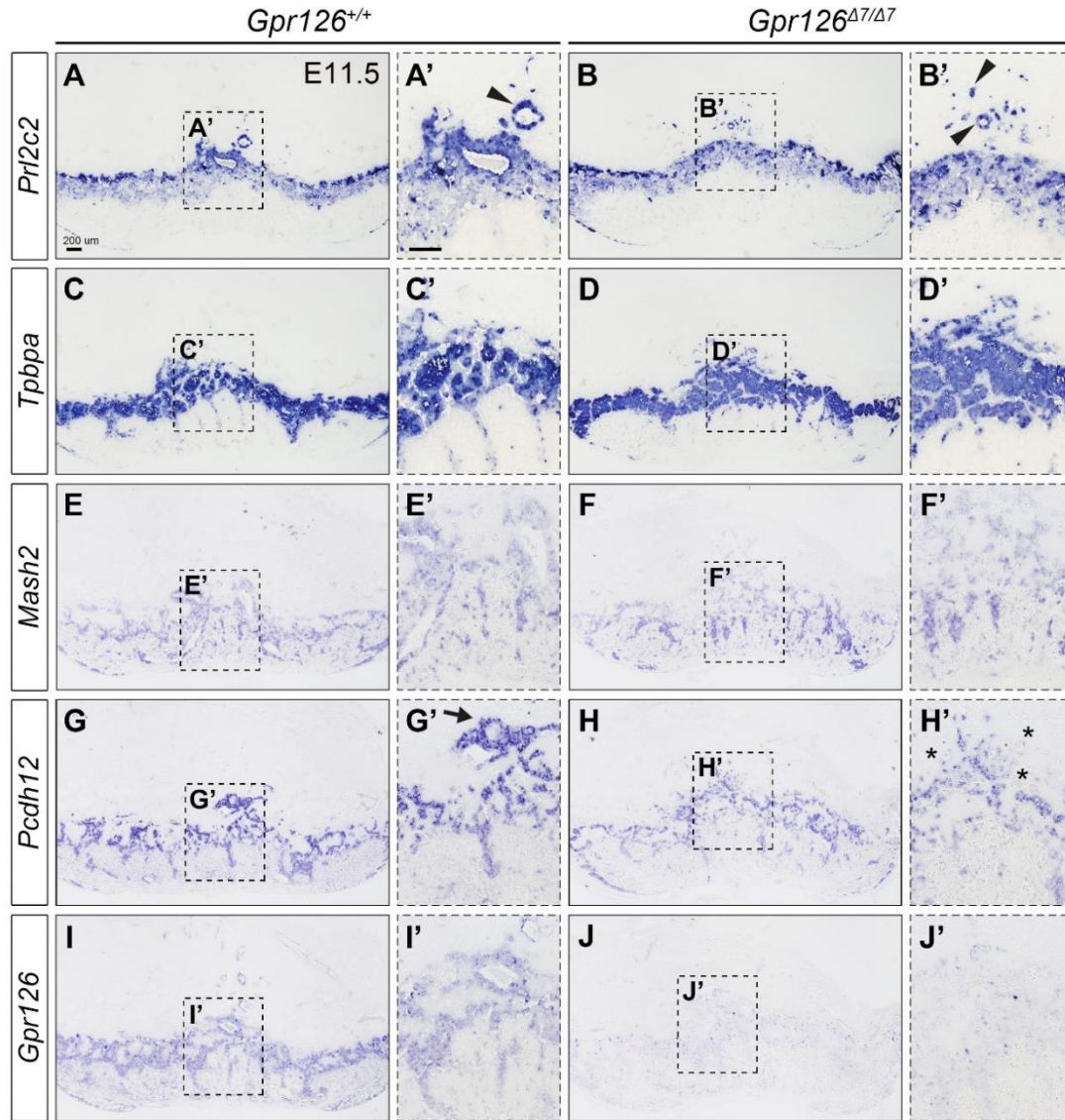


Figure 34. Gene expression analysis by ISH of trophoblast-subtype associated markers in *Gpr126*^{Δ7/Δ7} placentas. (A-J') ISH of *Prl2c2*/*Plf* (A-B'), *Tpbpa* (C-D'), *Mash2*/*Ascl2* (E-F'), *Pcdh12* (G-H') and *Gpr126* (I-J') on sagittal sections of E11.5 *Gpr126*^{+/+} and *Gpr126*^{Δ7/Δ7} placentas WT placentas. High power magnification views corresponding to boxed areas are displayed on the right ('). Arrowheads in (A', B') indicate *Prl2c2*-positive Spa-TGCs; arrows in (G') point to multi-layered expression of *Pcdh-12*-positive Spa-TGCs; asterisks in (H') indicate patchy expression of *Pcdh12*. Scale bars, 200 μm.

Gpr126*^{Δ7/Δ7} placentas show downregulation of the preeclampsia marker *Mmp9

Pregnancy success entails a synchronized cross-talk between the invading fetal trophoblasts and maternal endometrial cells (Croy et al., 2014). This paracrine dialogue involves a fine regulation of a wide range of molecules, and signaling disturbance can lead to pregnancy disorders, like preeclampsia (McMaster and Fisher, 2003). In women, a two-stage disease model has been proposed to describe the pathogenesis of preeclampsia. The first stage involves poor trophoblast invasion, the incomplete vascular remodeling of spiral arteries from small, high-resistance vessels into large, high-capacitance vessels, and the creation of a hypoxic environment. The second stage is manifested as a systemic inflammatory response, endothelial dysfunction, maternal hypertension and proteinuria (Chaiworapongsa et al., 2014; Sones and Davisson, 2016). Thus, to explore whether typical features of preeclampsia were manifested in *Gpr126*^{Δ7/Δ7} mutants, we examined by qRT-PCR the expression levels of a panel of genes previously associated with this syndrome.

First, we focused on the invasive and vascular remodeling capacity of fetal trophoblasts, which depends on the activity of different extracellular proteases, such as matrix metalloproteases (MMPs), ADAMs and cathepsins. *Mmp2* and *Mmp9* are the most abundant gelatinases expressed during trophoblast invasion in humans in early and middle pregnancy, respectively, and reduced expression of *Mmp9* is associated with preeclampsia in mice and humans (Plaks et al., 2013; Shokry et al., 2009). Although *Mmp2* was expressed at extremely low levels at E11.5 (data not shown), *Mmp9* was significantly downregulated in *Gpr126*^{Δ7/Δ7} mutant placentas (Fig. 35A), indicating a defect in the remodeling of maternal spiral arteries. On the other hand, *Adam17*, whose expression is induced by oxidative stress in preeclamptic placentas (Ma et al., 2011), is normally expressed in our mutants (Fig. 35A). Because invasive trophoblast and decidua cells also express protease inhibitors, such as tissue inhibitors of metalloproteinases (TIMPs) and cystatins (Cts), which are cathepsin inhibitors, we also assessed their transcript levels. In this case, preeclampsia associates with high expression of the inhibitors, resulting in the downregulation of their targets (Gutiérrez et al., 2020). However, *Cst3* (*cystatin C*), *Serpine1* (*serine peptidase inhibitor, clade E, member 1*), and *Timp1* (*tissue inhibitor of metalloproteinase 1*), were normally expressed in mutant placentas compared to their WT siblings (Fig. 35A).

Second, we evaluated the expression levels of several immunomodulators, whose production is altered in preeclampsia due to (at least in part) hypoxia (Keelan and Mitchell, 2007), like the proinflammatory cytokine interleukin 1alpha (*IL-1α*) and the chemokine (C-X-C motif) receptors 4 (*Cxcr4*) and 7 (*Cxcr7*). We did not detect differences between WT and mutant placentas (Fig. 35B). Beyond the inflammatory process, preeclampsia also results in endothelial dysfunction. Placental secretion of endogenous circulating anti-angiogenic factors, such as soluble forms of

vascular endothelial growth factor receptor 1 (sVEGFR1) and endoglin (sENG), is upregulated in preeclampsia. On one hand, sVEGFR1 binds and neutralizes the proangiogenic effect of vascular endothelial growth factor (VEGF-A) and placental growth factor (PGF), by reducing their bioavailability and preventing their interaction with endogenous receptors (Kendall and Thomas, 1993). On the other hand, sEng does likewise by binding to TGF- β 1 (Venkatesha et al., 2006). Decreased VEGF-A, PGF, and TGF- β 1-mediated signaling results in the downregulation of the endothelial nitric oxide synthase (eNOS), which is responsible for the production of nitric oxide, a potent vasodilatory factor necessary for the maintenance of endothelial function and integrity (Sanchez et al., 2014; Wang et al., 2009). These alterations lead to impaired endothelium-dependent vasorelaxation and increased endothelial permeability, clinically manifested as hypertension and proteinuria, respectively (Khan et al., 2005). However, all these preeclampsia markers did not show significant changes in *Gpr126* ^{Δ 7/ Δ 7} placentas compared to WT littermates (Fig. 35C), suggesting normal vascular homeostasis at E11.5.

Finally, we analyzed the expression levels of some genes recently reported to be dysregulated in placenta samples from women with preeclampsia due to abnormal placental imprinting, including distal-less homeobox 5 (*Dlx5*), GATA binding protein 3 (*Gata3*) and apolipoprotein B mRNA editing enzyme, catalytic polypeptide 2 (*Apobec2*) (Zadora et al., 2017). None of the genes was dysregulated either in *Gpr126* ^{Δ 7/ Δ 7} placentas (Fig. 35D).

In summary, our gene expression analysis of factors known to play a role in preeclampsia revealed the specific downregulation of *Mmp9* transcripts in *Gpr126* ^{Δ 7/ Δ 7} placentas. This result, along with the pronounced downregulation of placental cathepsins *Cts7* and *Cts8*, suggests that *Gpr126* is implicated in the invasive behavior of trophoblast giant cells and the remodeling of the uterine vasculature by controlling the expression of extracellular proteases.

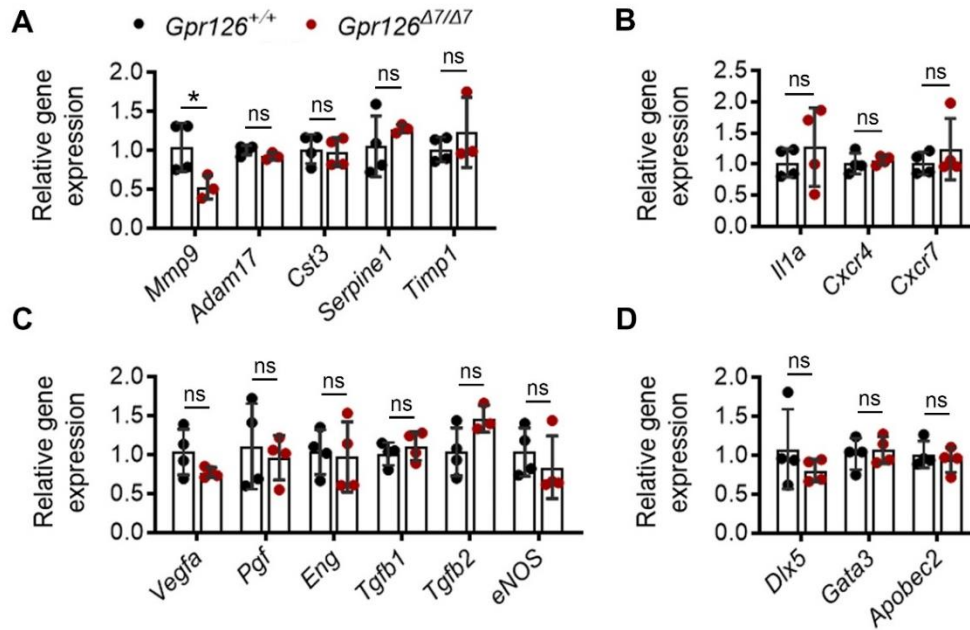


Figure 35. Gene expression analysis of preeclampsia markers in *Gpr126*^{Δ7/Δ7} placentas. (A-D) qRT-PCR showing relative gene expression of known preeclampsia-associated factors, like proteases and protease inhibitors (A), cytokines and chemokine receptors (B), angiogenic/ growth factors (C), and imprinted genes (D) in E11.5 *Gpr126*^{+/+} and *Gpr126*^{Δ7/Δ7} placentas. *B-actin* was used as a housekeeping gene. Data are means ± SD (n= 3 or 4 WT and 3 mutant placentas). Statistical significance was determined by unpaired Student's *t*-test (ns, not significant, **P* < 0.05).

5

DISCUSSION

The results of this doctoral thesis describe a previously unknown role for Gpr126 in the development of the mouse placenta. Previous studies reported its essential function in the peripheral nervous system and heart development in zebrafish and mice (Monk et al., 2009; Monk et al., 2011; Patra et al., 2013; Petersen et al., 2015; Waller-Evans et al., 2010). Although *gpr126* loss of function is compatible with embryo survival in zebrafish (Diamantopoulou et al., 2019; Geng et al., 2013; Leon et al., 2020; Liebscher et al., 2014; Monk et al., 2009; Paavola et al., 2014; Petersen et al., 2015), deletion in mice leads to embryonic lethality, and heart defects were thought to be the major cause of death (Monk et al., 2009; Patra et al., 2013; Waller-Evans et al., 2010). Here, we demonstrate that cardiac abnormalities associated with global Gpr126 inactivation are secondary defects and arise as a result of placental insufficiency, thus highlighting the existence of a critical placenta-heart axis (Camm et al., 2018; Hemberger and Cross, 2001). Using conditional loss-of-function and gain-of-function analysis, we show that heterozygous and homozygous embryos associated with *Gpr126* null placentas are dead after E12.5, like global knockouts, while homozygous embryos with a heterozygous placenta survive to birth. Thus, restoring Gpr126 function in the trophoblast lineage is sufficient to rescue the embryonic lethality of homozygous mutants, which does not occur because of heart defects. Instead, heart defects arise as a consequence of abnormal placental development and function. Interestingly, the adhesive CUB and PTX domains within the NTF, encoded by exons 3 and 4, are dispensable for this extraembryonic function, but critical in the embryo for PNS myelination. Besides, our data demonstrate that Gpr126 is dispensable for heart development not only in mice but also in zebrafish. Strikingly, larvae bearing a homozygous deletion in the *gpr126* promoter or a PTC in exon 10, survive to adulthood and do not exhibit trabeculation defects as it was previously described in morphants (Patra et al., 2013). In contrast, they have swollen ears, resembling other previously characterized *gpr126* zebrafish mutants.

We report *Gpr126* expression in the SpT and the four different TGC subtypes (Spa-TGCs, P-TGCs, C-TGCs, and S-TGCs) of the mouse placenta, and provide evidence for its role in the organization of the maternal blood spaces in the labyrinth, and vascular remodeling in the decidua. Hence, maternal sinusoids were abnormally enlarged in *Gpr126*-deficient placentas, resulting in enhanced accumulation of maternal blood in the labyrinth. This phenotype is accompanied by impaired maternal spiral artery remodeling, supported by the downregulation of different extracellular proteases, such as *Mmp9* and placental cathepsins *Cts7* and *Cts8*, and the abnormal distribution of GlyT around maternal spiral arteries, which leads to the persistence of vascular smooth muscle cells in their walls. It is well established that incomplete vascular remodeling of the uterine spiral arteries by trophoblasts is a crucial contributing factor to preeclampsia, a major complication of pregnancy, albeit the exact pathophysiology of this syndrome remains poorly understood. Thus, our results support Gpr126 as a key regulator of spiral artery remodeling in the

placental bed, whose expression is a prerequisite for normal protease function and maternal physiological adaptation to pregnancy. Consistent with our findings, a recent publication reported that *GPR126* expression was altered in pre-eclamptic human placentas (Zadora et al., 2017), which provides significant value to this mouse model not only for investigating and expanding the current knowledge about the etiology of preeclampsia, but also for the potential therapeutic implications in human disease.

The major findings and relevant suggestions drawn from this research are addressed in greater detail in the following subsections.

The CUB and PTX domains of *Gpr126* are essential for PNS development in mice

Although the majority of *Gpr126* studies have been carried out using the zebrafish model, Kelly Monk's group characterized for the first time the role of *Gpr126* in myelination and other aspects of peripheral nerve development in mammals. Using *Gpr126* knockout mice from Lexicon/Taconic, in which exons 3 and 4 (termed 2 and 3 in the original publication) are replaced by a β -geo-puromycin selection cassette, only 7.8% of homozygous mutants survived to birth. These pups were distinguishable from their WT and heterozygous littermates by abnormal joint contractures of the forelimbs and hindlimbs, uncoordinated locomotion, and died between P8 and P16 (Monk et al., 2011). Interestingly, *Gpr126* ^{$\Delta 3,4/\Delta 3,4$} mutants recapitulate the same phenotype as early as birth but were viable during embryonic development. Contracted joints were apparent in the limbs, leading to mobility difficulties, but also in the jaw, thus impeding proper feeding. To prevent animal suffering, mutant pups were sacrificed at P2 at the latest, and the postnatal period of lethality could not be determined. Since both mouse models have been obtained on the same mixed background (129/SvEv-C57BL/6), the differences in the *Gpr126* targeting strategy might explain why *Gpr126* ^{$\Delta 3,4$} deletion is not embryonically lethal and mutant mice are born in the expected Mendelian ratios. Unlike the *Gpr126*^{-/-} mutant allele from Lexicon Pharmaceuticals, which is a null allele due to the insertion of a selection cassette, the *Gpr126* ^{$\Delta 3,4$} allele lacks exons 3 and 4, likely encoding a shorter truncated protein without the CUB and PTX domains. As expected, *Gpr126*^{*fl/fl*}; *Sox2-Cre* mutant pups, in which *Gpr126* expression has been ablated in the epiblast derivatives contributing to the embryo, phenocopied the same joint stiffness defects. Since embryonic lethality of global *Gpr126* null knockouts is caused by placental dysfunction (see *Discussion* subsection below), the fact that constitutive deletion of exons 3 and 4 can circumvent that embryonic lethality reveals a distinct domain-dependent signaling mechanism in the embryo and the placenta. Thus, our work confirms the previous finding that *Gpr126* signaling is essential for myelination in the mammalian PNS, and demonstrates that the CUB and PTX

domains are essential for this function in the embryo proper, but dispensable in the extraembryonic tissue for embryonic progression.

Previous findings identified type IV collagen as an activating ligand for Gpr126, which specifically binds the CUB/PTX-containing region of zebrafish gpr126 *in vitro* (Paavola et al., 2014). This interaction results in the activation of gpr126 signaling and a cAMP second-messenger cascade that serves as a readout of G-protein activation. Since Schwann cell myelination is dependent on gpr126 activation and the secretion of type IV collagen to the basal membrane, the authors suggest that they act together to promote myelin synthesis. Nevertheless, this physical binding has not been detected *in vivo*. In a different study, ligand testing was performed using different human IgG Fc-tagged mouse GPR126-NTF constructs on P3 mouse sciatic nerves (containing Schwann cells), but no binding was detected to the CUB and PTX containing GPR126 fragment (Petersen et al., 2015). In contrast, they found Laminin-211 bound C-terminally to the PTX domain, whose interaction with Gpr126 also regulates myelination during Schwann cell development. Besides, a recent study showed that the large extracellular domain of zebrafish gpr126 adopts a close conformation where the most N-terminal CUB domain interacts with the more C-terminal HormR domain. Importantly, the CUB domain contains a calcium-binding site that is essential to mediate the close conformation of the extracellular region and gpr126 function *in vivo*, so that zebrafish mutants for the calcium-binding site show defective SC and ear development. Our analysis suggests that the regulatory function of the CUB domain of Gpr126 in peripheral myelination is conserved in mammals. In addition to the *in vitro* evidence that type IV collagen is an activatory ligand for Gpr126, a subset of CUB domains from other proteins coordinate calcium to mediate ligand-binding (Gaboriaud et al., 2011). These observations raise the question of whether the CUB and PTX domains act as a ligand-binding site necessary for Gpr126 activation in mammalian Schwann cells, or whether they favor a protein conformation necessary for ligand binding, or both. Future studies are required to investigate these possibilities.

Of note, the joint phenotype of *Gpr126* ^{$\Delta 3,4/\Delta 3,4$} and *Gpr126*^{*fl/fl*}; *Sox2-Cre* mutants is reminiscent of human patients with arthrogryposis multiplex congenita (AMC), as Monk's group previously reported for *Gpr126*^{*-/-*} mutants (Monk et al., 2011). AMC is a heterogeneous group of disorders defined by the presence of congenital joint contractures in two or more areas of the body, and is sometimes associated with fetal or neonatal death (Ravenscroft et al., 2015). The incidence is ~1 in 3,000 live births, and it is considered a rare disorder in the National Organization for Rare Disorders (NORD). Interestingly, loss-of-function mutations in *GPR126* have been identified in three consanguineous families that are affected by lethal AMC, providing the first evidence that *GPR126* mutations also disrupt myelination in humans (Ravenscroft et al., 2015). The exact cause of arthrogryposis multiplex congenita (AMC) is not fully understood, but

is thought to be related to decreased fetal movement in the uterus during development, due to genetic and environmental factors (multifactorial inheritance). It is conceivable that abnormal PNS development caused by *Gpr126* abrogation could be the trigger of the diminished fetal movement, resulting in congenital contractures. Hence, the *Gpr126*^{Δ3,4} mouse line could be used as a model to explore the pathogenesis of this complex disorder and to facilitate the development of novel therapeutic approaches in humans. Despite the life span of individuals affected with AMC is often normal (Dubousset and Guillaumat, 2015), it is appealing that in Ravenscroft et al. study, all fetuses and newborns carrying homozygous deleterious mutations in *GPR126* were aborted or dead at birth, concurrent with intrauterine growth retardation or severe preeclampsia (Ravenscroft et al., 2015). Based on our findings, *Gpr126* function in the placenta could apply to humans and be the reason for fetal death, while embryonic function in PNS development could be responsible for the AMC disorder. If applicable, this hypothesis would open an avenue for future research in humans and entails important clinical implications.

Gpr126 is dispensable for heart trabeculation in zebrafish

Previously, it has been suggested that in the heart, the N-terminal fragment of *Gpr126* can function independently of the C-terminal fragment and act in a paracrine fashion to control cardiac trabeculation in zebrafish (Patra et al., 2013). In contrast, our analysis of *gpr126* mutants demonstrates that *gpr126* is dispensable for zebrafish heart development. In collaboration with Prof. Didier Stainier, we generated two different *gpr126* mutant alleles, the *gpr126*^{bns341} and the *gpr126*^{bns342}. Similar to the *Gpr126*^{Δ7} mouse line, the *gpr126*^{bns341} knockout allele lacks exons 7 and 8, and harbors a PTC in exon 10. Contrary to mouse mutants, *gpr126* transcript is detected in homozygous *gpr126*^{bns341} zebrafish, raising the possibility that the resulting truncated protein only contains the signal peptide, CUB and PTX domains. This mutation is comparable to that of *gpr126*^{st86}, which introduces a premature stop codon at position 406 (exon 7) without affecting gene expression (Paavola et al., 2014). The phenotype of homozygous *gpr126*^{bns341} larvae resemble that of *gpr126*^{st86} mutants, hence exhibiting ear defects but normal heart development. Normal trabeculae are formed at 80 hpf and 100 hpf, when trabeculation is already advanced. These results raise the possibility that the CUB and PTX domains alone could be sufficient for heart trabeculation in zebrafish. Nevertheless, the lack of a heart phenotype was also described for homozygous *gpr126*^{bns342} mutants, which lack the promoter region and fail to transcribe *gpr126*. El Brolosy et al. recently published that alleles that fail to transcribe the mutated gene can circumvent transcriptional adaptation mediated by mutant mRNA decay (El-Brolosy et al., 2019). Thus, the *gpr126*^{bns342} mutant allele will prevent the upregulation of potential compensatory gene(s) that could assume the function of the mutated gene. However, one might think that the *gpr126*^{bns341} allele, as it does not lead to mutant mRNA decay, neither will elicit the

transcriptional adaption response. In any case, disruption of *gpr126* expression is also compatible with heart trabeculation and animal survival, as homozygous mutants reach adulthood and are fertile. Like other mutant alleles for *gpr126*, homozygous mutants could be easily identified by the “swollen ear” phenotype. Likely, myelination defects are also present in both *gpr126^{bns341}* and *gpr126^{bns342}* mutants, although this has not been examined.

One explanation for the lack of a heart phenotype in *gpr126^{bns341}* and *gpr126^{bns342}* zygotic mutants is the possible maternal function of *gpr126*. Despite *gpr126* is very lowly expressed until 3 dpf (Harty et al., 2015), some phenotypes caused by loss of maternal gene products into the egg can be manifested beyond the maternal-zygotic transition period (Wagner et al., 2004). This hypothesis has been already tested using the *gpr126^{st86}* zebrafish line, and maternal-zygotic *gpr126^{st86/st86}* mutants also have normal hearts (Paavola et al., 2014). Together with our data, these findings indicate that, in the very hypothetical case that *gpr126* is playing a role in zebrafish heart trabeculation, it is fulfilled by the maternally transmitted CUB and PTX domains of *gpr126*, unlike in mice.

Thus, the only evidence for a role of *gpr126* in zebrafish heart development is based on morpholino experiments (Patra et al., 2013). Despite the large number of zebrafish *gpr126* mutant alleles that have been identified or generated, no cardiac defects have been reported (Diamantopoulou et al., 2019; Leon et al., 2020; Liebscher et al., 2014; Monk et al., 2009; Paavola et al., 2014; Petersen et al., 2015). These discrepancies between mutants and morpholino-induced phenotypes do not represent an isolated case. A comparison of published morphant defects with the Sanger Zebrafish Mutation Project revealed that approximately 80% of morphant phenotypes were not observed in mutant embryos (Kok et al., 2015). Our findings are consistent with previous genetic studies interrogating *gpr126* function in zebrafish and suggest that heart defects described in morpholino-injected larvae might be an off-target effect.

The placenta-heart axis underlies cardiac defects in *Gpr126* mutant mice

Previous studies with three different constitutive *Gpr126* knockout mouse lines have shown that homozygous deletion leads to embryonic lethality between E11.5 and E12.5 due to cardiac abnormalities. On one hand, Waller-Evans et al. described a normal ventricular wall in homozygous mutants at E10.5, which undergoes a pronounced thinning at E11.5, therefore suggesting that ventricular function was initially normal and might fail under increased load (Waller-Evans et al., 2010). On the other hand, Patra et al. reported that *Gpr126* mutant hearts were characterized by thinner ventricular wall and trabeculae with aberrant mitochondrial function, and proposed that cardiomyocyte proliferation and differentiation was driven by *Gpr126* in the endocardium (Patra et al., 2013). However, no published studies have performed tissue-

specific gene ablation to elucidate whether cardiac defects are the direct consequence of *Gpr126* loss in the heart, or rather secondary to *Gpr126* deficiency in (a) different organ(s). To address this question, in this study we used CRISPR-Cas9 technology to generate a new *Gpr126* standard knockout model (*Gpr126^{Δ7}*), which lacks exon 7 and results in frameshifting and the generation of a PTC, and a corresponding conditional knockout model (*Gpr126^{fllox}*), where the exon 7 is flanked by loxP sites. In both cases, *Gpr126* expression was efficiently inactivated, indicated by a strong downregulation of transcript levels. This data suggests that the mutant mRNA may be degraded through NMD, which is one of the best-studied RNA surveillance pathways responsible for the removal of PTC-containing mRNAs (Lykke-Andersen and Bennett, 2014). However, the unavailability of a good commercial antibody recognizing *Gpr126* is a limiting factor in this study, so that we could not confirm the absence of a truncated protein in mutant embryos. Notwithstanding, rapid degradation by the proteasome of specific PTC protein products escaping NMD also prevents the expression of abnormal proteins (Kuroha et al., 2009), further supporting that *Gpr126^{Δ7}* is very likely a null allele.

Our analysis of *Gpr126^{Δ7/Δ7}* mutants confirmed previous evidence that homozygous deletion causes fully penetrant embryonic lethality (Fig. 36A, B, 37A, B). Nevertheless, the timing of lethality widened from E10.5 to E13.5, in contrast to the previously published range of E11.5 to E12.5 (Waller-Evans et al., 2010). Accordingly, the penetrance of the cardiac phenotype in mutants is also variable, despite the use of the isogenic C57BL/6N mouse strain. Thus, while some homozygous mutants recapitulated the same reported heart defects, characterized by a marked thinning of the compact and trabecular myocardium, chamber dilation, and underdeveloped interventricular septa, some others were indistinguishable from their WT and heterozygous littermates before E13.5. These results suggest that heart defects may not be the cause of embryonic lethality. The heart is the first organ to form in the mammalian embryo, and its rapid growth in the earlier stages (up to E11.5) (de Boer et al., 2012) makes that embryonic demise resulting from disruption of any key event of cardiogenesis occurs at a precise developmental stage, which can vary by the individual embryonic growth rate differences. Thus, the fact that global *Gpr126* deletion elicits a 4 days lethality window, raises the possibility that fetal demise is unrelated to the loss of *Gpr126* function in the heart.

Indeed, we genetically demonstrate that cardiac-specific inactivation of *Gpr126* is compatible with embryonic survival and heart development. Targeted endocardial-specific inactivation of *Gpr126* using both the endocardial-specific driver line *Nfatc1pan-Cre*, and the endothelial-specific transgenic line *Tie2-Cre*, does not recapitulate any developmental defect observed in global *Gpr126^{Δ7/Δ7}* null embryos (Fig. 36C). Noteworthy, ablation of *Gpr126* in the *Mesp1* lineage, affecting the early cardiogenic mesoderm, nor does disrupt embryonic progression nor cardiovascular function, clearly indicating that cardiac *Gpr126* is not essential for embryonic

development (Fig. 36D). The lack of phenotype is also recapitulated in embryos bearing both the conditional allele and the global knockout allele ($Gpr126^{fl/\Delta 7}$), in which $Gpr126^{lox}$ recombination is specifically targeted in endothelial or cardiac precursor cells, using the *Tie2*- and *Mesp1*-*Cre* drivers, respectively. Likewise, $Gpr126$ null embryos cannot be rescued by endothelial-specific $GPR126$ overexpression, which is consistent with the loss-of-function studies (Fig. 36E). These findings strongly argue against a specific requirement of $Gpr126$ in the heart during embryonic development.

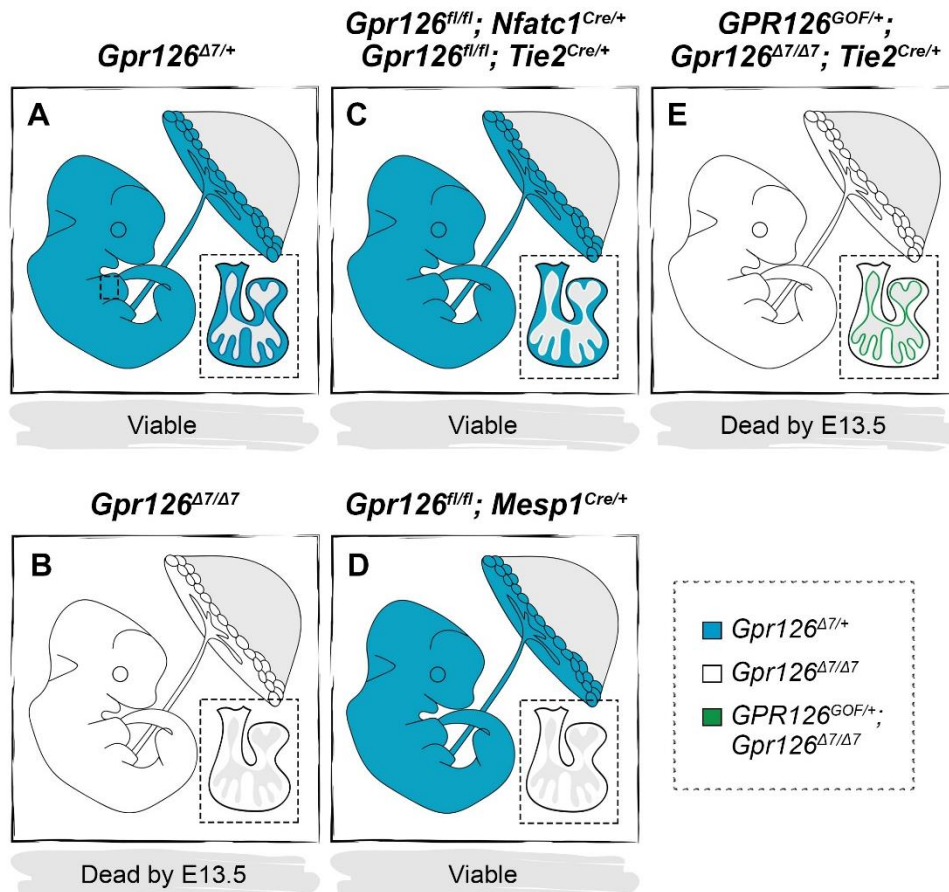


Figure 36. Summary of the outcomes of embryonic viability when conditionally deleting/overexpressing *Gpr126* using cardiac-specific Cre drivers. (A-D) Cartoons illustrating *Gpr126* expression (blue areas) and *Gpr126* deletion (white areas) in E12.5 *Gpr126*^{Δ7/+} (A), *Gpr126*^{Δ7/Δ7} (B), *Gpr126*^{fl/fl}; *Nfatc1*-*Cre*, *Gpr126*^{fl/fl}; *Tie2*-*Cre* (C) and *Gpr126*^{fl/fl}; *Mesp1*-*Cre* (D) hearts, embryos and placentas. (E) Cartoon illustrating *GPR126* overexpression (green area in the chamber endocardium) and *Gpr126* deletion (white areas) in an E12.5 *GPR126*^{GOF/+}; *Gpr126*^{Δ7/Δ7}; *Tie2*-*Cre* heart, embryo and placenta. The maternal decidua is shown in grey color.

In this study, we demonstrate that embryonic lethality and cardiac defects of *Gpr126*^{Δ7/Δ7} null embryos are a secondary consequence of *Gpr126* abrogation in the extraembryonic compartment,

in which *Gpr126* plays a critical role in placentation. Epiblast-specific deletion of *Gpr126* using the paternally transmitted *Sox2-Cre* allele rescues the embryonic lethality of roughly 75% of homozygous mutant offspring (Fig. 37C). In contrast, germline deletion of *Gpr126* via maternal inheritance of the Cre transgene/ protein leads to fully penetrant embryonic lethality, resembling the global *Gpr126^{Δ7/Δ7}* knockouts (Fig. 37D). In other words, 75% of mutant embryos associated with a *Gpr126* heterozygous placenta are viable throughout development, while mutant embryos attached to a mutant placenta die. Interestingly, the genetic rescue does not occur in 25% of the *Gpr126^{fl/fl}; Sox2^{Cre}* mutants. One possible explanation is related to *Sox2* expression. Although it is expressed primarily in the epiblast, some expression has been also reported in the multipotential cells of the extraembryonic ectoderm (ExE) at E6.5 (Avilion et al., 2003). The ExE is the source of undifferentiated trophoblast stem cells, which contribute to the ectoplacental cone and the mature placenta (Woods et al., 2018). Thus, a certain degree of *Gpr126* deletion driven by *Sox2-Cre*-mediated recombination in the ExE could potentially lead to placental abnormalities and embryonic lethality. Due to the variability in the efficiency of Cre between littermates, it is likely that the aforementioned 25% of dead mutant embryos have undergone *Gpr126* deletion in the ExE, in addition to the epiblast, due to *Sox2-Cre* leakiness. One approach to overcome the low recombination rates of the *Sox2-Cre* transgene in the ExE is the tetraploid embryo complementation strategy. The rationale is that tetraploid cells can only give rise to the extraembryonic tissues, whereas diploid cells contribute primarily to the embryo proper (Nagy et al., 1990). Thus, aggregations of WT tetraploid (4N) embryos with *Gpr126^{Δ7/Δ7}* diploid (2N) embryos would lead to *Gpr126^{Δ7/Δ7}* mutant embryos supplied with a WT placenta. However, if some diploid cells partially contribute to placental trophoblasts, resulting in a placenta that is a chimera of 4N and 2N cells (James et al., 1995), the embryonic lethality might not be rescued in 100% of mutant embryos, leading to the same results obtained by genetic ablation using the *Sox2-Cre* driver. To support that placental trophoblast defects cause lethality in *Gpr126^{Δ7/Δ7}* null embryos, we show that restoring *Gpr126* function in the epiblast is not sufficient to rescue the embryonic lethality. In this setting, *GPR126*-overexpressing embryos associated with a *Gpr126*-deficient placenta are already dead by E13.5, resembling global knockouts (Fig. 37E). Based on these results, we would expect that germline overexpression of *GPR126* would result in a functional placenta and allow normal embryonic progression (Fig. 37F). Hence, this hypothesis can be tested in future research by crossing *R26-GPR126^{GOF/GOF}; Gpr126^{Δ7/+}* males with *Gpr126^{Δ7/+}; Sox2^{Cre/+}* females, and ascertain whether *R26-GPR126^{GOF/+}; Gpr126^{Δ7/Δ7/+}; Sox2^{Cre/+}* embryos are born. The generation and analysis of the three different *Gpr126* mouse genetic lines (*Gpr126^{Δ7}*, *Gpr126^{lox}* and *R26-GPR126^{GOF}*) represent a powerful tool for deleting and overexpressing *Gpr126* within a specific tissue and at a given time point, and their combination with different Cre drivers has been critical for elucidating its role in the extraembryonic tissue, hence becoming the key strength of the present study.

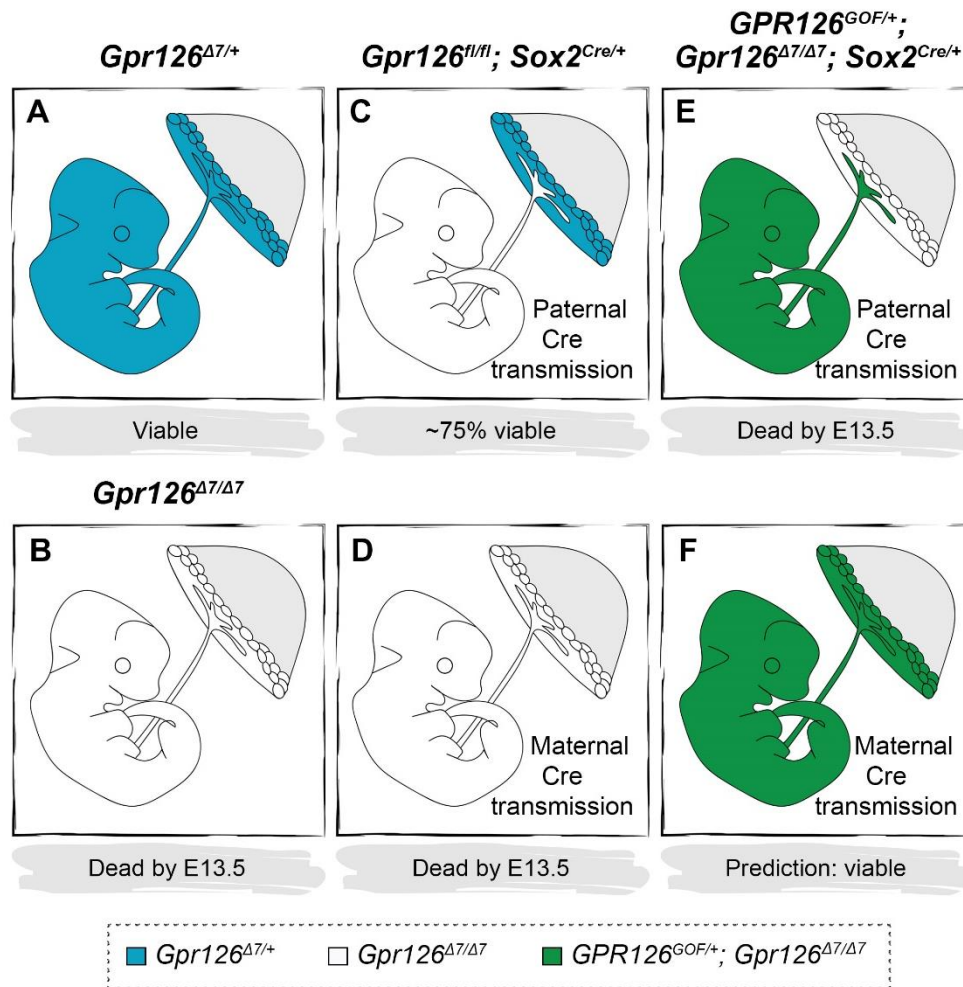


Figure 37. Summary of the outcomes of embryonic viability when conditionally deleting/overexpressing *Gpr126* using the *Sox2-Cre* driver. (A-D) Cartoons illustrating *Gpr126* expression (blue areas) and *Gpr126* deletion (white areas) in E12.5 *Gpr126*^{Δ7/+} (A), *Gpr126*^{Δ7/Δ7} (B) and *Gpr126*^{fl/fl}; *Sox2-Cre* (C, D) embryos and placentas. The origin of the *Sox2-Cre* transgene is paternal in (C) and maternal in (D). (E-F) Cartoons illustrating *GPR126* overexpression (green areas) and *Gpr126* deletion (white areas) in E12.5 *GPR126*^{GOF/+}; *Gpr126*^{Δ7/Δ7}; *Sox2-Cre* embryos and placentas. The origin of the *Sox2-Cre* transgene is paternal in (E) and maternal in (F). The maternal decidua is shown in grey color.

Altogether, these findings highlight the close connection between the placenta and the embryo, and particularly, the heart. This phenomenon has been described as the “placenta-heart axis”, based on the inter-dependence in the development of both organs and the requirement of common molecular pathways (Courtney et al., 2018; Linask, 2013). Remarkably, the enlargement of the chambers and thinning of the ventricular walls observed in *Gpr126*^{Δ7/Δ7} embryos have been also described as secondary phenotypes in other global knockout mice, owing to the primary placental gene function. Some examples are the *SUMO-specific protease 2* (*Senp2*) (Maruyama et al., 2016), *fibronectin leucine-rich repeat transmembrane protein* (*Flrt2*) (Müller et al., 2011;

Tai-Nagara et al., 2017), the *programmed cell death 5* (*Pdcd5*) (Li et al., 2017), *c-Myc* (Dubois et al., 2008), *lymphocyte antigen 6 complex, locus E* (Langford et al., 2018; Zammit et al., 2002), *p38alpha MAP kinase* (Adams et al., 2000) and the *peroxisome proliferator-activated receptor γ* (*PPAR γ*) (Barak et al., 1999), whose ablation also results in fetal demise between E10.5-E15.5. Although our analysis mainly focuses on the cardiovascular defects of *Gpr126*^{*Δ7/Δ7*} mutants, it has been reported that placental abnormalities can also co-associate with vascular and neural defects (Perez-Garcia et al., 2018). Hence, the possibility that other organs may be affected by *Gpr126* deletion should be considered for future studies.

Regulation of maternal spiral artery remodeling by *Gpr126* and its potential implication in preeclampsia

Waller Evans et al. first reported *Gpr126* expression in the P-TGC of the mouse placenta, but did not detect morphological abnormalities that led them to associate placental dysfunction to embryonic lethality (Waller-Evans et al., 2010). Here, we show that *Gpr126* is broadly expressed in the placenta at different developmental stages (E9.5 to E12.5). At E12.5, when mouse *Gpr126* transcripts were detected in all TGC subtypes (Spa-TGC, P-TGC, C-TGC, and S-TGC) and the SpT by ISH analysis. However, because GlyT may originate from spongiotrophoblasts (Adamson et al., 2002; Coan et al., 2006), and their distribution around maternal spiral arteries is reduced in the absence of *Gpr126*, as supported by PAS and *Pcdhl2* stainings, we speculate that *Gpr126* is also expressed in GlyT. Since all these placental cell types can have different developmental origins (Simmons et al., 2007), it is conceivable that *Gpr126* begins to be expressed in common precursor cells. Thus, it will be interesting to determine the onset of *Gpr126* expression in the trophoblast lineage, which would help to gain a better understanding of *Gpr126* function in placental development, to characterize in greater detail the impact of deleterious mutations in this organ, and to establish the embryonic stage when developmental defects arise. Likewise, whether *Gpr126* expression in the placenta remains constant beyond E12.5 or changes throughout pregnancy, is another open question.

Here, we report that *Gpr126* deletion impairs maternal vascularization in the mouse placenta. In the hemochorial placentas of humans and rodents, fetal vessels are lined by endothelial cells, whereas maternal blood spaces are taken over and built by invasive fetal trophoblasts, instead of endothelial cells (Rai and Cross, 2014). Interestingly, *Gpr126* is expressed in the three TGC subtypes that lie the maternal vasculature within the mouse placenta, starting at the level of spiral arteries in the decidua (Spa-TGC), that direct maternal blood through central canals (C-TGC) towards the sinusoidal spaces of the labyrinth (S-TGC). Thus, it is not surprising that *Gpr126* mutants show defects in the maternal vascular circuit. However, the fact that *Gpr126* is expressed

in several cell types also complicates the interpretation of their relative contribution to the global phenotype.

We examined the expression of several trophoblast cell subtype-specific markers in *Gpr126*^{Δ7/Δ7} mutant placentas, which allow for their identification. Intriguingly, one common feature shared among all downregulated genes is their exclusive expression in trophoblast cells that invade the maternal decidua (*Cts7*, *Cts8*, *Pr17b1*). *Mmp9* levels are also decreased in mutant placentas, and it is expressed not only by invasive trophoblasts, but also by decidual macrophages and natural killer cells (NK), which contribute to trophoblast invasion and localize in sites of disruption near the spiral arteries (Ander et al., 2019). On one hand, *Mmp9*-null mouse embryos exhibit deficiencies in trophoblast differentiation and invasion along with intrauterine growth restriction or embryonic death. Pregnant females also exhibit features of preeclampsia including VEGF dysregulation and proteinuria accompanied by pre-existing elevated blood pressure (Plaks et al., 2013). Accordingly, *MMP9* was found to be downregulated in placental bed biopsies from patients diagnosed with preeclampsia (Zhu et al., 2014). On the other hand, mouse placental cathepsins *Cts7* and *Cts8* are expressed in P-TGCs surrounding the implantation site as early as E5.5. Later in development, they are also expressed by Spa-TGC, with *Cts8* being extremely important for the remodeling of spiral arteries through the degradation of vascular smooth muscle cells, thus allowing their transformation into high capacitance vessels (Screen et al., 2008). Further confirmation of impaired vascular remodeling would need smooth-muscle α-actin (SMA), CD31 (endothelial marker), and cytokeratin (trophoblast marker) staining on *Gpr126*^{Δ7/Δ7} placentas, thus allowing the visualization of SMA around maternal spiral arteries, and endothelial replacement by fetal trophoblasts. Whether this is the case in humans remains to be determined. Placental cathepsins have undergone a series of duplications in the mouse genome, so that the ancestral cathepsin L (*CTSL*) gene found in humans has given rise to a family of eight placenta-specific cathepsins in mice. How GPR126 regulates the expression of placental cathepsins in humans should be explored in future studies. Indeed, our findings suggest a requirement of *Gpr126* for the transcriptional regulation of proteases playing a key role in trophoblast invasion and spiral artery remodeling during placenta formation.

The labyrinth architecture is also impaired in *Gpr126*^{Δ7/Δ7} placentas. Maternal sinusoid spaces are enlarged, which presumably decreases the surface area available for gas and nutrient exchange. However, the capacity of trans-placental transport is not altered in the mutants, as evaluated by measuring hypoxia levels, GLUT1 expression levels, and the maternal-fetal passage of rhodamine 123. Hence, it is unlikely that the lack of energy and glucose underlies embryonic death in *Gpr126*^{Δ7/Δ7} mutants. Markers for the different layers that compose the interhemal membrane are also normally expressed, further supporting that its function is not compromised. The sinusoid spaces, filled with maternal blood, are formed as the chorioallantoic interface

branches (Rodriguez et al., 2004). Thus, a reduction of chorioallantoic branching could potentially explain the enlargement of maternal sinusoids and the formation of large blood pools in the labyrinth. A second possibility could be based on the increased blood pressure entering the exchange surface by abnormal spiral artery remodeling. High blood pressure can cause rupture of the delicate placental sinusoids and contribute to fetal death. However, the wide range of the lethality window (E10.5-E13.5) complicates to detect signs of vessel break in mutant placentas, as it may occur just before embryonic death. The impaired placental perfusion caused by abnormal vascular remodeling could be evaluated by Doppler ultrasound (US) of the maternal uterine arteries, which is considered a useful method for the prediction of preeclampsia (Lopez-Mendez et al., 2013). Apart from Spa-TGC and S-TGC, we cannot exclude additional defects in other trophoblast cell types that might be masked by the early and severe placenta phenotype of mutants. *Gpr126* deletion in specific trophoblast cell types is required to clarify each cell-type-specific function.

Our findings point to *Gpr126* dysregulation as a potential contributing factor to the etiology of preeclampsia and pregnancy loss, due to defective trophoblast invasion and spiral artery remodeling, which are considered hallmarks of this syndrome. A recent study identified increased *GPR126* expression in human preeclamptic placentas (Zadora et al., 2017), supporting the hypothesis that disturbed *GPR126* expression and preeclampsia could indeed be associated. Although preeclampsia is a multisystem disorder clinically manifested as gestational hypertension, proteinuria, and vascular dysfunction, none of these features have been measured in pregnant females bearing *Gpr126*-null embryos. Based on the stages of embryonic lethality, we speculate that *Gpr126* mutants die as a result of a severe disruption of the maternal vascular remodeling before clinical manifestations arise in the mother. Interestingly, the onset of fetal demise is E10.5, when the mature placenta is just established, and the spiral artery remodeling process is over (~E7.5 and E10.5). From around E10.5 onwards, there is a switch from the yolk sac to placental nutrient supply that entails an absolute requirement of a functional placenta to ensure embryo survival (Woods et al., 2018), which may be compromised in *Gpr126*^{Δ7/Δ7} embryos.

Altogether, we have identified *Gpr126* as a new marker labeling all TGC subtypes and the SpT. We propose that during placental development, *Gpr126* function is critical in the TGCs at the implantation site for the expression of extracellular proteases that are associated with trophoblast invasion into the maternal decidua, like the gelatinase *Mmp9*, and maternal spiral artery remodeling, such as the placental cathepsin *Cst8* (Fig. 38A, B). *Mmp9* is involved in the breakdown of collagen IV, which is the main component of the maternal basal membrane, thus playing a critical role in decidual ECM remodeling and cell migration (Hamutoğlu et al., 2020) (Fig. 38B). *Cst8* mediates the loss of SMA from the vessel wall, thus facilitating the transformation of narrow high-resistance, low-flow vessels into dilated low-resistant, high-flow

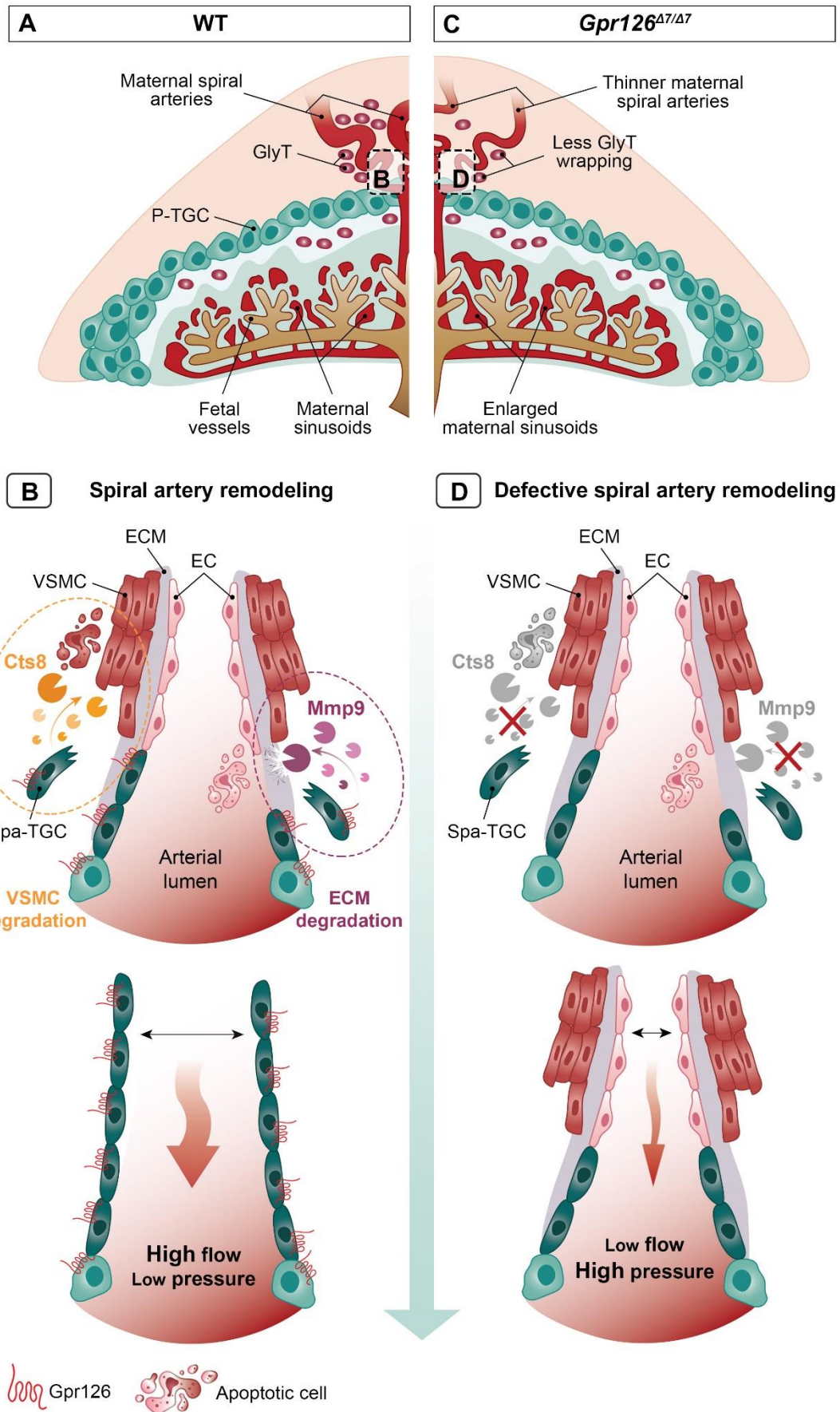


Figure 38. Model of *Gpr126* function in the remodeling of the maternal vasculature of the mouse placenta. (A-D) Cartoon illustrating an E12.5 WT (A, B) and *Gpr126*^{Δ7/Δ7} (B, C) placenta. (A, B) In a WT scenario, *Gpr126* endows TGC with invasive behavior by the production of *Mmp9*, together with the capacity of degrading vascular smooth muscle cells by the expression of *Cts8*. Both activities are required for uterine trophoblast invasion and vascular remodeling during placental development, in which maternal spiral arteries are transformed from narrow high-resistance, low flow vessels into dilated vessels, comprising higher blood flow at lower pressure. Thus, Spa-TGCs replace the maternal endothelial lining and GlyT congregate around spiral arteries. (C, D) In contrast, *Gpr126*-null placentas fail to express *Mmp9* and *Cts8*, thus impairing trophoblast migration and spiral artery adaptation. Fewer GlyT cells wrapped around un-remodeled maternal spiral arteries. As a result of the altered uteroplacental hemodynamics, increased blood pressure triggers an enlargement of maternal sinusoids. EC, endothelial cells; ECM, extracellular matrix; GlyT, glycogen trophoblasts; P-TGC, parietal trophoblast giant cells; Spa-TGC, spiral artery-associated trophoblast giant cells; VSMC, vascular smooth muscle cells.

vessels that lack maternal vasomotor control (Fig. 38B). By the secretion of both proteases, Spa-TGCs finally replace the endothelial lining of maternal spiral arteries and acquire a pseudoendothelial phenotype (Harris, 2010; Red-Horse et al., 2004) (Fig. 38B). This process is thought to be coordinated by SpA-TGCs and uNK cells (not shown) and results in increased blood flow to the developing embryo (Cross et al., 2002). A proportion of GlyT also invades interstitially into the decidua from the junctional zone to congregate around maternal spiral arteries (Fig. 38A) (Adamson et al., 2002). Inactivation of *Gpr126* causes a reduction of *Mmp9* and *Cts8* transcript levels, leading to shallow trophoblast invasion, defective vascular remodeling and less GlyT around maternal spiral arteries (Fig. 38C, D). Narrow high-resistance, non-remodeled vessels associate with high perfusion blood pressure into the labyrinth and shear stress in the trophoblast layer, likely resulting in an enlargement of maternal blood spaces and aberrant labyrinth architecture (Fig. 38C, D). These defects compromise embryonic progression and might be involved in the development of pregnancy diseases, like preeclampsia.

The *Gpr126*^{Δ7/Δ7} mouse line could represent a valuable animal model for investigating the molecular mechanisms involved in preeclampsia. Furthermore, as previous pieces of evidence support a role in human placentation (Zadora et al., 2017) (Ravenscroft et al., 2015), our results could become the basis for a future clinical application in preimplantation genetic diagnosis (PGD). This diagnostic tool is used to screen for a particular genetic condition in embryos that have been created through *in vitro* fertilization before they are transferred to the uterus. The aim is to prevent certain inherited genetic disorders from being passed on to subsequent generations and discard genetic abnormalities that may compromise embryo viability. Thus, deleterious *Gpr126* mutations could be potentially included in the list of monogenic disorders that are evaluated in PGD if a definitive molecular diagnosis is established.

Altered uteroplacental hemodynamics as a potential explanation for cardiac defects in *Gpr126* mutants

In this study, we demonstrate that the leading cause of the heart defects and embryonic lethality previously reported in *Gpr126* mutant embryos is defective placental development. However, how placental abnormalities impact on heart development remains unexplored.

We found that expression of chamber patterning markers, cardiac metabolism, and cellular proliferation are normal in *Gpr126* mutant hearts and do not contribute to morphological defects. In contrast, comparative transcriptome profiling of WT and mutant ventricles and subsequent GO analysis revealed an enrichment of downregulated DEG involved in “angiogenesis” and “vasculature development”. In the heart, there are two types of endothelial cells: the endocardial endothelial cells, lining the lumen of the heart, and the microvascular endothelial cells, lining the blood vessels of the heart. Forasmuch as *Gpr126* is not expressed in the embryonic microvasculature (Stehlik et al., 2004), one possible explanation for the transcriptional alteration of endothelial/endocardial specific genes is the activation of pathways sensing shear stress in response to altered placental hemodynamics in *Gpr126* null placentas. Deficient remodeling of uterine spiral arteries can lead to an increase in placental vascular resistance and cardiac afterload, thus increasing the mechanical force to which the heart is subjected (Camm et al., 2018). In the heart, the endocardium acts as a sensor of biophysical forces induced by blood flow, and translate them into a response during cardiac development and homeostasis (Haack and Abdelilah-Seyfried, 2016). Hence, dysregulation of endocardial gene expression in *Gpr126*^{Δ7/Δ7} mutants could be explained by a mechanosensitive transcriptional response to altered hemodynamic forces. Some examples of known shear stress sensors downregulated in the mutants are *Kdr* (Coon et al., 2015), *Eng* (Sugden et al., 2017), *Plxd1* (Mehta et al., 2020) and *Tie1* (Woo et al., 2011). A question that remains to be elucidated is whether *Gpr126* also participates in the regulation of endocardial homeostasis as a flow-responsive gene, thus explaining why it is expressed in the endocardium. Moreover, we excluded the possibility that the embryonic function of *Gpr126* was required for adult heart homeostasis, as assessed by a cross-sectional ECG analysis and histological examination of *Gpr126*^{fl/fl}; *Tie2-Cre* adult hearts. Although ECG is the cornerstone in diagnosing patients with heart disease, echocardiography is also frequently used for the evaluation of cardiac function in mice, as it provides valuable information regarding the size, shape, and internal structure of the heart, and how blood flows through it. Thus, it would be interesting to combine our electrophysiological and morphological data with echocardiography measurements to further confirm that *Gpr126* is dispensable for adult cardiac function.

6

CONCLUSIONS

1. *Gpr126* expression in the heart is confined to the endocardium of the cardiac chambers, and it is dispensable in this organ for mouse heart development and adult cardiac function.
2. *Gpr126* is not required for heart trabeculation in zebrafish.
3. Endocardial/ endothelial *GPR126* overexpression is not sufficient to rescue hypotrabeulation defects nor embryonic lethality of *Dll4^{fl/fl}*; *Tie2-Cre* mouse mutants.
4. *Gpr126* is expressed in the SpT and the four TGC subtypes (Spa-TGC, C-TGC, P-TGC and S-TGC) of the mature placenta.
5. *Gpr126* signaling in the trophoblast lineage is crucial for embryonic progression beyond E10.5, and placental abnormalities are the primary cause of embryonic lethality and heart defects of *Gpr126*-null mutants.
6. *Gpr126* has distinct and domain-specific functions in the embryo and the placenta. The adhesive CUB and PTX domains, encoded by exons 3 and 4 respectively, are essential for peripheral nervous system development, but dispensable in the trophoblast lineage for placental development.
7. *Gpr126* is required for the organization of maternal blood sinusoids in the placental labyrinth.
8. *Gpr126* is involved in placental glycogen storage and congregation of GlyT around maternal spiral arteries.
9. *Gpr126* regulates the expression of *Mmp9*, *Prl7b1* and cathepsins 7 (*Cts7*) and 8 (*Cts8*), which are involved in trophoblast invasion and spiral artery remodeling during placental development.

CONCLUSIONES

1. *Gpr126* se expresa en el endocardio de las cámaras cardíacas, pero es prescindible para el desarrollo del corazón embrionario y la función cardíaca en el adulto.
2. La señalización mediada por *gpr126* no es necesaria para el proceso de trabeculación en el pez cebra.
3. La sobreexpresión de *GPR126* en el endocardio/ endotelio no rescata el defecto de hipotrabeculación ni la letalidad embrionaria de los mutantes *Dll4^{fl/fl}; Tie2-Cre*.
4. *Gpr126* se expresa en el espongiotrofoblasto y en los cuatro subtipos de células gigantes del trofoblasto (Spa-TGC, C-TGC, P-TGC y S-TGC) de la placenta madura.
5. La señalización mediada por *Gpr126* en el linaje trofoblástico juega un papel fundamental en la viabilidad embrionaria a partir del día de gestación 10.5 (E10.5). La alteración del desarrollo placentario provoca la letalidad embrionaria y los defectos cardíacos característicos de los mutantes de *Gpr126*.
6. *Gpr126* desempeña funciones distintas asociadas a dominios proteicos específicos. Los dominios de adhesión CUB y PTX, codificados por los exones 3 y 4 respectivamente, son esenciales para el desarrollo del sistema nervioso periférico, pero no para el desarrollo placentario.
7. *Gpr126* está implicado en la organización de los sinusoides maternos del laberinto placentario.
8. *Gpr126* es necesario para el almacenamiento de glucógeno placentario y la movilización de GlyT alrededor de las arterias espirales maternas.
9. *Gpr126* regula la expresión de *Mmp9*, *Prl7b1* y de las catepsinas 7 (*Cts7*) y 8 (*Cts8*), cuya secreción y función es necesaria para la invasión trofoblástica y el remodelado de las arterias espirales maternas durante el desarrollo placentario.



REFERENCES

- Adams, R.H., Porras, A., Alonso, G., Jones, M., Vintersten, K., Panelli, S., Valladares, A., Perez, L., Klein, R., and Nebreda, A.R. (2000). Essential role of p38alpha MAP kinase in placental but not embryonic cardiovascular development. *Mol Cell* 6, 109-116.
- Adamson, S.L., Lu, Y., Whiteley, K.J., Holmyard, D., Hemberger, M., Pfarrer, C., and Cross, J.C. (2002). Interactions between trophoblast cells and the maternal and fetal circulation in the mouse placenta. *Dev Biol* 250, 358-373.
- Altschul, S.F., Gish, W., Miller, W., Myers, E.W., and Lipman, D.J. (1990). Basic local alignment search tool. *Journal of Molecular Biology* 215, 403-410.
- Ander, S.E., Diamond, M.S., and Coyne, C.B. (2019). Immune responses at the maternal-fetal interface. *Sci Immunol* 4.
- Andrés-Delgado, L., and Mercader, N. (2016). Interplay between cardiac function and heart development. *Biochim Biophys Acta* 1863, 1707-1716.
- Artavanis-Tsakonas, S., Rand, M.D., and Lake, R.J. (1999). Notch signaling: cell fate control and signal integration in development. *Science* 284, 770-776.
- Arthur, H.M., Ure, J., Smith, A.J., Renforth, G., Wilson, D.I., Torsney, E., Charlton, R., Parums, D.V., Jowett, T., Marchuk, D.A., *et al.* (2000). Endoglin, an ancillary TGFbeta receptor, is required for extraembryonic angiogenesis and plays a key role in heart development. *Dev Biol* 217, 42-53.
- Avilion, A.A., Nicolis, S.K., Pevny, L.H., Perez, L., Vivian, N., and Lovell-Badge, R. (2003). Multipotent cell lineages in early mouse development depend on SOX2 function. *Genes Dev* 17, 126-140.
- Barak, Y., Nelson, M.C., Ong, E.S., Jones, Y.Z., Ruiz-Lozano, P., Chien, K.R., Koder, A., and Evans, R.M. (1999). PPAR gamma is required for placental, cardiac, and adipose tissue development. *Mol Cell* 4, 585-595.
- Ben-Shachar, G., Arcilla, R.A., Lucas, R.V., and Manasek, F.J. (1985). Ventricular trabeculations in the chick embryo heart and their contribution to ventricular and muscular septal development. *Circ Res* 57, 759-766.
- Bevilacqua, E.M., and Abrahamsohn, P.A. (1988). Ultrastructure of trophoblast giant cell transformation during the invasive stage of implantation of the mouse embryo. *J Morphol* 198, 341-351.

7. REFERENCES

- Bokslag, A., van Weissenbruch, M., Mol, B.W., and de Groot, C.J.M. (2016). Preeclampsia; short and long-term consequences for mother and neonate. *Early Human Development* 102, 47-50.
- Braren, R., Hu, H., Kim, Y.H., Beggs, H.E., Reichardt, L.F., and Wang, R. (2006). Endothelial FAK is essential for vascular network stability, cell survival, and lamellipodial formation. *J Cell Biol* 172, 151-162.
- Brown, D.R., Samsa, L.A., Qian, L., and Liu, J. (2016). Advances in the Study of Heart Development and Disease Using Zebrafish. *J Cardiovasc Dev Dis* 3.
- Buckingham, M., Meilhac, S., and Zaffran, S. (2005). Building the mammalian heart from two sources of myocardial cells. *Nat Rev Genet* 6, 826-835.
- Camm, E.J., Botting, K.J., and Sferruzzi-Perri, A.N. (2018). Near to One's Heart: The Intimate Relationship Between the Placenta and Fetal Heart. *Frontiers in Physiology* 9.
- Cazorla, O., Lucas, A., Poirier, F., Lacampagne, A., and Lezoualc'h, F. (2009). The cAMP binding protein Epac regulates cardiac myofilament function. *Proc Natl Acad Sci U S A* 106, 14144-14149.
- Chaiworapongsa, T., Chaemsathong, P., Yeo, L., and Romero, R. (2014). Pre-eclampsia part 1: current understanding of its pathophysiology. *Nat Rev Nephrol* 10, 466-480.
- Chakraborty, D., Rumi, M.A.K., Konno, T., and Soares, M.J. (2011). Natural killer cells direct hemochorial placentation by regulating hypoxia-inducible factor dependent trophoblast lineage decisions. *Proceedings of the National Academy of Sciences* 108, 16295-16300.
- Chen, H., Shi, S., Acosta, L., Li, W., Lu, J., Bao, S., Chen, Z., Yang, Z., Schneider, M.D., Chien, K.R., *et al.* (2004). BMP10 is essential for maintaining cardiac growth during murine cardiogenesis. *Development* 131, 2219-2231.
- Cheng, M.H., and Wang, P.H. (2009). Placentation abnormalities in the pathophysiology of preeclampsia. *Expert Rev Mol Diagn* 9, 37-49.
- Chi, N.C., Shaw, R.M., De Val, S., Kang, G., Jan, L.Y., Black, B.L., and Stainier, D.Y. (2008). Foxn4 directly regulates tbx2b expression and atrioventricular canal formation. *Genes Dev* 22, 734-739.
- Christoffels, V.M., Keijser, A.G., Houweling, A.C., Clout, D.E., and Moorman, A.F. (2000). Patterning the embryonic heart: identification of five mouse Iroquois homeobox genes in the developing heart. *Dev Biol* 224, 263-274.

- Coan, P.M., Conroy, N., Burton, G.J., and Ferguson-Smith, A.C. (2006). Origin and characteristics of glycogen cells in the developing murine placenta. *Dev Dyn* 235, 3280-3294.
- Conway, S.J., and Molkentin, J.D. (2008). Periostin as a heterofunctional regulator of cardiac development and disease. *Curr Genomics* 9, 548-555.
- Coon, B.G., Baeyens, N., Han, J., Budatha, M., Ross, T.D., Fang, J.S., Yun, S., Thomas, J.-L., and Schwartz, M.A. (2015). Intramembrane binding of VE-cadherin to VEGFR2 and VEGFR3 assembles the endothelial mechanosensory complex. *Journal of Cell Biology* 208, 975-986.
- Courtney, J.A., Cnota, J.F., and Jones, H.N. (2018). The Role of Abnormal Placentation in Congenital Heart Disease; Cause, Correlate, or Consequence? *Front Physiol* 9, 1045.
- Cross, J.C., Hemberger, M., Lu, Y., Nozaki, T., Whiteley, K., Masutani, M., and Adamson, S.L. (2002). Trophoblast functions, angiogenesis and remodeling of the maternal vasculature in the placenta. *Molecular and Cellular Endocrinology* 187, 207-212.
- Croy, B.A., Ashkar, A.A., Minhas, K., and Greenwood, J.D. (2000). Can Murine Uterine Natural Killer Cells Give Insights Into the Pathogenesis of Preeclampsia? *The Journal of the Society for Gynecologic Investigation: JSGI* 7, 12-20.
- Croy, B.A., Yamada, A., DeMayo, F., and Adamson, S.L. (2014). *The Guide to Investigation of Mouse Pregnancy*.
- D'Amato, G., Luxán, G., and de la Pompa, J.L. (2016a). Notch signalling in ventricular chamber development and cardiomyopathy. *Febs j* 283, 4223-4237.
- D'Amato, G., Luxán, G., del Monte-Nieto, G., Martínez-Poveda, B., Torroja, C., Walter, W., Bochter, M.S., Benedito, R., Cole, S., Martinez, F., *et al.* (2016b). Sequential Notch activation regulates ventricular chamber development. *Nat Cell Biol* 18, 7-20.
- D'Amico, L., Scott, I.C., Jungblut, B., and Stainier, D.Y. (2007). A mutation in zebrafish *hmgcr1b* reveals a role for isoprenoids in vertebrate heart-tube formation. *Curr Biol* 17, 252-259.
- Das, U.G., Sadiq, H.F., Soares, M.J., Hay, W.W., Jr., and Devaskar, S.U. (1998). Time-dependent physiological regulation of rodent and ovine placental glucose transporter (GLUT-1) protein. *Am J Physiol* 274, R339-347.
- de Boer, B.A., van den Berg, G., de Boer, P.A., Moorman, A.F., and Ruijter, J.M. (2012). Growth of the developing mouse heart: an interactive qualitative and quantitative 3D atlas. *Dev Biol* 368, 203-213.

- de la Pompa, J.L., and Epstein, J.A. (2012). Coordinating tissue interactions: notch signaling in cardiac development and disease. *Dev Cell* 22, 244-254.
- de la Pompa, J.L., Timmerman, L.A., Takimoto, H., Yoshida, H., Elia, A.J., Samper, E., Potter, J., Wakeham, A., Marengere, L., Langille, B.L., *et al.* (1998). Role of the NF-ATc transcription factor in morphogenesis of cardiac valves and septum. *Nature* 392, 182-186.
- Del Monte, G., Grego-Bessa, J., González-Rajal, A., Bolós, V., and De La Pompa, J.L. (2007). Monitoring Notch1 activity in development: evidence for a feedback regulatory loop. *Dev Dyn* 236, 2594-2614.
- Diamantopoulou, E., Baxendale, S., de la Vega de León, A., Asad, A., Holdsworth, C.J., Abbas, L., Gillet, V.J., Wiggin, G.R., and Whitfield, T.T. (2019). Identification of compounds that rescue otic and myelination defects in the zebrafish *adgrg6* (*gpr126*) mutant. *Elife* 8.
- Dubois, N.C., Adolphe, C., Ehninger, A., Wang, R.A., Robertson, E.J., and Trumpp, A. (2008). Placental rescue reveals a sole requirement for c-Myc in embryonic erythroblast survival and hematopoietic stem cell function. *Development* 135, 2455-2465.
- Dubousset, J., and Guillaumat, M. (2015). Long-term outcome for patients with arthrogryposis multiplex congenita. *J Child Orthop* 9, 449-458.
- Dunwoodie, S.L. (2009). The role of hypoxia in development of the Mammalian embryo. *Dev Cell* 17, 755-773.
- Dupressoir, A., Vernochet, C., Bawa, O., Harper, F., Pierron, G., Opolon, P., and Heidmann, T. (2009). Syncytin-A knockout mice demonstrate the critical role in placentation of a fusogenic, endogenous retrovirus-derived, envelope gene. *Proc Natl Acad Sci U S A* 106, 12127-12132.
- El-Brolosy, M.A., Kontarakis, Z., Rossi, A., Kuenne, C., Günther, S., Fukuda, N., Kikhi, K., Boezio, G.L.M., Takacs, C.M., Lai, S.L., *et al.* (2019). Genetic compensation triggered by mutant mRNA degradation. *Nature* 568, 193-197.
- Gaboriaud, C., Gregory-Pauron, L., Teillet, F., Thielens, N.M., Bally, I., and Arlaud, G.J. (2011). Structure and properties of the Ca(2+)-binding CUB domain, a widespread ligand-recognition unit involved in major biological functions. *Biochem J* 439, 185-193.
- Gagnon, J.A., Valen, E., Thyme, S.B., Huang, P., Akhmetova, L., Pauli, A., Montague, T.G., Zimmerman, S., Richter, C., and Schier, A.F. (2014). Efficient mutagenesis by Cas9 protein-

mediated oligonucleotide insertion and large-scale assessment of single-guide RNAs. *PLoS One* 9, e98186.

Geng, F.S., Abbas, L., Baxendale, S., Holdsworth, C.J., Swanson, A.G., Slanchev, K., Hammerschmidt, M., Topczewski, J., and Whitfield, T.T. (2013). Semicircular canal morphogenesis in the zebrafish inner ear requires the function of *gpr126* (*lauscher*), an adhesion class G protein-coupled receptor gene. *Development* 140, 4362-4374.

Gitler, A.D., Lu, M.M., and Epstein, J.A. (2004). PlexinD1 and semaphorin signaling are required in endothelial cells for cardiovascular development. *Dev Cell* 7, 107-116.

Glenn, T.D., and Talbot, W.S. (2013). Analysis of *Gpr126* function defines distinct mechanisms controlling the initiation and maturation of myelin. *Development* 140, 3167-3175.

Grant, M.G., Patterson, V.L., Grimes, D.T., and Burdine, R.D. (2017). Modeling Syndromic Congenital Heart Defects in Zebrafish. *Curr Top Dev Biol* 124, 1-40.

Grego-Bessa, J., Luna-Zurita, L., del Monte, G., Bolós, V., Melgar, P., Arandilla, A., Garratt, A.N., Zang, H., Mukoyama, Y.S., Chen, H., *et al.* (2007). Notch signaling is essential for ventricular chamber development. *Dev Cell* 12, 415-429.

Gutiérrez, J.A., Gómez, I., Chiarello, D.I., Salsoso, R., Klein, A.D., Guzmán-Gutiérrez, E., Toledo, F., and Sobrevia, L. (2020). Role of proteases in dysfunctional placental vascular remodelling in preeclampsia. *Biochim Biophys Acta Mol Basis Dis* 1866, 165448.

Haack, T., and Abdelilah-Seyfried, S. (2016). The force within: endocardial development, mechanotransduction and signalling during cardiac morphogenesis. *Development* 143, 373-386.

Hamada, Y., Hiroe, T., Suzuki, Y., Oda, M., Tsujimoto, Y., Coleman, J.R., and Tanaka, S. (2007). Notch2 is required for formation of the placental circulatory system, but not for cell-type specification in the developing mouse placenta. *Differentiation* 75, 268-278.

Hamutoğlu, R., Bulut, H.E., Kaloğlu, C., Önder, O., Dağdeviren, T., Aydemir, M.N., and Korkmaz, E.M. (2020). The regulation of trophoblast invasion and decidual reaction by matrix metalloproteinase-2, metalloproteinase-7, and metalloproteinase-9 expressions in the rat endometrium. *Reproductive Medicine and Biology* 19, 385-397.

Harms, D.W., Quadros, R.M., Seruggia, D., Ohtsuka, M., Takahashi, G., Montoliu, L., and Gurumurthy, C.B. (2014). Mouse Genome Editing Using the CRISPR/Cas System. *Curr Protoc Hum Genet* 83, 15.17.11-27.

7. REFERENCES

- Harris, I.S., and Black, B.L. (2010). Development of the endocardium. *Pediatr Cardiol* 31, 391-399.
- Harris, L.K. (2010). Review: Trophoblast-vascular cell interactions in early pregnancy: how to remodel a vessel. *Placenta* 31 Suppl, S93-98.
- Harty, B.L., Krishnan, A., Sanchez, N.E., Schiöth, H.B., and Monk, K.R. (2015). Defining the gene repertoire and spatiotemporal expression profiles of adhesion G protein-coupled receptors in zebrafish. *BMC Genomics* 16, 62.
- Hayashi, S., Lewis, P., Pevny, L., and McMahon, A.P. (2002). Efficient gene modulation in mouse epiblast using a Sox2Cre transgenic mouse strain. *Gene Expr Patterns* 2, 93-97.
- Hayashi, S., Tenzen, T., and McMahon, A.P. (2003). Maternal inheritance of Cre activity in a Sox2Cre deleter strain. *Genesis* 37, 51-53.
- Hemberger, M., and Cross, J.C. (2001). Genes governing placental development. *Trends Endocrinol Metab* 12, 162-168.
- Hemberger, M., Hanna, C.W., and Dean, W. (2020). Mechanisms of early placental development in mouse and humans. *Nat Rev Genet* 21, 27-43.
- Hemberger, M., Nozaki, T., Winterhager, E., Yamamoto, H., Nakagama, H., Kamada, N., Suzuki, H., Ohta, T., Ohki, M., Masutani, M., *et al.* (2003). Parp1-deficiency induces differentiation of ES cells into trophoblast derivatives. *Developmental Biology* 257, 371-381.
- Hernandez, K.R., Karim, Z.A., Qasim, H., Druey, K.M., Alshbool, F.Z., and Khasawneh, F.T. (2019). Regulator of G-Protein Signaling 16 Is a Negative Modulator of Platelet Function and Thrombosis. *J Am Heart Assoc* 8, e011273.
- Heximer, S.P., Knutsen, R.H., Sun, X., Kaltenbronn, K.M., Rhee, M.H., Peng, N., Oliveira-dos-Santos, A., Penninger, J.M., Muslin, A.J., Steinberg, T.H., *et al.* (2003). Hypertension and prolonged vasoconstrictor signaling in RGS2-deficient mice. *J Clin Invest* 111, 445-452.
- High, F.A., and Epstein, J.A. (2008). The multifaceted role of Notch in cardiac development and disease. *Nat Rev Genet* 9, 49-61.
- Hu, D., and Cross, J.C. (2010). Development and function of trophoblast giant cells in the rodent placenta. *Int J Dev Biol* 54, 341-354.

- Hua, L.L., Vedantham, V., Barnes, R.M., Hu, J., Robinson, A.S., Bressan, M., Srivastava, D., and Black, B.L. (2014). Specification of the mouse cardiac conduction system in the absence of Endothelin signaling. *Dev Biol* 393, 245-254.
- Hunkapiller, N.M., Gasperowicz, M., Kapidzic, M., Plaks, V., Maltepe, E., Kitajewski, J., Cross, J.C., and Fisher, S.J. (2011). A role for Notch signaling in trophoblast endovascular invasion and in the pathogenesis of pre-eclampsia. *Development* 138, 2987-2998.
- Itoh, M., Kim, C.H., Palardy, G., Oda, T., Jiang, Y.J., Maust, D., Yeo, S.Y., Lorick, K., Wright, G.J., Ariza-McNaughton, L., *et al.* (2003). Mind bomb is a ubiquitin ligase that is essential for efficient activation of Notch signaling by Delta. *Dev Cell* 4, 67-82.
- James, R.M., Klerkx, A.H., Keighren, M., Flockhart, J.H., and West, J.D. (1995). Restricted distribution of tetraploid cells in mouse tetraploid<=> diploid chimaeras. *Dev Biol* 167, 213-226.
- Jarriault, S., Brou, C., Logeat, F., Schroeter, E.H., Kopan, R., and Israel, A. (1995). Signalling downstream of activated mammalian Notch. *Nature* 377, 355-358.
- Kaipainen, A., Korhonen, J., Pajusola, K., Aprelikova, O., Persico, M.G., Terman, B.I., and Alitalo, K. (1993). The related FLT4, FLT1, and KDR receptor tyrosine kinases show distinct expression patterns in human fetal endothelial cells. *J Exp Med* 178, 2077-2088.
- Keelan, J.A., and Mitchell, M.D. (2007). Placental cytokines and preeclampsia. *Front Biosci* 12, 2706-2727.
- Kelly, R.G., Brown, N.A., and Buckingham, M.E. (2001). The arterial pole of the mouse heart forms from Fgf10-expressing cells in pharyngeal mesoderm. *Dev Cell* 1, 435-440.
- Kendall, R.L., and Thomas, K.A. (1993). Inhibition of vascular endothelial cell growth factor activity by an endogenously encoded soluble receptor. *Proc Natl Acad Sci U S A* 90, 10705-10709.
- Khan, F., Belch, J.J., MacLeod, M., and Mires, G. (2005). Changes in endothelial function precede the clinical disease in women in whom preeclampsia develops. *Hypertension* 46, 1123-1128.
- Kisanuki, Y.Y., Hammer, R.E., Miyazaki, J., Williams, S.C., Richardson, J.A., and Yanagisawa, M. (2001). Tie2-Cre transgenic mice: a new model for endothelial cell-lineage analysis in vivo. *Dev Biol* 230, 230-242.

- Kitagaki, J., Miyauchi, S., Asano, Y., Imai, A., Kawai, S., Michikami, I., Yamashita, M., Yamada, S., Kitamura, M., and Murakami, S. (2016). A Putative Association of a Single Nucleotide Polymorphism in GPR126 with Aggressive Periodontitis in a Japanese Population. *PLoS One* *11*, e0160765.
- Koch, U., Fiorini, E., Benedito, R., Besseyrias, V., Schuster-Gossler, K., Pierres, M., Manley, N.R., Duarte, A., Macdonald, H.R., and Radtke, F. (2008). Delta-like 4 is the essential, nonredundant ligand for Notch1 during thymic T cell lineage commitment. *J Exp Med* *205*, 2515-2523.
- Koibuchi, N., and Chin, M.T. (2007). CHF1/Hey2 plays a pivotal role in left ventricular maturation through suppression of ectopic atrial gene expression. *Circ Res* *100*, 850-855.
- Kok, F.O., Shin, M., Ni, C.W., Gupta, A., Grosse, A.S., van Impel, A., Kirchmaier, B.C., Peterson-Maduro, J., Kourkoulis, G., Male, I., *et al.* (2015). Reverse genetic screening reveals poor correlation between morpholino-induced and mutant phenotypes in zebrafish. *Dev Cell* *32*, 97-108.
- Kopan, R., and Ilagan, M.X. (2009). The canonical Notch signaling pathway: unfolding the activation mechanism. *Cell* *137*, 216-233.
- Kou, I., Takahashi, Y., Johnson, T.A., Takahashi, A., Guo, L., Dai, J., Qiu, X., Sharma, S., Takimoto, A., Ogura, Y., *et al.* (2013). Genetic variants in GPR126 are associated with adolescent idiopathic scoliosis. *Nat Genet* *45*, 676-679.
- Kuroha, K., Tatematsu, T., and Inada, T. (2009). Upf1 stimulates degradation of the product derived from aberrant messenger RNA containing a specific nonsense mutation by the proteasome. *EMBO Rep* *10*, 1265-1271.
- Langford, M.B., Outhwaite, J.E., Hughes, M., Natale, D.R.C., and Simmons, D.G. (2018). Deletion of the Syncytin A receptor Ly6e impairs syncytiotrophoblast fusion and placental morphogenesis causing embryonic lethality in mice. *Scientific Reports* *8*, 3961.
- Lanza, D.G., Gaspero, A., Lorenzo, I., Liao, L., Zheng, P., Wang, Y., Deng, Y., Cheng, C., Zhang, C., Seavitt, J.R., *et al.* (2018). Comparative analysis of single-stranded DNA donors to generate conditional null mouse alleles. *BMC Biol* *16*, 69.
- Leon, K., Cunningham, R.L., Riback, J.A., Feldman, E., Li, J., Sosnick, T.R., Zhao, M., Monk, K.R., and Araç, D. (2020). Structural basis for adhesion G protein-coupled receptor Gpr126 function. *Nat Commun* *11*, 194.

- Li, B., and Dewey, C.N. (2011). RSEM: accurate transcript quantification from RNA-Seq data with or without a reference genome. *BMC bioinformatics* 12, 323.
- Li, D.Y., Sorensen, L.K., Brooke, B.S., Urness, L.D., Davis, E.C., Taylor, D.G., Boak, B.B., and Wendel, D.P. (1999). Defective angiogenesis in mice lacking endoglin. *Science* 284, 1534-1537.
- Li, G., Xu, C., Lin, X., Qu, L., Xia, D., Hongdu, B., Xia, Y., Wang, X., Lou, Y., He, Q., *et al.* (2017). Deletion of *Pdcd5* in mice led to the deficiency of placenta development and embryonic lethality. *Cell Death & Disease* 8, e2811-e2811.
- Liao, W., Bisgrove, B.W., Sawyer, H., Hug, B., Bell, B., Peters, K., Grunwald, D.J., and Stainier, D.Y. (1997). The zebrafish gene *cloche* acts upstream of a *flk-1* homologue to regulate endothelial cell differentiation. *Development* 124, 381-389.
- Liebscher, I., Schön, J., Petersen, S.C., Fischer, L., Auerbach, N., Demberg, L.M., Mogha, A., Cöster, M., Simon, K.U., Rothmund, S., *et al.* (2014). A tethered agonist within the ectodomain activates the adhesion G protein-coupled receptors GPR126 and GPR133. *Cell Rep* 9, 2018-2026.
- Linask, K.K. (2013). The Heart-Placenta Axis in the First Month of Pregnancy: Induction and Prevention of Cardiovascular Birth Defects. *Journal of Pregnancy* 2013, 320413.
- Liu, J., Bressan, M., Hassel, D., Huisken, J., Staudt, D., Kikuchi, K., Poss, K.D., Mikawa, T., and Stainier, D.Y.R. (2010). A dual role for ErbB2 signaling in cardiac trabeculation. *Development* 137, 3867-3875.
- Liu, J., and Stainier, D.Y.R. (2012). Zebrafish in the study of early cardiac development. *Circulation research* 110, 870-874.
- Livak, K.J., and Schmittgen, T.D. (2001). Analysis of relative gene expression data using real-time quantitative PCR and the 2⁻($\Delta\Delta C_T$) Method. *Methods* 25, 402-408.
- Lopez-Mendez, M.A., Martinez-Gaytan, V., Cortes-Flores, R., Ramos-Gonzalez, R.M., Ochoa-Torres, M.A., Garza-Veloz, I., Martinez-Acuña, M.I., Badillo-Almaraz, J.I., and Martinez-Fierro, M.L. (2013). Doppler ultrasound evaluation in preeclampsia. *BMC Res Notes* 6, 477.
- Luxán, G., D'Amato, G., MacGrogan, D., and de la Pompa, J.L. (2016). Endocardial Notch Signaling in Cardiac Development and Disease. *Circ Res* 118, e1-e18.
- Lykke-Andersen, J., and Bennett, E.J. (2014). Protecting the proteome: Eukaryotic cotranslational quality control pathways. *J Cell Biol* 204, 467-476.

7. REFERENCES

- Ma, R., Gu, Y., Groome, L.J., and Wang, Y. (2011). ADAM17 regulates TNF α production by placental trophoblasts. *Placenta* 32, 975-980.
- MacGrogan, D., Münch, J., and de la Pompa, J.L. (2018). Notch and interacting signalling pathways in cardiac development, disease, and regeneration. *Nat Rev Cardiol* 15, 685-704.
- Martin, M. (2011). Cutadapt removes adapter sequences from high-throughput sequencing reads. 2011 17, 3.
- Maruyama, E.O., Lin, H., Chiu, S.Y., Yu, H.M., Porter, G.A., and Hsu, W. (2016). Extraembryonic but not embryonic SUMO-specific protease 2 is required for heart development. *Sci Rep* 6, 20999.
- Mazzuca, M.Q., and Khalil, R.A. (2012). Vascular endothelin receptor type B: structure, function and dysregulation in vascular disease. *Biochem Pharmacol* 84, 147-162.
- McMaster, M.T., and Fisher, S.J. (2003). Placental Development. In *Encyclopedia of Hormones*, H.L. Henry, and A.W. Norman, eds. (New York: Academic Press), pp. 213-219.
- Mehta, V., Pang, K.L., Rozbesky, D., Nather, K., Keen, A., Lachowski, D., Kong, Y., Karia, D., Ameismeier, M., Huang, J., *et al.* (2020). The guidance receptor plexin D1 is a mechanosensor in endothelial cells. *Nature* 578, 290-295.
- Meloty-Kapella, L., Shergill, B., Kuon, J., Botvinick, E., and Weinmaster, G. (2012). Notch ligand endocytosis generates mechanical pulling force dependent on dynamin, epsins, and actin. *Dev Cell* 22, 1299-1312.
- Menendez-Montes, I., Escobar, B., Palacios, B., Gómez, M.J., Izquierdo-Garcia, J.L., Flores, L., Jiménez-Borreguero, L.J., Aragonés, J., Ruiz-Cabello, J., Torres, M., *et al.* (2016). Myocardial VHL-HIF Signaling Controls an Embryonic Metabolic Switch Essential for Cardiac Maturation. *Dev Cell* 39, 724-739.
- Mitchell, G.F., Jeron, A., and Koren, G. (1998). Measurement of heart rate and Q-T interval in the conscious mouse. *Am J Physiol* 274, H747-751.
- Moens, C.B., Stanton, B.R., Parada, L.F., and Rossant, J. (1993). Defects in heart and lung development in compound heterozygotes for two different targeted mutations at the N-myc locus. *Development* 119, 485-499.

- Mogha, A., Benesh, A.E., Patra, C., Engel, F.B., Schöneberg, T., Liebscher, I., and Monk, K.R. (2013). Gpr126 functions in Schwann cells to control differentiation and myelination via G-protein activation. *J Neurosci* 33, 17976-17985.
- Monk, K.R., Hamann, J., Langenhan, T., Nijmeijer, S., Schöneberg, T., and Liebscher, I. (2015). Adhesion G Protein-Coupled Receptors: From In Vitro Pharmacology to In Vivo Mechanisms. *Mol Pharmacol* 88, 617-623.
- Monk, K.R., Naylor, S.G., Glenn, T.D., Mercurio, S., Perlin, J.R., Dominguez, C., Moens, C.B., and Talbot, W.S. (2009). A G protein-coupled receptor is essential for Schwann cells to initiate myelination. *Science* 325, 1402-1405.
- Monk, K.R., Oshima, K., Jörs, S., Heller, S., and Talbot, W.S. (2011). Gpr126 is essential for peripheral nerve development and myelination in mammals. *Development* 138, 2673-2680.
- Moorman, A.F., and Christoffels, V.M. (2003). Cardiac chamber formation: development, genes, and evolution. *Physiol Rev* 83, 1223-1267.
- Moriguchi, T., Haraguchi, K., Ueda, N., Okada, M., Furuya, T., and Akiyama, T. (2004). DREG, a developmentally regulated G protein-coupled receptor containing two conserved proteolytic cleavage sites. *Genes Cells* 9, 549-560.
- Müller, P.-S., Schulz, R., Maretto, S., Costello, I., Srinivas, S., Bikoff, E., and Robertson, E. (2011). The fibronectin leucine-rich repeat transmembrane protein Flrt2 is required in the epicardium to promote heart morphogenesis. *Development* 138, 1297-1308.
- Musa, G., Cazorla-Vázquez, S., van Amerongen, M.J., Stemmler, M.P., Eckstein, M., Hartmann, A., Braun, T., Brabletz, T., and Engel, F.B. (2019). Gpr126 (Adgrg6) is expressed in cell types known to be exposed to mechanical stimuli. *Ann N Y Acad Sci* 1456, 96-108.
- Nagy, A., Gócza, E., Diaz, E.M., Prideaux, V.R., Iványi, E., Markkula, M., and Rossant, J. (1990). Embryonic stem cells alone are able to support fetal development in the mouse. *Development* 110, 815-821.
- Paavola, K.J., Sidik, H., Zuchero, J.B., Eckart, M., and Talbot, W.S. (2014). Type IV collagen is an activating ligand for the adhesion G protein-coupled receptor GPR126. *Sci Signal* 7, ra76.
- Parks, A.L., Klueg, K.M., Stout, J.R., and Muskavitch, M.A. (2000). Ligand endocytosis drives receptor dissociation and activation in the Notch pathway. *Development* 127, 1373-1385.

- Passer, D., van de Vrugt, A., Atmanli, A., and Domian, I.J. (2016). Atypical Protein Kinase C-Dependent Polarized Cell Division Is Required for Myocardial Trabeculation. *Cell Rep* 14, 1662-1672.
- Patra, C., Monk, K.R., and Engel, F.B. (2014). The multiple signaling modalities of adhesion G protein-coupled receptor GPR126 in development. *Receptors Clin Investig* 1, 79.
- Patra, C., van Amerongen, M.J., Ghosh, S., Ricciardi, F., Sajjad, A., Novoyatleva, T., Mogha, A., Monk, K.R., Mühlfeld, C., and Engel, F.B. (2013). Organ-specific function of adhesion G protein-coupled receptor GPR126 is domain-dependent. *Proc Natl Acad Sci U S A* 110, 16898-16903.
- Pearson, W.R. (2013). An introduction to sequence similarity ("homology") searching. *Curr Protoc Bioinformatics Chapter 3*, Unit3.1.
- Perez-Garcia, V., Fineberg, E., Wilson, R., Murray, A., Mazzeo, C.I., Tudor, C., Sienerth, A., White, J.K., Tuck, E., Ryder, E.J., *et al.* (2018). Placentation defects are highly prevalent in embryonic lethal mouse mutants. *Nature* 555, 463-468.
- Perl, E., and Waxman, J.S. (2019). Reiterative Mechanisms of Retinoic Acid Signaling during Vertebrate Heart Development. *J Dev Biol* 7.
- Perschbacher, K.J., Deng, G., Fisher, R.A., Gibson-Corley, K.N., Santillan, M.K., and Grobe, J.L. (2018). Regulators of G protein signaling in cardiovascular function during pregnancy. *Physiol Genomics* 50, 590-604.
- Petersen, S.C., Luo, R., Liebscher, I., Giera, S., Jeong, S.J., Mogha, A., Ghidinelli, M., Feltri, M.L., Schöneberg, T., Piao, X., *et al.* (2015). The adhesion GPCR GPR126 has distinct, domain-dependent functions in Schwann cell development mediated by interaction with laminin-211. *Neuron* 85, 755-769.
- Plaks, V., Rinkenberger, J., Dai, J., Flannery, M., Sund, M., Kanasaki, K., Ni, W., Kalluri, R., and Werb, Z. (2013). Matrix metalloproteinase-9 deficiency phenocopies features of preeclampsia and intrauterine growth restriction. *Proc Natl Acad Sci U S A* 110, 11109-11114.
- Pogoda, H.M., Sternheim, N., Lyons, D.A., Diamond, B., Hawkins, T.A., Woods, I.G., Bhatt, D.H., Franzini-Armstrong, C., Dominguez, C., Arana, N., *et al.* (2006). A genetic screen identifies genes essential for development of myelinated axons in zebrafish. *Dev Biol* 298, 118-131.

- Puri, M.C., Rossant, J., Alitalo, K., Bernstein, A., and Partanen, J. (1995). The receptor tyrosine kinase TIE is required for integrity and survival of vascular endothelial cells. *Embo j* 14, 5884-5891.
- Qin, W., Kutny, P.M., Maser, R.S., Dion, S.L., Lamont, J.D., Zhang, Y., Perry, G.A., and Wang, H. (2016). Generating Mouse Models Using CRISPR-Cas9-Mediated Genome Editing. *Curr Protoc Mouse Biol* 6, 39-66.
- Rai, A., and Cross, J.C. (2014). Development of the hemochorial maternal vascular spaces in the placenta through endothelial and vasculogenic mimicry. *Dev Biol* 387, 131-141.
- Ranger, A.M., Grusby, M.J., Hodge, M.R., Gravalles, E.M., de la Brousse, F.C., Hoey, T., Mickanin, C., Baldwin, H.S., and Glimcher, L.H. (1998). The transcription factor NF-ATc is essential for cardiac valve formation. *Nature* 392, 186-190.
- Ravenscroft, G., Nolent, F., Rajagopalan, S., Meireles, A.M., Paavola, K.J., Gaillard, D., Alanio, E., Buckland, M., Arbuckle, S., Krivanek, M., *et al.* (2015). Mutations of GPR126 are responsible for severe arthrogryposis multiplex congenita. *Am J Hum Genet* 96, 955-961.
- Rawn, S., and Cross, J. (2008). The Evolution, Regulation, and Function of Placenta-Specific Genes. *Annual review of cell and developmental biology* 24, 159-181.
- Ream, M., Ray, A.M., Chandra, R., and Chikaraishi, D.M. (2008). Early fetal hypoxia leads to growth restriction and myocardial thinning. *Am J Physiol Regul Integr Comp Physiol* 295, R583-595.
- Red-Horse, K., Zhou, Y., Genbacev, O., Prakobphol, A., Foulk, R., McMaster, M., and Fisher, S.J. (2004). Trophoblast differentiation during embryo implantation and formation of the maternal-fetal interface. *J Clin Invest* 114, 744-754.
- Richardson, C.D., Ray, G.J., DeWitt, M.A., Curie, G.L., and Corn, J.E. (2016). Enhancing homology-directed genome editing by catalytically active and inactive CRISPR-Cas9 using asymmetric donor DNA. *Nat Biotechnol* 34, 339-344.
- Rivera-Torres, J., Calvo, C.J., Llach, A., Guzmán-Martínez, G., Caballero, R., González-Gómez, C., Jiménez-Borreguero, L.J., Guadix, J.A., Osorio, F.G., López-Otín, C., *et al.* (2016). Cardiac electrical defects in progeroid mice and Hutchinson-Gilford progeria syndrome patients with nuclear lamina alterations. *Proc Natl Acad Sci U S A* 113, E7250-E7259.

7. REFERENCES

- Robinson, M.D., McCarthy, D.J., and Smyth, G.K. (2010). edgeR: a Bioconductor package for differential expression analysis of digital gene expression data. *Bioinformatics* (Oxford, England) 26, 139-140.
- Rodriguez, T.A., Sparrow, D.B., Scott, A.N., Withington, S.L., Preis, J.I., Michalicek, J., Clements, M., Tsang, T.E., Shioda, T., Beddington, R.S., *et al.* (2004). Cited1 is required in trophoblasts for placental development and for embryo growth and survival. *Mol Cell Biol* 24, 228-244.
- Rossant, J., and Cross, J.C. (2001). Placental development: lessons from mouse mutants. *Nat Rev Genet* 2, 538-548.
- Saga, Y., Miyagawa-Tomita, S., Takagi, A., Kitajima, S., Miyazaki, J., and Inoue, T. (1999). MesP1 is expressed in the heart precursor cells and required for the formation of a single heart tube. *Development* 126, 3437-3447.
- Sakata, Y., Kamei, C.N., Nakagami, H., Bronson, R., Liao, J.K., and Chin, M.T. (2002). Ventricular septal defect and cardiomyopathy in mice lacking the transcription factor CHF1/Hey2. *Proceedings of the National Academy of Sciences* 99, 16197-16202.
- Sakata, Y., Koibuchi, N., Xiang, F., Youngblood, J.M., Kamei, C.N., and Chin, M.T. (2006). The spectrum of cardiovascular anomalies in CHF1/Hey2 deficient mice reveals roles in endocardial cushion, myocardial and vascular maturation. *J Mol Cell Cardiol* 40, 267-273.
- Sanchez, L., Prada, C., Riaño-Medina, C., and Lopez, M. (2014). Endothelial Dysfunction and Preeclampsia: Role of Oxidative Stress. *Frontiers in physiology* 5, 372.
- Savolainen, S.M., Foley, J.F., and Elmore, S.A. (2009). Histology atlas of the developing mouse heart with emphasis on E11.5 to E18.5. *Toxicol Pathol* 37, 395-414.
- Screen, M., Dean, W., Cross, J.C., and Hemberger, M. (2008). Cathepsin proteases have distinct roles in trophoblast function and vascular remodelling. *Development* 135, 3311-3320.
- Sedmera, D., Pexieder, T., Vuillemin, M., Thompson, R.P., and Anderson, R.H. (2000). Developmental patterning of the myocardium. *The Anatomical Record* 258, 319-337.
- Sedmera, D., Reckova, M., DeAlmeida, A., Coppen, S.R., Kubalak, S.W., Gourdie, R.G., and Thompson, R.P. (2003). Spatiotemporal pattern of commitment to slowed proliferation in the embryonic mouse heart indicates progressive differentiation of the cardiac conduction system. *Anat Rec A Discov Mol Cell Evol Biol* 274, 773-777.

- Shokry, M., Omran, O.M., Hassan, H.I., Elsedfy, G.O., and Hussein, M.R. (2009). Expression of matrix metalloproteinases 2 and 9 in human trophoblasts of normal and preeclamptic placentas: preliminary findings. *Exp Mol Pathol* 87, 219-225.
- Simmons, D.G., and Cross, J.C. (2005). Determinants of trophoblast lineage and cell subtype specification in the mouse placenta. *Dev Biol* 284, 12-24.
- Simmons, D.G., Fortier, A.L., and Cross, J.C. (2007). Diverse subtypes and developmental origins of trophoblast giant cells in the mouse placenta. *Dev Biol* 304, 567-578.
- Simmons, D.G., Natale, D.R., Begay, V., Hughes, M., Leutz, A., and Cross, J.C. (2008a). Early patterning of the chorion leads to the trilaminar trophoblast cell structure in the placental labyrinth. *Development* 135, 2083-2091.
- Simmons, D.G., Rawn, S., Davies, A., Hughes, M., and Cross, J.C. (2008b). Spatial and temporal expression of the 23 murine Prolactin/Placental Lactogen-related genes is not associated with their position in the locus. *BMC Genomics* 9, 352.
- Somekawa, S., Imagawa, K., Hayashi, H., Sakabe, M., Ioka, T., Sato, G.E., Inada, K., Iwamoto, T., Mori, T., Uemura, S., *et al.* (2012). Tmem100, an ALK1 receptor signaling-dependent gene essential for arterial endothelium differentiation and vascular morphogenesis. *Proc Natl Acad Sci U S A* 109, 12064-12069.
- Sones, J.L., and Davisson, R.L. (2016). Preeclampsia, of mice and women. *Physiol Genomics* 48, 565-572.
- Song, J., Yang, D., Xu, J., Zhu, T., Chen, Y.E., and Zhang, J. (2016). RS-1 enhances CRISPR/Cas9- and TALEN-mediated knock-in efficiency. *Nat Commun* 7, 10548-10548.
- Soriano, P. (1999). Generalized lacZ expression with the ROSA26 Cre reporter strain. *Nat Genet* 21, 70-71.
- Stainier, D.Y., Weinstein, B.M., Detrich, H.W., 3rd, Zon, L.I., and Fishman, M.C. (1995). Cloche, an early acting zebrafish gene, is required by both the endothelial and hematopoietic lineages. *Development* 121, 3141-3150.
- Stanley, E.G., Biben, C., Elefanty, A., Barnett, L., Koentgen, F., Robb, L., and Harvey, R.P. (2002). Efficient Cre-mediated deletion in cardiac progenitor cells conferred by a 3'UTR-ires-Cre allele of the homeobox gene Nkx2-5. *Int J Dev Biol* 46, 431-439.

7. REFERENCES

- Stehlik, C., Kroismayr, R., Dorfleutner, A., Binder, B.R., and Lipp, J. (2004). VIGR--a novel inducible adhesion family G-protein coupled receptor in endothelial cells. *FEBS Lett* 569, 149-155.
- Sugden, W.W., Meissner, R., Aegerter-Wilmsen, T., Tsaryk, R., Leonard, E.V., Bussmann, J., Hamm, M.J., Herzog, W., Jin, Y., Jakobsson, L., *et al.* (2017). Endoglin controls blood vessel diameter through endothelial cell shape changes in response to haemodynamic cues. *Nat Cell Biol* 19, 653-665.
- Sun, P., He, L., Jia, K., Yue, Z., Li, S., Jin, Y., Li, Z., Siwko, S., Xue, F., Su, J., *et al.* (2020). Regulation of body length and bone mass by Gpr126/Adgrg6. *Science Advances* 6, eaaz0368.
- Tai-Nagara, I., Yoshikawa, Y., Numata, N., Ando, T., Okabe, K., Sugiura, Y., Ieda, M., Takakura, N., Nakagawa, O., Zhou, B., *et al.* (2017). Placental labyrinth formation in mice requires endothelial FLRT2/UNC5B signaling. *Development* 144, 2392-2401.
- Tallquist, M.D., and Soriano, P. (2000). Epiblast-restricted Cre expression in MORE mice: a tool to distinguish embryonic vs. extra-embryonic gene function. *Genesis* 26, 113-115.
- Thai, S.N., and Iruela-Arispe, M.L. (2002). Expression of ADAMTS1 during murine development. *Mech Dev* 115, 181-185.
- Van Kempen, M.J., Vermeulen, J.L., Moorman, A.F., Gros, D., Paul, D.L., and Lamers, W.H. (1996). Developmental changes of connexin40 and connexin43 mRNA distribution patterns in the rat heart. *Cardiovasc Res* 32, 886-900.
- Venkatesha, S., Toporsian, M., Lam, C., Hanai, J., Mammoto, T., Kim, Y.M., Bdolah, Y., Lim, K.H., Yuan, H.T., Libermann, T.A., *et al.* (2006). Soluble endoglin contributes to the pathogenesis of preeclampsia. *Nat Med* 12, 642-649.
- Wagner, D.S., Dosch, R., Mintzer, K.A., Wiemelt, A.P., and Mullins, M.C. (2004). Maternal control of development at the midblastula transition and beyond: mutants from the zebrafish II. *Dev Cell* 6, 781-790.
- Waller-Evans, H., Prömel, S., Langenhan, T., Dixon, J., Zahn, D., Colledge, W.H., Doran, J., Carlton, M.B., Davies, B., Aparicio, S.A., *et al.* (2010). The orphan adhesion-GPCR GPR126 is required for embryonic development in the mouse. *PLoS One* 5, e14047.
- Wang, A., Rana, S., and Karumanchi, S.A. (2009). Preeclampsia: the role of angiogenic factors in its pathogenesis. *Physiology (Bethesda)* 24, 147-158.

- Watson, E.D., and Cross, J.C. (2005). Development of structures and transport functions in the mouse placenta. *Physiology (Bethesda)* 20, 180-193.
- Westerfield, M. (2000). *The Zebrafish Book: A Guide for the Laboratory Use of Zebrafish (Danio Rerio)* (University of Oregon Press).
- Whitfield, T.T., Granato, M., van Eeden, F.J., Schach, U., Brand, M., Furutani-Seiki, M., Haffter, P., Hammerschmidt, M., Heisenberg, C.P., Jiang, Y.J., *et al.* (1996). Mutations affecting development of the zebrafish inner ear and lateral line. *Development* 123, 241-254.
- Whitley, G.S.J., and Cartwright, J.E. (2010). Cellular and Molecular Regulation of Spiral Artery Remodelling: Lessons from the Cardiovascular Field. *Placenta* 31, 465-474.
- Wiemers, D.O., Ain, R., Ohboshi, S., and Soares, M.J. (2003). Migratory trophoblast cells express a newly identified member of the prolactin gene family. *J Endocrinol* 179, 335-346.
- Winterhager, E., and Gellhaus, A. (2017). Transplacental Nutrient Transport Mechanisms of Intrauterine Growth Restriction in Rodent Models and Humans. *Front Physiol* 8, 951.
- Woo, K.V., Qu, X., Babaev, V.R., Linton, M.F., Guzman, R.J., Fazio, S., and Baldwin, H.S. (2011). Tie1 attenuation reduces murine atherosclerosis in a dose-dependent and shear stress-specific manner. *J Clin Invest* 121, 1624-1635.
- Wooding, F.B.P., and Flint, A.P.F. (1994). Placentation. In *Marshall's Physiology of Reproduction: Volume 3 Pregnancy and Lactation*, G.E. Lamming, ed. (Dordrecht: Springer Netherlands), pp. 233-460.
- Woods, L., Perez-Garcia, V., and Hemberger, M. (2018). Regulation of Placental Development and Its Impact on Fetal Growth-New Insights From Mouse Models. *Front Endocrinol (Lausanne)* 9, 570.
- Wu, B., Zhang, Z., Lui, W., Chen, X., Wang, Y., Chamberlain, A.A., Moreno-Rodriguez, R.A., Markwald, R.R., O'Rourke, B.P., Sharp, D.J., *et al.* (2012). Endocardial cells form the coronary arteries by angiogenesis through myocardial-endocardial VEGF signaling. *Cell* 151, 1083-1096.
- Zadora, J., Singh, M., Herse, F., Przybyl, L., Haase, N., Golic, M., Yung, H.W., Huppertz, B., Cartwright, J.E., Whitley, G., *et al.* (2017). Disturbed Placental Imprinting in Preeclampsia Leads to Altered Expression of DLX5, a Human-Specific Early Trophoblast Marker. *Circulation* 136, 1824-1839.

7. REFERENCES

- Zambon, A.C., Gaj, S., Ho, I., Hanspers, K., Vranizan, K., Evelo, C.T., Conklin, B.R., Pico, A.R., and Salomonis, N. (2012). GO-Elite: a flexible solution for pathway and ontology over-representation. *Bioinformatics* 28, 2209-2210.
- Zammit, D.J., Berzins, S.P., Gill, J.W., Randle-Barrett, E.S., Barnett, L., Koentgen, F., Lambert, G.W., Harvey, R.P., Boyd, R.L., and Classon, B.J. (2002). Essential role for the lymphostromal plasma membrane Ly-6 superfamily molecule thymic shared antigen 1 in development of the embryonic adrenal gland. *Mol Cell Biol* 22, 946-952.
- Zhao, W.X., Huang, T.T., Jiang, M., Feng, R., and Lin, J.H. (2014). Expression of notch family proteins in placentas from patients with early-onset severe preeclampsia. *Reprod Sci* 21, 716-723.
- Zhou, B., von Gise, A., Ma, Q., Rivera-Feliciano, J., and Pu, W.T. (2008). Nkx2-5- and Isl1-expressing cardiac progenitors contribute to proepicardium. *Biochem Biophys Res Commun* 375, 450-453.
- Zhu, J., Zhong, M., Pang, Z., and Yu, Y. (2014). Dysregulated expression of matrix metalloproteinases and their inhibitors may participate in the pathogenesis of pre-eclampsia and fetal growth restriction. *Early Hum Dev* 90, 657-664.

ANNEXES

SCRIPTS

Script 1. Quantification of Hypoxyprobe mean thresholded intensity levels and the area occupied by the Hypoxyprobe positive staining as a proportion of the total placental area (ratio).

```
//Getting Fiji and ROI Manager ready

run("Close All");
run("Clear Results");
roiManager("Reset");
run("Colors...", "foreground=white background=black selection=yellow");

input=getDirectory("Choose folder with ND2 images...");
output=getDirectory("Choose folder to save results...");
lista = getFileList(input);
myposition=0;
setBatchMode(true);
for (i=0; i<lista.length; i++) {
    if (endsWith(lista[i], "nd2")==1) {
        run("Bio-Formats Importer", "open=["+input+lista[i]+"]
        color_mode=Composite view=Hyperstack stack_order=XYCZT");
        myname=getTitle();
        myORI=getImageID();
        selectImage(myORI);
        getPixelSize(unit, pixelWidth, pixelHeight);
        rename("ORI");
        run("Split Channels");
        selectWindow("C2-ORI");
        close();

        //Detect tissue area

        run("Duplicate...", "title=Tissue");
        run("Enhance Contrast...", "saturated=10");
        run("Gaussian Blur...", "sigma=2");
        setThreshold(10, 4095);
        run("Analyze Particles...", "size=8000-Infinity pixel show=Masks include");
        setThreshold(1, 255);
        run("Create Selection");
        roiManager("Add");

        //Measure tissue area and get Mean and Integrated Density intensity values

        selectWindow("C1-ORI");
        roiManager("Select", 0);
        getStatistics(areatissue);
        List.setMeasurements;
        MeanIntensity=List.getValue("Mean");
        IntegratedDensity=List.getValue("IntDen");

        //% of green signal
    }
}
```

```
//Use intensity threshold
//setAutoThreshold("Otsu dark");
setThreshold(578, 4095);
getThreshold(lower, upper);
List.setMeasurements("limit");
MeanThresholdIntensity=List.getValue("Mean");
PositiveAreaPercentaje=List.getValue("%Area");

//Save Result image

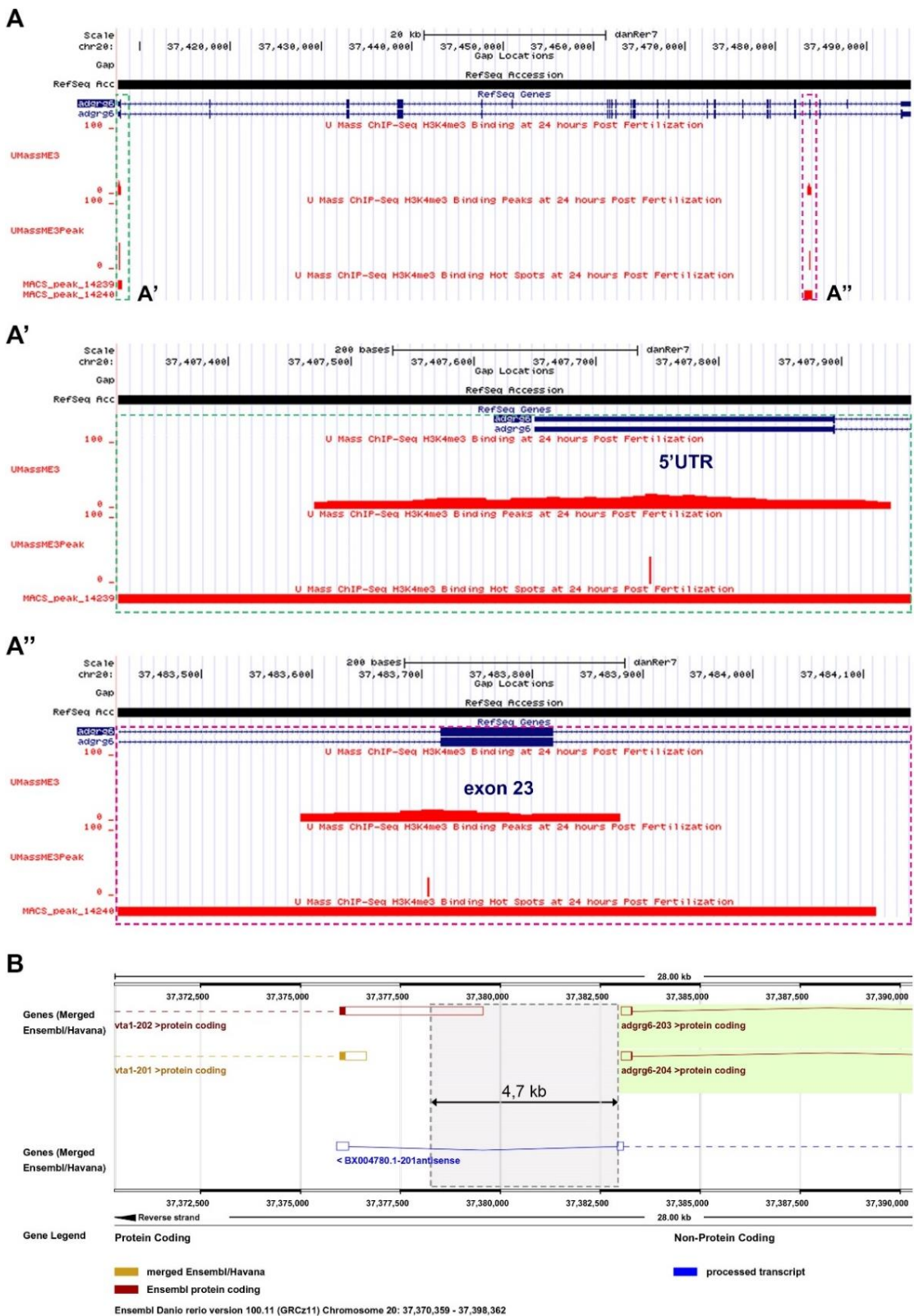
selectWindow("C1-ORI");
run("Flatten");
saveAs("tif", output+myname+"_Selection_Hypoxiprobe");
run("Close All");
roiManager("reset");

//Create Result Table

run("Clear Results");
if (isOpen("TempResults")){Table.rename("TempResults", "Results");}
setResult("Image name", myposition, myname);
setResult("Tissue Area "+unit+"^2", myposition, areatissue);
setResult("Tissue Mean Intensity", myposition, MeanIntensity);
setResult("Tissue Integrated Density", myposition, IntegratedDensity);
setResult("Min Threshold Value", myposition, lower);
setResult("Positive Area % "+unit+"^2", myposition, PositiveAreaPercentaje);
setResult("Thresholded Mean Intensity", myposition, MeanThresholdIntensity);
updateResults();
Table.rename("Results", "TempResults");
myposition++;
}
}

if (isOpen("TempResults")){Table.rename("TempResults", "Results");}
selectWindow("Results");
saveAs("Results", output+"Hypoxiprobe_Results.xls");
saveAs("Results", output+"Hypoxiprobe_Results.txt");
```

SUPPLEMENTARY FIGURES



Supplementary Figure 1. Identification of *gpr126* active promoters by ChIP-seq data set analysis. (A) Genome browser view of H3K4me3 histone modification marks in the *adgrg6* locus from a sample of zebrafish embryos at 24 hpf. Two strong H3K4me3 binding peaks can be detected in a ~470 bp region around the TSS (A') and a ~250 bp region around exon 23 (A''). (B) ENSEMBL view of the zebrafish *gpr126* gene and the upstream adjacent gene *vta1*. The region highlighted in grey corresponds to the 4.7 kb sequence targeted for CRISPR-mediated deletion.

SUPPLEMENTARY TABLES

Stage	<i>Gpr126</i> ^{+/+}	<i>Gpr126</i> ^{Δ3,4/+}	<i>Gpr126</i> ^{Δ3,4/Δ3,4}	Resorptions	Total pups	Litters
E9.5	2 20.00%	6 60.00%	2 20.00%	0	10	1
E10.5	4 26.67%	5 33.33%	6 40.00%	0	15	2
E11.5	1 12.50%	6 75.00%	1 12.50%	1	8	1
E12.5	4 19.05%	9 42.86%	8 38.10%	1	21	3
E14.5	4 23.53%	8 47.06%	5 35.29%	0	17	2
E16.5	5 20.83%	11 45.83%	8 25.00%	3	24	4
E17.5	2 14.29%	9 64.29%	3 42.86%	0	14	2
E18.5	12 26.67%	16 35.56%	17 13.33%	0	45	7
P0	1 14.29%	3 42.86%	3 85.71%	0	7	1
P2	2 28.57%	2 28.57%	3 85.71%	0	7	1

Supplementary Table 1. Genotype analysis of embryos derived from heterozygous *Gpr126*^{Δ3,4/+} intercrosses.

Stage	<i>Gpr126</i> ^{+/+}	<i>Gpr126</i> ^{Δ7/+}	<i>Gpr126</i> ^{Δ7/Δ7}	Resorptions	Total pups	Litters
E9.5	4 22.22%	9 50.00%	5 27.78%	0	18	2
E10.5	7 22.58%	13 41.94%	9 + 2* 35.48%	2	31	4
E11.5	30 18.07%	80 + 1* 48.80%	45 + 10* 33.13%	23	166	24
E12.5	107 + 2* 25.83%	200 + 1* 47.63%	92 + 20* 26.54%	64	422	67
E13.5	6 17.65%	20 58.82%	2 + 6* 23.53%	4	34	5
E15.5	16 25.00%	39 60.94%	9* 14.06%	2	64	9

* Dead

Supplementary Table 2. Genotype analysis of embryos derived from heterozygous *Gpr126*^{Δ7/+} intercrosses.

Supplementary Table 3 (CD-ROM). RNA-seq analysis of *Gpr126*^{Δ7/Δ7} versus *Gpr126*^{+/+} ventricles at E12.5.

List of the differentially expressed genes (DEG) identified by RNA-seq ($P < 0.05$). Upregulation is shown in orange and downregulation in blue.

Supplementary Table 4 (CD-ROM). GO enrichment analysis of DEG genes.

Overrepresented GO terms and KEGG pathways for the differentially upregulated and downregulated genes. Oversecretion is shown in red, and downsecretion in blue. GO terms are listed by the Z-score value. Data are the standard output from GO Elite.

Stage	<i>Gpr126^{fl/+}; Nfatc1^{+/+}</i>	<i>Gpr126^{fl/fl}; Nfatc1^{+/+}</i>	<i>Gpr126^{fl/+}; Nfatc1^{Cre/+}</i>	<i>Gpr126^{fl/fl}; Nfatc1^{Cre/+}</i>	Resorptions	Total pups	Litters
E11.5	2 25.00%	2 25.00%	1 12.50%	3 37.50%	0	8	1
E13.5	6 40.00%	2 13.33%	4 26.67%	3 20.00%	0	15	2
E15.5	4 33.33%	1 8.33%	4+1* 41.67%	2 16.67%	0	12	2
E18.5	3 17.65%	5 29.41%	4 23.53%	4 23.53%	0	17	3

* Dead

Supplementary Table 5. Genotype analysis of embryos derived from crosses of *Gpr126^{fl/+};* *Nfatc1^{Cre/+}* (male) and *Gpr126^{fl/fl}* (female) mice.

Stage	<i>Gpr126^{fl/+}; Tie2^{+/+}</i>	<i>Gpr126^{fl/fl}; Tie2^{+/+}</i>	<i>Gpr126^{fl/+}; Tie2^{Cre/+}</i>	<i>Gpr126^{fl/fl}; Tie2^{Cre/+}</i>	Resorptions	Total pups	Litters
E11.5	2 28.57%	2 28.57%	1 14.29%	2 28.57%	0	7	1
E13.5	3 50.00%	1 16.67%	0 0.00%	2 33.33%	0	6	1
E15.5	8 38.10%	4 19.05%	6 28.57%	3 14.29%	0	21	3
E18.5	2 22.22%	2 22.22%	2 22.22%	1 11.11%	0	9	1

Supplementary Table 6. Genotype analysis of embryos derived from crosses of *Gpr126^{fl/+};* *Tie2^{Cre/+}* (male) and *Gpr126^{fl/fl}* (female) mice.

Stage	<i>Gpr126^{fl/+}; Mesp1^{+/+}</i>	<i>Gpr126^{fl/fl}; Mesp1^{+/+}</i>	<i>Gpr126^{fl/+}; Mesp1^{Cre/+}</i>	<i>Gpr126^{fl/fl}; Mesp1^{Cre/+}</i>	Resorptions	Total pups	Litters
E12.5	6 17.65%	8 23.53%	6 17.65%	14 41.18%	4	34	5
E13.5	3 37.50%	2 25.00%	0 0.00%	3 37.50%	0	8	1
E15.5	3 42.86%	0 0.00%	1 14.29%	3 42.86%	0	7	1
E18.5	3 23.08%	5 38.46%	2 15.38%	3 23.08%	0	13	2

Supplementary Table 7. Genotype analysis of embryos derived from crosses of *Gpr126^{fl/+};* *Mesp1^{Cre/+}* (male) and *Gpr126^{fl/fl}* (female) mice.

Stage	<i>Gpr126^{fl/Δ7}; Tie2^{+/+}</i>		<i>Gpr126^{Δ7/+}; Tie2^{+/+}</i>		<i>Gpr126^{+/+}; Tie2^{+/+}</i>		<i>Gpr126^{fl/Δ7}; Tie2^{Cre/+}</i>		<i>Gpr126^{Δ7/+}; Tie2^{Cre/+}</i>		<i>Gpr126^{fl/+}; Tie2^{Cre/+}</i>		<i>Gpr126^{+/+}; Tie2^{Cre/+}</i>		Resorp.	Total pups	Litters
E14.5	0	0.00%	0	0.00%	1	12.50%	4	50.00%	1	12.50%	0	0.00%	2	25.00%	0	8	1
E15.5	9	11.25%	11	13.75%	4	5.00%	8	10.00%	9 + 1*	12.50%	16	20.00%	5	6.25%	5	80	11
E16.5	10	14.29%	6	8.57%	2	2.86%	16	22.86%	5	7.14%	15	21.43%	5	7.14%	5	70	9
E18.5	1	3.70%	6	22.22%	2	7.41%	5	18.52%	3	11.11%	2	7.41%	0	0.00%	2	27	4

* Dead

Supplementary Table 8. Genotype analysis of embryos derived from crosses of *Gpr126^{Δ7/+}; Tie2^{Cre/+}* (male) and *Gpr126^{fl/fl}* (female) mice.

Resorp, resorptions.

Supplementary Table 9. Genotype analysis of embryos derived from crosses of *Gpr126*^{Δ7/+}; *Mesp1*^{Cre/+} (male) and *Gpr126*^{fl/fl} (female) mice.

Resorp, resorptions.

Stage	<i>Gpr126</i> ^{fl/Δ7} ; <i>Mesp1</i> ^{+/+}		<i>Gpr126</i> ^{Δ7/+} ; <i>Mesp1</i> ^{+/+}		<i>Gpr126</i> ^{+/+} ; <i>Mesp1</i> ^{+/+}		<i>Gpr126</i> ^{fl/Δ7} ; <i>Mesp1</i> ^{Cre/+}		<i>Gpr126</i> ^{Δ7/+} ; <i>Mesp1</i> ^{Cre/+}		<i>Gpr126</i> ^{fl/+} ; <i>Mesp1</i> ^{Cre/+}		Resorp.	Total pups	Litters
E14.5	0	0.00%	3	13.64%	6	27.27%	2	9.09%	2	9.09%	2	9.09%	4	18.18%	3
E15.5	3	9.38%	1	3.13%	3	9.38%	5 + 1*	18.75%	5	15.63%	3	9.38%	7	21.88%	5
E16.5	2	11.76%	2	11.76%	0	0.00%	2	11.76%	3	17.65%	3	17.65%	1	5.88%	2

* Dead

Stage	<i>R26-GPR126^{+/+}; Nkx2.5^{Cre/+}</i>	<i>R26-GPR126^{GOF/+}; Nkx2.5^{Cre/+}</i>	Resorptions	Total pups	Litters
E9.5	2 25.00%	6 75.00%	5	8	2
E10.5	11 50.00%	11 50.00%	0	22	3

Supplementary Table 10. Genotype analysis of embryos derived from crosses of *Nkx2.5^{Cre/Cre}* (male) and *GPR126^{GOF/+}* (female) mice.

Stage	<i>R26-GPR126^{+/+}; Tie2^{Cre/+}</i>	<i>R26-GPR126^{GOF/+}; Tie2^{Cre/+}</i>	Resorptions	Total pups	Litters
E9.5	15 65.22%	8 34.78%	0	23	2
E10.5	2 25.00%	6 75.00%	0	8	1
E11.5	1 25.00%	3 75.00%	1	4	1
E13.5	2 25.00%	6 75.00%	0	8	1
E16.5	3 30.00%	7 70.00%	0	10	1

Supplementary Table 11. Genotype analysis of embryos derived from crosses of *Tie2^{Cre/Cre}* (male) and *GPR126^{GOF/+}* (female) mice.

Stage	<i>R26-GPRI126^{GOF/+}; R26-GPRI126^{GOF/+}; Gpr126^{Δ7/Δ7}; Tie2^{Crel/+}</i>						Total pups	Litters
	<i>R26-GPRI126^{GOF/+}; R26-GPRI126^{GOF/+}; Gpr126^{Δ7/Δ7}; Tie2^{Crel/+}</i>	<i>R26-GPRI126^{GOF/+}; R26-GPRI126^{GOF/+}; Gpr126^{Δ7/+}; Tie2^{+/+}</i>	<i>R26-GPRI126^{GOF/+}; R26-GPRI126^{GOF/+}; Gpr126^{+/+}; Tie2^{Crel/+}</i>	<i>R26-GPRI126^{GOF/+}; R26-GPRI126^{GOF/+}; Gpr126^{Δ7/+}; Tie2^{+/+}</i>	<i>R26-GPRI126^{GOF/+}; R26-GPRI126^{GOF/+}; Gpr126^{+/+}; Tie2^{Crel/+}</i>	<i>R26-GPRI126^{GOF/+}; R26-GPRI126^{GOF/+}; Gpr126^{Δ7/+}; Tie2^{+/+}</i>		
E13.5	3* 5.26%	3* + 2 8.77%	17 29.82%	16 28.07%	8 15.38%	8 15.387%	160	57
E14.5	2* 40.00%	1* 20.00%	0 0.00%	2 40.00%	0 0.00%	0 0.00%	2	5
* Dead								

Supplementary Table 12. Genotype analysis of embryos derived from crosses of *Gpr126*^{Δ7/+}; *Tie2*^{Cre/+} (male) and *GPR126*^{GOF/+}; *Gpr126*^{Δ7/+} (female) mice.

Resorp, resorptions.

Stage	R26- GPR126 ^{GOF/+} ; Dtl4 ^{fl/fl} , Tie2 ^{Cre/+}	R26- GPR126 ^{GOF/+} ; Dtl4 ^{fl/fl} , Tie2 ^{+/+}	R26- GPR126 ^{GOF/+} ; Dtl4 ^{fl/+} , Tie2 ^{Cre/+}	R26- GPR126 ^{GOF/+} ; Dtl4 ^{fl/+} , Tie2 ^{+/+}	R26- GPR126 ^{GOF/+} ; Dtl4 ^{+/+} , Tie2 ^{Cre/+}	R26- GPR126 ^{GOF/+} ; Dtl4 ^{+/+} , Tie2 ^{+/+}	Resorp.	Total pups	Litters
E9.5	3 21.43%	0 0.00%	5 35.71%	4 28.57%	1 7.14%	1 7.14%			
	4 28.57%	R26-GPR126 ^{+/+} ; Dtl4 ^{fl/fl} , Tie2 ^{+/+}	R26-GPR126 ^{+/+} ; Dtl4 ^{fl/+} , Tie2 ^{Cre/+}	R26-GPR126 ^{+/+} ; Dtl4 ^{fl/+} , Tie2 ^{+/+}	R26-GPR126 ^{+/+} ; Dtl4 ^{+/+} , Tie2 ^{Cre/+}	R26-GPR126 ^{+/+} ; Dtl4 ^{+/+} , Tie2 ^{+/+}	0	14	4
		3 21.43%	6 42.86%	3 21.43%	1 7.14%	0 0.00%			
E10.5	R26- GPR126 ^{GOF/+} ; Dtl4 ^{fl/fl} , Tie2 ^{Cre/+}	R26- GPR126 ^{GOF/+} ; Dtl4 ^{fl/fl} , Tie2 ^{+/+}	R26- GPR126 ^{GOF/+} ; Dtl4 ^{fl/+} , Tie2 ^{Cre/+}	R26- GPR126 ^{GOF/+} ; Dtl4 ^{fl/+} , Tie2 ^{+/+}	R26- GPR126 ^{GOF/+} ; Dtl4 ^{+/+} , Tie2 ^{Cre/+}	R26- GPR126 ^{GOF/+} ; Dtl4 ^{+/+} , Tie2 ^{+/+}			
	5 + 1* 11.32%	6 11.32%	9 16.98%	6 11.32%	0 0.00%	2 3.77%	9	53	7
		R26-GPR126 ^{+/+} ; Dtl4 ^{fl/fl} , Tie2 ^{+/+}	R26-GPR126 ^{+/+} ; Dtl4 ^{fl/+} , Tie2 ^{Cre/+}	R26-GPR126 ^{+/+} ; Dtl4 ^{fl/+} , Tie2 ^{+/+}	R26-GPR126 ^{+/+} ; Dtl4 ^{+/+} , Tie2 ^{Cre/+}	R26-GPR126 ^{+/+} ; Dtl4 ^{+/+} , Tie2 ^{+/+}			
	7 13.21%	6 11.32%	5 9.43%	5 9.43%	0 0.00%	1 1.89%			

* Dead

Supplementary Table 13.
Genotype analysis of embryos
derived from crosses of *Dtl4*^{fl/+};
Tie2^{Cre/+} (male) and *Dtl4*^{fl/+};
GPR126^{GOF/+} (female) mice.

Resorp, resorptions.

Supplementary Table 14 (CD-ROM). Sequence similarity analysis of zebrafish *gpr126*.

Supplementary Table 15 (CD-ROM). Sequence similarity analysis of mouse *Gpr126*.

Stage	<i>Gpr126^{fl/ko};</i> <i>Sox2^{Cre/+}</i>	<i>Gpr126^{fl/ko};</i> <i>Sox2^{+/+}</i>	<i>Gpr126^{ko/+};</i> <i>Sox2^{Cre/+}</i>	<i>Gpr126^{fl/+};</i> <i>Sox2^{+/+}</i>	Resorptions	Total pups	Litters
E13.5	9 + 3* 50.00%	8 33.33%	4 16.67%	4 16.67%	3	24	4
E15.5	10 + 3* 18.57%	16 22.86%	19 27.14%	22 31.43%	5	70	11
E16.5	9 + 3* 30.77%	9 23.08%	18 46.15%	13 33.33%	5	39	8
P0	4 + 4* 13.56%	18 30.51%	12 + 1* 22.03%	20 33.90%	0	59	10
P1	3 18.75%	3 18.75%	3 + 1* 25.00%	6 37.50%	0	16	2

* Dead

Supplementary Table 16. Genotype analysis of embryos derived from crosses of *Gpr126^{fl/+};*
Sox2^{Cre/+} (male) and *Gpr126^{fl/fl}* (female) mice.

Stage	<i>Gpr126^{ko/ko};</i> <i>Sox2^{Cre/+}</i>	<i>Gpr126^{ko/ko};</i> <i>Sox2^{+/+}</i>	<i>Gpr126^{ko/+};</i> <i>Sox2^{Cre/+}</i>	<i>Gpr126^{ko/+};</i> <i>Sox2^{+/+}</i>	Resorptions	Total pups	Litters
E13.5	8* 13.56%	6* 10.17%	26 44.07%	19 32.20%	8	59	9
E14.5	1* 6.67%	0 0.00%	8 53.33%	6 40.00%	2	15	2
E15.5	4* 12.90%	2 + 2* 12.90%	11 35.48%	12 38.71%	12	31	6

* Dead

Supplementary Table 17. Genotype analysis of embryos derived from crosses of *Gpr126^{fl/fl}*
(male) and *Gpr126^{fl/+};* *Sox2^{Cre/+}* (female) mice.

Stage	<i>R26-GPR126^{GOF/+}; Gpr126^{Δ7/Δ7}; Sox2^{Cre/+}</i>		<i>R26-GPR126^{GOF/+}; Gpr126^{Δ7/Δ7}; Sox2^{Cre/+}</i>		<i>R26-GPR126^{GOF/+}; Gpr126^{Δ7/+}; Sox2^{Cre/+}</i>		<i>R26-GPR126^{GOF/+}; Gpr126^{Δ7/+}; Sox2^{Cre/+}</i>		<i>R26-GPR126^{GOF/+}; Gpr126^{+/+}; Sox2^{+/+}</i>		Resorp.	Total pups	Litters
E13.5	0 0.00%	1* 1.85%	21 38.89%	18 33.33%	6 11.11%	8 14.81%	23	54	10				
E14.5	2* 4.55%	0 0.00%	10 22.73%	17 38.64%	9+1* 22.73%	5 11.36%	15	44	9				
E15.5	0 0.00%	0 0.00%	11 34.38%	15 46.88%	2 6.25%	4 12.50%	10	32	6				
E16.5	1* 20.00%	0 0.00%	1 20.00%	0 0.00%	1 20.00%	2 40.00%	0	5	1				

* Dead

Supplementary Table 18. Genotype analysis of embryos derived from crosses of *Gpr126^{Δ7/+}*; *Sox2^{Cre/+}* (male) and *GPR126^{GOF/GOF}*; *Gpr126^{Δ7/+}* (female) mice.

Resorp, resorptions.

Cover and back cover.

Artwork illustrating the placenta-heart connection, by David Alcántara Rubio.

